Volume 3 Issue 2 | April 2023

MICROSTRUCTURES

Editor-in-Chief: Prof. Shujun Zhang

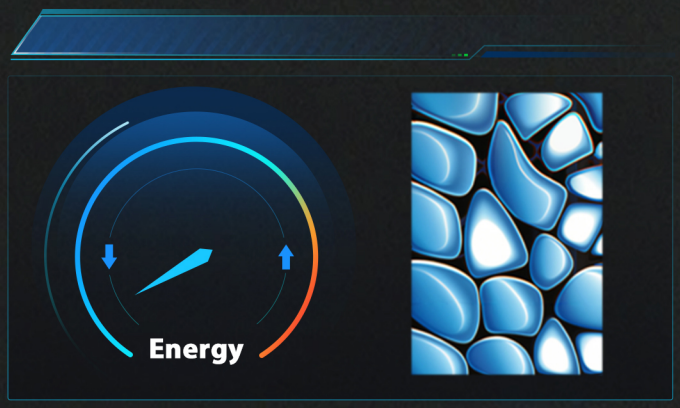

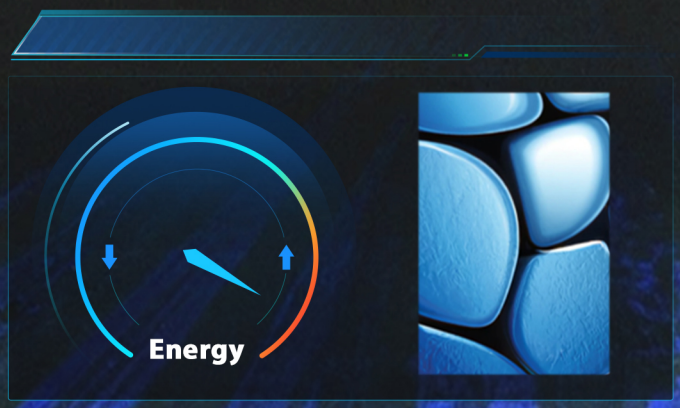

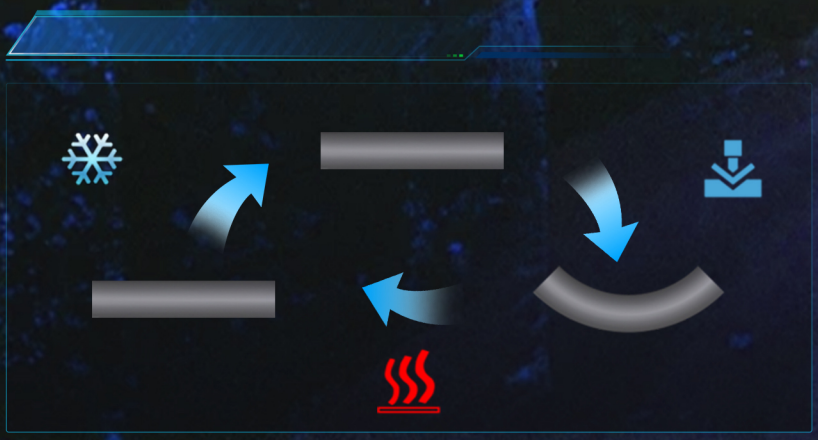

Microstructure evolution in laser powder bed fusion- built Fe-Mn-Si shape memory alloy

Michael Leo Dela Cruz, Vladislav Yakubov, Xiaopeng Li, Michael Ferry

Open Access
ISSN 2770-2995 (Online)
www.microstructj.com

EDITORIAL BOARD

Editor-in-Chief

Shujun Zhang (Australia)

Executive Editors

Jun Chen (China)
Xiaozhou Liao (Australia)

Junior Executive Editors

Zibin Chen (China)
Shiqing Deng (China)

Associate Editors

Yida Deng (China)
Ning Gao (China)
Lin Gu (China)
Jiamian Hu (USA)
Xiaoning Jiang (USA)
Liangzhi Kou (Australia)
Fei Li (China)
Charlene Lobo (Australia)
Yang Ren (USA)
Andrea Sanson (Italy)
Lianzhou Wang (Australia)
Yandong Wang (China)
Chengtie Wu (China)
Qian Yu (China)
Ting Zhu (USA)
Xiaoying Zhuang (Germany)

Senior Editorial Board Members

Nazanin Bassiri-Gharb (USA)
Daolun Chen (Canada)
Zhi-Gang Chen (Australia)
Neus Domingo (USA)
Yi Du (Australia)
Alexei Gruverman (USA)
Zaiping Guo (Australia)
Xiaodong Han (China)
Sergei V. Kalinin (USA)
Huijun Li (Australia)
Jiangyu Li (China)
Yun Liu (Australia)
Yunhau Ng (China)
Timon Rabczuk (Germany)
Dong Su (China)
Litao Sun (China)
Jian Wang (USA)
Yin Xiao (Australia)
Shanqing Zhang (Australia)
Chun-Xia Zhao (Australia)
Yuntian Zhu (USA)
Rongkun Zheng (Australia)

Editorial Board Members

Matthew Cabral (USA)
Shaobo Cheng (China)
Charlotte Cochard (UK)
Zhanxi Fan (China)
Xuewen Fu (China)
Sophia Gu (Australia)
Yuxiao Lai (China)
Si Lan (China)
Ting Li (China)
Junhao Lin (China)
Danmin Liu (China)
Shen Liu (China)
Hongshi Ma (China)
Kasra Momeni (USA)
Mojca Otoničar (Slovenia)
Zhihua Sun (China)
Chunming Wang (China)
Dawei Wang (China)
Haitao Li (China)
Xiupeng Wang (Japan)
Zhenglong Xu (China)
Tao Yang (China)
Yulin Zhong (Australia)
Chunqiang Zhuang (China)
Sarina Sarina (Australia)
Xusheng Yang (China)
Yang Cao (China)

GENERAL INFORMATION

About the Journal

Microstructures, ISSN 2770-2995 (Online), is a peer-reviewed and continuously published online journal with print on demand compilation of articles published. The journal's full text is available online at www.jcmtjournal.com. The journal allows free access (Open Access) to its contents and permits authors to self-archive final accepted version of Microstructure, which is the nature, quantity and distribution of structural elements or phases that make up materials, determines the properties of materials. Understanding microstructure-properties relationships is critical for the design of materials. With the increase of demand and investment in new materials around the globe, there has been a great deal of interest in the exploration and manipulation of microstructure in materials science and engineering.

Information for Authors

Manuscripts should be prepared in accordance with Author Instructions.
Please check www.microstructj.com/pages/view/author_instructions for details.
All manuscripts should be submitted online at https://oaemesas.com/login?JournalId=microstructures.

Copyright

The entire contents of the *Microstructures* are protected under international copyrights. The journal, however, grants to all users a free, irrevocable, worldwide, perpetual right of access to, and a license to copy, use, distribute, perform and display the work publicly and to make and distribute derivative works in any digital medium for any reasonable purpose, subject to proper attribution of authorship and ownership of the rights. The journal also grants the right to make small numbers of printed copies for their personal use under the Creative Commons Attribution 4.0 License.
Copyright is reserved by © The Author(s) 2023.

Permissions

For information on how to request permissions to reproduce articles/information from this journal, please visit www.microstructj.com.

Disclaimer

The information and opinions presented in the journal reflect the views of the authors and not of the journal or its Editorial Board or the Publisher. Publication does not constitute endorsement by the journal. Neither the *Microstructures* nor its publishers nor anyone else involved in creating, producing or delivering the *Microstructures* or the materials contained therein, assumes any liability or responsibility for the accuracy, completeness, or usefulness of any information provided in the *Microstructures*, nor shall they be liable for any direct, indirect, incidental, special, consequential or punitive damages arising out of the use of the *Microstructures*. The *Microstructures*, nor its publishers, nor any other party involved in the preparation of material contained in the *Microstructures* represents or warrants that the information contained herein is in every respect accurate or complete, and they are not responsible for any errors or omissions or for the results obtained from the use of such material. Readers are encouraged to confirm the information contained herein with other sources.

Publisher

OAE Publishing Inc.
245 E Main Street st112, Alhambra, CA 91801, USA
Website: www.oaepublish.com

Contacts

E-mail: editorialoffice@microstructj.com
Website: www.microstructj.com

Microstructures

CONTENTS

Volume 3 / Issue 2 / April 2023 /

Liu *et al. Microstructures* 2023;3:2023009
DOI: 10.20517/microstructures.2022.29

Microstructures

Research Article

Open Access

Check for updates

Energy storage properties of $NaNbO_3$-based lead-free superparaelectrics with large antiferrodistortion

Guanfu Liu, Liang Chen, He Qi

Beijing Advanced Innovation Center for Materials Genome Engineering, Department of Physical Chemistry, University of Science and Technology Beijing, Beijing 100083, China.

Correspondence to: Prof./Dr. He Qi, Beijing Advanced Innovation Center for Materials Genome Engineering, Department of Physical Chemistry, University of Science and Technology Beijing, No. 30 Xueyuan Road, Haidian District, Beijing 100083, China. E-mail: qiheustb@ustb.edu.cn

How to cite this article: Liu G, Chen L, Qi H. Energy storage properties of $NaNbO_3$-based lead-free superparaelectrics with large antiferrodistortion. *Microstructures* 2023;3:2023009. https://dx.doi.org/10.20517/microstructures.2022.29

Received: 25 Sep 2022 **First Decision:** 7 Nov 2022 **Revised:** 28 Nov 2022 **Accepted:** 26 Dec 2022 **Published:** 12 Jan 2023

Academic Editors: Zhihua Sun, Ruzhong Zuo **Copy Editor:** Fangling Lan **Production Editor:** Fangling Lan

Abstract

$NaNbO_3$-based lead-free energy storage ceramics are essential candidates for next-generation pulsed power capacitors, especially under the background of energy saving and environmental protection. However, the room-temperature antiferroelectric P phase of pure $NaNbO_3$ ceramics limits its further development in energy storage owing to the irreversible antiferroelectric to ferroelectric phase transition under electric fields. In this work, $CaZrO_3$ was introduced to $NaNbO_3$ ceramics to destroy the long-range polarization ordering but keep large antiferrodistortion, causing the formation of superparaelectric state with macrodomains, which can be identified by the refinement results of high-energy synchrotron X-ray diffraction, neutron diffraction and TEM results. Combined with the fine grains, dense and homogeneous microstructure, ergodic relaxation behaviors, and delayed polarization saturation, a high recoverable energy storage density of ~5.4 J/cm^3 and efficiency of ~82% can be realized in $0.85NaNbO_3$-$0.15CaZrO_3$ ceramics at an ultrahigh breakdown electric field of ~68 kV/mm. The results found in this work suggest that the supersparaelectric with non-cubic phase would be a good candidate for generating excellent dielectric energy storage properties.

Keywords: $NaNbO_3$, energy storage, relaxor ferroelectric, oxygen octahedral distortion

INTRODUCTION

Energy plays an irreplaceable role in the development of human society, and how to efficiently store energy

© The Author(s) 2023. **Open Access** This article is licensed under a Creative Commons Attribution 4.0 International License (https://creativecommons.org/licenses/by/4.0/), which permits unrestricted use, sharing, adaptation, distribution and reproduction in any medium or format, for any purpose, even commercially, as long as you give appropriate credit to the original author(s) and the source, provide a link to the Creative Commons license, and indicate if changes were made.

has gradually become the focus of research. Currently, energy storage devices are mainly divided into four categories: lithium-ion batteries, fuel cells, electrochemical super-capacitors, and dielectric capacitors[1-3]. Solid-state dielectric capacitors, compared with other energy storage devices, possess high power density and ultrafast charge-discharge rates, which are widely used in advanced high power and pulse power electronic devices, such as hybrid electric vehicles, distributed power systems, and directional energy weapons[4,5]. However, the low recoverable energy storage density (W_{rec}) limits their energy storage development.

In the context of energy saving and environmental protection, to effectively improve the W_{rec} of dielectric capacitors, lead-free perovskite energy storage ceramics have become a research hotspot[6,7]. The total energy storage density (W_{total}), W_{rec}, and efficiency (η) are the main parameters to evaluate energy storage performance which can be calculated based on the following formula:

$$W_{rec} = \int_{P_r}^{P_{max}} EdP \tag{1}$$

$$W_{total} = \int_{0}^{P_{max}} EdP \tag{2}$$

$$\eta = \frac{W_{rec}}{W_{total}} \tag{3}$$

where P_{max}, P_r, and E are the maximum polarization, remanent polarization, and applied electric field, respectively. As a result, large ΔP (P_{max}-P_r) and high E_b are indispensable for materials with high W_{rec} [8]. The researches on lead-free energy storage materials generally focus on linear dielectrics, ferroelectrics, antiferroelectrics, and relaxor ferroelectrics. Linear dielectrics possess ultrahigh η and E_b but low W_{rec} due to their low polarization characteristic[9]. Both high P_{max} and P_r can be found in ferroelectrics, resulting in highly inferior W_{rec} and η. Similarly, antiferroelectrics also own unsatisfactory energy storage properties with low η and poor cycle stability because of irreversible antiferroelectric to ferroelectric phase transition under applied electric field and comparatively significant difference between E_F and E_A [10-12]. Relaxor ferroelectrics are characterized by a diffuse phase transition over a broad temperature range, from the Burns temperature (T_B) at which nanodomains appear, to the intermediate temperature (T_m) at which nanodomains grow and the permittivity reaches the maximum, and finally to the freezing temperature (T_f) at which nanodomains become frozen($T_f < T_m < T_B$)[13,14]. In particular, relaxor ferroelectrics located at the temperature range of T_m-T_B can be defined as superparaelectrics, in which the size of nanodomains is further decreased, and the domain interaction is further weakened[14]. Therefore, Relaxor ferroelectrics, especially for superparaelectrics[15,16], show excellent performance superiority for achieving both high W_{rec} and η simultaneously[17-20].

$NaNbO_3$ (NN) is one of the typical lead-free ferroelectrics with complex crystal structure and phase transition under various temperatures. Despite the remaining controversies, it is commonly agreed that NN adopts seven major phases with the sequence of U→T2→T1→S→R→P→N on cooling, where the common P and R phases are antiferroelectrics[21,22]. The complex temperature-driven structure also means great potential for performance regulation. NN ceramic exhibits antiferroelectric P phase structure with Pbma space group at room temperature[23,24]. Generally, an effective strategy to improve the energy storage of NN ceramics focuses on stabilizing their antiferroelectric phase. For example, ultrahigh W_{rec} of 12.2 J/cm^3 was obtained in $0.76NaNbO_3$-$0.24(Bi_{0.5}N_{0.5})TiO_3$ ceramics due to stable relaxor antiferroelectric phase, however,

accompanied by a relatively low η of 69% owing to large polarization hysteresis for the first-order antiferroelectric-ferroelectric phase transition under high electric field[25]. Therefore, a practical approach is urgently required to simultaneously regulate the W_{rec} and η of NN ceramics. In this work, $CaZrO_3$ (CZ) was introduced into NN ceramics to not only destroy long-range antiferroelectric ordering but also remain large antiferrodistortion. On the one hand, the enhanced local random field along with the strengthened dielectric relaxation behavior would benefit the high η owing to the fast response of nanoclusters to the external electric field. On the other hand, the existence of large oxygen octahedron tilt would hinder the formation of long-range ferroelectric ordering under electric field, leading to the delayed polarization saturation process. Combined with the fine grains, dense and homogeneous microstructure, ergodic relaxation behavior, and delayed polarization saturation, a high recoverable energy storage density of ~5.4 J/cm^3 and a large efficiency of ~82% can be realized in $0.85NaNbO_3$-$0.15CaZrO_3$ ceramics at an ultrahigh breakdown electric field of ~68 kV/mm, showing a great application potential in the field of dielectric energy storage.

MATERIALS AND METHODS

Sample preparation

The ceramics of (1-x)$NaNbO_3$-$x$$CaZrO_3$ ((1-x)NN-xCZ, x = 0-0.15) were prepared by the conventional solid-state reaction process. The raw materials of Na_2CO_3 (> 99.9%), $CaCO_3$ (> 99.5%), Nb_2O_5 (> 99.9%), and ZrO_2 (> 99.9%) were weighed according to the chemical formula and mixed by planetary ball milling for 8 h using ethanol as ball milling media. The mixed powders were calcined at 850 °C for 5 h after drying. Then, the calcined powders were ball-milled again by high-energy ball milling (700 r/min for 8 h) with ethanol and 0.5 wt% PVB binder. Afterward, the powders were pressed into pellets with a diameter of 8 mm and a thickness of ~1 mm. The pellets were sheathed using the corresponding calcined powders in crucibles and sintered at 1370 °C for 2 h. Finally, the sintered ceramics were polished to a thickness of ~0.1 mm with a diameter of ~6.5 mm and coated with silver electrodes with a diameter of ~2 mm, which were fired under 550 °C for 30 min to measure their electrical properties.

Structural and performance characterizations

The high-energy synchrotron X-ray diffraction (SXRD) data was measured on the 11-ID-C beamline of advanced photon source. Powder neutron diffraction data were collected at CSNS (China Spallation Neutron Source, MPI) using time-of-flight powder diffractometers. The diffraction data refinement was taken by the Rietveld method on software GSAS II. Temperature- and frequency-dependent dielectric properties were carried out using an impedance analyzer (Keysight E4990A, Santa Clara, CA). Domain morphology and selected area electron diffraction (SAED) were observed on a field-emission transmission electron microscope (TEM, JEM-F200, JEOL, Japan) at an accelerating voltage of 200 kV. High-angle annular dark-field (HAADF) atomic-scale images were obtained using an atomic-resolution scanning transmission microscope (STEM, aberration-corrected Titan Themis 3300), and the polarization vectors, polarization magnitude, and polarization angle maps were calculated by customized MATLAB scripts. The morphology of grains was filmed using a scanning electron microscope (SEM, LEO1530, ZEISS SUPRA 55, Oberkochen, Germany). Energy-storge properties of ceramics were investigated by a ferroelectric analyzer (aix ACCT, TF Analyzer 1000, Aachen, Germany).

RESULTS AND DISCUSSION

Figure 1A shows the temperature-dependent dielectric permittivity (ε_r) of (1-x)NN-xCZ ceramics at 1 MHz. Pure NN is determined to be antiferroelectric P phase structure at room temperature accompanied by two dielectric anomaly peaks at 130 °C and 370 °C, representing the transitions from antiferroelectric P phase to incommensurate (INC) phase and INC phase to antiferroelectric R phase, respectively[26-28]. With the

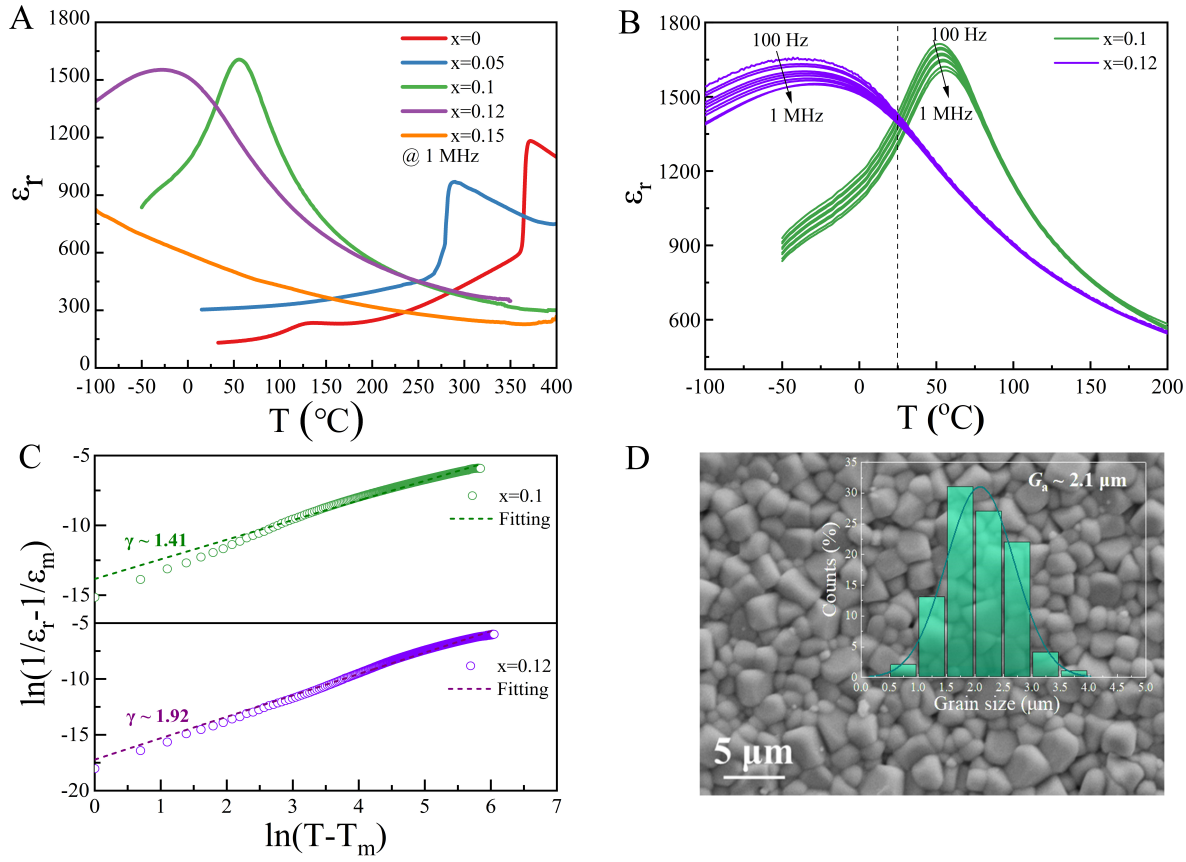

Figure 1. (A) Temperature-dependent dielectric permittivity for (1-*x*)NN-*x*CZ ceramics. (B) Frequency-dependent dielectric permittivity and (C) diffuseness degree (γ) fitted from the modified Curie-Weiss law for x = 0.1 and 0.12. (D) SEM surface morphology and grain size distribution of 0.85NN-0.15CZ ceramic.

increase of CZ, the dielectric anomaly peak at 130 °C disappears, and the maximum dielectric peak shifts gradually to low temperature together with the transition of phase structure. To characterize the relaxor feature, the dielectric properties of x = 0.1 and 0.12 at different frequencies are shown in Figure 1B. Both samples exhibit apparent frequency dispersion behavior. As shown in Figure 1C, the diffuseness degree (γ) for x = 0.1 and 0.12 was obtained using the modified *Curie-Weiss* Law:

$$\frac{1}{\varepsilon_r} - \frac{1}{\varepsilon_m} = \frac{(T - T_m)^\gamma}{C} \quad (T > T_m) \tag{4}$$

where ε_m is the maximum dielectric permittivity and T_m is the according temperature, C is the Curie constant. The γ value of 0.9NN-0.1CZ and 0.88NN-0.12CZ ceramics are ~1.41 and ~1.92, respectively, indicating that the (1-x)NN-xCZ ceramics should be relaxor ferroelectrics for x ≥ 0.1. These also demonstrate that the Ca^{2+} and Zr^{4+} are substituted into the lattice of NN matrix, breaking the long-range antiferroelectric order and increasing the local random field. Especially, the relaxed dielectric peak of 0.85NN-0.15CZ ceramic located far below room temperature and the T_B ~85 °C obtained according to the *Curie-Weiss* Law, as shown in Supplementary Figure 1, indicate it should be superparaelectric state around room temperature. It is recognized that ultrasmall and highly active polar nanoregions (PNRs) can be found in the superparaelectric region, leading to the improvement of η[29-31]. Compared with other samples, 0.85NN-0.15CZ ceramic has moderate room-temperature ε_r ~545, which can effectively delay the

polarization saturation process under a low electric field and reduce the possibility of electromechanical breakdown generated by the electrostriction effect. These phenomena indicate that 0.85NN-0.15CZ ceramic shows excellent potential to become a high energy storage material.

Another basic guarantee for realizing high energy storage properties is the uniform and compact microstructure. As shown in Figure 1D, the surface morphology of 0.85NN-0.15CZ ceramic presents a dense microstructure with few pores. A uniform grain size distribution can be found in 0.85NN-0.15CZ ceramic with a smaller average grain size (G_a) of ~2.1 μm compared with that of pure NN ceramic shown in Supplementary Figure 2. Moreover, the uniform distribution of elements in Supplementary Figure 3 suggests the achievement of a pure phase structure. It is believed that good sample quality, along with small grain size and dense structure, is beneficial to strengthening E_b.

Even though a superparaelectric state for the 0.85NN-0.15CZ ceramic can be easily identified by using dielectric spectra, however, it is widely known that there are several different paraelectric states as well as (anti)ferroelectric states in NN ceramics at different temperature ranges. To analyze the phase structure of 0.85NN-0.15CZ ceramic, as shown in Figure 2A and B, high-energy SXRD and powder neutron diffraction data were collected and refined. Together with the EDS images shown in Supplementary Figure 3, the sample should certainly be a pure perovskite phase. Moreover, apparent non-cubic phase structure can be identified for 0.85NN-0.15CZ ceramic according to the split main diffraction peaks and superlattice diffraction peaks. This feature is quite different from the average structure characteristics of traditional superparaelectrics[15,16], indicating the existence of lattice distortion. The lattice distortion in (anti)ferroelectrics mainly includes oxygen octahedron tilt and cation off-centering displacement. Considering the macro nonpolar feature of superparaelectrics, the lattice distortion in the studied sample should be attributed to the oxygen octahedron tilt. As the insensitive response of X-ray to the oxygen ions, powder neutron diffraction was measured. Rietveld refinement using the model with $P2_1ma$ space group was taken simultaneously on the SXRD and neutron diffractions, and the satisfying results with low-reliability factors of weighted patterns (R_{wp}) are shown in Figure 2A and B. To convince the best refinement result, Rietveld refinement of SXRD data using the model with cubic space group of Pm-3m was also carried out in Supplementary Figure 4. It can be found that the 0.85NN-0.15CZ ceramic should be a ferroelectric Q phase with $P2_1ma$ space group and $a^-b^+c^-$ oxygen octahedron tilt system but small polarization displacement, which is different from that of NN ceramic (P phase: $a^-b^-c^-/a^-b^+c^-$). According to Glazer notation, the superscripts +, -, and 0 represent in-phase tilt, anti-phase tilt, and no tilt of oxygen octahedral along one axis, respectively[32]. The tilt degree of oxygen octahedron can be calculated using $\omega = (180° - \angle B\text{-}O\text{-}B)/2$. As shown in Supplementary Figure 5, the oxygen octahedron tilt degree for NN ceramics with Pbcm space group at room temperature is calculated as ~7.9°-13.15°. According to the lattice parameters obtained from the refinement results of SXRD and powder neutron diffraction, the crystal structure model of 0.85NN-0.15CZ ceramic was drawn and displayed in Figure 2C. A large oxygen octahedron tilt of ~10.89°-12.20° can be calculated according to the ∠B-O1-B ~157.55°, ∠B-O2-B ~156.61°, ∠B-O3-B ~155.61°, and ∠B-O4-B ~158.22°, which is much larger than that of traditional relaxor ferroelectrics such as $Pb(Mg_{1/3}Nb_{2/3})O_3$ and $Ba(Ti, Zr)O_3$. That is to say, the relaxor ferroelectric Q phase can be identified in 0.85NN-0.15CZ ceramic, which is quite different from the previously reported results that the addition of CZ would stabilize antiferroelectric P phase in NN ceramic[33-35]. The decreased tolerance factor after doping CZ into NN ceramic would increase the oxygen octahedron tilt. However, according to the statistics of recently reported antiferroelectrics (NN, $AgNbO_3$, $(Bi_{0.5}Na_{0.5})TiO_3$-based, $BiFeO_3$-based, $PbZrO_3$, and $PbHfO_3$-based ceramics), it can be found that the antiferroelectric phase only exists in a narrow tolerance factor range. The perovskites with ultralow tolerance factor are usually paraelectrics, such as $CaZrO_3$ and $CaHfO_3$. Therefore, the polarization ordering would be destroyed when the amount of CZ is over a critical value, leading to the

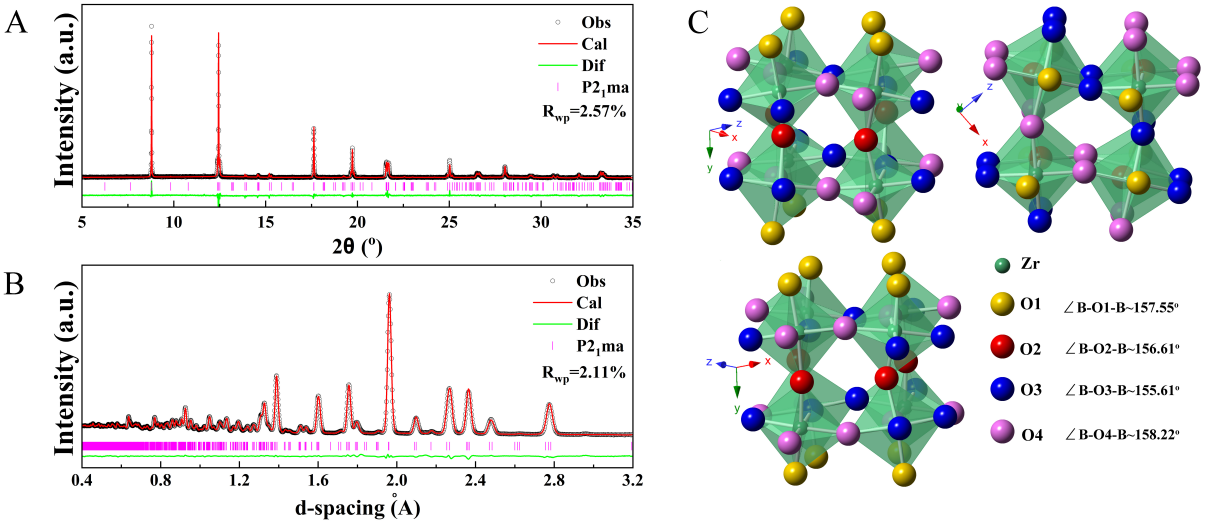

Figure 2. (A) High-energy synchrotron XRD, and (B) powder neutron diffraction structure refinement patterns of 0.85NN-0.15CZ Ceramic. (C) Schematic diagram of the large antiferrodistortion in 0.85NN-0.15CZ ceramic.

disappearance of anti-phase tilt modules along b axis. Moreover, the formation of dielectric relaxation behavior would also destroy the long-range polarization ordering. As a result, a superparaelectric state with large antiferrodistortion can be detected in 0.85NN-0.15CZ ceramic at room temperature.

TEM is an essential and helpful method to characterize the domain morphology and lattice microstructure for ferroelectric materials. Figure 3A suggests that 0.85NN-0.15CZ ceramic exhibits apparent 90° and 180° microdomains. Figure 3B and C display high-resolution TEM lattice fringe images along $[100]_c$ and $[111]_c$ directions, respectively, demonstrating good sample quality. Figure 3D and E show the SAED image along $[100]_c$ and $[111]_c$ directions, respectively, which once again confirm that 0.85NN-0.15CZ ceramic should be pure perovskite structure. It is recognized that the 1/2 types of superlattice diffractions of (ooe)/2 and (ooo)/2 (o and e are odd and even, respectively) are mainly related to the in-phase and anti-phase oxygen octahedron tilt, respectively[32]. Therefore, the 1/2 type superlattice diffraction spots observed in the accordingly SAED images further prove the existence of oxygen octahedral distortion. It is widely accepted that normal ferroelectrics with macrodomains exhibit poor energy storage properties ascribed to the large polarization hysteresis along with irreversible domain switching, which occurs together with polarization reorientation. However, there is no macroscopic polarization alignment in this superparaelectric sample, which could be further directly confirmed by the quantitative analysis of the polarization mapping using HAADF-STEM results, as shown in Figure 4. Therefore, these macrodomains should be ferroelastic domains constructed by the ordered oxygen octahedron tilt, and the domain switching process has very little influence on polarization reorientation. According to the polarization mapping, ultrasmall PNRs with a size of about 2-3 nm can be seen, which is at the same level as other superparaelectrics. Namely, fast response of PNRs with little polarization hysteresis during charging and discharging processes can also be expected for this sample, benefiting excellent energy storage properties. Moreover, large antiferrodistortion would also delay the polarization saturation process, which would also favor the energy storage properties.

Due to the irreversible phase transition from antiferroelectric to ferroelectric under electric fields for pure NN ceramic, a square P-E loop with poor energy storage properties can be achieved, as shown in Supplementary Figure 6. With the stabilization of antiferroelectric P phase by adding a small content of CZ[35], even though increased energy storage density can be obtained along with the appearance of

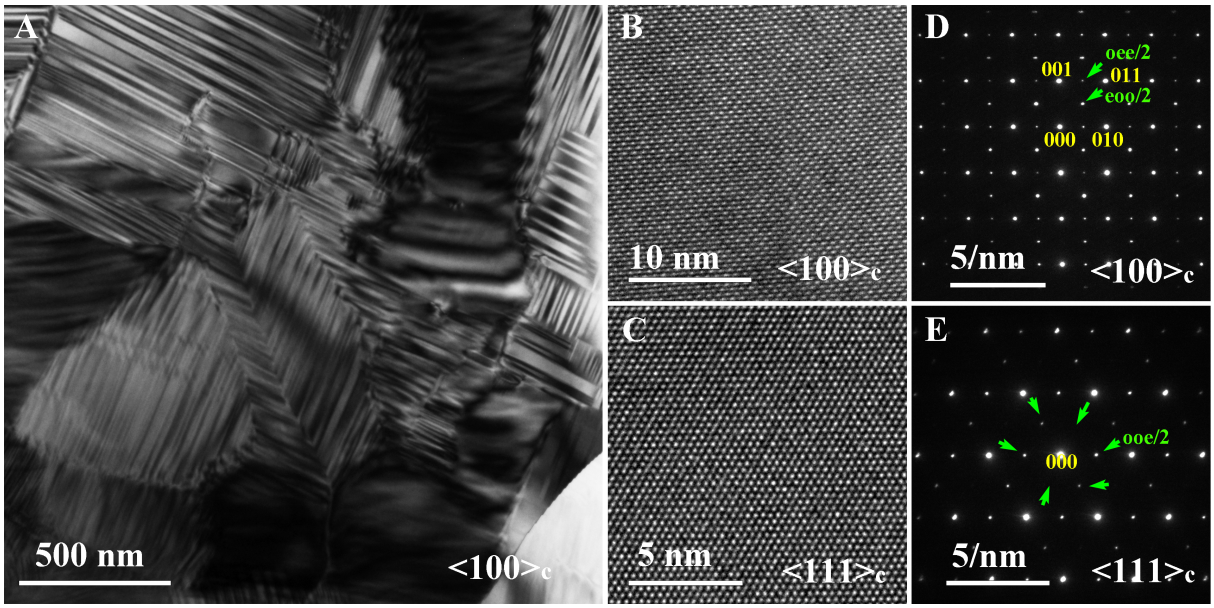

Figure 3. (A) Domain morphology of 0.85NN-0.15CZ ceramic. Lattice fringes and SAED patterns of 0.85NN-0.15CZ ceramic along (B and D) $[100]_c$, and (C and E) $[111]_c$.

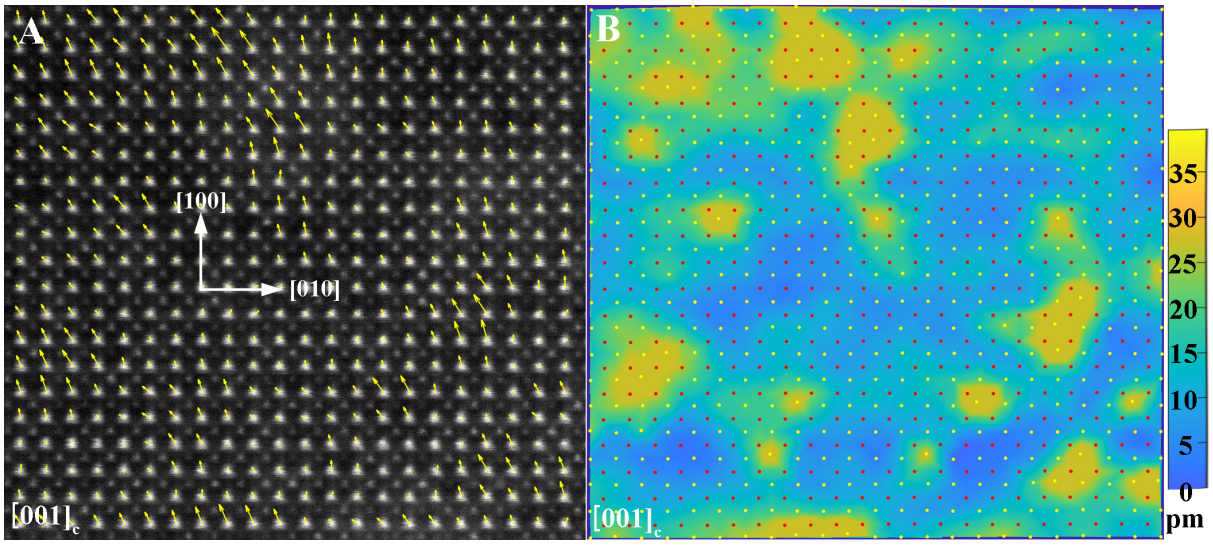

Figure 4. (A) Atomic-resolution HAADF-STEM polarization vector image and (B) polarization displacement distribution mappings along $[100]_c$.

repeatable double P-E loop, quite low energy efficiency can also be found owing to the large hysteresis caused by the first order antiferroelectric-ferroelectric phase transition. An obvious increase in both energy storage density and efficiency can be detected with the entrance of relaxor ferroelectric phase zone of $x > 0.1$, accompanied by the generation of slim P-E loops. Moreover, energy efficiency tends to increase with increasing relaxor behavior. Thus a good balance with both large W_{rec} and η can be commonly realized in superparaelectrics. Figure 5A shows the *P-E* loops and energy storage properties of 0.85NN-0.15CZ ceramic under various electric fields. It is found that P_{max} and P_r gradually increase when the electric field is applied from 2 kV/mm to 68 kV/mm, showing the characteristic of relaxor ferroelectric. As the electric field

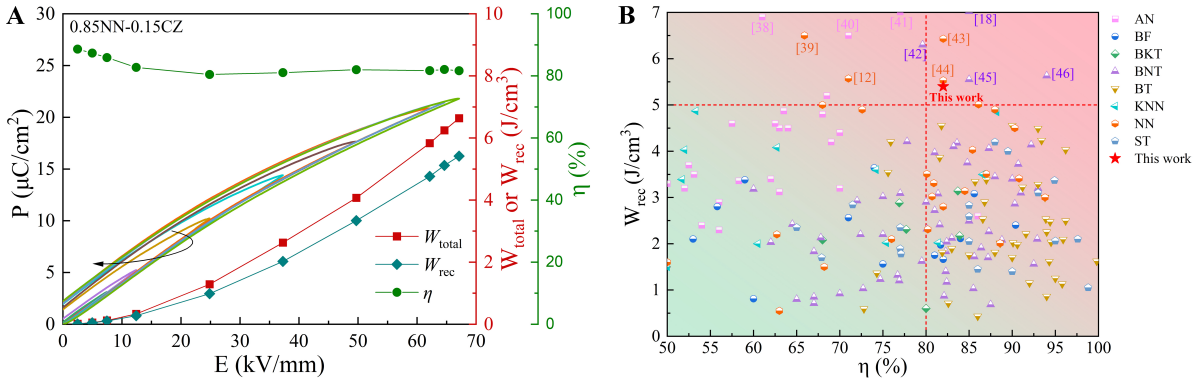

Figure 5. (A) *P-E* loops and energy storage performance under various electric fields for 0.85NN-0.15CZ ceramics. (B) Comparison of energy storage performance among 0.85NN-0.15CZ ceramic and some other systems[6].

increases, W_{total} and W_{rec} present an almost parabolic growth trend. Eventually, a comprehensive performance of W_{rec} ~5.4 J/cm³ and η ~82% can be obtained in 0.85NN-0.15CZ ceramic under an ultrahigh external electric field of 68 kV/mm. It is believed that the excellent energy storage performance is associated with the following sections: Firstly, the sample with a small grain size of ~2.1 μm has high grain boundary density, and the grain boundary with large resistance can act as a dissipative layer, effectively hindering the conduction of space charge and reducing the generation of leakage current. In addition, according to the relationship of $E_b \propto 1/\sqrt{G_a}$[36], small grain size is favorable for the enhancement of E_b. Complex impedance spectroscopy of pure NN and 0.85NN-015CZ ceramics measured at 500 °C are shown in Supplementary Figure 7. The Z″-Z′ curves of the two exhibited nearly a single semicircle arc with good fitting results using a series R||CPE equivalent circuit model, and 0.85NN-0.15CZ showed twice as much resistance as pure NN, which proves the dominant role to the enhanced E_b of the grain boundary. Secondly, the dense and uniform internal structure with few pores is beneficial to decreasing the possibility of local breakdown, which can broadly promote E_b[3]; Thirdly, the introduction of CZ induces the transition from antiferroelectric P phase to superparaelectric phase, leading to an enhanced relaxor behavior in ergodic relaxor region at room temperature. PNRs with fast electric field response characteristics can cause 0.85NN-0.15CZ ceramic to form the fast and reversible transition between relaxor ferroelectric and ferroelectric phase under an external electric field, resulting in a small P_r and a large η. Finally, 0.85NN-0.15CZ ceramic with moderate room-temperature ε_r can enhance W_{rec} by inhibiting early polarization saturation under external electric fields.

Advanced ceramic capacitors are developing toward large energy storage density and high efficiency[37]. Figure 5B shows the comparison of energy-storage performance among 0.85NN-0.15CZ ceramic and other relevant dielectric energy storage ceramics ($AgNbO_3$(AN), $BiFeO_3$(BF), $Bi_{0.5}K_{0.5}TiO_3$(BKT), $Bi_{0.5}Na_{0.5}TiO_3$ (BNT), $BaTiO_3$(BT), $K_{0.5}Na_{0.5}NbO_3$(KNN), $SrTiO_3$(ST))[6,12,18,38-46]. Obviously, 0.85NN-0.15CZ ceramic exhibits great performance superiority, making it one of the prospective materials for advanced pulse power capacitor applications.

CONCLUSIONS

In this work, (1-*x*)NN-*x*CZ ceramics are prepared by a conventional solid-state reaction method. With increasing CZ content to 0.15, the structure of samples changes from antiferroelectric P phase to relaxor ferroelectric Q phase with superparaelectric state, leading to the destruction of long-range polarization ordering but reservation of antiferrodistortion ordering, which can be confirmed by the high energy synchrotron XRD and powder neutron diffraction refinement results as well as TEM images. In this case,

the grain size of the sample decreases to 2.1 μm, accompanied by dense and homogeneous microstructure. The 0.85NN-0.15CZ ceramics showed comprehensive energy storage performance of W_{rec} = 5.4 J/cm^3 and η = 82% under an ultrahigh breakdown electric field of 68 kV/mm. The excellent energy storage performance is believed to originate from the small grain size, dense and homogeneous microstructure, superparaelectric state with fast polarization response, and delayed polarization saturation relating to the large oxygen octahedron tilt. The results of this work indicate that 0.85NN-0.15CZ ceramics exhibit colossal application potential in the field of dielectric energy storage.

DECLARATIONS

Authors' contributions

Experiment, characterization, writing original draft: Liu G
Review & editing, supervision: Qi H, Chen L
Conceptualization, review, supervision: Qi H

Availability of data and materials

Not applicable.

Financial support and sponsorship

This work was supported by the National Natural Science Foundation of China (Grant Nos. 52172181 and 22105017).

Conflicts of interest

All authors declared that there are no conflicts of interest.

Ethical approval and consent to participate

Not applicable.

Consent for publication

Not applicable.

Copyright

© The Author(s) 2023.

REFERENCES

1. Hao X, Zhai J, Kong LB, Xu Z. A comprehensive review on the progress of lead zirconate-based antiferroelectric materials. *Prog Mater Sci* 2014;63:1-57. DOI
2. Qi H, Xie A, Zuo R. Local structure engineered lead-free ferroic dielectrics for superior energy-storage capacitors: a review. *Energy Stor Mater* 2022;45:541-67. DOI
3. Yang L, Kong X, Li F, et al. Perovskite lead-free dielectrics for energy storage applications. *Prog Mater Sci* 2019;102:72-108. DOI
4. Wang G, Lu Z, Li Y, et al. Electroceramics for high-energy density capacitors: current status and future perspectives. *Chem Rev* 2021;121:6124-72. DOI PubMed PMC
5. Li J, Shen Z, Chen X, et al. Grain-orientation-engineered multilayer ceramic capacitors for energy storage applications. *Nat Mater* 2020;19:999-1005. DOI PubMed
6. Yang Z, Du H, Jin L, Poelman D. High-performance lead-free bulk ceramics for electrical energy storage applications: design strategies and challenges. *J Mater Chem A* 2021;9:18026-85. DOI
7. Yao FZ, Yuan Q, Wang Q, Wang H. Multiscale structural engineering of dielectric ceramics for energy storage applications: from bulk to thin films. *Nanoscale* 2020;12:17165-84. DOI PubMed
8. Veerapandiyan V, Benes F, Gindel T, Deluca M. Strategies to improve the energy storage properties of perovskite lead-free relaxor ferroelectrics: a review. *Materials* 2020;13:5742. DOI PubMed PMC
9. Guo X, Pu Y, Wang W, et al. Ultrahigh energy storage performance and fast charge-discharge capability in Dy- modified $SrTiO_3$ linear ceramics with high optical transmissivity by defect and interface engineering. *Ceram Int* 2020;46:21719-27. DOI

10. Xie A, Qi H, Zuo R, Tian A, Chen J, Zhang S. An environmentally-benign $NaNbO_3$ based perovskite antiferroelectric alternative to traditional lead-based counterparts. *J Mater Chem C* 2019;7:15153-61. DOI
11. Dong X, Li X, Chen X, et al. High energy storage density and power density achieved simultaneously in $NaNbO_3$-based lead-free ceramics via antiferroelectricity enhancement. *J Materiomics* 2021;7:629-39. DOI
12. Tian A, Zuo R, Qi H, Shi M. Large energy-storage density in transition-metal oxide modified $NaNbO_3$-$Bi(Mg_{0.5}Ti_{0.5})O_3$ lead-free ceramics through regulating the antiferroelectric phase structure. *J Mater Chem A* 2020;8:8352-9. DOI
13. Bokov AA, Ye Z. Dielectric relaxation in relaxor ferroelectrics. *J Adv Dielectr* 2012;2:1241010. DOI
14. Cross LE. Relaxor ferroelectrics. *Ferroelectrics* 1987;76:241-67. DOI
15. Pan H, Lan S, Xu S, et al. Ultrahigh energy storage in superparaelectric relaxor ferroelectrics. *Science* 2021;374:100-104. DOI
16. Chen L, Wang N, Zhang Z, et al. Local diverse polarization optimized comprehensive energy-storage performance in lead-free superparaelectrics. *Adv Mater* 2022;34:e2205787. DOI
17. Yang W, Zeng H, Yan F, et al. Superior energy storage properties in $NaNbO_3$-based ceramics via synergistically optimizing domain and band structures. *J Mater Chem A* 2022;10:11613-24. DOI
18. Qi H, Zuo R. Linear-like lead-free relaxor antiferroelectric $(Bi_{0.5}Na_{0.5})TiO_3$-$NaNbO_3$ with giant energy-storage density/efficiency and super stability against temperature and frequency. *J Mater Chem A* 2019;7:3971-8. DOI
19. Ye H, Yang F, Pan Z, et al. Significantly improvement of comprehensive energy storage performances with lead-free relaxor ferroelectric ceramics for high-temperature capacitors applications. *Acta Mater* 2021;203:116484. DOI
20. Kang R, Wang Z, Lou X, et al. Energy storage performance of $Bi_{0.5}Na_{0.5}TiO_3$-based relaxor ferroelectric ceramics with superior temperature stability under low electric fields. *Chem Eng J* 2021;410:128376. DOI
21. Glazer AM, Megaw HD. Studies of the lattice parameters and domains in the phase transitions of $NaNbO_3$. *Acta Crystallogr A* 1973;29:489-95. DOI
22. Megaw HD. The seven phases of sodium niobate. *Ferroelectrics* 1974;7:87-9. DOI
23. Megaw HD, Wells M. The space group of $NaNbO_3$ and $(Na_{0.995}K_{0.005})NbO_3$. *Acta Crystallogr* 1958;11:858-62. DOI
24. Guo H, Shimizu H, Mizuno Y, Randall CA. Strategy for stabilization of the antiferroelectric phase (Pbma) over the metastable ferroelectric phase ($P2_1ma$) to establish double loop hysteresis in lead-free (1-*x*)$NaNbO_3$-*x*$SrZrO_3$ solid solution. *J Appl Phys* 2015;117:214103. DOI
25. Qi H, Zuo R, Xie A, et al. Ultrahigh energy-storage density in $NaNbO_3$-based lead-free relaxor antiferroelectric ceramics with nanoscale domains. *Adv Funct Mater* 2019;29:1903877. DOI
26. Guo H, Shimizu H, Randall CA. Direct evidence of an incommensurate phase in $NaNbO_3$ and its implication in $NaNbO_3$-based lead-free antiferroelectrics. *Appl Phys Lett* 2015;107:112904. DOI
27. Reznichenko LA, Shilkina LA, Gagarina ES, et al. Structural instabilities, incommensurate modulations and *P* and *Q* phases in sodium niobate in the temperature range 300-500 K. *Crystallogr Rep* 2003;48:448-56. DOI
28. Wang X, Shen Z, Hu Z, Qin L, Tang S, Kuok M. High temperature Raman study of phase transitions in antiferroelectric $NaNbO_3$. *J Mol Struct* 1996;385:1-6. DOI
29. Bokov AA, Ye Z. Recent progress in relaxor ferroelectrics with perovskite structure. *J Mater Sci* 2006;41:31-52. DOI
30. Hu Q, Tian Y, Zhu Q, et al. Achieve ultrahigh energy storage performance in $BaTiO_3$-$Bi(Mg_{1/2}Ti_{1/2})O_3$ relaxor ferroelectric ceramics via nano-scale polarization mismatch and reconstruction. *Nano Energy* 2020;67:104264. DOI
31. Yan F, Zhou X, He X, et al. Superior energy storage properties and excellent stability achieved in environment-friendly ferroelectrics via composition design strategy. *Nano Energy* 2020;75:105012. DOI
32. Glazer AM. Simple ways of determining perovskite structures. *Acta Crystallogr A* 1975;31:756-62. DOI
33. Guo H, Shimizu H, Randall CA. Microstructural evolution in $NaNbO_3$-based antiferroelectrics. *J Appl Phys* 2015;118:174107. DOI
34. Liu Z, Lu J, Mao Y, Ren P, Fan H. Energy storage properties of $NaNbO_3$-$CaZrO_3$ ceramics with coexistence of ferroelectric and antiferroelectric phases. *J Eur Ceram Soc* 2018;38:4939-45. DOI
35. Shimizu H, Guo H, Reyes-Lillo SE, Mizuno Y, Rabe KM, Randall CA. Lead-free antiferroelectric: $xCaZrO_3$-(1-x)$NaNbO_3$ system ($0 \leq x \leq 0.10$). *Dalton Trans* 2015;44:10763-72. DOI
36. Tunkasiri T, Rujijanagul G. Dielectric strength of fine grained barium titanate ceramics. *J Mater Sci Lett* 1996;15:1767-9. DOI
37. Luo N, Han K, Cabral MJ, et al. Constructing phase boundary in $AgNbO_3$ antiferroelectrics: pathway simultaneously achieving high energy density and efficiency. *Nat Commun* 2020;11:4824. DOI
38. Chao W, Gao J, Yang T, Li Y. Excellent energy storage performance in La and Ta co-doped $AgNbO_3$ antiferroelectric ceramics. *J Eur Ceram Soc* 2021;41:7670-7. DOI
39. Chen J, Qi H, Zuo R. Realizing Stable Relaxor Antiferroelectric and Superior Energy Storage Properties in $(Na_{1-x/2}La_{x/2})(Nb_{1-x}Ti_x)O_3$ Lead-Free Ceramics through A/B-Site Complex Substitution. *ACS Appl Mater Interfaces* 2020;12:32871-9. DOI
40. Lu Z, Bao W, Wang G, et al. Mechanism of enhanced energy storage density in $AgNbO_3$-based lead-free antiferroelectrics. *Nano Energy* 2021;79:105423. DOI
41. Li S, Hu T, Nie H, et al. Giant energy density and high efficiency achieved in silver niobate-based lead-free antiferroelectric ceramic capacitors via domain engineering. *Energy Stor Mater* 2021;34:417-26. DOI
42. Guo B, Yan Y, Tang M, et al. Energy storage performance of $Na_{0.5}Bi_{0.5}TiO_3$ based lead-free ferroelectric ceramics prepared via non-uniform phase structure modification and rolling process. *Chem Eng J* 2021;420:130475. DOI
43. Chen H, Shi J, Dong X, et al. Enhanced thermal and frequency stability and decent fatigue endurance in lead-free $NaNbO_3$-based

ceramics with high energy storage density and efficiency. *J Materiomics* 2022;8:489-97. DOI

44. Pang F, Chen X, Sun C, et al. Ultrahigh energy storage characteristics of sodium niobate-based ceramics by introducing a local random field. *ACS Sustain Chem Eng* 2020;8:14985-95. DOI
45. Zhu C, Cai Z, Luo B, et al. Multiphase engineered BNT-based ceramics with simultaneous high polarization and superior breakdown strength for energy storage applications. *ACS Appl Mater Interfaces* 2021;13:28484-92. DOI
46. Yan F, Huang K, Jiang T, et al. Significantly enhanced energy storage density and efficiency of BNT-based perovskite ceramics via A-site defect engineering. *Energy Stor Mater* 2020;30:392-400. DOI

Zhang *et al. Microstructures* 2023;3:2023010
DOI: 10.20517/microstructures.2022.39

Microstructures

Research Article

Open Access

Check for updates

Elastic properties and Ion-mediated domain switching of self-assembled heterostructures $CuInP_2S_6$-$In_{4/3}P_2S_6$

Xiangping Zhang[1,#], Xingan Jiang[1,#], Guoshuai Du[1], Qi Ren[1], Wenfu Zhu[1], Jiaqian Kang[1], Yingzhuo Lun[1], Tingjun Wang[1], Bofang Bai[1], Zixuan Yu[1], Jianming Deng[1,2], Yabin Chen[3], Xueyun Wang[1], Jiawang Hong[1]

[1]School of Aerospace Engineering, Beijing Institute of Technology, Beijing 100081, China.
[2]Guangdong Provincial Key Laboratory of Electronic Functional Materials and Devices, Huizhou University, Huizhou 516001, Guangdong, China.
[3]Advanced Research Institute of Multidisciplinary Sciences, and School of Materials Science and Engineering, Beijing Institute of Technology, Beijing 100081, China.
[#]These authors contribute equally to this work.

Correspondence to: Prof./Dr. Xueyun Wang, School of Aerospace Engineering, Beijing Institute of Technology, #5 ZhongGuanCun South Street, Beijing 100081, China. E-mail: xueyun@bit.edu.cn; Prof./Dr. Jiawang Hong, School of Aerospace Engineering, Beijing Institute of Technology, #5 ZhongGuanCun South Street, Beijing 100081, China. E-mail: hongjw@bit.edu.cn

How to cite this article: Zhang X, Jiang X, Du G, Ren Q, Zhu W, Kang J, Lun Y, Wang T, Bai B, Yu Z, Deng J, Chen Y, Wang X, Hong J. Elastic properties and Ion-mediated domain switching of self-assembled heterostructures $CuInP_2S_6$-$In_{4/3}P_2S_6$. *Microstructures* 2023;3:2023010. https://dx.doi.org/10.20517/microstructures.2022.39

Received: 2 Nov 2022 **First Decision:** 2 Dec 2022 **Revised:** 8 Dec 2022 **Accepted:** 4 Jan 2023 **Published:** 17 Jan 2023

Academic Editor: Shujun Zhang **Copy Editor:** Fangling Lan **Production Editor:** Fangling Lan

Abstract

Van der Waals (vdW) ferroelectric $CuInP_2S_6$ (CIPS) has attracted intense research interest due to its unique ferroelectric properties that make it promising for potential applications in flexible electronic devices. A mechanical mean, or so-called strain gradient engineering, has been proven as an effective method to modulate its ferroelectric properties, but the key parameter elastic constants *Cij* has not been accurately measured. Here, we utilized nanoindentation and contact resonance atomic force microscopy (CR-AFM) techniques to measure the elastic modulus on the (001) plane of nanoscale phase separated $CuInP_2S_6$-$In_{4/3}P_2S_6$ (CIPS-IPS). The Young's modulus of the CIPS was slightly less than that of the IPS. Density Functional Theory was introduced to obtain the accurate full elastic constant *Cij* of CIPS and IPS, and we deduced their respective Young's moduli, all of which are in good agreement with our experimental values. We further discovered the asymmetrical domain switching and proposed an ion-mediated domain switching model. The results provide a reliable experimental reference for strain gradient engineering in the phase field simulation in CIPS-IPS.

© The Author(s) 2023. **Open Access** This article is licensed under a Creative Commons Attribution 4.0 International License (https://creativecommons.org/licenses/by/4.0/), which permits unrestricted use, sharing, adaptation, distribution and reproduction in any medium or format, for any purpose, even commercially, as long as you give appropriate credit to the original author(s) and the source, provide a link to the Creative Commons license, and indicate if changes were made.

Keywords: $CuInP_2S_6$-$In_{4/3}P_2S_6$, ferroelectric, elastic modulus, nanoindentation, CR-AFM

INTRODUCTION

Van der Waals layered ferroelectric $CuInP_2S_6$ (CIPS) has attracted intense research interest due to its unique ferroelectric characteristics. A series of novel properties have been discovered in recent years, such as giant negative piezoelectricity[1], tunable quadruple energy wells[2], large room temperature electrocaloric effect[3,4], and strong coupling between ferroelectric polarization and ionic conductivity[5-7]. Based on these fascinating attributes, large quantities of 2D device applications have shown up in the past several years, including ferroelectric field-effect transistors[8-10], ferroelectric tunneling junctions[11], negative capacitance field-effect transistors[12,13], memristors[5,14] and prototype neuromorphic computing[15-18].

The crystal structure of CIPS can be described as a sulfur framework in which metal cations (Cu and In) and P-P pairs fill the octahedral voids[19]. It is noteworthy that when Cu is deficient, the system undergoes a chemical phase separation into a paraelectric IPS phase and a ferroelectric CIPS phase[20,21] due to the intentionally induced off-stoichiometry. Compared with normal CIPS, CIPS-IPS has a higher Curie temperature (340 K > 315 K)[21-23], a tunable dielectric property[24] and a porous structure in which the IPS phase is more conducive to the lateral migration of Cu ions[6,19]. In addition, the ferroelectric properties of CIPS-IPS have sensitive response to out-of-plane mechanical stimuli[7]. Recently, the utilization of strain engineering to modulate the domain and phase has become a promising method[25,26]. However, there is a lack of key parameters such as elastic coefficient to give accurate reference for the experimental and theoretical investigation of this system[27,28].

In this work, we use a combination of contact resonance atomic force microscopy and piezoresponse force microscopy (CR-AFM and PFM) to achieve accurate Young's modulus of CIPS and IPS in the nanoscale phase separated CIPS-IPS. The results reveal that the Young's modulus of the CIPS phase was 27.42 ± 0.05 GPa, slightly less than that of the IPS phase of 27.51 ± 0.04 GPa. Meanwhile, the two phases can also be well-distinguished by the magnitude of the frictional force. The density functional theory was introduced to obtain the accurate full elastic constant C_{ij} of CIPS and IPS, and their respective Young's modulus was deduced, which are in good agreement with our experimental values. In addition, we quantified the equivalent piezoelectric coefficient for the CIPS phase, which has an exceptionally large value, ~40 pm/V, compared to previously reported values of 5-12 pm/V[29]. Finally, we also discovered an asymmetrical domain switching and proposed an ion-mediated domain switching model.

METHODS

Sample preparation and structure characterization

We synthesized $Cu_xIn_yP_2S_6$ single crystal through the chemical vapor transport method[20]. The starting materials were sealed in fused silica ampules, then heated to 750-775 °C at a rate of 30 °C/h and held at that temperature for 4 days, followed by a rate of 20 °C/h cooling. The thin flakes were obtained by mechanical exfoliation and transferred to the conductive Au/SiO_2/Si substrate. The energy dispersive spectroscopy (EDS) was performed using a commercial ultra-high resolution cold-field emission scanning electron microscopy system (Hitachi, Regulus 8230) to characterize the elemental compositions. The actual chemical composition was determined to be $Cu_{0.57}In_{1.04}P_2S_6$.

DFT calculations

The density functional theory (DFT) calculation was carried out using the projector augmented wave (PAW)[30] scheme with the Perdew-Burke-Ernzerhof (PBE) functional of generalized gradient

approximation (GGA)[31] method as implemented in the Vienna *ab initio* simulation package (VASP)[32,33]. A plane wave cutoff of 450 eV was set in our calculations. K-point samplings of 5 × 3 × 2 were used. DFT-D3(BJ) level[34,35] was used in our calculations to take into consideration of the van der Waal forces. Atomic relaxation was performed until the force on each atom was smaller than 0.001 eV Å^{-1}, and the total energy change was less than 10^{-6} eV. The space group of $CuInP_2S_6$ and $In_{4/3}P_2S_6$ are *Cc* and $P2_1/c$, respectively. The unit cell $CuInP_2S_6$ contains 4 Cu, 4 In, 8 P and 24 S atoms, while the $In_{4/3}P_2S_6$ contains 8 In, 12 P and 36 S atoms. The calculated lattice parameters are listed in Supplementary Table 1, which are consistent with previously reported experimental values[36,37].

Scanning probe microscopy

Piezoresponse force microscopy (PFM) and conductive-atomic force microscopy (c-AFM) measurements were performed using a commercial atomic force microscope (Asylum Research MFP-3D) with Pt/Ir-coated Si cantilever tips (radius of ~25 nm). The spring constant is in the range of ~0.5-9.5 N/m. The out-of-plane (OP) phase and amplitude images were acquired using the dual-frequency resonance tracking piezoresponse force microscopy (DART-PFM) mode with an *ac* voltage (V_{ac} = 2 V). The conductive Si cantilever was excited with an *ac* voltage of 2 V at the tip-sample contact resonant frequency of ~350 kHz. The switching spectroscopy PFM (SS-PFM) was performed to obtain the hysteresis loops to characterize the local ferroelectricity. In c-AFM measurement, the voltage was applied to the conducting Au bottom electrode, which was continuously swept and simultaneously read the current. In contact resonance atomic force microscopy (CR-AFM) measurement, the NCL Pt-coated tips with k ≈ 48 N/m were used. The contact force between the cantilever and the sample was ~25 μN. More calculation details of Young's modulus are presented in the Supplementary Information.

Raman measurement

Raman spectra were collected using a micro-Raman system with a Horiba iHR550 spectrometer and a 100X objective (Olympus, NA = 0.95). A 633 nm Helium-Neon Laser (Newport) was used to excite the Raman scattering and the laser power was low enough to avoid excessive heating of the sample. Raman measurements were performed under a microscope in backscattering configuration with linear polarized excitation and unpolarized detection.

Nanoindentation measurement

The nanoindentation experiments were performed using a commercial nanoindenter (G200 Keysight), which has load and displacement resolutions of 50 nN and 0.01 nm, respectively. The indentation tests were conducted normal to the (001) plane at room temperature with a Berkovich indenter. Calibration was performed using fused silica with a modulus of 72.1 GPa. The sample was fixed to the silicon wafer by the commercially provided mounting glue. Then the glue and sample were cured for at least 24 h.

RESULTS AND DISCUSSION

The CIPS-IPS crystal has millimeter-sized lateral dimension and a thickness of ~tens micrometers, as shown in Figure 1A. The crystal is transparent and flexible. For the subsequent structural characterization, thin flakes of CIPS-IPS were prepared by mechanical exfoliation, as shown in the bottom panel of Figure 1A. Figure 1B shows the crystal structure of IPS, CIPS and CIPS-IPS heterostructure. IPS is non-polar due to a lack of Cu ions. To confirm that this sample is indeed a two-phase coexisted CIPS-IPS crystal, we compare the Raman spectrum with that of CIPS crystal, as shown in Figure 1C. Two peaks appear at ~255 and ~270 cm^{-1} in CIPS-IPS, which is different from that of pure CIPS. Therefore, the Cu-deficient CIPS crystal exhibits a local chemical phase separation, presenting both a Cu-free paraelectric IPS phase and a ferroelectric CIPS phase. Figure 1D shows the topography of CIPS-IPS, which displays a labyrinth-like distribution. The corresponding elemental mappings confirmed the non-uniform distribution of Cu

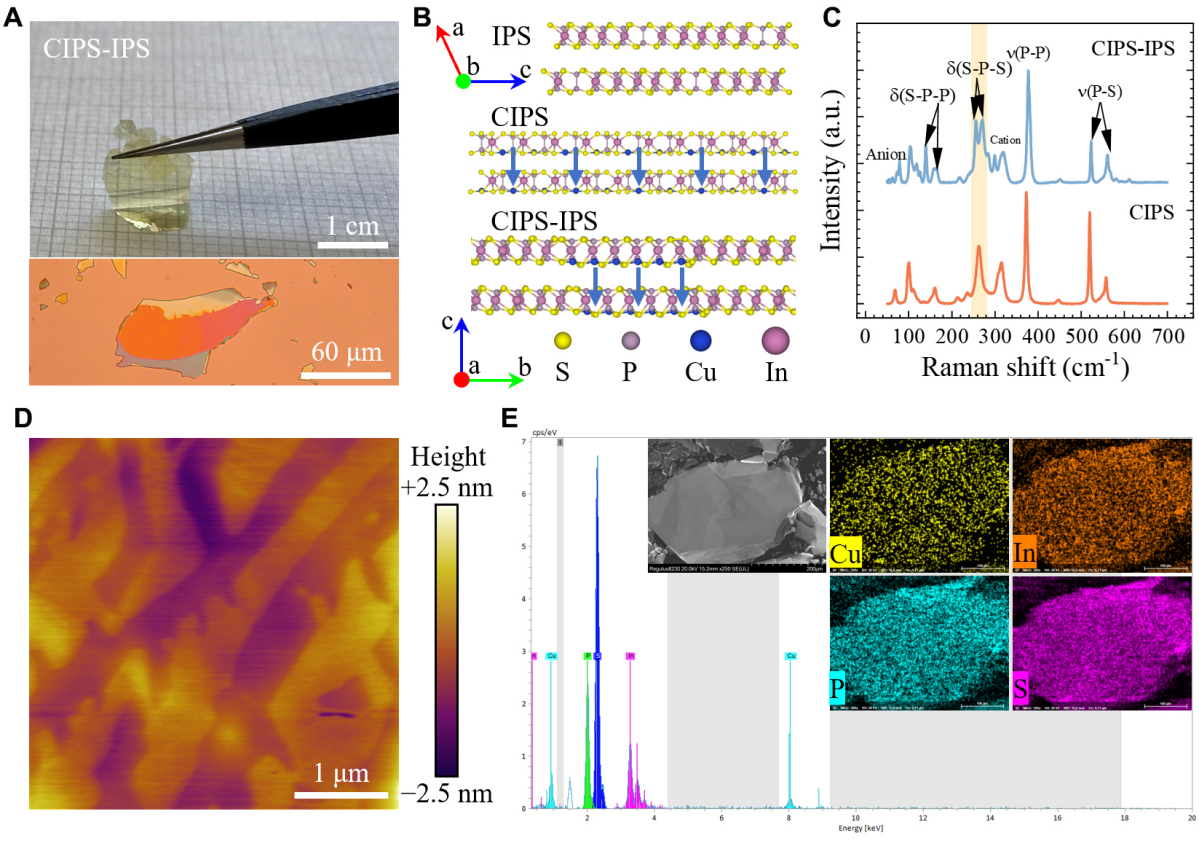

Figure 1. Structural and chemical characterizations. (A) a CIPS-IPS crystal (up) and nano flakes on conductive Au/SiO_2/Si substrates(down). (B) crystal structure of IPS (viewed along the *b*-axis), CIPS and CIPS-IPS heterostructure (viewed along the *a*-axis), respectively. The blue arrows represent the direction of polarization. (C) Raman spectra of CIPS-IPS and IPS flakes. (D) a representative surface topography of CIPS-IPS nano flake measured by AFM. (E) a representative energy-dispersive x-ray spectrum of the CIPS-IPS crystal. The inset shows the SEM image and corresponding elemental mappings.

element, as shown in Figure 1E and Supplementary Figure 1. Quantitative energy-dispersive x-ray spectroscopy (EDS) revealed an average composition of $Cu_{0.57}In_{1.04}P_2S_6$ (see EDS results in Supplementary Table 2).

To accurately measure the Young's modulus (E_s) of the (001) plane of the crystal, three independent quasi-static nanoindentation tests were performed. The indentation depth was kept well below 1/10 of the total thickness of the single crystal. The peak loading was set as 16 mN with the purpose of obtaining the depth-independent elastic modulus, and the loading/unloading rates were set as 0.25 mN/s. To minimize the influence of time-dependent plastic effects and obtain entirely elastic unloading curves, the peak loading was maintained for 10 s before unloading. All nanoindentation *P-h* curves are shown in Figure 2A. We can see a few pop-ins which are caused by fracture or dislocation[38]. The reduced modulus can then be deduced from the slope of load-displacement curve, d*P*/d*h*, upon unloading, using the following Oliver-Phar model[39]:

$$S = \frac{dP}{dh} = \beta \frac{2}{\sqrt{\pi}} E_r \sqrt{A} \quad (1)$$

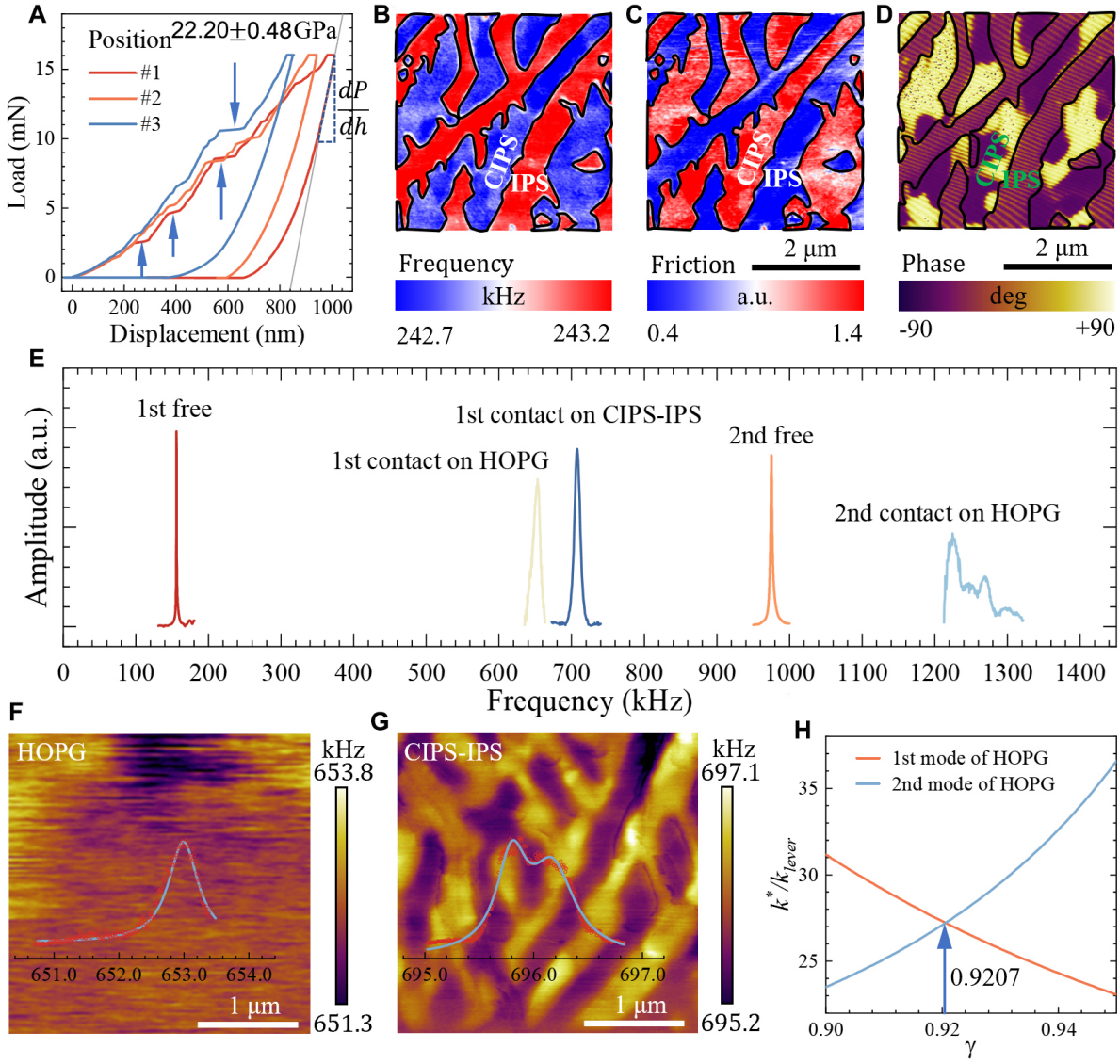

Figure 2. Elastic property characterizations. (A) Nanoindentation Load–displacement curves measured on the (001) plane of CIPS-IPS crystal. The blue arrows indicate pop-ins due to fracture damage. (B) The contact resonant frequency image measured by CR-AFM. (C) The friction force image measured by LFM. (D) The phase image measured by PFM. (B-D) and Figure 1D are in the same region. (E) The resonance frequencies of the cantilever from free resonance to contact resonance on HOPG and CIPS-IPS. (F and G) CR-AFM mapping of the first-order contact resonance frequency in HOPG and CIPS-IPS, respectively. Inset: Frequency histogram and Gauss fitting curves. (H) The relationship between the normalized contact stiffness *k*/klever* and the relative tip position γ.

where E_r is the reduced Young's modulus, β is the geometry constant close to unity (1.058 for Berkovich indenter), and A is the projected area of the indentation at the contact depth h_c. For a Berkovich tip, $A \cong 24.5\ h_c^2$. The reduced modulus E_r is related to Young's modulus E_s through the following relationship from contact mechanics:

$$\frac{1}{E_r} = \frac{1-\nu_s^2}{E_s} + \frac{1-\nu_I^2}{E_I} \quad (2)$$

where E_I is the elastic modulus of the indenter (1140 GPa for diamond), ν_s and ν_I are the Poisson's ratios of the sample and the indenter. The Poisson's ratio of diamond is 0.07 and that of CIPS-IPS is close to zero. The E_s of CIPS-IPS is calculated to be around 22.20 ± 0.48 GPa.

A critical issue is that we do not know whether the nanoindentation position is CIPS or IPS. To further correlate it with the corresponding regions, we characterize the same regions with the aid of CR-AFM, Lateral Force Microscopy (LFM), and PFM. Figure 2B-D show resonance frequency, friction force and phase images, respectively. The corresponding complete PFM amplitude and deflection images are shown in Supplementary Figure 2. The frequency and friction force images corresponding to the CIPS phase and IPS show a labyrinth-like distribution which can also be seen from the frequency statistics curve in Supplementary Figure 3. In addition, the CIPS phase resonance frequency is larger, and the corresponding friction force is smaller. This phenomenon can be understood as follows: the higher the resonance frequency, the higher the Young's modulus, which is simply the harder. When measuring the lateral force under the same pressure, the friction force of the harder material is smaller if ignoring other interface factors, which is consistent with our experimental observation. Note that the direction of polarization has little effect on the magnitude of the modulus and the magnitude of the frictional force. In addition, we also ruled out the influence of topography fluctuation itself on the friction measurement; the magnitude of the friction is still continuous, even if in the two regions of the fault [Supplementary Figure 4].

In order to quantify the magnitude of elastic modulus of different phases of CIPS-IPS, a reference material of highly oriented pyrolytic graphite (HOPG) with a modulus of 15 GPa[40] was used for calibration, given the difficulty in accurately determining the tip radius and contact area. Typical first and second-order contact resonance frequency (CRF) spectra are shown in Figure 2E, from which the higher CRF of CIPS reflects its higher modulus. The relative tip position γ was determined as 0.92 from the intersection of curves for the first and second modes of HOPG [Figure 2H]. Then, the mappings of the first-order CRF were also carried out in HOPG and CIPS-IPS, as shown in Figure 2F and G. By fitting the resonance frequency-frequency distribution curves of Figure 2F and G inset, the mean value and deviation of the resonance frequency were obtained. In order to more accurately determine the value of elastic modulus, single-point measurements of the contact resonance frequency were performed on the basis of the modulus mapping image, and the results are shown in Supplementary Table 3.

The process of the contact resonance model to quantify Young's modulus is as follows:

When the cantilever vibrates freely in the air, according to the cantilever flexural vibration governing equation and boundary conditions, the characteristic equation can be obtained:

$$1+\cos x_n^0 L \cosh x_n^0 L = 0 \tag{3}$$

The first two roots of Equation (3) are $[x_1{}^0L, x_2{}^0L,] = [1.8751,4.6941]$[41,42]. When the cantilever tip is in contact with the sample, the normalized contact stiffness k^*/k_{lever} can be expressed as the nth order flexural contact resonance and the relative tip position γ as[41]:

$$\frac{k^*}{k_{lever}} = \frac{2}{3}\left(x_n L\gamma\right)^3 \frac{\left(1+\cos x_n L \cosh x_n L\right)}{B} \tag{4}$$

where k^* and k_{lever} are the contact stiffness and the spring constant of the cantilever, respectively. γ is the relative position of the tip at the end of the cantilever. The values of flexural resonance wavenumber x_nL can be calculated with the nth order resonant frequency f_n of the tip-sample system[41]:

$$x_nL = c_BL\sqrt{f_n} = x_n^0L\sqrt{\frac{f_n}{f_n^0}} \tag{5}$$

Therefore, the cantilever parameter c_BL for each mode can be obtained directly from the free resonance frequencies f_n^0. Because the normalized contact stiffness of the first and second modes k^*/k_{lever} should be the same, the relative tip position γ can be determined by the intersection of the two modes k^*/k_{lever}-γ curves plotted from Equation (4), as shown in Figure 2H. On this basis, the reduced modulus E_s^* of the sample can be calculated from the normalized contact stiffness k^*/k_{lever} as:

$$E_s^* = E_{ref}^*\left(\frac{k_s^*}{k_{ref}^*}\right)^{3/2} = E_{ref}^*\left(\frac{k_s^*/k_{lever}}{k_{ref}^*/k_{lever}}\right)^{3/2} \tag{6}$$

where E_{ref}^* is the reduced modulus of reference material, and can be obtained from Equation (2). k_s^*/k_{lever} and k_{ref}^*/k_{lever} are the normalized contact stiffness of sample and reference material, respectively. Then, the elastic modulus E_s of the sample can be calculated from the reduced modulus E_s^* using Equation (2).

Combined with the Equations (2 and 4-6), the elastic modulus of CIPS-IPS was calculated and the results are listed in Table 1. It is worth noting that the Poisson's ratio used in the actual calculation comes from the result obtained from the conversion of the elastic coefficient calculated by DFT. The Poisson's ratio of CIPS is -0.044 (the value of the reference is -0.060[43]), and the Poisson's ratio of IPS is 0.107, as shown in Table 1. The elastic modulus of CIPS phase is 27.42 ± 0.05 GPa, which is slightly smaller than that of IPS phase, which is 27.51 ± 0.04 GPa. The moduli obtained by the CR-AFM measurement of both CIPS and IPS are larger than the Young's modulus result of 22.20 ± 0.48 GPa from the nanoindentation measurement. This may be induced by the fractures or the effect of dislocations during the indenting process. Through the results of the continuous stiffness method [Supplementary Figure 5], we can find that the modulus gradually decreases with the increase of the indentation depth, which confirms the effect of fracture in reducing the measured modulus value of nanoindentation measurement.

In order to confirm the difference in the elastic modulus of the two phases, we used density functional theory (DFT) to accurately calculate the elastic matrices of the CIPS phase and the IPS phase (The crystal structure parameters of CIPS and IPS are listed in Supplementary Table 1), and the results are shown in Table 2. From the table, we can find that the modulus of IPS is larger than that of CIPS, with a difference of nearly 1.23 GPa, which is consistent with our experimental results.

To further study the ferroelectric property of CIPS-IPS, the flakes were obtained by mechanical exfoliation and then transferred to Au-coated silicon. Figure 3A shows the topography, which indicates the thickness is around 176.2 nm. The corresponding phase image is shown in Figure 3B, and the enlarged amplitude and phase signals of blue-boxed region are shown in Figure 3D and E, respectively. The vanish of amplitude signal indicates the region of non-ferroelectric IPS phase. In contrast, there are two opposite polarization states in the CIPS phase, such as the yellow domain (point P1) and the black domain (point P2). There are three phase state distribution characteristics, in which the intermediate contrast is from non-polarized IPS.

Table 1. Elastic modulus of CIPS and IPS by CR-AFM

Properties	Tip Si	HOPG	CIPS	IPS
1st CRF (kHz)		653.01 ± 0.25	695.81 ± 0.11	696.15 ± 0.08
E_z (GPa)	160	15	27.42 ± 0.05	27.51 ± 0.04
v (Poisson's ratio)	0.28	0.2	-0.044	0.107

CIPS: $CuInP_2S_6$; IPS: $In_{4/3}P_2S_6$; CR-AFM: contact resonance atomic force microscopy; HOPG: highly oriented pyrolytic graphite.

Table 2. Elastic properties of CIPS and IPS by DFT

Properties (GPa)	C_{11}	C_{22}	C_{33}	C_{23}	C_{13}	C_{12}	C_{44}	C_{55}	C_{66}	C_{15}	C_{25}	C_{35}	C_{64}	E_z
CIPS	99.86	101.68	28.02	-3.85	-4.71	25.49	6.99	6.71	37.56	1.93	4.10	2.55	0.91	26.57
IPS	89.07	75.74	33.27	9.72	10.03	23.12	25.96	11.67	9.90	-6.86	-13.56	3.77	-8.33	27.80

CIPS: $CuInP_2S_6$; IPS: $In_{4/3}P_2S_6$.

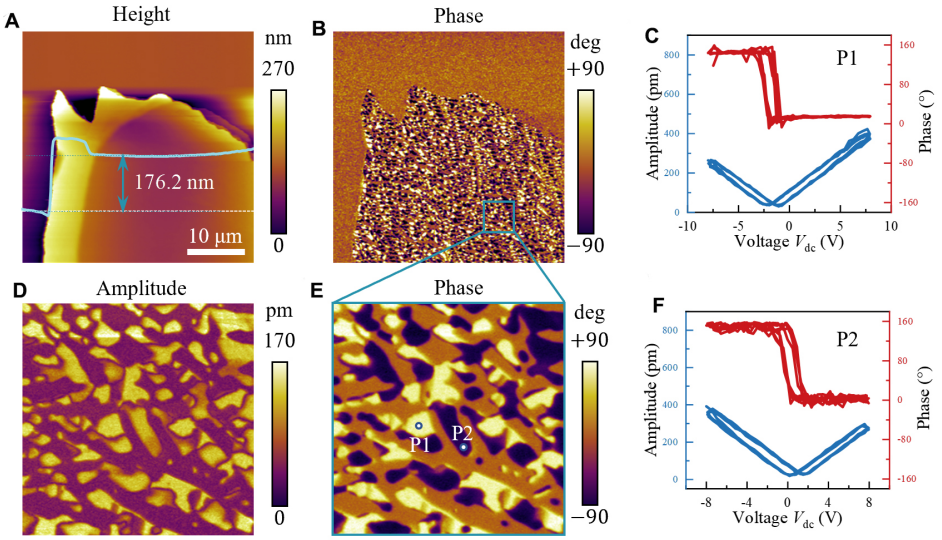

Figure 3. Ferroelectric characterizations of CIPS-IPS crystal. (A and B): a representative topography and phase images. Inset: height curve at white section line. (C and F): the PFM phase and amplitude hysteresis loops in P1 (polarization downward) and P2 (polarization upward), respectively. (D and E): the enlarged amplitude and phase images in the blue boxed region of (B).

We also found this common phenomenon in other regions and performed statistical analysis on its area distribution, and the results are shown in Supplementary Figure 6. In addition, we measured the ferroelectric hysteresis curves of the two domains of CIPS phase, and the results are shown in Figure 3C-F. We can clearly see that the phases and amplitudes of both domains exhibit typical characteristics of ferroelectric materials. It is worth mentioning that the hysteresis curves of different domains deviate from the 0 V, which is mainly caused by the difference in the depolarization fields. Based on the amplitude-voltage curves, we calculated the equivalent piezoelectric coefficient d_{33} of the CIPS phase, and the value of d_{33} is about 40.1 ± 2.2 pm/V, as shown in Supplementary Figure 7. The piezoelectric coefficient d_{33} is larger than the reported value (ranging from 5 to 12 pm/V)[29]. The local effective d_{33} by the scanning probe technique includes the possible contributions from electrostatic interaction and ionic strain. Similar phenomena have been found in ferroelectric materials[44].

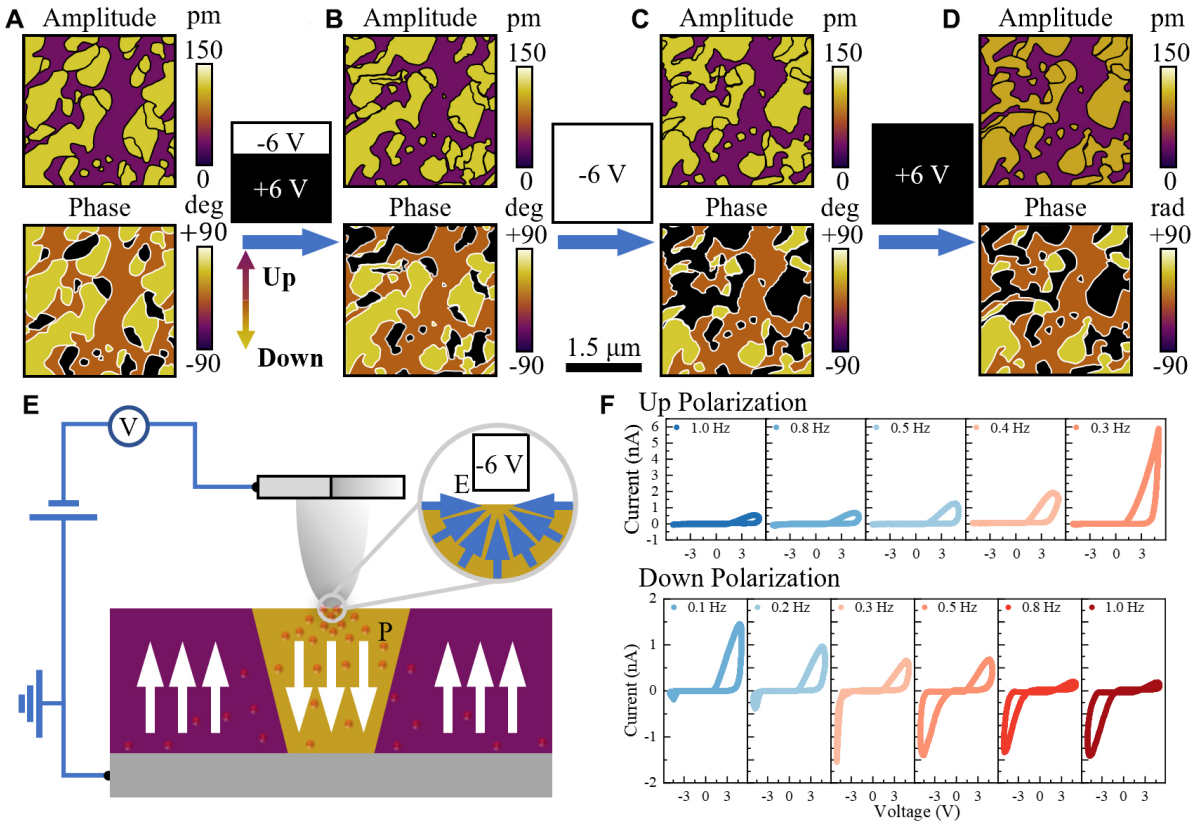

Figure 4. Domain switching and ionic migration characterizations of CIPS-IPS crystal. (A-D) The amplitude and phase images of initial, after applying -6 V/+6 V bias, after applying -6 V bias and after applying +6 V bias, respectively. The scale bar is 1.5 μm. (E) Schematic diagram of ion migration in CIPS under tip electric field. Red balls represent copper ions. The white and blue arrows indicate the polarization direction and the electric field direction, respectively. (F) Current-voltage(I-V) curves at different scan rates in different polarization areas.

The polarization direction is determined by switching domains in random regions, and the results are shown in Figure 4A and B. The voltage of writing domain is shown in the inset, -6 V for the upper 1/3 area and +6 V for the lower 2/3 area. As a result, most of the yellow domains in the upper 1/3 area were switched into black domains, while the lower 2/3 area did not change significantly. Thus, the yellow (black) domains represent the downward (upward) polarization. To further confirm this speculation, we continued to write domains in the same region with -6 V voltage, and the results are shown in Figure 4C. We can clearly find that most of the yellow domain switch to black domain, while the original non-polarization IPS phase and black domains do not change significantly. This again confirms that the black domain corresponds to upward polarization. We then applied a +6 V voltage at the same region, and the result is shown in Figure 4D. The entire domain did not change, and the amplitude signal of the PFM was weakened. The mean value was only 2/3 of the original amplitude in the CIPS phase. This means that a voltage of +6 V is not able to switch the polarization or even reduce its piezoelectric response. Note that Figure 4A-D are modified images by clustering method to facilitate readers to see the changes in domain structure clearly. The original images are shown in Supplementary Figure 8.

To explain this interesting phenomenon, we refer to previous studies on ion migration in CIPS and propose a model of ion migration-mediated nonreciprocal domain switching, as shown in Figure 4E. In the schematic diagram, red balls represent Cu ions. When a voltage of tip bias -6 V is applied to the sample

surface, the electric field converges towards the probe tip, as the inset indicates. The Cu ions migrate to the probe and decrease the Schottky barrier between the probe and the sample. The effective electric field directly acting on the CIPS phase is enough to switch the domain, and the yellow domain is switched to the black domain. On the contrary, when a voltage of +6 V is applied, the direction of the electric field diverges from the probe, and the Cu ions are driven away from the tip, and the effective electric field acting on the CIPS phase therefore cannot switch domain. As a result, all domains did not change significantly, and the overall piezoelectric response decreased. To confirm ion mobility in CIPS-IPS, we characterized the macroscopically manifested I-V curves, and the results are shown in Figure 4F. In the upward polarization region, we can find that the forward current gradually increases as the rate of the applied bias cycle decreases. Likewise, in the downward polarization region, the forward current is also large at lower voltage sweep speeds. Nevertheless, with the increase of scanning speed, the whole forward current decreases until zero, while the reverse current gradually increases and tends to be stable. All suggest that Cu ion migration dominates the current feature, which is consistent with our previous studies on current regulation in pure CIPS[16]. These results favorably confirm that Cu ions mediate the switching of ferroelectric domains.

CONCLUSIONS

In conclusion, we accurately characterized the Young's modulus of the CIPS-IPS two phases for the first time by various experimental methods (nanoindentation method and atomic force contact resonance method) in this study, and the Young's modulus of the CIPS phase was 27.42 ± 0.05 GPa, slightly less than that of the IPS phase, which was 27.51 ± 0.04 GPa. In addition, we calculated the elastic matrices of the two phases of CIPS-IPS using the first-principles method, and deduced their respective Young's modulus, all of which are in good agreement with our experimental values. Finally, we also discover the asymmetry of domain switching and propose an ion-mediated nonreciprocal domain switching model, which strongly explains this interesting phenomenon. Our work provides a reliable experimental reference for the follow-up study of the elastic properties of CIPS-IPS and the phase field simulation for regulating the domain structure.

DECLARATIONS

Authors' contributions

AFM characterization, writing original draft: Zhang X
Review & editing, supervision: Jiang X
Raman characterization: Du G
DFT calculation: Ren Q
EDS characterization: Zhu W
Sample synthesis: Kang J, Deng J
Guidance for experiment and data analysis: Lun Y, Wang T, Bai B, Yu Z
Conceptualization, review, supervision: Hong J, Wang X, Chen Y

Availability of data and materials

The list of elemental atomic percentages of different CIPS flakes obtained from EDS, single-point CRF measurement results of CIPS-IPS and HOPG by CR-AFM, CR-AFM method, A: frequency and friction histogram and original PFM data are provided in Supplementary Information.

Financial support and sponsorship

The work at Beijing Institute of Technology is supported by National Natural Science Foundation of China with Grant Nos. 12172047, 11604011, 92163101, 12202056, National Key Research and Development Program of China (2019YFA0307900), the Beijing Natural Science Foundation (Z190011), and Beijing Institute of Technology Research Fund Program for Young Scholars.

Conflicts of interest

All authors declared that there are no conflicts of interest.

Ethical approval and consent to participate

Not applicable.

Consent to publication

Not applicable.

Copyright

© The Author(s) 2023.

REFERENCES

1. You L, Zhang Y, Zhou S, et al. Origin of giant negative piezoelectricity in a layered van der Waals ferroelectric. *Sci Adv* 2019;5:eaav3780. DOI PubMed PMC
2. Brehm JA, Neumayer SM, Tao L, et al. Tunable quadruple-well ferroelectric van der Waals crystals. *Nat Mater* 2020;19:43-8. DOI PubMed
3. Niu L, Liu F, Zeng Q, et al. Controlled synthesis and room-temperature pyroelectricity of $CuInP_2S_6$ ultrathin flakes. *Nano Energy* 2019;58:596-603. DOI
4. Si M, Saha AK, Liao PY, et al. Room-temperature electrocaloric effect in layered ferroelectric $CuInP_2S_6$ for solid-state refrigeration. *ACS Nano* 2019;13:8760-5. DOI
5. Zhou S, You L, Chaturvedi A, et al. Anomalous polarization switching and permanent retention in a ferroelectric ionic conductor. *Mater Horiz* 2020;7:263-74. DOI
6. Xu D, Ma R, Zhao Y, et al. Unconventional out-of-plane domain inversion via in-plane ionic migration in a van der Waals ferroelectric. *J Mater Chem C* 2020;8:6966-71. DOI
7. Neumayer SM, Brehm JA, Tao L, et al. Local strain and polarization mapping in ferrielectric materials. *ACS Appl Mater Interfaces* 2020;12:38546-53. DOI PubMed
8. Si M, Liao PY, Qiu G, Duan Y, Ye PD. Ferroelectric field-effect transistors based on MoS_2 and $CuInP_2S_6$ two-dimensional van der waals heterostructure. *ACS Nano* 2018;12:6700-5. DOI
9. Huang W, Wang F, Yin L, et al. Gate-coupling-enabled robust hysteresis for nonvolatile memory and programmable rectifier in van der waals ferroelectric heterojunctions. *Adv Mater* 2020;32:e1908040. DOI PubMed
10. Singh P, Baek S, Yoo HH, Niu J, Park JH, Lee S. Two-dimensional CIPS-InSe van der Waal heterostructure ferroelectric field effect transistor for nonvolatile memory applications. *ACS Nano* 2022;16:5418-26. DOI PubMed
11. Liu F, You L, Seyler KL, et al. Room-temperature ferroelectricity in $CuInP_2S_6$ ultrathin flakes. *Nat Commun* 2016;7:12357. DOI PubMed PMC
12. Wang X, Yu P, Lei Z, et al. Van der Waals negative capacitance transistors. *Nat Commun* 2019;10:3037. DOI PubMed PMC
13. Neumayer SM, Tao L, O'hara A, et al. The concept of negative capacitance in ionically conductive van der Waals ferroelectrics. *Adv Energy Mater* 2020;10:2001726. DOI
14. Li B, Li S, Wang H, et al. An electronic synapse based on 2D ferroelectric $CuInP_2S_6$. *Adv Electron Mater* 2020;6:2000760. DOI
15. Yue K, Liu Y, Lake RK, Parker AC. A brain-plausible neuromorphic on-the-fly learning system implemented with magnetic domain wall analog memristors. *Sci Adv* 2019;5:eaau8170. DOI PubMed PMC
16. Jiang X, Wang X, Wang X, et al. Manipulation of current rectification in van der Waals ferroionic $CuInP_2S_6$. *Nat Commun* 2022;13:574. DOI
17. Chen J, Zhu C, Cao G, et al. Mimicking neuroplasticity via ion migration in van der waals layered copper indium thiophosphate. *Adv Mater* 2022;34:e2104676. DOI PubMed
18. Guo R, Zhou Y, Wu L, et al. Control of synaptic plasticity learning of ferroelectric tunnel memristor by nanoscale interface engineering. *ACS Appl Mater Interfaces* 2018;10:12862-9. DOI PubMed
19. Zhang D, Luo ZD, Yao Y, et al. Anisotropic ion migration and electronic conduction in van der Waals ferroelectric $CuInP_2S_6$. *Nano Lett* 2021;21:995-1002. DOI
20. Susner MA, Belianinov A, Borisevich A, et al. High-Tc layered ferrielectric crystals by coherent spinodal decomposition. *ACS Nano* 2015;9:12365-73. DOI PubMed
21. Susner MA, Chyasnavichyus M, Puretzky AA, et al. Cation-eutectic transition via sublattice melting in $CuInP_2S_6$-$In_{4/3}P_2S_6$ van der Waals layered crystals. *ACS Nano* 2017;11:7060-73. DOI
22. Rao R, Selhorst R, Conner BS, Susner MA. Ferrielectric-paraelectric phase transitions in layered $CuInP_2S_6$ and $CuInP_2S_6$-$In_{4/3}P_2S_6$ heterostructures: a Raman spectroscopy and x-ray diffraction study. *Phys Rev Mater* 2022; 6:045001. DOI
23. Checa M, Ivanov I, Neumayer SM, et al. Correlative piezoresponse and micro-Raman imaging of $CuInP_2S_6$-$In_{4/3}P_2S_6$ flakes unravels

phase-specific phononic fingerprint via unsupervised learning. *Appl Phys Lett* 2022;121:062901. DOI

24. Neumayer SM, Eliseev EA, Susner MA, et al. Giant negative electrostriction and dielectric tunability in a van der Waals layered ferroelectric. *Phys Rev Mater* 2019;3:024401. DOI
25. Chen C, Liu H, Lai Q, et al. Large-scale domain engineering in two-dimensional ferroelectric $CuInP_2S_6$ via giant flexoelectric effect. *Nano Lett* 2022;22:3275-82. DOI
26. Rao R, Conner BS, Selhorst R, Susner MA. Pressure-driven phase transformations and phase segregation in ferrielectric $CuInP_2S_6$-$In_{4/3}P_2S_6$ self-assembled heterostructures. *Phys Rev B* 2021;104:235421. DOI
27. Ming W, Huang B, Zheng S, et al. Flexoelectric engineering of van der Waals ferroelectric $CuInP_2S_6$. *Sci Adv* 2022;8:eabq1232. DOI
28. Eliseev EA, Fomichov YM, Kalinin SV, Vysochanskii YM, Maksymovich P, Morozovska AN. Labyrinthine domains in ferroelectric nanoparticles: manifestation of a gradient-induced morphological transition. *Phys Rev B* 2018;98:054101. DOI
29. Checa M, Jin X, Millan-Solsona R, et al. Revealing fast cu-ion transport and enhanced conductivity at the $CuInP_2S_6$-$In_{4/3}P_2S_6$ heterointerface. *ACS Nano* 2022;16:15347-57. DOI
30. Blöchl PE, Jepsen O, Andersen OK. Improved tetrahedron method for Brillouin-zone integrations. *Phys Rev B Condens Matter* 1994;49:16223-33. DOI PubMed
31. Perdew JP, Burke K, Ernzerhof M. Generalized gradient approximation made simple. *Phys Rev Lett* 1996;77:3865-8. DOI PubMed
32. Kresse G, Furthmüller J. Efficient iterative schemes for ab initio total-energy calculations using a plane-wave basis set. *Phys Rev B* 1996;54:11169-86. DOI PubMed
33. Kresse G, Furthmüller J. Efficiency of ab-initio total energy calculations for metals and semiconductors using a plane-wave basis set. *Comput Mater Sci* 1996;6:15-50. DOI
34. Grimme S, Antony J, Ehrlich S, Krieg H. A consistent and accurate ab initio parametrization of density functional dispersion correction (DFT-D) for the 94 elements H-Pu. *J Chem Phys* 2010;132:154104. DOI PubMed
35. Grimme S, Ehrlich S, Goerigk L. Effect of the damping function in dispersion corrected density functional theory. *J Comput Chem* 2011;32:1456-65. DOI PubMed
36. Maisonneuve V, Evain M, Payen C, Cajipe V, Molinié P. Room-temperature crystal structure of the layered phase $CuInP_2S_6$. *J Alloys Compd* 1995;218:157-64. DOI
37. Diehl R, Carpentier C. The structural chemistry of indium phosphorus chalcogenides. *Acta Crystallogr B Struct Sci* 1978;34:1097-105. DOI
38. Fang X, Bishara H, Ding K, et al. Nanoindentation pop-in in oxides at room temperature: dislocation activation or crack formation? *J Am Ceram Soc* 2021;104:4728-41. DOI
39. Oliver W, Pharr G. An improved technique for determining hardness and elastic modulus using load and displacement sensing indentation experiments. *J Mater Res* 1992;7:1564-83. DOI
40. Xiao J, Zhang L, Zhou K, Li J, Xie X, Li Z. Anisotropic friction behaviour of highly oriented pyrolytic graphite. *Carbon* 2013;65:53-62. DOI
41. Zhu Q, Pan K, Xie S, Liu Y, Li J. Nanomechanics of multiferroic composite nanofibers via local excitation piezoresponse force microscopy. *J Mech Phys Solids* 2019;126:76-86. DOI
42. Hurley DC. Contact resonance force microscopy techniques for nanomechanical measurements. In Applied scanning probe methods XI. Heidelberg, Berlin: Springer, 2009; pp. 97-138. DOI
43. Zhang C, Nie Y, Du A. Intrinsic ultrahigh negative Poisson's ratio in two-dimensional ferroelectric ABP2x6 materials. *Acta Physico-Chimica Sinica* 2019;35:1128-33. DOI
44. Ming W, Huang B, Li J. Decoupling competing electromechanical mechanisms in dynamic atomic force microscopy. *J Mech Phys Solids* 2022;159:104758. DOI

Luo *et al. Microstructures* 2023;3:2023011
DOI: 10.20517/microstructures.2022.41

Microstructures

Research Article

Open Access

Check for updates

Triethanolamine assisted synthesis of bimetallic nickel cobalt nitride/nitrogen-doped carbon hollow nanoflowers for supercapacitor

Qiao Luo, Congcong Lu, Lingran Liu, Maiyong Zhu

Research School of Polymeric Materials, School of Materials Science & Engineering, Jiangsu University, Zhenjiang 212013, Jiangsu, China.

Correspondence to: Dr. Maiyong Zhu, Research School of Polymeric Materials, School of Materials Science & Engineering, Jiangsu University, Zhenjiang 212013, Jiangsu, China. E-mail: maiyongzhu@ujs.edu.cn

How to cite this article: Luo Q, Lu C, Liu L, Zhu M. Triethanolamine assisted synthesis of bimetallic nickel cobalt nitride/nitrogen-doped carbon hollow nanoflowers for supercapacitor. *Microstructures* 2023;3:2023011. https://dx.doi.org/10.20517/microstructures.2022.41

Received: 12 Nov 2022 **First Decision:** 8 Dec 2022 **Revised:** 22 Dec 2022 **Accepted:** 13 Jan 2023 **Published:** 30 Jan 2023

Academic Editor: Lianzhou Wang **Copy Editor:** Fangling Lan **Production Editor:** Fangling Lan

Abstract

Supercapacitors (SCs) have drawn growing attention due to their advantages in fast charge/discharge over batteries. Benefiting from their prominent electrical conductivity and metal-like characteristics, transition metal nitrides have emerged as promising electrode materials for SCs. Traditional ways to prepare metal nitrides through ammonolysis are inconvenient and induce severe environmental pollution. Herein, we report a facile synthetic method toward heterogenous Ni_3N-$Co_2N_{0.67}$/nitrogen-doped carbon (Ni_3N-$Co_2N_{0.67}$/NC) hollow nanoflower via pyrolyzing NiCo-TEOA (triethanolamine) complex precursor applying urea as nitrogen source. Electrochemical tests demonstrate that the Ni_3N-$Co_2N_{0.67}$/NC nanoflower delivers good specific capacitance (1582 F g^{-1} at 1 A g^{-1}) and steady cycle performance (83.79% after 5000 cycles). Moreover, the as-assembled Ni_3N-$Co_2N_{0.67}$/NC//AC cell can reach a peak energy density of 32.4 W h kg^{-1} at a power density of 851.3 W kg^{-1}. The excellent electrochemical performance confirms extensive application prospects of the Ni_3N-$Co_2N_{0.67}$/NC nanoflower.

Keywords: Nanoflower, hollow structure, transition metal nitride, nitrogen-doped carbon, supercapacitor

INTRODUCTION

The rapid development of clean and renewable energy in various fields including electric vehicles and

© The Author(s) 2023. **Open Access** This article is licensed under a Creative Commons Attribution 4.0 International License (https://creativecommons.org/licenses/by/4.0/), which permits unrestricted use, sharing, adaptation, distribution and reproduction in any medium or format, for any purpose, even commercially, as long as you give appropriate credit to the original author(s) and the source, provide a link to the Creative Commons license, and indicate if changes were made.

portable electronic devices desires high-efficiency and high-capacity energy storage devices[1,2]. Supercapacitors (SCs) have attracted much interest due to their enhanced power density and long service life[3]. Standing in the intermediate zone of batteries and traditional capacitors, SCs could be generally divided into two types. Electric double-layer capacitors (EDLCs) rely on the electrostatic attraction of ions at the interfaces between electrode and electrolyte to complete charge storage, whereas pseudocapacitors (PCs) take advantage of redox reactions during faradaic redox processes to store electric energies[4,5]. Importantly, developing SCs with stronger energy storage capacity inevitably demands the utilization of better electrode materials[6].

Numerous transition metal nitrides (TMNs) such as Ni_3N[7], Co_2N[8], Fe_2N[9], VN[10] and MoN[11] have emerged as potential electrode materials for SCs by virtue of their distinctive electronic structure, stable chemical resistance, remarkable electric conductivity, and flexible mechanical deformability[12]. However, most of the TMNs are synthesized by pyrolyzing the precursor under NH_3 atmosphere, which leads to massive waste of NH_3 and causes immeasurable environmental pollution. Consequently, there is a desperate need to develop a more convenient and green approach to prepare TMNs. Importantly, applying nontoxic and environmentally friendly nitrogen sources is a priority. Nitrogenous organic small molecules, which are easy to store and can produce NH_3 under high temperatures, might serve as ideal substitutes for NH_3. For example, Yang *et al.* converted vanadium-organic compounds (VAORCS) into vanadium nitride quantum dots/nitrogen-doped hierarchical carbon nanocomposites (VNQD/NDHCs) by annealing the mixture of VAORCS powder and melamine[13]. Jin *et al.* mixed chloride salts of five different metals with urea by ball-milling to form a metal-urea gel and obtained high-entropy metal nitride via calcining the gel[14]. Inspired by these previous reports, we chose urea as the nontoxic and cheap nitrogen source to prepare metal nitrides. In addition, different from individual ones, bimetallic nanoparticles often exhibit higher catalytic activities, richer redox sites, and better chemical stabilities[15-17]. Meanwhile, nickel and cobalt are chosen because they have comparable atomic size and chemical valence state[18].

On the other hand, it is known to all that the most important factor affecting the performance of materials is their morphology and structure. Compared to solid structures, hollow ones possess large inner voids, reactive inner surfaces and indestructible structures[19]. Hence, constructing hollow structures with low mass transport resistance, rapid ion diffusion channels and high-volume electrical capacity stands out as an efficient strategy to enhance SCs performance[20]. Metal-small organic molecule complexes are ideal precursors for hollow structures. Liu *et al.* coordinated Ni^{2+} and Co^{2+} with glycerol and then transformed the solid complex into a yolk-shell structure via the hydrothermal method[21]. Dong *et al.* synthesized hollow carbon spheres by etching SiO_2 template with HF[22]. To avoid the use of a template and multifarious synthesis steps, we designed a one-step strategy toward hollow structure by coordinating Ni^{2+} and Co^{2+} with triethanolamine (TEOA) accompanied by the hydrolysis of metal alkoxide. Meanwhile, the nitrogenous organic network could be pyrolyzed into N-doped carbon via calcine, which further enhances the electrical conductivity and serves as strong support during long-term cycling[23].

Herein, we reported a hierarchical Ni_3N-$Co_2N_{0.67}$/nitrogen-doped carbon (NC) hollow nanoflower, which is derived from annealing nickel/cobalt-TEOA complex (N_1C_2-TEOA) precursor with urea as nitrogen source. The as-prepared Ni_3N-$Co_2N_{0.67}$/NC delivers larger specific surface area, superior energy storage capacity and longer cycle lifespan. The Ni_3N-$Co_2N_{0.67}$/NC transformed from N_1C_2-TEOA sample shows an excellent specific capacitance of 1582 F g^{-1} at 1 A g^{-1} and 83.79% capacitance retention after 5000 cycles. Furthermore, the assembled Ni_3N-$Co_2N_{0.67}$/NC//AC asymmetric device demonstrates a maximum energy density of 32.4 Wh kg^{-1} and steady cycle performance of 95.8% after 5000 cycles.

MATERIALS AND METHODS

Materials

Nickel chloride hexahydrate ($NiCl_2·6H_2O$), Cobalt chloride hexahydrate ($CoCl_2·6H_2O$), triethanolamine (TEOA) and urea were all purchased from Shanghai Aladdin Biochemical Technology Co., Ltd and used without further purification. The deionized water (DI water) involved in the experiment with an electrical resistivity of 18.2 MΩ cm^{-1} was prepared by ultrapure water polishing system.

Sample preparation and characterization

Synthesis of heterogenous Ni3N-Co2N0.67/NC hollow nanoflowers

Firstly, 2 g TEOA was dissolved in 18 mL DI water under vigorous stirring. Subsequently, x mmol $NiCl_2·6H_2O$ and y mmol $CoCl_2·6H_2O$ (x + y = 3, x:y = 0:3, 1:2, 1:1, 2:1, 3:0) were added into the above mixture to form a homogenous solution. The solution was then transferred to a 50 mL Teflon-lined stainless-steel autoclave, which was heated at 160 °C and kept for 12 h. The obtained product was washed with DI water and ethanol three times, respectively. Finally, the product was collected by centrifugation and vacuum dried in an oven for 12 h at 60 °C to obtain N_xC_y-TEOA hollow nanoflowers. The samples are labeled as N_0C_3-TEOA, N_1C_2-TEOA, N_1C_1-TEOA, N_2C_1-TEOA and N_3C_0-TEOA.

The heterogenous Ni_3N-$Co_2N_{0.67}$/NC was synthesized by the following process. Initially, 50 mg N_1C_2-TEOA and 500 mg urea (mass ratio: 1:10) were uniformly dispersed in the porcelain boats. Then the boat with urea and N_1C_2-TEOA was placed upstream and downstream of the tube furnace, respectively. The furnace was heated to 400 °C at a heating rate of 2 °C min^{-1} under N_2 atmosphere and kept for 2 h. After natural cooling down to room temperature, heterogenous Ni_3N-$Co_2N_{0.67}$/NC hollow nanoflowers were obtained.

Structure and morphological characterization

X-ray diffraction (XRD) was tested using Rigaku Ultimate IV powder X-ray diffractometer with Cu Kα radiation (λ = 1.5418 Å) at a scanning speed of 5°/min. Scanning electron microscopy (SEM) was performed on Zeiss sigma 300 scanning electron microscope. Transmission electron microscopy (TEM), high-resolution transmission electron microscopy (HRTEM) and selected area electron diffraction (SAED) were carried out on FEI Talos F200x transmission electron microscope. Brunauer-Emmett-Teller (BET) specific surface areas and pore volumes were measured on ASAP 2460. X-ray photoelectron spectroscopy (XPS) data was collected on Thermo Scientific K-Alpha using Al Ka X-ray as the excitation source (hv = 1486.6 eV). Fourier transform infra-red (FTIR) tests were performed on a FTIR apparatus (Nicolet MX-1E, USA).

Electrochemical characterization

The electrochemical measurements were tested by a three-electrode configuration in 1 M KOH electrolyte. Platinum electrode and saturated calomel electrode were used as the counter electrode and reference electrode, respectively. All the electrochemical performance was studied on a CHI760E electrochemical workstation. The working electrode was fabricated by the following procedures. Active material (Ni_3N-$Co_2N_{0.67}$/NC), polyvinylidene fluoride (PVDF), and acetylene black (mass ratio: 7.5:1:1.5) were homogenously mixed and ground using 1-methyl-2-pyrrolidinone as solvent to form a slurry. The slurry was then uniformly coated on 1 × 1 cm^2 square area of a 1 × 5 cm^2 nickel foam (NF). After vacuum drying in an oven at 60 °C for 12 h, the slurry-coated NF area was pressed under 10 Mpa for 2 min. Finally, the NF was soaked into 1 M KOH for 3 h for pre-activation. The mass load of the active material on the NF was around 2~3 mg. The specific capacitance (F g^{-1}) can be calculated from the following Eq. (1)[24]:

$$C = \frac{I\Delta t}{m\Delta V} \quad (1)$$

where I, Δt, m, ΔV indicate the applied current (A), discharge time (s), the mass load of the active material (g) and the working potential (V), respectively.

In the Ni_3N-$Co_2N_{0.67}$/NC//AC asymmetric supercapacitor system, active carbon (AC) was applied as the negative electrode material, which was prepared using the same steps as the positive electrode. The mass of AC can be computed based on the charge balance equation showing as follows[25]:

$$\frac{m_+}{m_-} = \frac{C_- \times V_-}{C_+ \times V_+} \quad (2)$$

where m_+, m_-, C_+, C_-, V_+, V_- represent the mass (g), specific capacitance (F g^{-1}) and operating voltage window (V) of the positive and negative electrode, respectively.

In addition, the energy density (Wh kg^{-1}) and power density (W kg^{-1}) at different current densities were calculated from the following Eqs.[26]:

$$E = \frac{C\Delta V^2}{2 \times 3.6} \quad (3)$$

$$P = \frac{3600 \times E}{\Delta t} \quad (4)$$

where C, ΔV, Δt are the specific capacitance (F g^{-1}), working potential (V) and discharge time (s) of the device, respectively.

RESULTS AND DISCUSSION

As schemed in Figure 1, the complete synthesis route of Ni_3N-$Co_2N_{0.67}$/NC includes two steps. In the first hydrothermal process, TEOA could serve as an ideal solvent and more importantly as a ligand for metal complexes[27]. To avoid inhibition of the complex growth kinetics and nonuniform dispersion of the reaction system due to strong viscosity of TEOA, DI water was chosen as the only cosolvent. Initially, TEOA molecules react with Ni (II) and Co (II) to form Ni_xCo_y-TEOA complex at low temperatures. With the temperature rising, this metal alkoxide begins to hydrolyze, leading to the hollow porous nanoflower structure[21]. In the subsequent thermal treatment, carbon skeleton is pyrolyzed at 400 °C and transformed to N-doped carbon owing to the existence of N center atom of TEOA. Simultaneously, urea decomposes into NH_3 which further reacts with Ni (II) and Co (II), producing Ni_3N and $Co_2N_{0.67}$ eventually. Additionally, various mass ratios of Ni^{2+} to Co^{2+} (0:3, 1:2, 1:1, 2:1, 3:0) were used to investigate the impact on morphology and electrochemical performance of the complex and the best one was chosen to further derivative to the final product.

XRD patterns of N_0C_3-TEOA, N_1C_2-TEOA, N_1C_1-TEOA, N_2C_1-TEOA and N_3C_0-TEOA are presented in Supplementary Figure 1. As expected, all the precursors show no sharp and distinct peaks, exhibiting salient amorphous characteristics[28]. The wide peak bulge at 15°-25° is assigned to the (002) crystal face of carbon, indicating the successful formation of nitrogen-doped carbon after calcining [Figure 2A][29]. The peaks at 38.9°, 42.1°, 44.5°, 58.5°, 70.6° and 78.4° could be attributed to the (110), (002), (111), (112), (300) and (113)

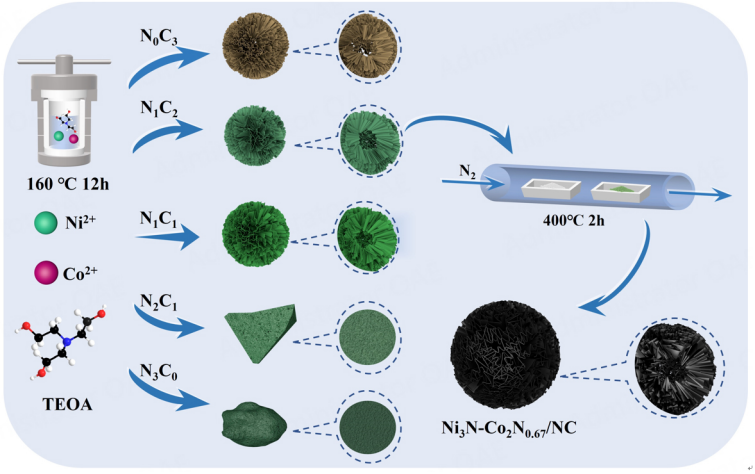

Figure 1. Schematic illustration of preparation process of Ni_3N-$Co_2N_{0.67}$/NC.

crystal faces of Ni_3N (JCPDS:06-0691), while the peaks at 39.0°, 41.6°, 44.4°, 58.2°, 70.7° and 77.7° could correspond to the (100), (002), (101), (102), (110) and (103) crystal faces of $Co_2N_{0.67}$ (JCPDS:10-0280). All these peaks are sharp and narrow due to the good crystallinity of the material[30]. Moreover, no peaks were observed for nickel oxide or cobalt oxide, suggesting pristine metal nitrides were obtained.

The morphologies of precursors were investigated by SEM as displayed in Supplementary Figure 2A-J. N_0C_3-TEOA, N_1C_2-TEOA, and N_1C_1-TEOA are all hollow nanoflower shapes with self-assembled petal-like nanosheets and inner hollow space. However, with the increase of Ni ratio, the radius of these nanoflowers decrease gradually. The radius of N_0C_3-TEOA is about 1.5 μm, while the radius of N_1C_2-TEOA and N_1C_1-TEOA dwindle to 1 μm and 500 nm, respectively. When the Ni ratio further increases (N_2C_1-TEOA and N_3C_0-TEOA), the morphology and structure collapse to irregular shapes and expand greatly in size with a rough surface, which might be an important reason for their poor electrochemical performance. As plotted in Figure 2B and C, Ni_3N-$Co_2N_{0.67}$/NC maintain the hollow nanoflower-like structure with a radius of around 1 μm, revealing that the nitridation process did not destroy the sample's initial morphology. All the nanoflowers are distributed uniformly without excessive agglomerations or clustering. Interestingly, more pores were created during thermal treatment due to the gas escape during carbon decomposition, which greatly increases the specific surface area, providing plentiful active sites for redox reactions.

TEM was employed to gain a better understanding of the internal microstructure of Ni_3N-$Co_2N_{0.67}$/NC. As can be seen in Figure 2D, Ni_3N-$Co_2N_{0.67}$/NC shows a typical nanoflower structure with a hollow inner core, which is well consistent with SEM images. HRTEM was then carried out to analyze the composition of Ni_3N-$Co_2N_{0.67}$/NC. The black circular area and the white background in Figure 2E are metal nitrides and NC, respectively. SAED in the inset of Figure 2E reveals a typical polycrystalline characteristic[31]. The lattice ring is assigned to the (101) and (111) crystal faces of $Co_2N_{0.67}$ and Ni_3N, respectively. The result is further confirmed in Figure 2F. The interplanar spacing of 0.202 nm and 0.204 nm correspond well with (111) and (101) crystal faces of Ni_3N and $Co_2N_{0.67}$/NC, which is consistent with the XRD result. The EDS mapping images in Figure 2H-L swept from the HAADF TEM image in Figure 2G reveal uniform dispersion of Ni, Co, C, N and O elements. Furthermore, EDS spectrum in Figure 2M display the peaks corresponding to Ni, Co, C, N and O and their atomic fraction are 6.38%, 13.16%, 52.46%, 9.93% and 18.07%, respectively. The atomic number ratio of Ni and Co of Ni_3N-$Co_2N_{0.67}$/NC are the same as designed.

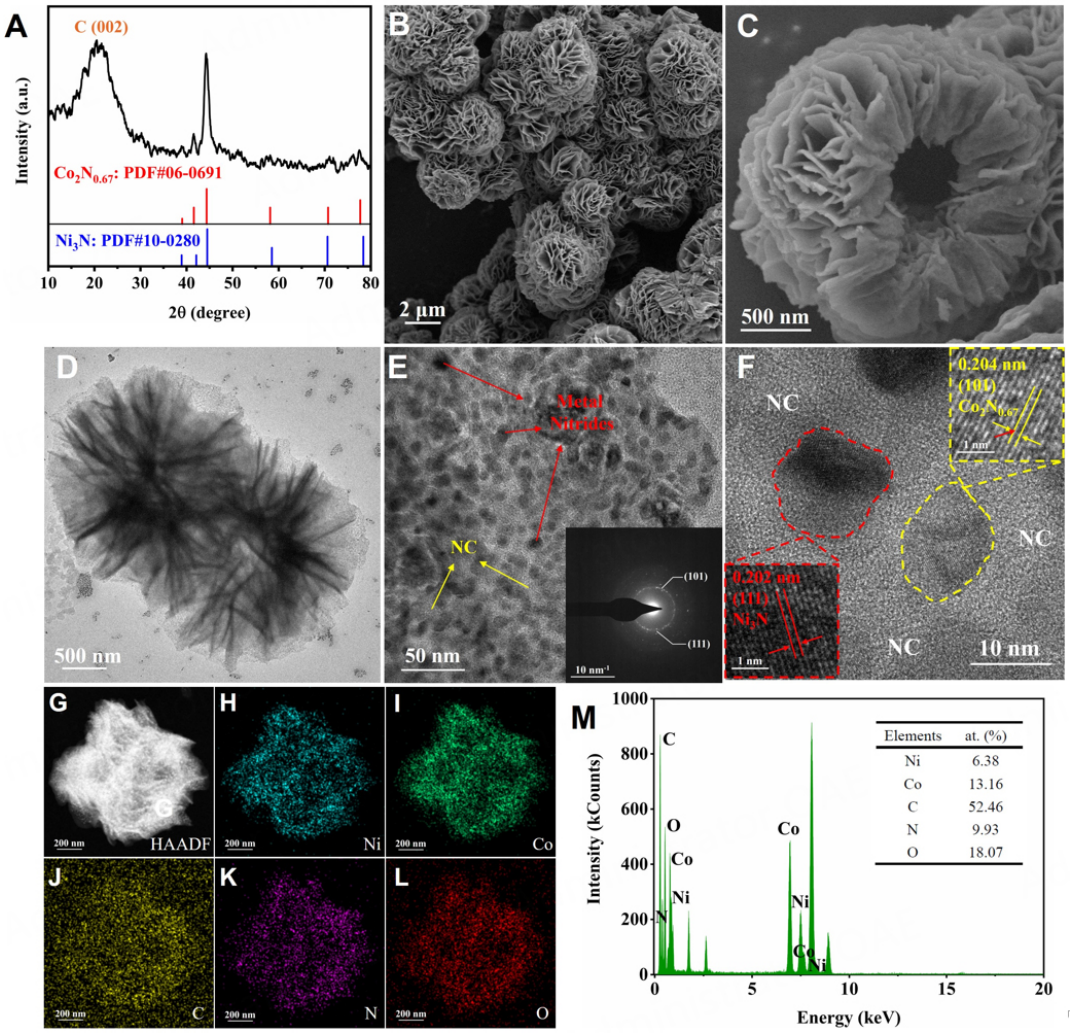

Figure 2. (A) XRD pattern of Ni_3N-$Co_2N_{0.67}$/NC. (B and C) SEM images of Ni_3N-$Co_2N_{0.67}$/NC. (D) TEM image. (E and F) high-resolution TEM image (Inset: SAED image). (G) high-angle annular dark field TEM image. (H and L) the EDS mapping images of Ni, Co, C, N, and O elements. (M) EDS diagram. XRD: X-ray diffraction; SEM: scanning electron microscopy; TEM: transmission electron microscopy; SAED: selected area electron diffraction.

To investigate the pore nature of the precursors and Ni_3N-$Co_2N_{0.67}$/NC, N_2 adsorption-desorption measurement was conducted, as shown in Supplementary Figure 3A-D and Figure 3A. All the isotherms belong to type IV, indicating their mesoporous characteristics[32]. The specific surface areas of N_0C_3-TEOA, N_1C_2-TEOA, N_1C_1-TEOA, N_2C_1-TEOA and N_3C_0-TEOA are found to be 18.88 m^2g^{-1}, 20.98 m^2g^{-1}, 18.35 m^2g^{-1}, 1.573 m^2g^{-1} and 0.844 m^2g^{-1}, respectively. With the nanoflower structure destroyed, the specific surface areas sharply decrease and the number of pores with a diameter larger than 30 nm reduces for N_2C_1-TEOA and N_3C_0-TEOA, which is identical to the SEM results shown in Supplementary Figure 2G and H. As expected, the specific surface area rises to 24.35 m^2g^{-1} due to the numerous pores created by the formation of porous carbon via pyrolysis. Moreover, it can be concluded from the pore size distribution pattern in the inset of Figure 3A that various sizes of pores exist, the main of which are mesopores. The favored specific area benefits from the self-assembled nanosheets and abundant pores, which not only provide fast diffusion channels for ions/electrons but offer sufficient sites for redox reactions.

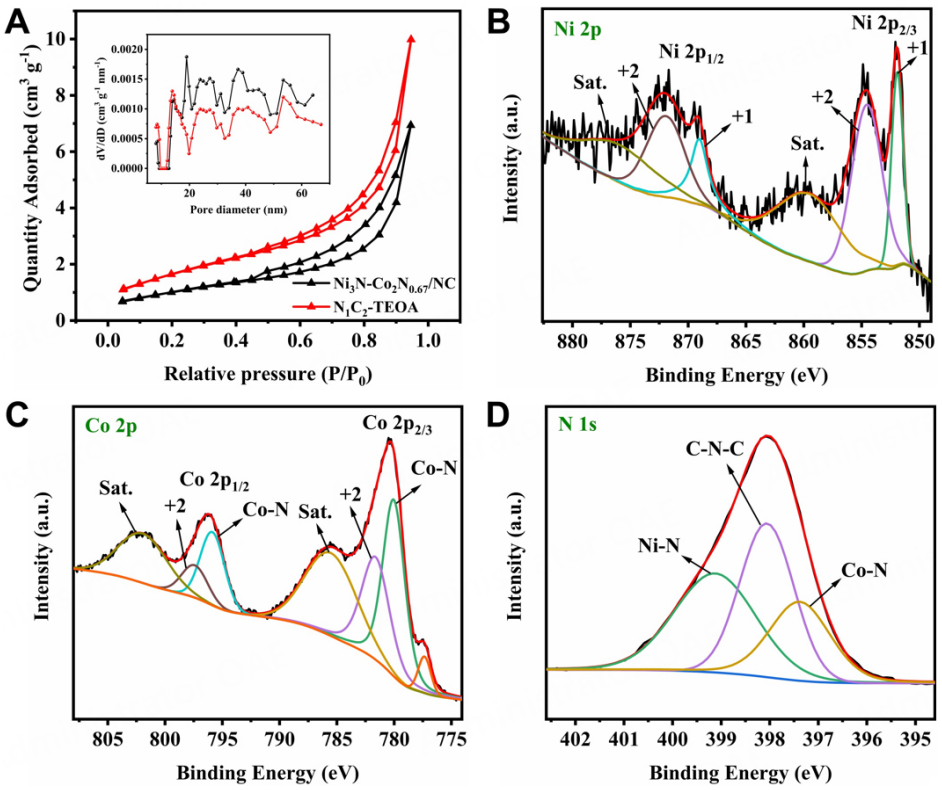

Figure 3. (A) N_2 adsorption-desorption isotherms of Ni_3N-$Co_2N_{0.67}$/NC and N_1C_2-TEOA (Inset: pore size distribution pattern). High-resolution XPS spectrum and simulation of (B) Ni 2p, (C) Co 2p and (D) N 1s for Ni_3N-$Co_2N_{0.67}$/NC.

The changes in chemical bonds are characterized by FTIR exhibited in Supplementary Figure 4. The peaks at around 3400 cm^{-1} are ascribed to the -OH group of adsorbed water molecules[33]. For the precursors, the peaks at about 2842-3062 cm^{-1} are related to the stretching vibration of -CH_2-, while the peaks at 1342-1533 cm^{-1} correspond to the bending vibration of -CH-. The peak at 1223 cm^{-1} is assigned to the C-N bond[34]. The peaks at around 917 cm^{-1} and 1633 cm^{-1} can be indexed to the stretching vibrations of C-O[35]. The peaks at around 974-1155 cm^{-1} are ascribed to the C-C bond. Moreover, the peak at 649 cm^{-1} belongs to the bending vibration of metal-O-metal groups, suggesting the successful formation of metal complex[36]. Rationally, most bonds mentioned above disappeared or shrank after calcining, revealing the carbonization of ligand skeleton. It can be concluded from the above data that metal-TEOA complex was formed as expected, which was transformed into metal nitrides/NC via pyrolysis. The rigid carbon skeleton can prevent the material from deformation and enhance conductivity. Furthermore, promoted number of exposure sites are offered by the considerable pores, achieving the material with large specific surface area and fast transportation channel.

XPS was determined to observe the surficial element and electronic interaction. Supplementary Figure 5 demonstrates the survey spectra of Ni_3N-$Co_2N_{0.67}$/NC, evidencing the presence of Ni, Co, C, N and O elements. For the Ni 2p spectra in Figure 3B, the peaks located at 854.57 and 871.94 eV are attributed to oxidized Ni^{2+}, while the peaks centered at 851.92 and 869.04 eV can be indexed to Ni^{+} species of Ni-N bonds[37]. For the Co 2p spectra in Figure 3C, the peaks at 781.62 and 797.41 eV are assigned to Co^{2+} and the peaks at 780.03 and 795.86 eV are caused by Co-N bonds[38]. The results above reveal the existence of Ni_3N and $Co_2N_{0.67}$, which is further proved in N 1 s spectra in Figure 3D. The peaks at 399.12 and 397.38 eV belong to Ni-N and Co-N bonds, respectively[39,40]. Moreover, the peak at 398.06 corresponds to C-N-C

groups, suggesting the successful establishment of nitrogen-doped carbon network[41]. Nitrogen doping could enhance the electrical conductivity of carbon, thus improving the energy storage performance of Ni_3N-$Co_2N_{0.67}$[42].

The electrochemical performances of all the samples were conducted in a three-electrode system in 1 M KOH aqueous electrolyte. As plotted in Figure 4A, the CV curves of all the samples at 20 mV s^{-1} show distinct redox peaks, revealing their energy storage mechanism of the combination of pseudocapacitance and double-layer capacitance[43]. To choose the best precursor for further nitridation, we initially compared the specific capacitance of all the precursors. The galvanostatic charge-discharge (GCD) profiles at 1 A g^{-1} displayed in Figure 4B of all the precursors show evident charge-discharge plateaus, which is well consistent with CV result. Interestingly, N_1C_1-TEOA and N_2C_1-TEOA could only reach a working potential window of 0.3 V with capacitances of 647 and 873 F g^{-1}, respectively. N_0C_3-TEOA, N_1C_2-TEOA and N_3C_0-TEOA could reach a working potential window of 0.5 V with capacitances of 158, 972 and 382 F g^{-1}, respectively. Obviously, N_1C_2-TEOA exhibited the best capacitive performance among the precursors and owned a favorable structure, so it was chosen for further annealing. As expected, Ni_3N-$Co_2N_{0.67}$/NC possessed the longest discharge time and an operating potential window of 0.5 V, surpassing all the precursors. Electrochemical impedance spectroscopy (EIS) was measured to figure out the charge transfer and ion diffusion mechanism of the samples in the frequency range from 100 kHz to 0.01 Hz. The curve in Figure 4C consists of three regions. The charge transfer resistance (R_{ct}) is determined by the diameter of the semicircle in the high-frequency region, while the diffusion resistance (R_w) of ions can be obtained from the linear slope of the straight line in the low-frequency region. As for the intercept of the curve in the high-frequency region, it means the series resistance (R_s) of the inductive element[44,45]. Benefiting from the excellent conductivity of metal nitrides and nitrogen-doped carbon, the curve of Ni_3N-$Co_2N_{0.67}$/NC owns the largest slope in the high-frequency region. Figure 4D shows the CV curve of Ni_3N-$Co_2N_{0.67}$/NC at different sweep rates. The curves almost maintain the initial shape with the scan rate increasing from 10 mV s^{-1} to 50 mV s^{-1}, indicating steady rate ability[46]. Moreover, the redox peaks sightly move to both sides of X axis when the scan rate increases due to the enhancement of internal resistance[47]. Based on the GCD profiles in Figure 4E, the specific capacitances of Ni_3N-$Co_2N_{0.67}$/NC at 1, 2, 3, 4, 5, 10 and 20 A g^{-1} are calculated as 1582, 1344, 1230, 1144, 1080, 860 and 840 F g^{-1} [Figure 4F], superior to other similar material reported previously in Supplementary Table 1. Even at a high current density of 20 A g^{-1}, the specific capacitance still preserves 53.1% of the initial value, reconfirming its outstanding rate capacity. The cycle life of Ni_3N-$Co_2N_{0.67}$/NC was tested at 10 A g^{-1}. As shown in Figure 4G, 83.79% capacitance retention can be reached after 5000 cycles. The good stability originated from the strong support of rigid carbon skeleton. To gain further insight into the electrochemical reaction kinetics of Ni_3N-$Co_2N_{0.67}$/NC, the capacitive contribution was calculated according to the following Eq.[48]:

$$i = av^b \tag{5}$$

where i and v represent peak current and scan rate, respectively. a and b are constants. The b value can be calculated through the slope of log(i) versus log(v). A b value of 0.5 means the process is a diffusion-controlled process, while a b value of 1 demonstrates a surface-controlled process[49]. The b value of Ni_3N-$Co_2N_{0.67}$/NC displays 0.68 and 0.70 from the cathodic and anodic peaks, respectively, which implies a combination of surface-controlled and diffusion-controlled processes [Figure 4H]. Further analysis of capacitive contribution ratio was conducted based on the following Eq.[50]:

$$i = k_1 v + k_2 v^{\frac{1}{2}} \tag{6}$$

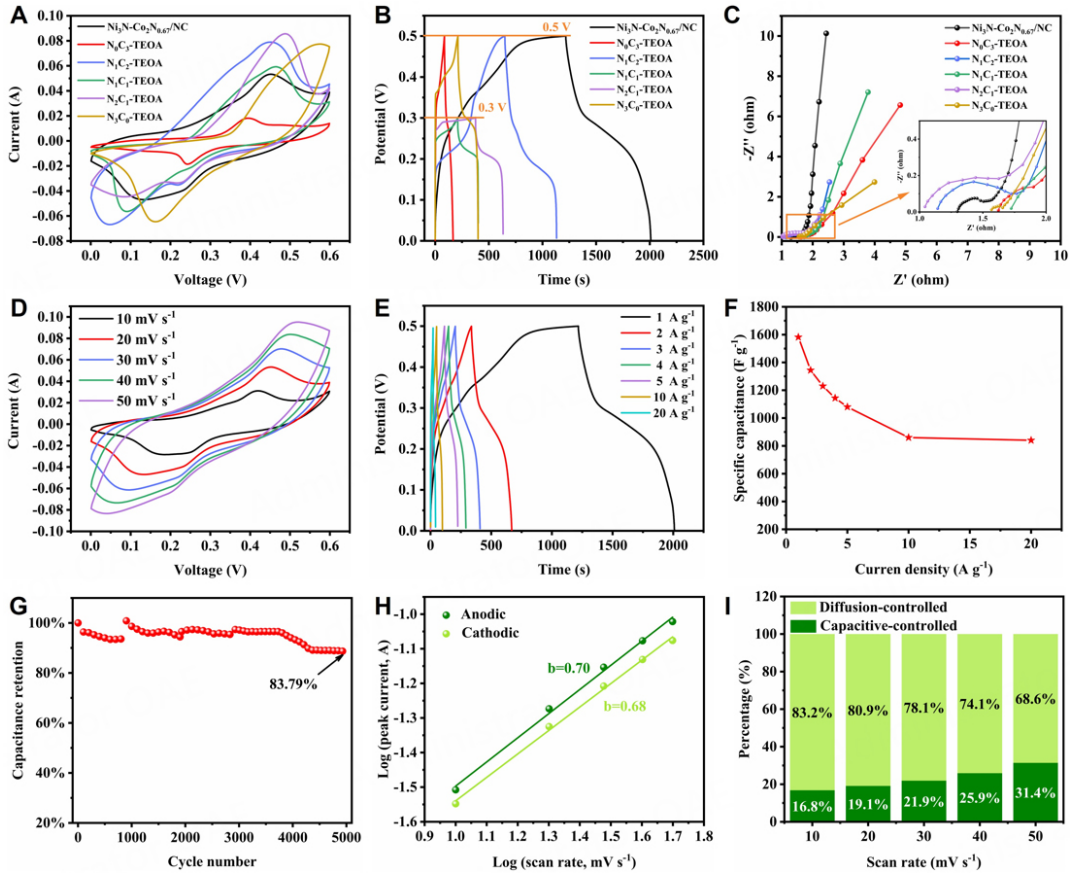

Figure 4. (A) CV curves, (B) GCD profiles and (C) Nyquist plots in the frequency range from 100 kHz to 0.01 Hz of Ni_3N-$Co_2N_{0.67}$/NC, N_0C_3-TEOA, N_1C_2-TEOA, N_1C_1-TEOA, N_2C_1-TEOA, N_3C_0-TEOA. (D) CV curves at different scan rates and (E) GCD profiles at different current densities of Ni_3N-$Co_2N_{0.67}$/NC. (F) Specific capacitance of Ni_3N-$Co_2N_{0.67}$/NC calculated from GCD profiles at different current densities. (G) The cycle performance curve of Ni_3N-$Co_2N_{0.67}$/NC at 10 A g^{-1}. (H) *b* values simulated from anodic and cathodic peak current and scan rate of Ni_3N-$Co_2N_{0.67}$/NC. (I) Contribution ratio between capacitance and the diffusion-controlled process under various scan rates.

where *i*, *v*, k_1 and k_2 are current, scan rate and determined parameters. The capacitive contribution area (green) inside CV curves at different scan rates for Ni_3N-$Co_2N_{0.67}$/NC are presented in Supplementary Figure 6A-E. Based on these plots, the percentage contribution of diffusion- and capacitive-controlled processes at different sweep rates is shown in Figure 4I. The capacitive-controlled percentage slightly rises with the increase in scan rate, confirming the excellent rate performance of Ni_3N-$Co_2N_{0.67}$/NC[51].

To explore the practical application of Ni_3N-$Co_2N_{0.67}$/NC electrode, an asymmetric device was configured applying Ni_3N-$Co_2N_{0.67}$/NC and active carbon as positive and negative electrodes in 1 M KOH, respectively. The scheme of the Ni_3N-$Co_2N_{0.67}$/NC//AC asymmetric supercapacitor (ASC) is shown in Figure 5A. CV curves and GCD profiles of AC were measured in Supplementary Figure 7A and B to determine the working potential window and mass ratio of positive electrode to negative electrode of the device. The mass ratio of Ni_3N-$Co_2N_{0.67}$/NC to AC was calculated to be 0.18 and the working potential widow was estimated to be 1.6 V based on the CV curve of Ni_3N-$Co_2N_{0.67}$/NC and AC at 20 mV s^{-1} [Figure 5B]. To further define the operating potential window, CV curves at 20 mV s^{-1} and GCD profiles at 1 A g^{-1} at different operating voltages were performed [Figure 5C and D]. The CV curve met a significant polarization when the

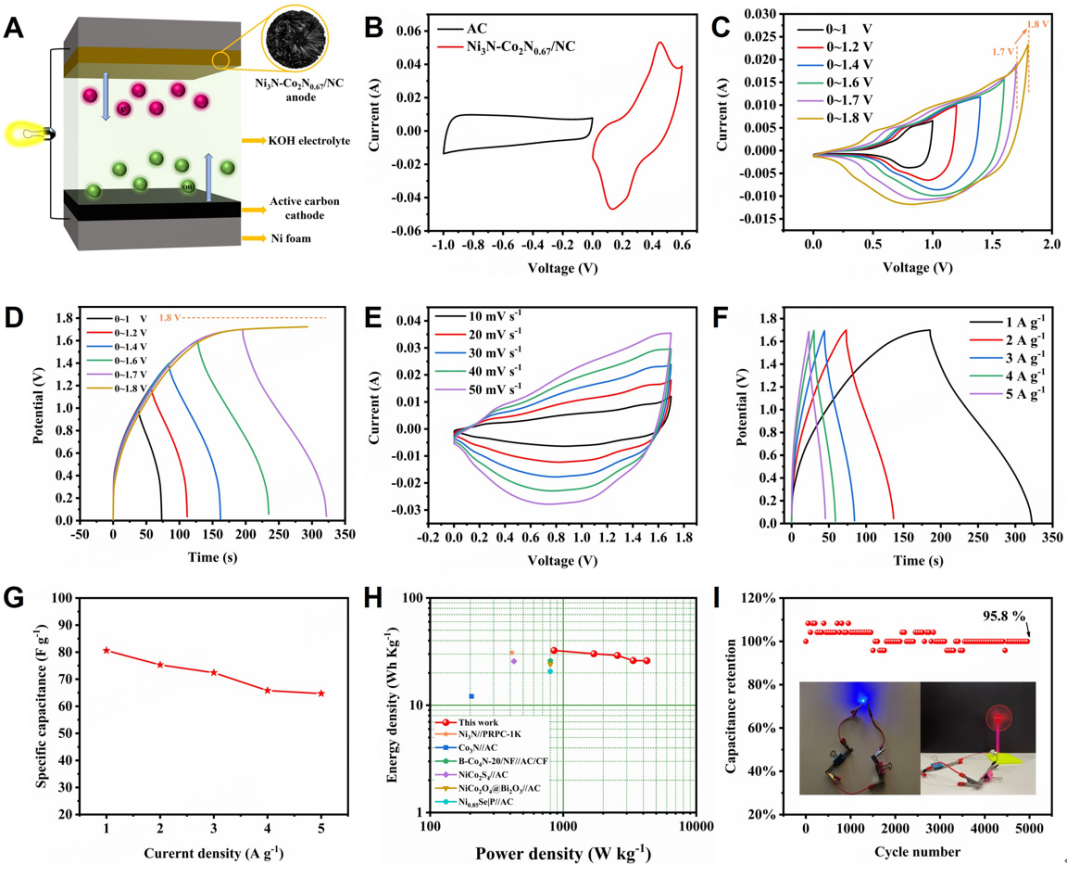

Figure 5. (A) Scheme of Ni_3N-$Co_2N_{0.67}$/NC//AC asymmetric supercapacitor. (B) CV curves of Ni_3N-$Co_2N_{0.67}$/NC and AC at 20 mV s^{-1}. (C) CV curves of Ni_3N-$Co_2N_{0.67}$/NC//AC ASC at different voltage ranges at 20 mV s^{-1}. (D) GCD profiles of Ni_3N-$Co_2N_{0.67}$/NC//AC ASC at different voltage ranges at 1 A g^{-1}. (E) CV curves of Ni_3N-$Co_2N_{0.67}$/NC//AC ASC at different scan rates. (F) GCD profiles of Ni_3N-$Co_2N_{0.67}$/NC//AC ASC at different current densities. (G) Specific capacitance of Ni_3N-$Co_2N_{0.67}$/NC//AC ACS calculated from GCD test. (H) Ragone plots comparing the Ni_3N-$Co_2N_{0.67}$/NC//AC with other similar electrode materials. (I) Cycle performance of Ni_3N-$Co_2N_{0.67}$/NC//AC ASC at 10 A g^{-1} (Inset: the photo of two ASC devices connected in series to light a LED bulb and to rotate a fan).

operating voltage increased from 1.7 V to 1.8 V and the GCD profile could only reach 1.7 V, so 1.7 V was finally selected as the practical working potential window. CV curves of the ACS at different sweep rates display a pair of redox peaks and remain stable, suggesting Faraday redox characteristics and superior rate capability [Figure 5E]. Calculated from GCD profiles in Figure 5F, the device demonstrates specific capacitance of 80.6, 75.3, 72.4, 65.8 and 64.7 F g^{-1} at 1, 2, 3, 4 and 5 A g^{-1} [Figure 5G]. The capacitance remains 80.3% of its initial value when the current density reaches 5 A g^{-1}, indicating excellent capacitive performance. The ASC device delivers a maximum energy density of 32.4 W h Kg^{-1} at a power density of 851.3 W Kg^{-1}. Even at the maximum power density of 4254.5 W Kg^{-1}, the energy density is still 26 W h Kg^{-1}, surpassing other similar devices reported before such as Ni_3N//PRPC-1k[52], Co_3N//AC[53], B-Co_4N-20/NF//AC/CF[54], $NiCo_2S_4$//AC[55], $NiCo_2O_4$@Bi_2O_3//AC[56] and $Ni_{0.85}Se$|P//AC[57] [Figure 5H]. After 5000 cycles at 10 A g^{-1}, the ASC device exhibited ultrahigh capacitance retention of 95.8% [Figure 5I]. The enhanced cycle performance of the device over a single electrode in the three electrodes system arises from the stable structure and long cycle life of AC electrode[58]. In addition, a LED bulb can be lighted for about 2 min and a small fan can be rotated for around 1 min with two ASC devices in series, showing its potentially broad applications (Insets of Figure 5I).

CONCLUSIONS

In conclusion, hollow Ni_3N-$Co_2N_{0.67}$/NC nanoflower was synthesized by pyrolyzing nickel/cobalt-TEOA complex precursor using urea as the nitrogen source and applied as positive electrode material for supercapacitor. Thanks to the remarkable electronic conductivity originating from metal nitrides and N-doped carbon and copious active sites provided by self-assembled nanosheets and porous structure, the Ni_3N-$Co_2N_{0.67}$/NC exhibits appreciable electrochemical performance. In a three-electrode system, the Ni_3N-$Co_2N_{0.67}$/NC delivers a high specific capacitance of 1582 F g^{-1} at 1 A g^{-1} and excellent cycle stability (83.79% after 5000 cycles at 10 A g^{-1}). Additionally, when fabricated as Ni_3N-$Co_2N_{0.67}$/NC//AC ASC device, it displays a favorable energy density of 32.4 W h Kg^{-1} at a power density of 851.3 W Kg^{-1} and outstanding capacitance retention (95.8% after 5000 cycles at 10 A g^{-1}). This work may create ideas to prepare metal nitride-based nanomaterials using nontoxic nitrogen source and pave the way for the rational design of hollow inorganic materials/carbon composites with high performance for SCs.

DECLARATIONS

Authors' contributions

Designed the study and supervised the overall project: Zhu M
Performed the experiments, collected data, and drafted the manuscript: Luo Q
Contributed to the result discussion: Luo Q, Lu C, Liu L, Zhu M

Availability of data and materials

Not applicable.

Financial support and sponsorship

The authors acknowledge the financial support from the Nation Natural Science Foundation of China (21403091).

Conflicts of interest

All authors declared that there are no conflicts of interest.

Ethical approval and consent to participate

Not applicable.

Consent for publication

Not applicable.

Copyright

© The Author(s) 2023.

REFERENCES

1. Wu S, Chen Y, Jiao T, et al. An aqueous Zn-Ion hybrid supercapacitor with high energy density and ultrastability up to 80,000 cycles. *Adv Energy Mater* 2019;9:1902915. DOI
2. Yu Z, Duong B, Abbitt D, Thomas J. Highly ordered MnO_2 nanopillars for enhanced supercapacitor performance. *Adv Mater* 2013;25:3302-6. DOI PubMed
3. Ji J, Zhang LL, Ji H, et al. Nanoporous $Ni(OH)_2$ thin film on 3D Ultrathin-graphite foam for asymmetric supercapacitor. *ACS Nano* 2013;7:6237-43. DOI PubMed
4. Dubal DP, Ayyad O, Ruiz V, Gómez-Romero P. Hybrid energy storage: the merging of battery and supercapacitor chemistries. *Chem Soc Rev* 2015;44:1777-90. DOI PubMed
5. Xu B, Zhang H, Mei H, Sun D. Recent progress in metal-organic framework-based supercapacitor electrode materials. *Coord Chem Rev* 2020;420:213438. DOI
6. Ma R, Chen Z, Zhao D, et al. $Ti_3C_2T_x$ MXene for electrode materials of supercapacitors. *J Mater Chem A* 2021;9:11501-29. DOI

7. Li K, Zhao B, Zhang H, et al. 3D porous honeycomb-like CoN-Ni_3N/N-C nanosheets integrated electrode for high-energy-density flexible supercapacitor. *Adv Funct Mater* 2021;31:2103073. DOI
8. Meng L, Bi J, Gao X, et al. Heterostructure Co_2N-Ni_3N/NF nanoarrays synthesized by in situ nitriding treatment for high-performance supercapacitor. *J Alloys Compd* 2022;909:164721. DOI
9. Zhu C, Sun Y, Chao D, et al. A 2.0 V capacitive device derived from shape-preserved metal nitride nanorods. *Nano Energy* 2016;26:1-6. DOI
10. Xiao X, Peng X, Jin H, et al. Freestanding mesoporous VN/CNT hybrid electrodes for flexible all-solid-state supercapacitors. *Adv Mater* 2013;25:5091-7. DOI PubMed
11. Xiao X, Yu H, Jin H, et al. Salt-templated synthesis of 2D metallic mon and other nitrides. *ACS Nano* 2017;11:2180-6. DOI PubMed
12. Wang H, Li J, Li K, et al. Transition metal nitrides for electrochemical energy applications. *Chem Soc Rev* 2021;50:1354-90. DOI PubMed
13. Yang H, Ning P, Cao H, et al. Selectively anchored vanadate host for self-boosting catalytic synthesis of ultra-fine vanadium nitride/nitrogen-doped hierarchical carbon hybrids as superior electrode materials. *Electrochim Acta* 2020;332:135387. DOI
14. Jin T, Sang X, Unocic RR, et al. Mechanochemical-assisted synthesis of high-entropy metal nitride via a soft urea strategy. *Adv Mater* 2018;30:e1707512. DOI PubMed
15. Patra S, Roy E, Madhuri R, Sharma PK. Agar based bimetallic nanoparticles as high-performance renewable adsorbent for removal and degradation of cationic organic dyes. *J Ind Eng Chem* 2016;33:226-38. DOI
16. Patra S, Roy E, Madhuri R, Sharma PK. Nanocomposite of bimetallic nanodendrite and reduced graphene oxide as a novel platform for molecular imprinting technology. *Anal Chim Acta* 2016;918:77-88. DOI PubMed
17. Aziz ST, Kumar S, Riyajuddin S, Ghosh K, Nessim GD, Dubal DP. Bimetallic phosphides for hybrid supercapacitors. *J Phys Chem Lett* 2021;12:5138-49. DOI PubMed
18. Ren F, Ji Y, Chen F, Qian Y, Tian J, Wang J. Flower-like bimetal Ni/Co-based metal-organic-framework materials with adjustable components toward high performance solid-state supercapacitors. *Mater Chem Front* 2021;5:7333-42. DOI
19. Huang K, Sun Y, Zhang Y, Wang X, Zhang W, Feng S. Hollow-structured metal oxides as oxygen-related catalysts. *Adv Mater* 2019;31:e1801430. DOI PubMed
20. Zhu M, Cheng Y, Luo Q, El-khateeb M, Zhang Q. A review of synthetic approaches to hollow nanostructures. *Mater Chem Front* 2021;5:2552-87. DOI
21. Liu X, Deng S, Xiao D, et al. Hierarchical bimetallic Ni-Co-P microflowers with ultrathin nanosheet arrays for efficient hydrogen evolution reaction over all pH values. *ACS Appl Mater Interfaces* 2019;11:42233-42. DOI PubMed
22. Dong J, Lu G, Yue J, Cheng Z, Kang X. Valence modulation in hollow carbon nanosphere/manganese oxide composite for high performance supercapacitor. *Appl Surf Sci* 2019;480:1116-25. DOI
23. Yang Y, Shao Z. Boron and nitrogen co-doped carbon nanospheres for supercapacitor electrode with excellent specific capacitance. *Nanotechnology* 2022;33:185403. DOI PubMed
24. Yang M, Ning H, Xiao L, Cui F, Zhang F. Mn_3O_4/MnS heterostructure for electrode and asymmetric supercapacitor under high charge/discharge current. *Electrochim Acta* 2022;424:140630. DOI
25. Qiu L, Yang W, Zhao Q, et al. NiS nanoflake-coated carbon nanofiber electrodes for supercapacitors. *ACS Appl Nano Mater* 2022;5:6192-200. DOI
26. Ran F, Yang X, Xu X, Li S, Liu Y, Shao L. Green activation of sustainable resources to synthesize nitrogen-doped oxygen-riched porous carbon nanosheets towards high-performance supercapacitor. *Chem Eng J* 2021;412:128673. DOI
27. Liang J, Li M, Chai Y, Luo M, Li L. TEOA-mediated formation of hollow core-shell structured $CoNi_2S_4$ nanospheres as a high-performance electrode material for supercapacitors. *J Power Sources* 2017;362:123-30. DOI
28. Chen Y, Yang D, Xin X, et al. Multi-stepwise charge transfer via MOF@MOF/TiO_2 dual-heterojunction photocatalysts towards hydrogen evolution. *J Mater Chem A* 2022;10:9717-25. DOI
29. Zhang H, Yao Z, Lan D, Liu Y, Ma L, Cui J. N-doped carbon/V_2O_3 microfibers as high-rate and ultralong-life cathode for rechargeable aqueous zinc-ion batteries. *J Alloys Compd* 2021;861:158560. DOI
30. Rezaei B, Hansen TW, Keller SS. Stereolithography-derived three-dimensional pyrolytic carbon/Mn_3O_4 nanostructures for free-standing hybrid supercapacitor electrodes. *ACS Appl Nano Mater* 2022;5:1808-19. DOI
31. Xing M, Gao A, Liang Y, et al. Defect-engineered 3D cross-network $Co_3O_{4-x}N_x$ nanostructure for high-performance solid-state asymmetric supercapacitors. *ACS Appl Energy Mater* 2021;4:888-98. DOI
32. Rabani I, Zafar R, Subalakshmi K, Kim HS, Bathula C, Seo YS. A facile mechanochemical preparation of Co_3O_4@g-C_3N_4 for application in supercapacitors and degradation of pollutants in water. *J Hazard Mater* 2021;407:124360. DOI
33. Vanaraj R, Vinodh R, Periyasamy T, et al. Capacitance enhancement of metal-organic framework (MOF) materials by their morphology and structural formation. *Energy Fuels* 2022;36:4978-91. DOI
34. Chen L, Huang Z, Liang H, Gao H, Yu S. Three-dimensional heteroatom-doped carbon nanofiber networks derived from bacterial cellulose for supercapacitors. *Adv Funct Mater* 2014;24:5104-11. DOI
35. Dong Z, Zhang W, Xiao Y, et al. One-pot-synthesized CoFe-glycerate hollow spheres with rich oxyhydroxides for efficient oxygen evolution reaction. *ACS Sustain Chem Eng* 2020;8:5464-77. DOI
36. Zhao J, Zou XX, Su J, Wang PP, Zhou LJ, Li GD. Synthesis and photocatalytic activity of porous anatase TiO_2 microspheres composed of {010}-faceted nanobelts. *Dalton Trans* 2013;42:4365-8. DOI PubMed

37. Hua W, Sun H, Liu H, Li Y, Wang J. Interface engineered NiMoN/Ni_3N heterostructures for enhanced alkaline hydrogen evolution reaction. *Appl Surf Sci* 2021;540:148407. DOI
38. Hu Y, Luo Z, Guo M, et al. Interface engineering of $Co_2N_{0.67}$/$CoMoO_4$ heterostructure nanosheets as a highly active electrocatalyst for overall water splitting and Zn-H_2O cell. *Chem Eng J* 2022;435:134795. DOI
39. Sun J, Lu J, Huang C, et al. Modification of Ni_3N with a cobalt-doped carbon shell for high-performance hydrogen evolution in alkaline media. *ACS Sustain Chem Eng* 2021;9:1994-2002. DOI
40. Tong R, Xu M, Huang H, et al. $Co_2N_{0.67}$/MoO_2 heterostructure as high-efficiency electrocatalysts for the hydrogen evolution reaction. *ACS Appl Energy Mater* 2022;5:440-8. DOI
41. Wang M, Ma W, Lv Z, Liu D, Jian K, Dang J. Co-doped Ni_3N nanosheets with electron redistribution as bifunctional electrocatalysts for efficient water splitting. *J Phys Chem Lett* 2021;12:1581-7. DOI PubMed
42. Inagaki M, Toyoda M, Soneda Y, Morishita T. Nitrogen-doped carbon materials. *Carbon* 2018;132:104-40. DOI
43. Shi B, Li L, Chen A, Jen TC, Liu X, Shen G. Continuous fabrication of $Ti_3C_2T_x$ MXene-based braided coaxial Zinc-Ion hybrid supercapacitors with improved performance. *Nanomicro Lett* 2021;14:34. DOI
44. Ma J, Xia J, Liang Z, Chen X, Du Y, Yan CH. Layered double hydroxide hollowcages with adjustable layer spacing for high performance hybrid supercapacitor. *Small* 2021;17:e2104423. DOI PubMed
45. Wang J, Huang Y, Han X, Li Z, Zhang S, Zong M. A flexible Zinc-Ion hybrid supercapacitor constructed by porous carbon with controllable structure. *Appl Surf Sci* 2022;579:152247. DOI
46. Peçenek H, Dokan FK, Onses MS, Yılmaz E, Sahmetlioglu E. Outstanding supercapacitor performance with intertwined flower-like NiO/MnO_2/CNT electrodes. *Mater Res Bull* 2022;149:111745. DOI
47. Wang H, Liang M, Duan D, Shi W, Song Y, Sun Z. Rose-like Ni_3S_4 as battery-type electrode for hybrid supercapacitor with excellent charge storage performance. *Chem Eng J* 2018;350:523-33. DOI
48. Houpt D, Ji J, Yang D, Choi JH. High-performance supercapacitor electrodes based on composites of MoS_2 nanosheets, carbon nanotubes, and ZIF-8 metal-organic framework nanoparticles. *ACS Appl Nano Mater* 2022;5:1491-9. DOI
49. Yesuraj J, Vajravijayan S, Yang R, et al. Self-assembly of hausmannite Mn_3O_4 triangular structures on cocosin protein scaffolds for high energy density symmetric supercapacitor application. *Langmuir* 2022;38:2928-41. DOI
50. Li H, Liu T, He Y, et al. Interfacial engineering and a low-crystalline strategy for high-performance supercapacitor negative electrodes: $Fe_2P_2O_7$ nanoplates anchored on N/P co-doped graphene nanotubes. *ACS Appl Mater Interfaces* 2022;14:3363-73. DOI
51. Kim SJ, Sharma V, Kshetri T, Kim NH, Lee JH. Freestanding binder-free electrodes with nanodisk-needle-like MnCuCo-LTH and $Mn_1Fe_2S_2$ porous microthorns for high-performance quasi-solid-state supercapacitors. *ACS Appl Mater Interfaces* 2022;14:12523-37. DOI
52. Peng H, Dai X, Sun K, et al. A high-performance asymmetric supercapacitor designed with a three-dimensional interconnected porous carbon framework and sphere-like nickel nitride nanosheets. *New J Chem* 2019;43:12623-9. DOI
53. Gao J, Zhang W, Zhao Z, Kong L. Solid-phase synthesis and electrochemical pseudo-capacitance of nitrogen-atom interstitial compound Co_3N. *Sustain Energy Fuels* 2018;2:1178-88. DOI
54. Wang Z, Qu G, Wang C, et al. Modified Co_4N by B-doping for high-performance hybrid supercapacitors. *Nanoscale* 2020;12:18400-8. DOI PubMed
55. Wang M, An L, Wu M, et al. Self-template synthesis of nickel cobalt sulfide hollow nanotubes for high-performance battery-type supercapacitors. *J Electrochem Soc* 2021;168:060510. DOI
56. Yu Z, Wang S, Huang Y, et al. Bi_2O_3 nanosheet-coated $NiCo_2O_4$ nanoneedle arrays for high-performance supercapacitor electrodes. *J Energy Storage* 2022;55:105486. DOI
57. Zhang Y, Wang T, Wang Y, et al. Metal organic frameworks derived hierarchical hollow $Ni_{0.85}$Se|P composites for high-performance hybrid supercapacitor and efficient hydrogen evolution. *Electrochim Acta* 2019;303:94-104. DOI
58. Li B, He Z, Zhao J, Liu W, Feng Y, Song J. Advanced Se_3P_4@C anode with exceptional cycling life for high performance potassium-ion batteries. *Small* 2020;16:e1906595. DOI

Dela Cruz *et al. Microstructures* 2023;3:2023012
DOI: 10.20517/microstructures.2022.33

Microstructures

Research Article

Open Access

Microstructure evolution in laser powder bed fusion-built Fe-Mn-Si shape memory alloy

Michael Leo Dela Cruz[1], Vladislav Yakubov[2], Xiaopeng Li[2], Michael Ferry[1]

[1]School of Material Science and Engineering, University of New South Wales, Sydney 2052, Australia.
[2]School of Mechanical and Manufacturing Engineering, University of New South Wales, Sydney 2052, Australia.

Correspondence to: Prof. Michael Ferry, School of Material Science and Engineering, University of New South Wales, Sydney 2052, Australia. E-mail: m.ferry@unsw.edu.au; Dr. Xiaopeng Li, School of Mechanical and Manufacturing Engineering, University of New South Wales, Sydney 2052, Australia. E-mail: xiaopeng.li@unsw.edu.au

How to cite this article: Dela Cruz ML, Yakubov V, Li X, Ferry M. Microstructure evolution in laser powder bed fusion-built Fe-Mn-Si shape memory alloy. *Microstructures* 2023;3:2023012. https://dx.doi.org/10.20517/microstructures.2022.33

Received: 4 Oct 2022 **First Decision:** 3 Nov 2022 **Revised:** 14 Dec 2022 **Accepted:** 19 Jan 2023 **Published:** 14 Feb 2023

Academic Editor: Ting Zhu **Copy Editor:** Fangling Lan **Production Editor:** Fangling Lan

Abstract

The need for specialty powder composition limits the processing of a wide range of alloy products via the laser powder bed fusion (LPBF) technique. This work extends the adaptability of the LPBF technique by fabricating the first-ever Fe-30Mn-6Si (wt.%) product for potential use as a biodegradable shape memory alloy (SMA). Different LPBF processing parameters were assessed by varying the laser power, scan speed, and the laser re-scan strategy to achieve a fully dense part. The microstructure was found to respond to the processing conditions. For example, the microstructure of the parts produced by the high linear energy density (LED) had a columnar and strong crystallographic texture, while in the low LED, the parts were almost equiaxed and had a weak texture. To explain the evolved microstructure, the thermal history of the LPBF products was computed using the finite element analysis (FEA) of the melt pool gathered from a single-track laser scan experiment. The FEA results showed a varying temperature gradient, cooling and solidification rates, and temperature profile as a function of LED. Then, the relationship of hardness between grain size, phases present, and crystallographic misorientation of the LPBF-built alloy was analysed with reference to a control alloy of similar composition but prepared by arc melting. This study validates the LPBF processability of Fe-Mn-Si SMA and provides a new insight into the influence of processing parameters on the formed microstructure and hardness.

Keywords: Laser powder bed fusion, microstructures, biodegradable, shape memory alloy, Fe-Mn, Fe-Mn-Si, EBSD

© The Author(s) 2023. **Open Access** This article is licensed under a Creative Commons Attribution 4.0 International License (https://creativecommons.org/licenses/by/4.0/), which permits unrestricted use, sharing, adaptation, distribution and reproduction in any medium or format, for any purpose, even commercially, as long as you give appropriate credit to the original author(s) and the source, provide a link to the Creative Commons license, and indicate if changes were made.

INTRODUCTION

Extensive research has been carried out on Fe-Mn-Si-based shape memory alloys (SMAs) since their first development in the 1980s[1]. Similarities with steels in terms of their compositions and production routes provide confidence for researchers in the quest for commercial applications[2]; these alloys are now finding their way into structural applications. Being more inexpensive than NiTi, the Fe-based and Cu-based SMAs were identified as viable options for applications requiring shape memory and pseudoelasticity[3]. For implant applications, the Fe-based SMAs, in particular, the Fe-Mn-Si alloy, are widely considered because it consists of essential and non-toxic elements[4-10], and was even reported to be biocompatible and noncytotoxic *in vivo*[11,12]. Therefore, there is a continuing investigation into its shape memory and biodegradable behaviour for implant applications[13-18].

Biodegradable implants have attractive properties because they can safely degrade to their elemental constituents over time, thus eliminating post-surgery removal. With this function in mind, the alloy composition would then be limited to biocompatible elements. A recent review of biodegradable SMAs identified Mg-Sc, Fe-Mn-Si, Fe-Pd, and Fe-Pt alloys as potential candidates[19], but the Fe-Mn-Si system is advantageous because of its widely available raw materials.

In contrast to the copious literature on conventionally processed Fe-based SMAs, research on the additive manufacturing of this alloy system is in its infancy[20-27]. To the best of the authors' knowledge, alloy compositions of Fe-36Mn-7Al-9Ni (wt.%), Fe-17Mn-10Cr-5Si-4Ni (wt.%), and Fe-34Mn-8Al-7Ni (at.%) have been LPBF fabricated to date. In Fe-36Mn-7Al-9Ni alloy, a columnar and highly textured microstructure was noted in 0.5 mm sized parts built on a 200 °C preheated substrate[26], but the microstructure changed to equiaxed and columnar grains with a weak texture when the substrate was heated to 500 °C[21]. The conflicting trend in microstructural features was associated with the difference in substrate temperature that altered the temperature gradient and solidification rate[21]. Both Ferretto *et al.* and Kim *et al.* investigated the Fe-17Mn-10Cr-5Si-4Ni alloy and reported a change in microstructure as the laser power was varied[22,23,28]. A fully austenitic and equiaxed grain structure exhibiting a weak crystallographic texture was achieved at high laser power, but this changed to a highly elongated, weakly textured and δ-ferrite dominated structure at lower laser power. The authors suggested that the nucleation of the austenite grains from the δ-ferrite was possible at high laser power because of the low cooling rate in this setting. Lastly, Patriarca *et al.* fabricated a bulk and micro-lattice structured Fe-34Mn-8Al-7Ni alloys and heat treated the alloys to achieve a microstructure desirable for the pseudoelastic property[27].

The limited source of pre-alloyed powder may have restricted the research progress on the adaptability of the LPBF technique to Fe-based SMAs. Most of the studies on the additive manufacturing of Fe-based SMAs used pre-alloyed precursors. It is worth noting that Niendorf *et al.* and Wiesener *et al.* fabricated a Fe-based alloy with Ag for biomedical applications by mixing Ag powder with pre-alloyed high-manganese TWIP steel powder and Fe-Mn powder, respectively[29,30]. These studies achieved a microstructure with well-dispersed Ag particles that accelerated the corrosion rate of the Fe-Mn alloy. Mixing of metallic powder would therefore enhance the potential of the technique. The LPBF of homogenised powder is however challenging due to the difference in the thermal and optical properties between the powders and chemical inhomogeneity in the product[31], and this warrants the careful selection of processing parameters.

This study demonstrates that a Fe-Mn-Si SMA, a potentially biodegradable alloy, can be prepared from a blended metallic powder and processed using the LPBF technique. The influence of laser power, scan speed, and laser re-scanning on the solidified microstructure of the built product was examined. Then the solidification mechanisms were explained based on the knowledge gained from both the microstructure and

the melt pool profile generated from a single laser scan track and the thermal profile of the melt pool region derived from a finite element analysis (FEA) method. The influence of grain size, composition of formed phases, and residual strain on the hardness of the as-built alloy were investigated according to the information gathered from XRD and EBSD analyses, and then compared with the reference as-cast alloy prepared using the arc-melting technique.

MATERIALS AND METHODS

Sample preparation

The Fe and Si powders used in the LPBF fabrication of Fe-Mn-Si alloy were gas atomised and provided by TLS Technik, Germany, while the Mn powder was from Merelex Corp, USA. Both the Fe and Si powders had a purity of > 99 wt.%, and the purity of Mn was > 98 wt.%, as estimated using the Malvern Panalytical Epsilon ED X-ray fluorescence spectroscopy (XRF), Supplementary Table 1. Figure 1A-C shows the scanning electron microscope (SEM) micrographs of the Fe, Mn, and Si powder. Their particle size and cumulative size distributions were measured using the Malvern Mastersizer 3000 and are shown in Figure 1D-F, respectively. A nominal powder composition of Fe-30Mn-6Si (wt.%) was homogenised for 4 h using the Turbula® T2F 3D mixer and then used as powder precursor. Meanwhile, the nominal concentration of Fe-30Mn-6Si reference as-cast alloy was prepared using the arc-melting technique from Fe, Mn, and Si high purity (> 99.9%) chips from Sigma-Aldrich. The arc-melted product was subsequently hot-rolled at ~800 °C and then homogenised at 1100 °C for 14 h in an argon-purged furnace. Homogenisation was performed by loading the sample at room temperature, heating it at 5 °C/min to 1100 °C, and followed by furnace cooling. The resulting sample is referred to hereafter as reference as-cast alloy and its properties were treated as a reference in the following investigations.

The LPBF fabrication was carried out using the Mlab Cusing 200R from Concept Laser GmbH equipped with 200 W Yb:YAG fibre laser and the print chamber atmosphere was maintained up to 0.2 vol.% O_2 using a high purity Ar gas. Only freshly homogenised powder was used, and all printed parts were built on a sandblasted stainless steel substrate. In identifying the optimum LBPF parameters, a 125 mm^3 cube model was prepared using the Materialise Magics v24 software. The influence of both laser power and laser scan speed on the density of the built part was investigated by varying the laser power (P) from 100 W to 175 W and the laser scan speed (v) from 400 mm/s to 600 mm/s while keeping a constant laser hatch spacing, layer thickness, and scan strategy at 45 μm, 50 μm, and island scan strategy, respectively. The scan strategy is unique to Concept Laser[32], where each island was maintained at 5 × 5 mm^2 and was scanned by the laser in one direction. The laser scan direction was rotated by 90° between the neighbour islands, and finally, this whole pattern was rotated by 45° in the subsequent layer. A laser re-scan strategy was also included. This was done by scanning the solidified layer again at a varying percentage of laser power (0%, 50%, and 100%) that was applied in the first scan, laser scan speed from 400 mm/s to 600 mm/s, and a similar scan strategy to increase the laser linear energy density (LED). LED is a simplified energy parameter defined as the P/v ratio and was considered when the layer thickness and laser space hatching were unchanged[33-35]. Table 1 summarises the parameters that were investigated.

LPBF product quality assessment

The density of the LPBF built parts was measured by applying the Archimedes method and using the Mettler Toledo XS105 balance with a density kit. All surfaces of the samples were ground down to 1200 SiC paper and then dried. Measurements were done on three replicates. The measured density was then divided by the theoretical density (7.408 g/cm^3) and reported as relative density. In addition, the surface of the LPBF-built parts along the build direction was viewed under the Hitachi TM4000Plus bench-top SEM coupled with a Bruker X-Flash 630Hc EDS detector to further evaluate the product quality.

Table 1. LPBF processing parameters used for the fabrication of Fe-30Mn-6Si alloy

Processing parameters	Values
Laser power (W)	100, 125, 150, 175
Scan speed (mm/s)	400, 500, 600
Re-scan (%)	0, 50, 100

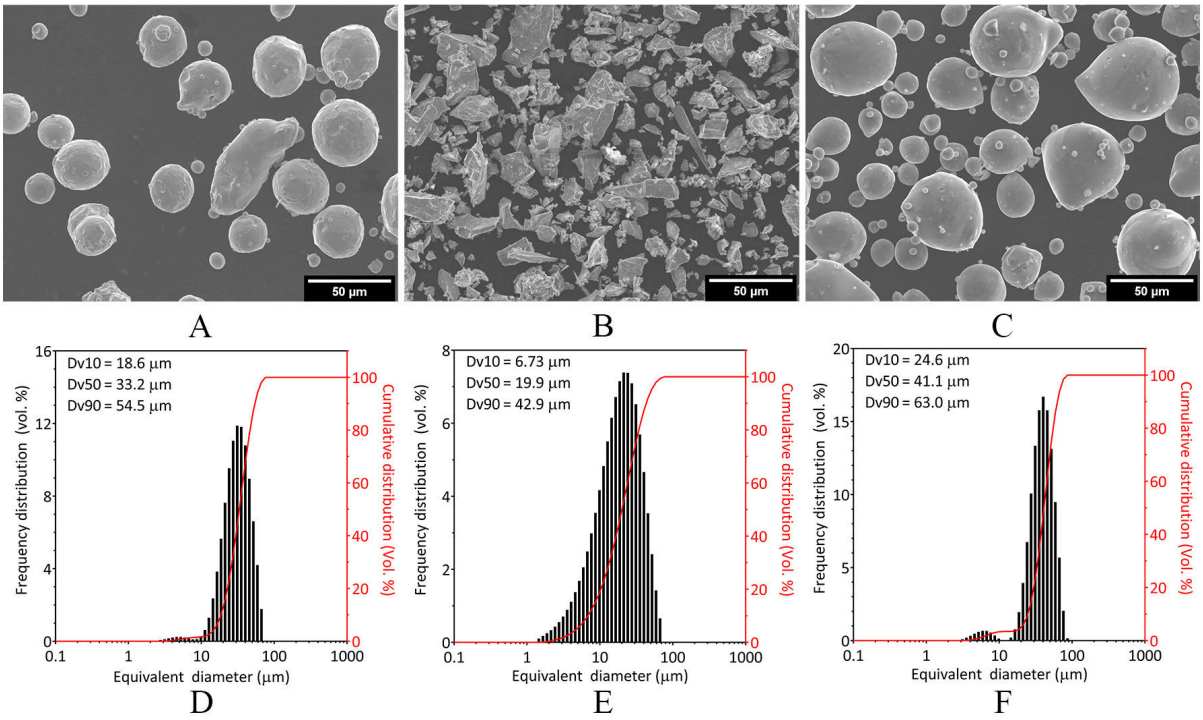

Figure 1. SEM micrographs of (A) Fe, (B) Mn, and (C) Si powders. Their corresponding particle size frequency and cumulative distributions are shown in (D-F), respectively.

Microstructure characterisation

The crystallography and the phase volume fraction of both the reference alloy and the LPBF fabricated alloy were evaluated using the PANalytical Empyrean with a Co target (λ = 1.79 Å) and a scan range from 40 to 130° 2θ at a step size of 0.02°. The volume fraction of the phases in the samples was computed by applying a Rietveld refinement[36,37] using the HighScore Plus v5.1 Suite[38,39]. Refinement parameters such as the expected profile *R*-value, profile *R*-value, weighted profile *R*-value, goodness of fit, Bragg *R*-value, and the difference plot between the experimental and calculated XRD pattern were closely monitored during the refinement process. Also, refinement was done at least three times to verify the results, and the γ-austenite and ε-martensite phase volume fractions were subsequently validated using the electron backscattered diffraction (EBSD) technique [Supplementary Figure 1].

The EBSD was carried out to characterise the microstructure, i.e., grain morphology, crystallographic texture, and grain characteristics, of the reference alloy and built products. The sample surfaces for EBSD analysis were final polished up to OPU finish and then ion milled using the Hitachi IM4000 at 30° and 6 kV for 1 h to remove any polishing artefacts. The Zeiss Auriga Crossbeam Field-emission SEM equipped with a NordlysF detector for EBSD and an Oxford Instruments X-Max 20 mm^2 silicon drift detector for EDS was used for the simultaneous SEM-EDS/EBSD analysis. The EDS and EBSD data were gathered using the

AZtec 3.3 and then analysed using the AZtecFlex software suite. For EBSD analysis, a 500 × 500 μm² area was scanned at a step size of 1 μm and only the results with at least 90% hit rate were analysed. Data cleaning was done by removing the wild spikes, and then using the "zero solutions removal" tool from level 1 up to level 4 while preserving any defects, i.e., cracks and pores, on the cleaned dataset. The grain size and shape analysis were subsequently done on the computed prior austenite grains[40] using the Shoji-Nishiyama orientation relationship[41] to reveal the likely austenite grains.

Simulation of melt pool thermal properties

Simulation of the 3D thermal profile during LPBF was conducted using the COMSOL™ Multiphysics software suite, in which a simplified finite element analysis (FEA) thermal model was developed. A tetrahedral mesh was used for the model geometry with a minimum and maximum mesh size of 2 μm and 16 μm, respectively. A 1 × 6 × 1 mm³ smooth flat plate model with no powder was used to provide a heat sink effect sufficient for simulating the single line scan. Laser irradiation heat input is modelled as[42,43],

$$Q(x,y,z) = \frac{2AP}{\pi\delta R^2} e^{\frac{-2(x^2+y^2)}{R^2}} \mathrm{e}^{\frac{-|z|}{\delta}} \quad (1)$$

where Q is volumetric heat flux (W/m²), P is laser power, A is laser absorption coefficient, R is laser beam radius, δ is laser penetration depth[44,45], |z| is z-coordinate absolute value, and x and y are laser x- and y-coordinates, respectively. The theoretical density was used as the material density for the simulation. Specific heat capacity and thermal conductivity at room temperature were taken from literature for the similar material Fe-28Mn-6Si-5Cr and are 544.2 J/(Kg·K) and 8.37 W/(mK), respectively[46,47]. A single-track scan was first performed on a polished material surface of similar composition. Then, in the numerical simulation, the coordination of x and y scan speeds, as well as P and R, were the same as those used for the single-track scan. Determination of penetration depth δ and absorption coefficient A was conducted via an iterative process by matching the simulated melt pool with the observed melt pool [Supplementary Figure 2]. Initial build platform and surrounding gas temperature were taken as 30 °C, surface emissivity was 0.3, and convective heat transfer coefficient was 10 W/m²·K.

Hardness test

The resistance to localised plastic deformation of the LPBF built and reference alloy was measured using the Struers DuraScan hardness machine following a standard procedure[48]. The samples were resin mounted and then the surface was OPU polished. At least 10 indentations were made on each sample.

RESULTS AND DISCUSSION

LPBF product quality

The interaction of the powder bed and the laser system in the LPBF fabrication of Fe-30Mn-6Si was assessed by looking into the influence of relative density as a function of LED, as shown in Figure 2A. The P/v ratio is the LED of the laser system where a high P value and a low v value translate to a large amount of LED, and this is similar to what is being used in conventional fusion welding techniques[49]. The lowest LED of 0.17 J/mm returned the lowest density at 95%, and the density was found to increase linearly with LED until ~0.30 J/mm. The relative density levelled at mostly above 99%, where the 0.44 J/mm LED recorded the highest value of 99.9%.

SEM micrographs of all samples built at different LBPF are analysed and their representative at low, mid, and high LEDs are shown in Figure 2B-D, respectively. These micrographs represent the LEDs labelled in Figure 2A. Pores of over 250 μm are seen at the low LED of 0.17 J/mm, and their morphologies are

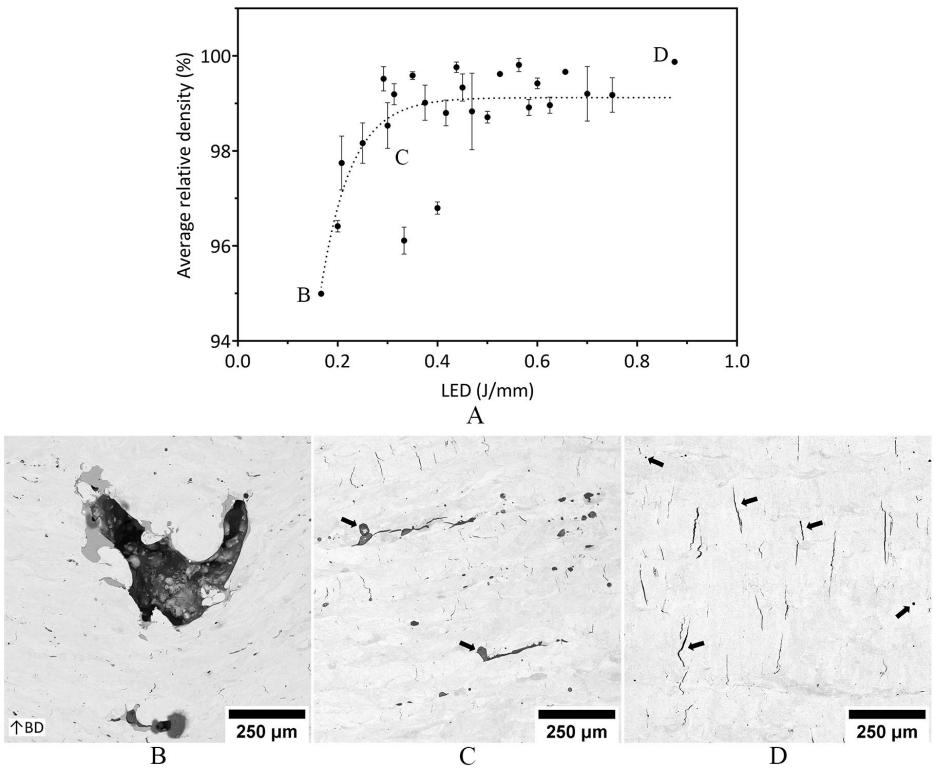

Figure 2. (A) The relationship between relative density and LED, and the representative SEM micrographs at (B) low (0.17 J/mm), (C) mid (0.25 /mm), and (D) high (0.88 J/mm) LEDs. Arrows in black highlight the defects in the built parts, the build direction is from bottom to top, and the error bars in (A) represent the standard error of the mean.

irregularly shaped, as seen in Figure 2B. At the mid LED of 0.25 J/mm, the large pores are not apparent, but chemical inhomogeneity is noted by the difference in contrast in the backscattered electron (BSE) micrograph and they are highlighted by the black arrows in Figure 2C. The high LED of 0.88 J/mm has no observed chemical segregation; defects like cracks and spherical pores are however noted, and they are marked by the black arrows in Figure 2D. Densification of LPBF fabricated parts is directly associated with the reduction of defects at high LED, and this is shown by the SEM micrographs in Figure 2B-D. Nevertheless, the high relative density and relatively few defects in the high LED above 0.44 J/mm, i.e., the lack of large irregularly shaped pores [Figure 2D and Supplementary Figure 3], make these parameters ideal for the LPBF fabrication of Fe-30Mn-6Si from homogeneously blended powder.

The recommended LED for Fe-30Mn-6Si alloy (≥ 0.44 J/mm) is higher than the suggested for pure Fe (≥ 0.33J/mm)[50,51], 316 L (0.21 to 0.30 J/mm)[52,53] and 304 L (0.14 J/mm)[54] stainless steels that were fabricated from pre-alloyed powders. Much higher energy is needed for the homogenised powder than for pre-alloyed powder, as noted in Al-Si[55] and FeCoCrNi[56], because more energy and a slow melt pool solidification rate are needed for the melting and alloying of the homogenised powder. The recommended energy for the LPBF of Fe-30Mn-6Si alloy is, however, less than of the Fe-17Mn-5Si-10Cr-4Ni alloy (0.53 J/mm), and the difference may be due to the high melting requirement of Cr in the latter.

Chemical composition

LPBF uses a high energy laser for melting and alloying of the metallic powders. Such energy may evaporate volatile components and alter the final composition of the alloy. An EDS analysis of the major elements Fe, Mn, and Si as a function of LED in Fe-30Mn-6Si LPBF alloy is shown in Figure 3A-C, respectively. As the

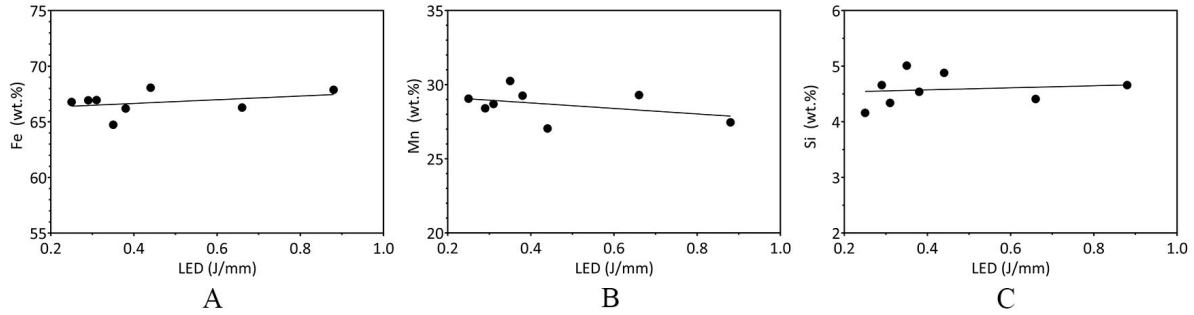

Figure 3. Chemical composition of (A) Fe, (B) Mn, and (C) Si in LPBF alloy as a function of LED.

LED is increased, the Fe content in the alloy is shown to increase, Mn is slightly decreased, and Si remains almost the same. The Mn element has the least melting point [Supplementary Table 2], high vapour pressure[57,58], and therefore more volatile than the other precursors[22,28]. Thus, its evaporation is expected during LPBF, resulting in a decrease in Mn concentration. Meanwhile, the slight increase in Fe likely influenced the relative density value. Fe had the highest density among the raw materials and the increase of its concentration likewise increased the alloy density. Therefore, careful selection of processing parameters and the adjustment of Mn concentration are necessary for the LPBF processing of homogenised powders.

Microstructure

The influence of LPBF processing parameters on the microstructure was investigated using the EBSD micrographs of the LPBF-built alloy surface parallel to the building direction. The LEDs at 0.25 J/mm and 0.44 J/mm represent the low (100 W) and high (175 W) laser power, 0.29 J/mm and 0.44 J/mm for the low (400 mm/s) and high (600 mm/s) scan speed, and 0.44 J/mm and 0.88 J/mm for the 0% (175W, 400 mm/s) and 100% (175W, 400 mm/s and then 175 W, 400 mm/s) re-scan strategy, respectively. Figure 4A, D, G, and J show the prior austenite grains[40,41] EBSD IPF map of the surface parallel to the build direction that seems to respond to the changes in the LPBF processing parameters. In Figure 4C, F, I, and L, the grain size distribution and the area-weighted average are also shown, and their corresponding aspect ratios are presented in Supplementary Figure 4. At a scan speed of 400 mm/s and a low laser power of 100 W (0.25 J/mm), the grain size was fine and nearly equiaxed [Figure 4A] with a size of 64 μm and an aspect ratio of 2.03. This changed to a coarse and columnar microstructure for the laser power of 175 W (0.44 J/mm), Figure 4G. Such an increase in laser power generated a grain size of almost three times and elongated the grains by ~90% compared to that of the low laser power. The microstructure was further modified for a constant laser power of 175 W when the scan speed was increased from 400 mm/s to 600 mm/s. The subsequent grain size was rather coarse (105 μm), and the grains were nearly equiaxed (aspect ratio = 1.97), Figure 4D and F. The columnar grains generated at high LED (0.44 J/mm) are seemingly retained when the already solidified layer was re-scanned at 100% (175 W, 400 mm/s) to generate an LED of 0.88 J/mm [Figure 4J]. However, the coarse columnar grains in a non-re-scanned alloy [Figure 4G] are replaced with a fine columnar grain in a laser re-scanned alloy. In addition, the clustering of fine grains is observed in the laser re-scanned alloy, as seen in the marked areas in Figure 4J, and this effectively reduced the grain size from 242 to 191 μm and the aspect ratio from 3.83 to 2.88.

The LPBF parameters also strongly influenced the crystallographic texture of the alloy. The predominance of a single colour in the EBSD IPF map indicated a substantially preferred orientation or strong texture. Figure 4G and J show that most of the cubic grains are aligned with their <001> direction parallel to the build direction in the 0.44 J/mm and 0.88 J/mm, whereas the texture was weak (broad range of colours) in 0.25 J/mm and 0.29 J/mm, Figure 4A and D, respectively. Therefore, the high LED and laser re-scan strategy

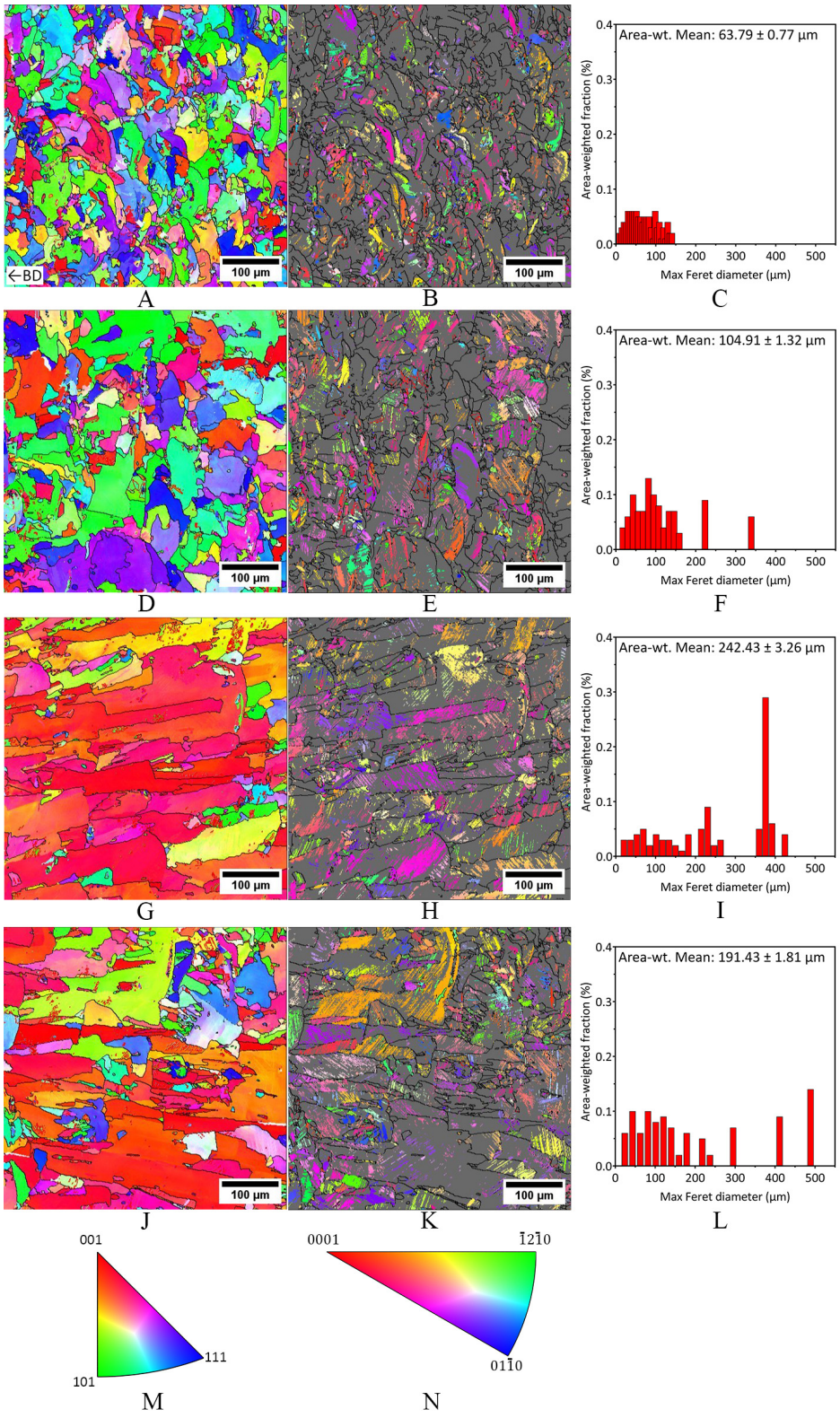

Figure 4. EBSD parent grain reconstructed IPF map, HCP ε-martensite IPF map, and the grain size distribution of Fe-30Mn-6Si LPBF-built alloy from LED of (A-C) 0.25 J/mm (100 W, 400 mm/s), (D-F) 0.29 J/mm (175 W, 600 mm/s), (G-I) 0.44 J/mm (175 W, 400 mm/s), and (J-L) 0.88 J/mm (175 W, 400 mm/s, and 100% re-scan), respectively, and the IPF colour key for (M) FCC and (N) HCP. The build direction is from right to left and the grain boundaries are outlined in black.

generated prior austenite columnar grains that grow in their <001> direction parallel to the building direction. Meanwhile, Figure 4B, E, H, and K display the randomly orientated HCP martensite phase within the austenite grains.

The X-ray spectra of the Fe-30Mn-6Si reference alloy and the LPBF alloy made from different processing parameters were gathered and quantified using the Rietveld refinement method. The results are then shown in Figure 5 and Table 2. The major phases identified in the LPBF alloy are γ-austenite and ε-martensite because of their intense XRD peaks and composition that is ≥ 19 wt.%, as seen in Table 2. A dual-phased microstructure is expected in the Fe-30Mn-6Si alloy that underwent post-process treatment[59], while the homogenised alloy may be single-phase austenite[60], and such is observed in Figure 5. The existence of the γ and ε phases in the LPBF alloy is due to the far-from-equilibrium process conditions of the technique. Table 2 also reveals three other phases in the LPBF alloy; α-FeMn, α-FeSi, and FeO. The presence and composition of these phases are observed to vary in the LPBF alloy prepared for different parameters. For example, FeO was identified at 0.25 J/mm and 0.44 J/mm but not at 0.29 J/mm and 0.88 J/mm. Upon close inspection at 54.3° 2θ in the 0.29 J/mm, its 10^{2} peak is visible. Several trials were made to include the low-intensity peaks from those three phases for a detailed analysis, but the quality of the resulting Rietveld refinement was unsatisfactory. A more detailed XRD scan is therefore necessary for a comprehensive analysis of those three phases.

Key microstructural features associated with LPBF processing, such as the types and volume fraction of phases present, solidified grain size, morphology, and texture of the processed samples, were strongly influenced by the laser power, scan speed, and re-scan strategy. This shows that the desired microstructure is tailored by controlling laser power and scan speed to change the LED. The information on the thermal history of the resultant product is, however, necessary to completely understand the development of the microstructure.

Melt pool of single laser track scan

A polished surface of the reference alloy was subjected to single track laser scans at various LEDs. This resulted in the melting and subsequent solidification along the laser tracks, which generated a certain melt pool morphology for a given LED, when viewing a cross section perpendicular to the laser track. The effect of LED on the cross section of melt pool morphology is shown in Figure 6. Figure 6C and D show that a high LED creates both a deep and wide melt pool that penetrates at least 120 μm below the polished surface. In contrast, a low LED generates a relatively shallow melt pool of 50 μm deep [Figure 6A]. In Figure 6B, the melt pool became wide and deep when the LED was slightly increased from 0.25 J/mm to 0.29 J/mm by increasing the laser power from 100 W to 175 W and scan speed from 400 mm/s to 600 mm/s. Overall, there is sufficient lateral overlap of the melt pool tracks because the width of the melt pool is wider than the 0.45 μm distance of the parallel laser tracks.

The melting mode at low LED (0.25 J/mm), as defined by Tenbrock *et al.*, is conduction mode, and the rest, 0.29 J/mm to 0.88 J/mm, are in keyhole mode[61]. In the authors' single laser track investigation on 316 L stainless steel, the group used the melt pool depth-to-width ratio threshold of less than 0.8 as the conduction mode; above 0.8, the keyhole mode of melting transpired. Conduction mode of melting was observed at low LED, where the underlying regions are heated through the energy conducted from the surface[62]. In the keyhole mode of melting, the high LED evaporated the metal and left a vapor cavity in the melt pool that enhanced laser absorption and enabled a deeper melt pool than in conduction mode[63].

Table 2. Derived crystal structure, lattice parameters, phase compositions, Bragg *R*-value (RBragg), and goodness of fit (GOF) of the LPBF parts built at 0.44 J/mm and 0.88 J/mm energy parameter and then homogenised and HIP treated and reference as-cast alloy using the Rietveld refinement of the XRD patterns.

LED (J/mm)	Phase	Space group	Lattice parameter		Content (vol.%)	R_{Bragg}	GOF
			a (Å)	c (Å)			
0.25	γ-austenite	$Fm\bar{3}m$	3.600	-	74.6	1.72	4
	ε-martensite	$P6_3/mmc$	2.535	4.133	19	1.99	
	α-FeMn	$Im\bar{3}m$	2.867	-	2.3	1.39	
	α-FeSi	$Im\bar{3}m$	2.840	-	2.2	2.19	
	FeO	$R\bar{3}m$	2.648	7.585	1.9	1.76	
0.29	γ-austenite	$Fm\bar{3}m$	3.600	-	68.5	2.76	3.518
	ε-martensite	$P6_3/mmc$	2.537	4.125	23.9	1.37	
	α-FeMn	$Im\bar{3}m$	2.868		2.8	1.33	
	α-FeSi	$Im\bar{3}m$	2.843		4.9	0.39	
0.44	γ-austenite	$Fm\bar{3}m$	3.600		62.1	1.07	2.196
	ε-martensite	$P6_3/mmc$	2.535	4.141	31.2	0.79	
	α-FeSi	$Im\bar{3}m$	2.847		6.3	0.44	
	FeO	$R\bar{3}m$	2.535		0.4	1.71	
0.88	γ-austenite	$Fm\bar{3}m$	3.598		52.5	2.31	3.928
	ε-martensite	$P6_3/mmc$	2.540	4.123	45.8	1.72	
	α-FeMn	$Im\bar{3}m$	2.868		1.4	0.84	
	α-FeSi	$Im\bar{3}m$	2.837		0.2	1.01	
As-cast	γ-austenite	$Fm\bar{3}m$	3.602		100	-	-

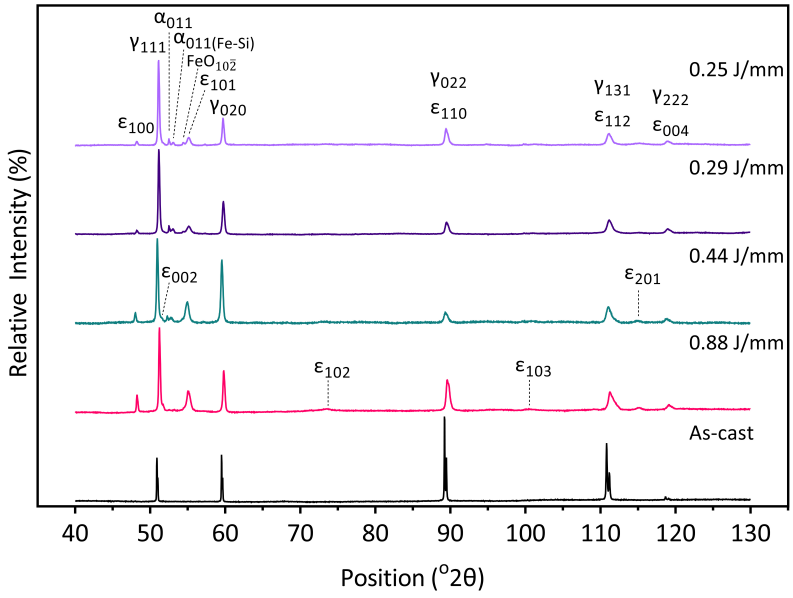

Figure 5. The XRD patterns of the Fe-30Mn-6Si reference alloy and the LPBF alloy prepared at different process settings.

Simulated melt pool thermal profile

Using the melt pool profiles and a finite element analysis technique[64] on the LPBF of Fe-30Mn-6Si alloy, the thermal profiles through the penetration distance of the melt pools were calculated as a function of laser scan strategy. The derived thermal conditions at different LPBF process settings as a function of melt pool depth are presented in Figure 7. It is known that the solidified microstructure prepared using the LPBF

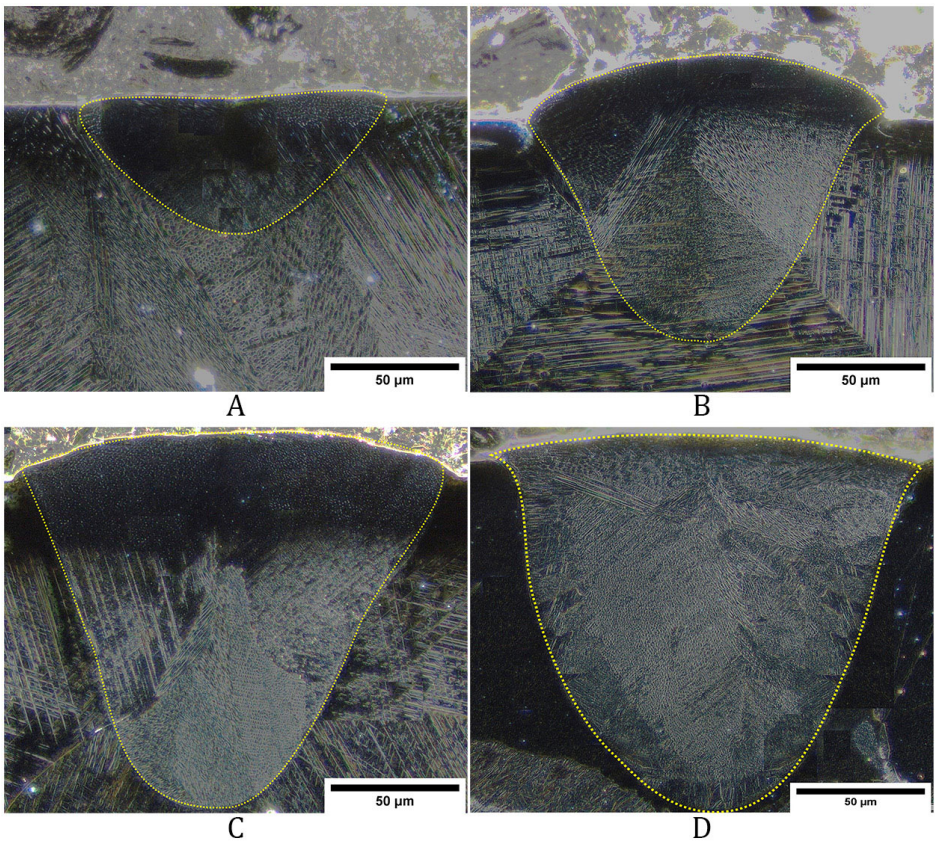

Figure 6. The single laser scan melt pool profile on the polished Fe-30Mn-6Si reference alloy at varying LEDs of (A) 0.25 J/mm, (B) 0.29 J/mm, (C) 0.44 J/mm, and (D) 0.88 J/mm.

technique follows the solidification theory[65-67], where the morphology is affected by the extent and direction of the temperature gradient and the solidification rate of the melt pool[68]. Likewise, the cooling rate, a product of temperature gradient and the solidification rate[69], dictates the size of the solidified structure[70]. Therefore, the temperature gradient and the solidification and cooling rates are computed, and the temperature profiles are also derived.

Figure 7A shows the variation in the temperature gradient within the melt pool for different LEDs. A low temperature gradient is initially observed from the surface of the melt pool, and it increases as solidification proceeds, leaving the bottom layer with the highest temperature gradient values of over 10^4 K/m. The LPBF process has a typical temperature gradient range of 10^4 to 10^7 K/m[71]. Temperature gradients between 10^4 to 10^5 K/m were associated with large melt pools[72], and such were observed in the melt pool profile [Figure 6C and D]. The 0.25 J/mm has the highest temperature gradient at the surface at 2.32×10^3 K/m as compared to the 1.03×10^3 K/m, 9.83×10^2 K/m, and 7.72×10^2 K/m for 0.29 J/mm, 0.44 J/mm, and 0.88 J/mm, respectively. Moreover, the 0.25 J/mm has the steepest slope in the temperature gradient, followed by 0.29 J/mm. The temperature gradient of 0.44 J/mm and 0.88 J/mm are almost constant up to 50 µm melt pool depth and it increased gradually afterwards. The low temperature gradient for 0.44 J/mm and 0.88 J/mm at 0-50 µm was caused by their comparatively wide melt pool size in this area. Therefore, the temperature of the surrounding material is high, and the heat sink effect is low. As the distance from the top of the melt pool is increased, the melt pool achieves a lower width and lower surrounding temperature.

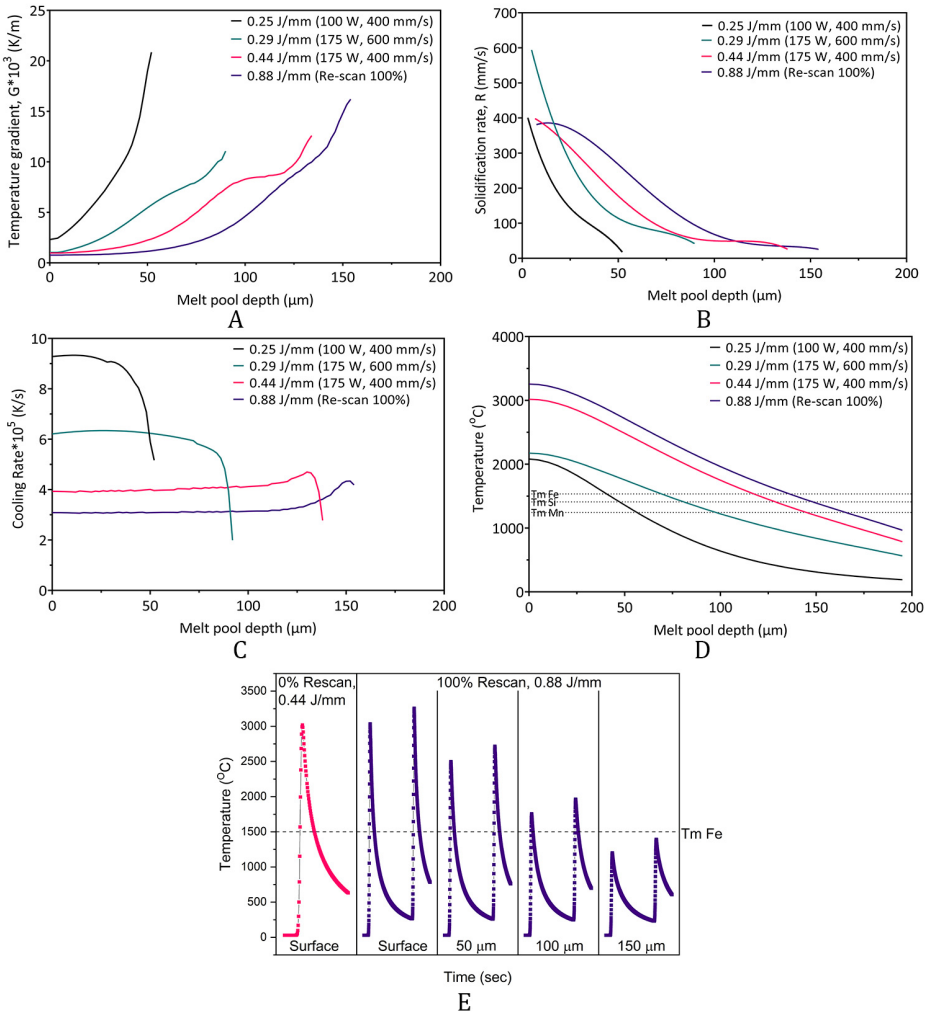

Figure 7. Computed thermal profile of the LPBF fabricated Fe-30Mn-6Si alloy. (A) temperature gradient, (B) solidification rate, (C) cooling rate, and (D) maximum temperature as a function of melt pool depth at different LEDs. (E) Temperature profile for 0% (0.44 J/mm) and 100% re-scan (0.88 J/mm) at varying melt pool depths and processing time.

The solidification and cooling rates were numerically evaluated and remarked to be significantly influenced by scan speed than by laser power[73,74]; hence, their influence at varying LED was evaluated. In the LPBF process, the solidification of the molten melt pool proceeds as the laser track leaves the melt pool. The rate of solidification at varying LED was presented in Figure 7B, where the rate at the surface of the melt pool was similar to the applied scan speed. The 0.29 J/mm LED had a faster solidification rate at the surface compared to the rest of the LEDs because a scan speed of 600 mm/s was applied. All the solidification rates decreased sharply from the surface of the melt pool until the 50 µm depth, but the slope was noticeably steeper at 0.25 J/mm and 0.29 J/mm LEDs than at 0.44 J/mm and 0.88 J/mm LEDs. After the 50 µm depth, the solidification rate for 0.29 J/mm LED decreased slowly. For 0.44 J/mm and 0.88 J/mm LEDs, the slope of the solidification rate only changed after ~90 µm and then became stable at 50 mm/s.

The fast-moving laser in LPBF imparts a high cooling rate of 10^4 to 10^6 K/s[75-77]. Presently, a cooling rate of 10^5 K/s was noted in the Fe-30Mn-6Si LPBF-built alloy. The relationship between LED and the cooling rate was observed in Figure 7C. From the surface of the melt pool, at 0 µm melt pool depth, the cooling rate was

constant and then dropped at a particular depth depending on the LED. Its magnitude was also dependent on LED. The low LED (0.25 J/mm) had a stable cooling rate of 9.28×10^5 K/s up to ~30 μm melt pool depth, and for 0.29 J/mm LED, it was stable at 6.21×10^5 K/s until ~60 μm deep. For the LEDs of 0.44 J/mm and 0.88 J/mm, the cooling rates were rather stable until ~120 μm deep at 3.93×10^5 K/s and 3.09×10^5 K/s, respectively. Moreover, the percentage change in the cooling rates after varying the laser power and scan speed was the same at ~58%. When the laser power was raised from 100 W to 175 W, the cooling rate dropped from 9.28×10^5 K/s to 3.93×10^5 K/s, while the increase in scan speed from 400 mm/s to 600 mm/s increased the cooling rate from 3.93×10^5 K/s to 6.21×10^5 K/s.

The maximum calculated temperature in the melt pool as a function of melt pool depth for different LEDs derived from the FEA analysis is shown in Figure 7D. The melt pool temperature responds positively to the increase in LED, and it is observed to decrease within the melt pool. For example, at the melt pool surface, a temperature of roughly 2081 °C, 2173 °C, 3019 °C, and 3256 °C was computed for 0.25 J/mm, 0.29 J/mm, 0.44 J/mm, and 0.88 J/mm LEDs, and it decreased to 1360 °C, 1755 °C, 2484 °C, and 2716 °C at 50 μm melt pool depth, respectively. As a guide for the melting of the powder, the melting points of the constituent elements (Fe = 1535 °C, Si = 1410 °C, and Mn = 1245 °C) in the blended powder are likewise inscribed in Figure 7D. The observed temperatures at the melt pool surface are beyond the melting temperature of the powder, which may have likely evaporated some elements. In particular, the loss of manganese is expected when an LED over 0.25 J/mm is applied because of its relatively low boiling temperature (Fe = 2750 °C, Si = 2357 °C, and Mn = 2062 °C), Figure 3B.

The solidified surface of the LPBF-built alloy fabricated at 0.44 J/mm LED was re-scanned at 175 W and 400 mm/s (100% re-scan) to further promote the alloying of the blended powders. The added step doubled the LED from 0.44 J/mm to 0.88 J/mm at each layer and consequently raised the temperature in the melt pool, as shown in Figure 7E. At the surface, the maximum temperature for 0.44 J/mm LED reached 3019 °C, and this was similar for 0.88 J/mm LED, as depicted by the first peak in the temperature profile on the surface of the laser re-scanned LPBF-built alloy. The alloy was expected to have solidified after the first scan because the temperature dropped to almost 270 °C. However, the additional re-scan step reached a much higher temperature of 3256 °C, as seen in the second peak, than in the first scan because the re-scan started at a relatively high temperature of 270 °C, and there is a difference in the thermal conductivity of the powder and the alloy[78,79]. A similar pattern showing the two temperature peaks was observed at different melt pool depths when the re-scan strategy was applied.

Microstructure evolution

Both the highly directional heat flow conditions and large temperature gradients generated during laser melting of an outermost layer of metal powder, which usually also resulted in the partial remelting of the already solidified grains of the underlying built substrate, favour epitaxial growth of these existing grains in certain crystallographic directions towards the heat source (i.e., they grow antiparallel to the direction of heat flow into the underlying substrate). For certain laser input conditions, a highly directional columnar morphology and strong texture were frequently observed in LPBF-built alloys[80,81]. However, the EBSD maps shown in Figure 4 revealed a gradual change in the microstructure from a nearly equiaxed to columnar grain structure as the LED was increased.

The equiaxed-to-columnar transition in the grain structure was commonly observed within the melt pool, and this transition depends on the alloy chemistry and the heat transfer conditions according to the LPBF processing conditions[64,82-86]. A near-homogeneous grain structure with weak texture was achieved when Attard *et al.* applied the island scan strategy or checkerboard style[87], a standard parameter unique to the

setup[32], and when Ewald *et al.* heated the build platform to 500 °C[21]. Attard's group associated this with the even distribution of heat in the island scan strategy. Meanwhile, the heated build platform in the 0.5 mm sized product reduced the temperature gradient in Ewald *et al.*'s LPBF product, which also reduced the temperature gradient and promoted a nearly homogeneous and equiaxed microstructure[21]. The lack of grain morphology transition in the melt pool in the present Fe-30Mn-6Si LPBF alloy may have been caused by the island scan strategy with 45° scan rotation in the subsequent layers, leading to a homogeneous grain morphology in each parameter setting.

The similar microstructures of LPBF processed parts and conventionally welded components make it convenient to describe the solidified LPBF microstructure in terms of the well-established physical metallurgy principles associated with fusion welding[69]. Grain shape and scale were defined by the solidification theory, and may be controlled by the temperature gradient G, solidification velocity R, the temperature solidification range of an alloy ΔT, and the liquid diffusion coefficient DL[65,67]. The relationships between these key solidification parameters are given below[66]:

$$\begin{aligned} &\frac{\mathrm{G}}{\mathrm{R}} < \frac{\Delta T}{D_L}, \text{ Equiaxed grains} \\ &\frac{G}{R} > \frac{\Delta T}{D_{L-}}, \text{ Columnar grains} \end{aligned} \tag{2}$$

where the G/R ratio and the G·R product, which is the cooling rate, can predict the morphology and dimensions of the solidified microstructure, respectively. For example, a low G/R value correlates to equiaxed grains, with the morphology transitioning to columnar dendritic, cellular, and then to planar for increasing values of G/R, and the high cooling rate resulted in a fine solidified grain structure[70]. Investigation of the thermal history of LPBF-processed alloy was necessary for understanding its expected final microstructure, and in Figures 4 and 7, the select parameters showed that the different thermal profiles affected both the morphology and dimensions of the solidified grains.

The solidification of grains in LPBF-processed alloys follows the well-established nucleation and growth processes in solidified metals and alloys. Li and Tan[88] provided the general grain characteristics of LPBF alloys and summarised two possible nucleation mechanisms: (i) bulk nucleation; and (ii) epitaxial or surface nucleation. Bulk nucleation occurs on the top side of the melt pool and at the head of a solidification front[88]. Nuclei also form from the partially melted powder in the melt pool[89], and they can survive given a sufficient volume of surrounding undercooled liquid metal[90]. These formed grains then assume an equiaxed morphology due to the low G/R ratio on the top side of the melt pool[91]. Epitaxial nucleation occurs at the interface of the melt pool and the substrate, or at the previously solidified layer[92]. A high LED and a low solidification rate in the melt pool encouraged grains to grow in a preferred crystallographic orientation[93], which was <100> for cubic and <1010> for hexagonal metals, respectively[69]. Grains possessing these favoured orientations outgrew grains with less favourable orientations[65], eventually generating a highly textured, columnar microstructure[94].

The prevalence of a highly textured and columnar grain morphology at the high LED settings [Figure 4G] suggested an epitaxial mechanism. Without an added and known potent nucleating particle in the elemental mixture and because of the steep temperature gradient on melting and solidification, the previously solidified layer would act as a suitable substrate for continued growth into the melt pool, whereby the partly melted grains propagate by epitaxial "nucleation" towards the heat source. Equiaxed grains may form on the top surface of the melt pool when the melt pool trail ended because of the low G/R ratio in this region, and such was seen on the last fabricated layer in NiTi[86]. In the Fe-30Mn-6Si, at 0.44 J/mm LED, a temperature

gradient = 9.83 × 10^2 K/m, cooling rate = 4 × 10^5 K/s, the slow solidification rate of R = 3.98 × 10^2 mm/s, and the melt pool temperature of ~1300 °C at 140 μm melt pool depth were sufficient to melt the solidified equiaxed grains in the previous laser scan and then subsequently re-solidify into columnar grains. A similar grain morphology holds for the laser re-scanned LPBF alloy, albeit grains were relatively fine and less columnar when laser re-scanning was applied.

The re-scan strategy had been reported to improve surface quality[66], increase density[95], and reduce residual stress[96] in AM components. This additional step was included in this study to enhance the alloying of the blended powders, and this resulted in a notably different microstructure from that of a non-re-scanned alloy. The melt pool width, depth and overall area associated with the re-scan strategy [Figure 6D] were considerably larger than after single scanning [Figure 6C], and this is caused by the higher thermal conductivity of the solidified layer than the powder material[97]. Hence, the enhanced heat transfer in the solidified layer resulted in a more pronounced melt pool, which was reflected in the calculated thermal profile. A coarse and columnar grain structure was still expected in the laser re-scanned LPBF alloy because the parent grains in the non-re-scanned alloy have solidified into columnar grains. The relatively gentle slope of solidification for 0.88 J/mm LED [Figure 7B] and its low cooling rate (3 × 10^5 K/s) promoted the epitaxial growth of columnar grains, but its temperature profile shown in Figure 7D suggested that remelting of the previously solidified layer had occurred.

Completely remelting an alloy reshapes its microstructure, and such was evident in this work by the decrease in the average grain size and aspect ratio in the remelted LPBF alloy. A region of coarse and refined grains was apparent on close inspection in the re-solidified structure (marked areas in Figure 4J). Xiong *et al.* reported a similar observation in pure tungsten[79]. During re-scanning, the laser irradiated heat initially remelted the surface and the convection current in the melt pool[98] engulfed and remelted the remaining solid within the melt pool. This caused some of the initially formed columnar grains to be separated and these freed grains became the nuclei for growth[66]. The fast-moving laser that drives the rapid cooling rate (10^5 K/s) in the LPBF process curbs the growth of the newly nucleated grains and freezes them into a fine microstructure[99], thereby forming regions of non-uniform microstructure.

For the low LED (0.25 J/mm), the melt pool temperature at 50 μm pool depth was 1360 °C which was enough to melt the blended powders and potentially melt the surface of the previously solidified layer. However, the high cooling rate of 9 × 10^5 K/s and the high solidification rate at this setting resulted in the retention of the equiaxed grain morphology. Moreover, the chemical segregation [Figure 2C] preserved in this LED suggests the presence of partially alloyed powder both in the melt pool and the solidified layer when the next layer was melted. The bulk nucleation mechanism was favoured in the presence of partially alloyed powder since they can act as heterogeneous nucleation sites and impede the epitaxial growth of the previously solidified equiaxed grains at the bottom of the melt pool[100].

For the high laser power and fast scan speed (175 W, 600 mm/s, 0.29 J/mm), the melt pool depth of 110 μm could get through an equivalent of two powder layers and had enough heat to sufficiently remelt the previously solidified layer and re-solidify them into a full-columnar structure. However, the solidified grains shown in Figure 4D were equiaxed and rather coarse (105 μm) compared to the finer grains (64 μm) associated with the low LED (0.25 J/mm) in Figure 4A. The partially melted powder observed at this setting could have induced the bulk nucleation of the grains and interrupted the epitaxial growth of grains.

The significant influence of the studied processing parameters on the resultant LPBF microstructure presents an opportunity to control the microstructure and texture, and therefore the properties of any given

component. For instance, a columnar and textured grain structure is ideal for the pseudoelastic behaviour seen in Fe-Mn-Al SMAs[101,102] and the unrestricted martensitic phase transformation for shape memory in Cu-based SMAs[103].

Possible factors influencing hardness

Effect of grain size

Figure 8 shows the hardness of the LPBF-built alloy prepared as a function of LED. The two low LEDs (0.25 and 0.29 J/mm) have a close hardness value (278 ± 7.6 and 273 ± 3.9 HV2, respectively). The hardness in the two high LEDs (0.44 and 0.88 J/mm) is also close (287 ± 5.5 and 292 ± 3.6 HV2, respectively.) Meanwhile, the reference as-cast alloy had the lowest hardness (226 ± 6.7 HV2). The hardness of the material varies with grain size according to the classic Hall-Petch relation[104,105]. Also, in Figure 8, the grain size increases with an increase in LED up to 0.44 J/mm, and then drops when the laser re-scanning step was added to achieve 0.88 J/mm LED. This change was associated with the thermal history of the LPBF alloy [Figure 7]. The reference alloy has a lower hardness than each of the LPBF-fabricated alloys. This is due to the coarse, equiaxed grains generated in the reference alloy by hot working and the 14-h homogenisation[17,106,107]. In the LPBF alloy, the hardness is seen to increase together with the grain size, thereby negating the established influence of grain size on hardness. This suggests that some other factor affects the hardness of the LPBF-fabricated alloys.

Effect of phase types

Figure 9 shows the relationship between the volume fraction of phases and hardness as the LED is increased. This parameter was also found to influence the relative volume fractions of austenite and ε-martensite in the LPBF alloy, whereby austenite decreases while ε-martensite increases with increasing LED. Martensite is formed from austenite by either a stress or thermally induced transformation[41,108-110], which results in the observed inverse relationship between the two phases. The effect of LED on the volume fractions of the phases was associated with the grain size, and that is, fine grains are detrimental to the formation of the ε-martensite phase[111,112]. The increase in ε-martensite volume fraction may also be caused by the decrease in Mn concentration at high LED [Figures 3B and 9][113]. Hardness as a function of phase volume fraction is also given in Figure 9, where it appears that hardness directly correlates with the amount of ε-martensite in the microstructure. This confirms that both the type and volume of phases present in the LPBF-fabricated alloy have a very strong effect on hardness.

Boundaries exist between the phases in a multi-phased material, and each phase has a distinct characteristic[114]. The reference alloy was fully austenitic, whereas the LPBF alloy contains both austenite and ε-martensite, and other minor phases [Figure 5 and Table 2]. Since austenite is much softer than ε-martensite[115], this resulted in the low hardness of the reference alloy. In comparison, the amount of austenite and the pre-existing ε-martensite in the LPBF alloy, for example, in 0.44 J/mm LED, were 62% and 31%, respectively. The relationship between hardness and the volume fraction of ε-martensite has also been reported in a powder metallurgy fabricated Fe-30Mn-6Si alloy[116]. A high hardness was found in the as-sintered condition, but it decreased after heat treatment because of the corresponding decrease in ε-martensite. The addition of 5 wt.% Cr, an austenite stabiliser[117,118], in an as-cast Fe-30Mn-6Si alloy also resulted in a soft alloy due to the absence of ε-martensite[119].

Pre-existing ε-martensite has been reported to block plastic flow, which leads to high work hardening[120]. The impeding action of pre-existing ε plates was observed by Sato *et al.* using TEM, and they also reported a hardened Fe-30Mn-1Si alloy[1]. The group likened the ε plate phase boundary to a grain boundary. In the Fe-30Mn-6Si reference and LPBF alloys, ε plates may have nucleated and grown in the austenite grains

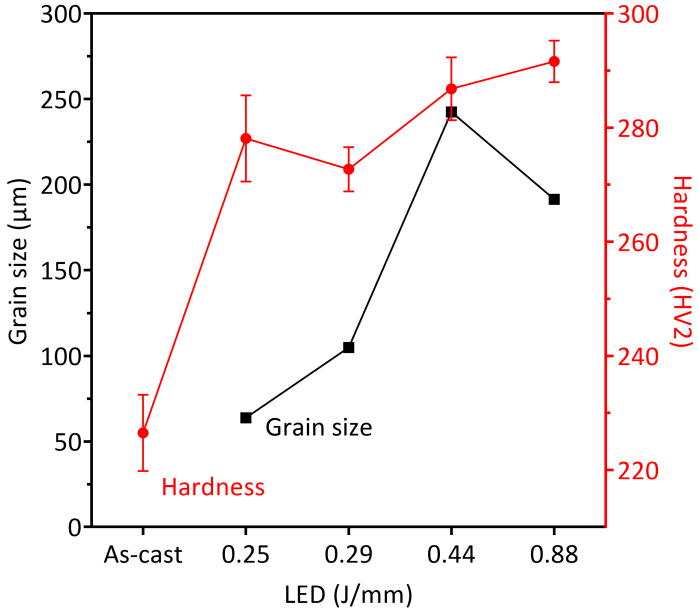

Figure 8. Relationship between grain size and hardness for both the reference alloy and the LPBF alloy fabricated at different LEDs.

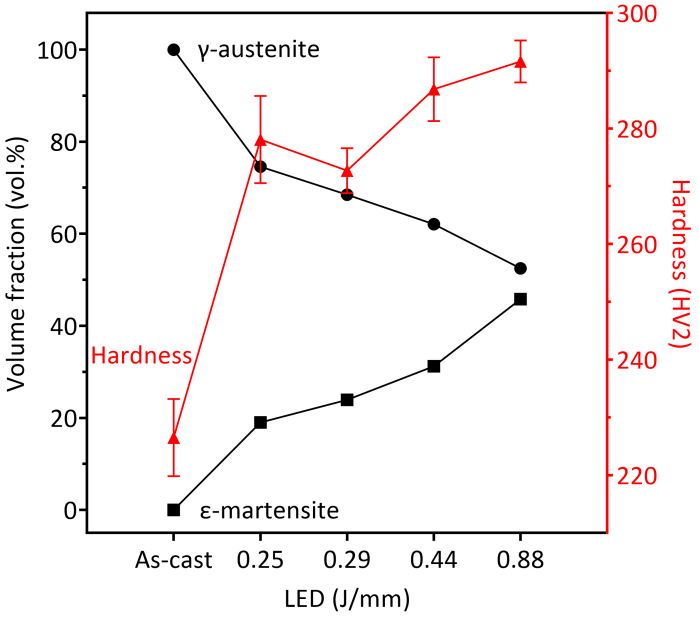

Figure 9. The relationship between γ-austenite and ε-martensite phase fractions and hardness for both the reference alloy and the LPBF alloy fabricated at different LEDs.

during the hardness test to accommodate strain. But the thick pre-existing ε-martensite plates [Figure 4B, E, H and K] may have restricted the nucleation and growth of the stress-induced ε plates. This is a contributing factor to the higher hardness found in the LPBF alloy than in the reference alloy and suggests that an increase in hardness is strongly related to the increase in the amount of ε-martensite in the microstructure.

Effect of residual strain

The far-from-equilibrium processing conditions in LPBF introduce residual strains that may also influence hardness. Since residual strain is associated with crystal misorientation[121-124], the relationship between crystal misorientation and hardness is presented in Figure 10. Comparing the reference alloy and the LPBF alloy prepared at 0.44 J/mm LED, the hardness of the former was significantly lower (227 HV2) than the latter (287 HV2). The corresponding average Kernel average misorientation (KAM) in the reference alloy is also lower (0.44°) than in the LPBF alloy (0.64°). A high residual strain has been associated with a high density of low-angle grain boundaries[125] and, as such, the density of these boundaries (2° to 10° misorientation) in both the reference and LPBF alloys were measured by EBSD to be 3% and 7%, respectively. Hu *et al.* reported that in pure Ti sheet, the hardening effect due to low-angle boundaries was dependent on the level of strain[126]. At strains up to 30%, the high-angle boundaries (HAGB) contributed to the hardness, but for strains above 30%, the density of the low-angle boundaries (LAGB) increased. The latter was suggested to be the biggest contributor to hardness. This was also noted in both 304 L stainless steel and Ni-Co alloys, whereby the hardness increased with increasing residual strain[127], and in a Fe-Ni alloy, the hardness decreased when the residual strain was relieved[128]. A dislocation has to overcome the grain boundary energy, both high- and low-angle, for it to move through the boundary, and the magnitude of the LAGB interfacial energy is a function of the degree of crystallographic misalignment[114]. Thus, the high hardness in the LPBF alloys as compared to the reference alloy was also caused by the inherent residual strain that resisted the localised deformation.

Figure 10 shows a positive correlation between the average crystal misorientation from EBSD analysis and the computed temperature gradient using the FEA of the melt pool as a function of LED at differing depths from the melt pool surface. On the top surface of the melt pool, the highest temperature gradient (2.32×10^3 K/m) was computed for 0.25 J/mm LED. It then decreased as the LED increased, with 0.88 J/mm LED having the lowest temperature gradient (7.72×10^2 K/m). At 50 μm depth from the melt pool surface, the temperature gradient in 0.25 J/mm LED increased substantially to 1.90×10^4 K/m (~7× increase) while it remained almost constant in 0.88 J/mm LED at 1.15×10^3 K/m (~0.5× increase). This then corresponds to an average misorientation of 0.65° and 0.49°, respectively, and suggests that a high average KAM indeed correlates with a high temperature gradient.

The residual strain in the LPBF alloy is caused by the local heat application of the laser, which introduces tensile stress in the molten layer and compressive stress in the solidified lateral and underlying layers[129]. These stresses, if not released, result in residual plastic strains. Several authors looked into minimising thermal stress in the LPBF-fabricated alloy. Vrancken *et al.*, Lu *et al.*, and Liu *et al.* agreed that a short laser scan length introduced less thermal stress, while Mishurova *et al.* emphasised the importance of large melt pool volume to lessen thermal stress[130-133]. The scan strategy was maintained during the LPBF of Fe-30Mn-6Si alloy, but the melt pool for 0.88 J/mm LED was comparably large than for the other LEDs [Figure 6D]. However, Liu *et al.* added that a low LED is necessary for a small thermal stress, and these workers pointed out that a low thermal stress in short laser scan length was caused by the release of stress through cracking[132]. A low average misorientation (0.49°) and a high hardness [Figure 10] in the highest LED (0.88 J/mm) suggest otherwise. More so, the ε-martensite formation in 0.88 J/mm LED may be stress induced and its volume fraction was high (45.8%). This entirely suggests that the residual strain may have been released through the formation of cracks since the LPBF alloy fabricated at 0.88 J/mm LED had comparably more cracks than the 0.25 J/mm LED (Figure 2C and D, respectively). A more thorough investigation is, however, warranted to understand the residual strain in the LPBF alloy fabricated from a homogeneously mixed Fe-30Mn-6Si powder.

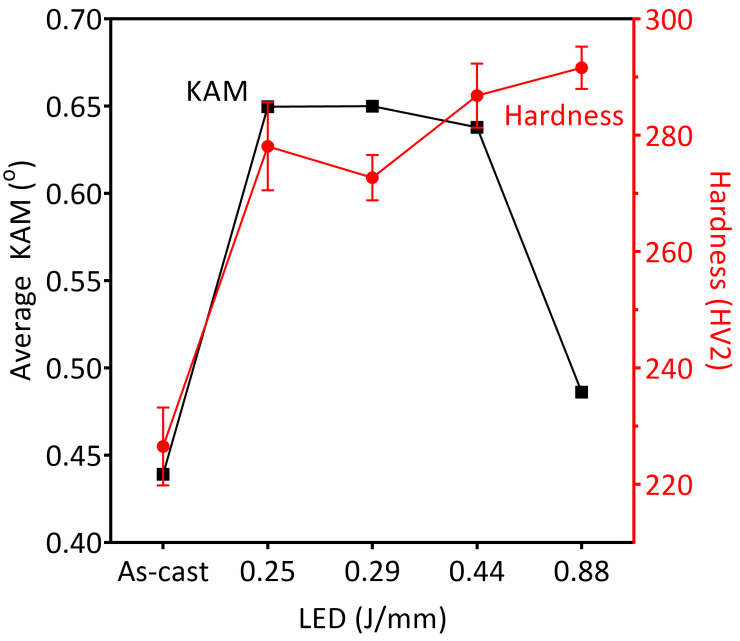

Figure 10. The relationship between residual strain (average KAM value) and hardness for both the reference alloy and the LPBF alloy fabricated at different LEDs.

The residual strain in the LPBF alloy, according to the average crystal misorientation data, was also shown in Figure 10 to decrease with increasing LED. This was reported to increase the hardness[127], and when the residual strain was relieved, the hardness decreased[128]. For this reason, the relationship between the average KAM value and hardness in both the reference alloy and LPBF alloy at different processing conditions was investigated. However, the decrease in residual strain corresponded to an increase in hardness, as seen in Figure 10, which differed from the previous reports[126-128]. Therefore, the residual strain may have indeed been relieved from the LPBF alloy through the formation of cracks, particularly in 0.88 J/mm LED.

The influence of grain size, presence and volume of phases, and residual strain was analysed to identify the possible factor affecting the hardness of the LPBF-fabricated Fe-30Mn-6Si alloy. Hardness is known to increase as the grain size decreases, ε-martensite volume fraction increases, and residual strain increases. It was observed that the increase in hardness was mainly influenced by ε-martensite at high LEDs of 0.44 J/mm and 0.88 J/mm [Figure 9], while grain size and residual stress were not seen to influence their hardness according to the accepted theories[104,105] and observations[126-128]. The sub-grain phase boundaries between the different variants of ε-martensite increased the hardness in those large-grained microstructures. Also, high hardness value was found in the LPBF alloy with low residual strain [Figure 11]. This suggests that the residual strain at the high LED was relieved after cracks were formed. At 0.25 J/mm LED, hardness has increased relative to the reference alloy because of the low grain size and high vol.% martensite (Figures 8 and 9, respectively). However, the hardness for 0.29 J/mm LED slightly decreased (2%) despite the increase in martensite vol.% (26%) as compared to that of 0.25 J/mm LED. Concurrently, the grain size of the former increased by 65%. From the given correlations, the increase in grain size was likely the main mechanism for the slight decrease in hardness from 0.25 to 0.29 J/mm LED.

CONCLUSIONS

A LPBF technique is normally carried out using pre-alloyed powder, but the supply of pre-alloyed powder is limited, thereby confining this technique's adaptability to readily available raw materials. It was

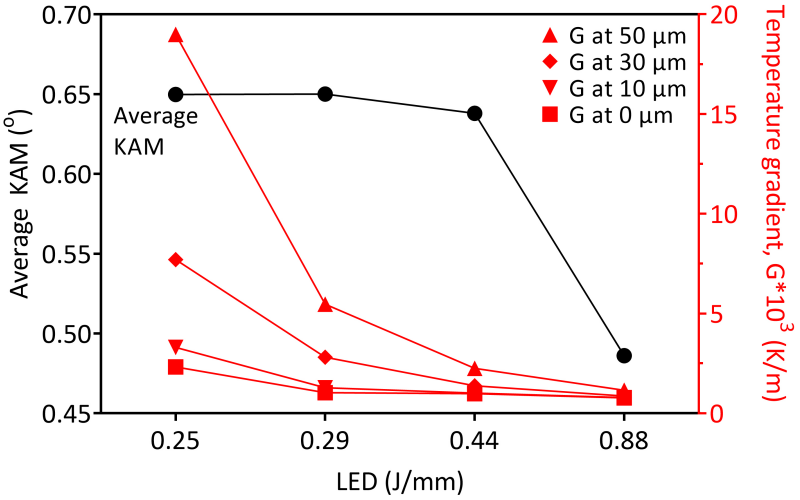

Figure 11. The relationship between crystal misorientation (average KAM) and temperature gradient derived from the simulated thermal profile of the melt pool as a function of LED at differing depths from the melt pool.

demonstrated for the first time that a Fe-30Mn-6Si alloy with a known combination of biodegradable and SMA properties can be built using the LPBF technique from a homogenised metal powder. The LPBF parameters were investigated by varying the laser power, scan speed, and re-scan strategy. A density of over 99% was achieved at a range of LED from 0.30 J/mm to 0.88 J/mm, with 0.44 J/mm as the recommended LED for a high-density product. The resultant microstructure was shown to respond with the laser power and scan speed settings, and the changes in microstructure were explained using the FEA analysis of the melt pool profile derived from the single laser track scan. For example, the microstructure transitioned from one that was highly columnar and textured at high laser power to one that was fine and nearly equiaxed with weak texture at low laser power. Increasing the scan speed at high laser power setting eliminated the strong texture and increased the grain size. However, laser re-scanning of the solidified layer remelted the columnar grains and re-solidified them into non-uniform microstructure.

The hardness of the as-built LPBF alloys was also systematically assessed. The relationships between grain size, types and amounts of phases, and crystal misorientation on the hardness of both the reference and the LPBF alloys at different process settings were investigated. The hardness of the single-phase austenitic reference alloy was found to be affected by the grain size and residual strain. In the LPBF alloy, the fraction of ε phase strongly influenced the hardness. The pre-existing, thick ε plates may have blocked the nucleation and growth of the stress-induced ε plates in the LPBF alloy, which effectively hardened the LPBF alloy. Overall, this study expanded the processing capability of the LPBF technique by fabricating a Fe-Mn-Si alloy from a homogenised powder and elucidated the influence of processing parameters on the microstructure and the hardness of the product.

DECLARATIONS

Authors' contributions

Conception, design, writing, and editing: Dela Cruz ML, Yakubov V, Li X, Ferry M
Data collection and analysis: Dela Cruz ML, Li X, Ferry M
FEA simulation methodology and analysis: Yakubov V, Dela Cruz ML
All authors contributed to the manuscript and were involved in discussion.

Availability of data and materials
Not applicable.

Financial support and sponsorship
The authors acknowledge the support of Australian Research Council (ARC) Discovery Early Career Researcher Award (DECRA) DE190101495, the Philippine Department of Science and Technology through the Engineering Research for Development and Technology Program (ERDT-DOST), UNSW Tuition Fee Scholarship, the Australian Government Research Training Program Scholarship for funding Michael Leo Dela Cruz's PhD fellowship, and the technical support from the Mark Wainwright Analytical Centre at UNSW including the facilities and staff of Microscopy Australia at the Electron Microscope Unit (EMU) and the Solid State & Elemental Analysis Unit (SSEAU).

Conflicts of interest
All authors declared that there are no conflicts of interest.

Ethical approval and consent to participate
Not applicable.

Consent for publication
Not applicable.

Copyright
© The Author(s) 2023.

REFERENCES
1. Sato A, Chishima E, Soma K, Mori T. Shape memory effect in γ□ϵ transformation in Fe-30Mn-1Si alloy single crystals. *Acta Metall* 1982;30:1177-83. DOI
2. Dunne D. Shape memory in ferrous alloys. In phase transformations in steels, Pereloma E, Edmonds DV, editors. Soston, UK: Woodhead Publishing; 2012, pp. 83-125.
3. Alaneme KK, Okotete EA. Reconciling viability and cost-effective shape memory alloy options - a review of copper and iron based shape memory metallic systems. *Eng Sci Technol Int J* 2016;19:1582-92. DOI
4. Carlisle EM. Silicon. In biochemistry of the essential ultratrace elements, Frieden E, editor. Boston, MA: Springer; 1984, pp. 257-91. DOI
5. Santamaria AB. Manganese exposure, essentiality & toxicity. *J Med Res* 2008;128:484-500. PubMed
6. Avila DS, Puntel RL, Aschner M. Manganese in health and disease. *Met Ions Life Sci* 2013;13:199-227. DOI
7. Tuschl K, Mills PB, Clayton PT. Chapter Twelve - manganese and the Brain, in international review of neurobiology, Bhatia KP, Schneider SA, editors. Cambridge: Academic Press; 2013, pp. 277-312. DOI
8. Ahire JH, Chambrier I, Mueller A, Bao Y, Chao Y. Synthesis of D-mannose capped silicon nanoparticles and their interactions with MCF-7 human breast cancerous cells. *ACS Appl Mater Interfaces* 2013;5:7384-91. DOI PubMed
9. Liu D, Mäkilä E, Zhang H, et al. Nanostructured porous silicon-solid lipid nanocomposite: towards enhanced cytocompatibility and stability, reduced cellular association, and prolonged drug release. *Adv Funct Mater* 2013;23:1893-902. DOI
10. Kafshgari MH, Voelcker NH, Harding FJ. Applications of zero-valent silicon nanostructures in biomedicine. *Nanomedicine* 2015;10:2553-71. DOI PubMed
11. Fântânariu M, Trincă LC, Solcan C, et al. A new Fe-Mn-Si alloplastic biomaterial as bone grafting material: *in vivo* study. *Appl Surf Sci* 2015;352:129-39. DOI
12. Trincă LC, Burtan L, Mareci D, et al. Evaluation of in vitro corrosion resistance and in vivo osseointegration properties of a FeMnSiCa alloy as potential degradable implant biomaterial. *Mater Sci Eng C Mater Biol Appl* 2021;118:111436. DOI PubMed
13. Liu B, Zheng Y, Ruan L. In vitro investigation of $Fe_{30}Mn_6Si$ shape memory alloy as potential biodegradable metallic material. *Mater Lett* 2011;65:540-3. DOI
14. Rațoi M, Stanciu S, Cimpoeşu N, Cimpoeşu I, Constantin B, Paraschiv C. A potential biodegradable metallic material with shape memory effect based on iron. In structural integrity of welded structures, Murariu AC, editor. Trans Tech Publications; 2013. p. 110-4.
15. Drevet R, Zhukova Y, Kadirov P, et al. Tunable corrosion behavior of calcium phosphate coated Fe-Mn-Si alloys for bone implant applications. *Metall Mat Trans A* 2018;49:6553-60. DOI
16. Drevet R, Zhukova Y, Malikova P, et al. Martensitic transformations and mechanical and corrosion properties of Fe-Mn-Si alloys for

biodegradable medical implants. *Metall Mat Trans A* 2018;49:1006-13. DOI

17. Prokoshkin S, Pustov Y, Zhukova Y, et al. Effect of thermomechanical treatment on structure and functional fatigue characteristics of biodegradable Fe-30Mn-5Si(wt %) shape memory alloy. *Materials* 2021;14:3327. DOI PubMed PMC
18. Babacan N, Kochta F, Hoffmann V, et al. Effect of silver additions on the microstructure, mechanical properties and corrosion behavior of biodegradable Fe-30Mn-6Si. *Mater Today Commun* 2021;28:102689. DOI
19. Wang Y, Venezuela J, Dargusch M. Biodegradable shape memory alloys: progress and prospects. *Biomaterials* 2021;279:121215. DOI PubMed
20. Del-río L, Nó M, Sota A, et al. Internal friction associated with ε martensite in shape memory steels produced by casting route and through additive manufacturing: influence of thermal cycling on the martensitic transformation. *J Alloys Compd* 2022;919:165806. DOI
21. Ewald FC, Brenne F, Gustmann T, Vollmer M, Krooß P, Niendorf T. Laser powder bed fusion processing of Fe-Mn-Al-Ni shape memory alloy-on the effect of elevated platform temperatures. *Metals* 2021;11:185. DOI
22. Ferretto I, Kim D, Della Ventura N, Shahverdi M, Lee W, Leinenbach C. Laser powder bed fusion of a Fe-Mn-Si shape memory alloy. *Addit Manuf* 2021;46:102071. DOI
23. Kim D, Ferretto I, Jeon JB, Leinenbach C, Lee W. Formation of metastable bcc-δ phase and its transformation to fcc-γ in laser powder bed fusion of Fe-Mn-Si shape memory alloy. *J Mater Res Technol* 2021;14:2782-8. DOI
24. Kim D, Ferretto I, Kim W, Leinenbach C, Lee W. Effect of post-heat treatment conditions on shape memory property in 4D printed Fe-17Mn-5Si-10Cr-4Ni shape memory alloy. *Mater Sci Eng A* 2022;852:143689. DOI
25. Kim D, Ferretto I, Leinenbach C, Lee W. 3D and 4D printing of complex structures of Fe Mn Si-based shape memory alloy using laser powder bed fusion. *Adv Mater Int* 2022;9:2200171. DOI
26. Niendorf T, Brenne F, Krooß P, et al. Microstructural evolution and functional properties of Fe-Mn-Al-Ni shape memory alloy processed by selective laser melting. *Metall Mat Trans A* 2016;47:2569-73. DOI
27. Patriarca L, Abuzaid W, Carlucci G, Belelli F, Casati R. Pseudoelasticity in FeMnNiAl shape memory alloy lattice structures produced by Laser Powder Bed Fusion. *Mater Lett* 2021;302:130349. DOI
28. Ferretto I, Borzì A, Kim D, et al. Control of microstructure and shape memory properties of a Fe-Mn-Si-based shape memory alloy during laser powder bed fusion. *Addit Manuf Lett* 2022;3:100091. DOI
29. Niendorf T, Brenne F, Hoyer P, et al. Processing of new materials by additive manufacturing: iron-based alloys containing silver for biomedical applications. *Metall Mat Trans A* 2015;46:2829-33. DOI
30. Wiesener M, Peters K, Taube A, et al. Corrosion properties of bioresorbable FeMn-Ag alloys prepared by selective laser melting. *Mater Corros* 2017;68:1028-36. DOI
31. Mosallanejad MH, Niroumand B, Aversa A, Saboori A. In-situ alloying in laser-based additive manufacturing processes: a critical review. *J Alloys Compd* 2021;872:159567. DOI
32. Carter LN, Martin C, Withers PJ, Attallah MM. The influence of the laser scan strategy on grain structure and cracking behaviour in SLM powder-bed fabricated nickel superalloy. *J Alloys Compd* 2014;615:338-47. DOI
33. Yadroitsev I, Bertrand P, Smurov I. Parametric analysis of the selective laser melting process. *Appl Surf Sci* 2007;253:8064-9. DOI
34. Krauss H, Zaeh M. Investigations on manufacturability and process reliability of selective laser melting. *Phys Procedia* 2013;41:815-22. DOI
35. Yan X, Chang C, Dong D, et al. Microstructure and mechanical properties of pure copper manufactured by selective laser melting. *Mater Sci Eng A* 2020;789:139615. DOI
36. Rietveld HM. Line profiles of neutron powder-diffraction peaks for structure refinement. *Acta Cryst* 1967;22:151-2. DOI
37. Rietveld HM. A profile refinement method for nuclear and magnetic structures. *J Appl Crystallogr* 1969;2:65-71. DOI
38. Will G. The rietveld method. In powder diffraction. Berlin Heidelberg: Springer; 2006, pp. 41-72. DOI
39. Degen T, Sadki M, Bron E, König U, Nénert G. The HighScore suite. *Powder Diffr* 2014;29:S13-8. DOI
40. Huang C, Ni H, Yen H. New protocol for orientation reconstruction from martensite to austenite in steels. *Materialia* 2020;9:100554. DOI
41. Nishiyama Z, Crystallography of martensite (general). In martensitic transformation, Fine ME, editor. Cambridge: Academic Press; 1978, pp. 14-134. DOI
42. Ansari MJ, Nguyen DS, Park HS. Investigation of SLM process in terms of temperature distribution and melting pool size: modeling and experimental approaches. *Materials* 2019;12:1272. DOI PubMed PMC
43. Li X, Kang C, Huang H, Zhang L, Sercombe T. Selective laser melting of an $Al_{86}Ni_6Y_{4.5}Co_2La_{1.5}$ metallic glass: processing, microstructure evolution and mechanical properties. *Mater Sci Eng A* 2014;606:370-9. DOI
44. Dong L, Makradi A, Ahzi S, Remond Y. Three-dimensional transient finite element analysis of the selective laser sintering process. *J Mater Process Technol* 2009;209:700-6. DOI
45. Roberts I, Wang C, Esterlein R, Stanford M, Mynors D. A three-dimensional finite element analysis of the temperature field during laser melting of metal powders in additive layer manufacturing. *Int J Mach Tools Manuf* 2009;49:916-23. DOI
46. Tsujimoto H, Kozaki S, Okutani Y, et al. Lifespan enhancement of crane rails, runway girders and overhead cranes using shape-memory alloyed fish-plates; 2017, pp. 72-80.
47. Cao B, Iwamoto T. An experimental investigation on rate dependency of thermomechanical and Stress-induced martensitic transformation behavior in Fe-28Mn-6Si-5Cr shape memory alloy under compression. *Int J Impact Eng* 2019;132:103284. DOI

48. ASTM E92-16. Standard test methods for Vickers hardness and Knoop hardness of metallic materials. PA, USA: ASTM International; 2016.
49. Darvish K, Chen Z, Pasang T. Reducing lack of fusion during selective laser melting of CoCrMo alloy: effect of laser power on geometrical features of tracks. *Mater Des* 2016;112:357-66. DOI
50. Carluccio D, Bermingham M, Kent D, Demir AG, Previtali B, Dargusch MS. Comparative study of pure iron manufactured by selective laser melting, laser metal deposition, and casting processes. *Adv Eng Mater* 2019;21:1900049. DOI
51. Letenneur M, Brailovski V, Kreitcberg A, Paserin V, Bailon-Poujol I. Laser powder bed fusion of water-atomized iron-based powders: process optimization. *J Manuf Mater Process* 2017;1:23. DOI
52. Liverani E, Toschi S, Ceschini L, Fortunato A. Effect of selective laser melting (SLM) process parameters on microstructure and mechanical properties of 316 L austenitic stainless steel. *J Mater Process Technol* 2017;249:255-63. DOI
53. Wang D, Song C, Yang Y, Bai Y. Investigation of crystal growth mechanism during selective laser melting and mechanical property characterization of 316 L stainless steel parts. *Mater Des* 2016;100:291-9. DOI
54. Nguyen Q, Zhu Z, Ng F, Chua B, Nai S, Wei J. High mechanical strengths and ductility of stainless steel 304 L fabricated using selective laser melting. *J Mater Sci Technol* 2019;35:388-94. DOI
55. Kang N, Coddet P, Dembinski L, Liao H, Coddet C. Microstructure and strength analysis of eutectic Al-Si alloy in-situ manufactured using selective laser melting from elemental powder mixture. *J Alloys Compd* 2017;691:316-22. DOI
56. Hou Y, Su H, Zhang H, Wang X, Wang C. Fabricating homogeneous FeCoCrNi high-entropy alloys via SLM in situ alloying. *Metals* 2021;11:942. DOI
57. Haynes WM, Lide DR. CRC handbook of chemistry and physics. In CRC handbook of chemistry and physics, Haynes WM, Lide DR, editors. Cleveland, Ohio: CRC Press; 2017, pp. 97-126.
58. Chu J, Bao Y. Volatilization behavior of manganese from molten steel with different alloying methods in vacuum. *Metals* 2020;10:1348. DOI
59. Yang C, Lin H, Lin K. Improvement of shape memory effect in Fe-Mn-Si alloy by slight tantalum addition. *Mater Sci Eng A* 2009;518:139-43. DOI
60. Watson A, Markus T. Ternary system Fe-Mn-Si. In ternary steel systems: phase diagrams and phase transition data, Watson A, Markus T, editors. Berlin Heidelberg: Springer; 2015, pp. 121-33. DOI
61. Tenbrock C, Fischer FG, Wissenbach K, et al. Influence of keyhole and conduction mode melting for top-hat shaped beam profiles in laser powder bed fusion. *J Mater Process Technol* 2020;278:116514. DOI
62. Bauereiß A, Scharowsky T, Körner C. Defect generation and propagation mechanism during additive manufacturing by selective beam melting. *J Mater Process Technol* 2014;214:2522-8. DOI
63. Madison JD, Aagesen LK. Quantitative characterization of porosity in laser welds of stainless steel. *Scripta Materialia* 2012;67:783-6. DOI
64. He P, Webster RF, Yakubov V, et al. Fatigue and dynamic aging behavior of a high strength Al-5024 alloy fabricated by laser powder bed fusion additive manufacturing. *Acta Mater* 2021;220:117312. DOI
65. DuPont JN. Fundamentals of weld solidification. In Welding Fundamentals and Processes. 2011; pp. 96-114. DOI
66. Liu B, Li B, Li Z. Selective laser remelting of an additive layer manufacturing process on $AlSi_{10}Mg$. *Results Phys* 2019;12:982-8. DOI
67. Ghayoor M, Lee K, He Y, Chang C, Paul BK, Pasebani S. Selective laser melting of 304 L stainless steel: role of volumetric energy density on the microstructure, texture and mechanical properties. *Addit Manuf* 2020;32:101011. DOI
68. Pham MS, Dovgyy B, Hooper PA, Gourlay CM, Piglione A. The role of side-branching in microstructure development in laser powder-bed fusion. *Nat Commun* 2020;11:749. DOI PubMed PMC
69. Lippold JC. Welding metallurgy principles. In welding metallurgy and weldability; 2014. pp. 9-83. DOI
70. Zhang X, Yocom CJ, Mao B, Liao Y. Microstructure evolution during selective laser melting of metallic materials: a review. *J Laser Appl* 2019;31:031201. DOI
71. Bertoli U, Macdonald BE, Schoenung JM. Stability of cellular microstructure in laser powder bed fusion of 316 L stainless steel. *Mater Sci Eng A* 2019;739:109-17. DOI
72. Pinomaa T, Lindroos M, Walbrühl M, Provatas N, Laukkanen A. The significance of spatial length scales and solute segregation in strengthening rapid solidification microstructures of 316 L stainless steel. *Acta Mater* 2020;184:1-16. DOI
73. Li Y, Gu D. Parametric analysis of thermal behavior during selective laser melting additive manufacturing of aluminum alloy powder. *Mater Des* 2014;63:856-67. DOI
74. Chen Y, Chen H, Chen J, Xiong J, Wu Y, Dong S. Numerical and experimental investigation on thermal behavior and microstructure during selective laser melting of high strength steel. *J Manuf Process* 2020;57:533-42. DOI
75. Jung HY, Choi SJ, Prashanth KG, et al. Fabrication of Fe-based bulk metallic glass by selective laser melting: a parameter study. *Mater Des* 2015;86:703-8. DOI
76. Suryawanshi J, Prashanth K, Scudino S, Eckert J, Prakash O, Ramamurty U. Simultaneous enhancements of strength and toughness in an Al-12Si alloy synthesized using selective laser melting. *Acta Mater* 2016;115:285-94. DOI
77. Prashanth K, Eckert J. Formation of metastable cellular microstructures in selective laser melted alloys. *J Alloys Compd* 2017;707:27-34. DOI
78. Guan J, Jiang Y, Zhang X, Chong X. Microstructural evolution and EBSD analysis of AlSi10Mg alloy fabricated by selective laser

remelting. *Mater Charact* 2020;161:110079. DOI
79. Xiong Z, Zhang P, Tan C, Dong D, Ma W, Yu K. Selective laser melting and remelting of pure tungsten. *Adv Eng Mater* 2020;22:1901352. DOI
80. Herzog D, Seyda V, Wycisk E, Emmelmann C. Additive manufacturing of metals. *Acta Mater* 2016;117:371-92. DOI
81. Debroy T, Wei H, Zuback J, et al. Additive manufacturing of metallic components - process, structure and properties. *Prog Mater Sci* 2018;92:112-224. DOI
82. Rafi HK, Karthik NV, Gong H, Starr TL, Stucker BE. Microstructures and mechanical properties of Ti_6Al_4V Parts fabricated by selective laser melting and electron beam melting. *J Mater Eng Perform* 2013;22:3872-83. DOI
83. Trevisan F, Calignano F, Lorusso M, et al. On the selective laser melting (SLM) of the $AlSi_{10}Mg$ alloy: process, microstructure, and mechanical properties. *Materials* 2017;10:76. DOI PubMed PMC
84. Spierings A, Dawson K, Dumitraschkewitz P, Pogatscher S, Wegener K. Microstructure characterization of SLM-processed Al-Mg-Sc-Zr alloy in the heat treated and HIPed condition. *Addit Manuf* 2018;20:173-81. DOI
85. Cao S, Zou Y, Lim CVS, Wu X. Review of laser powder bed fusion (LPBF) fabricated Ti-6Al-4V: process, post-process treatment, microstructure, and property. *Light Adv Manuf* 2021;2. DOI
86. Nigito E, Diemer F, Husson S, Ou S, Tsai M, Rézaï-aria F. Microstructure of NiTi superelastic alloy manufactured by selective laser melting. *Mater Lett* 2022;324:132665. DOI
87. Attard B, Cruchley S, Beetz C, Megahed M, Chiu Y, Attallah M. Microstructural control during laser powder fusion to create graded microstructure Ni-superalloy components. *Addit Manuf* 2020;36:101432. DOI
88. Li X, Tan W. Numerical investigation of effects of nucleation mechanisms on grain structure in metal additive manufacturing. *Comput Mater Sci* 2018;153:159-69. DOI
89. Antonysamy A, Meyer J, Prangnell P. Effect of build geometry on the β-grain structure and texture in additive manufacture of Ti6Al4V by selective electron beam melting. *Mater Charact* 2013;84:153-68. DOI
90. Mohebbi MS, Ploshikhin V. Implementation of nucleation in cellular automaton simulation of microstructural evolution during additive manufacturing of Al alloys. *Addit Manuf* 2020;36:101726. DOI
91. Yan F, Xiong W, Faierson EJ. Grain structure control of additively manufactured metallic materials. *Materials* 2017;10:1260. DOI
92. Yang M, Wang L, Yan W. Phase-field modeling of grain evolutions in additive manufacturing from nucleation, growth, to coarsening. *NPJ Comput Mater* 2021:7. DOI
93. Ikeda T, Yonehara M, Ikeshoji T, et al. Influences of process parameters on the microstructure and mechanical properties of CoCrFeNiTi based high-entropy alloy in a laser powder bed fusion process. *Crystals* 2021;11:549. DOI
94. Liu D, Wang S, Yan W. Grain structure evolution in transition-mode melting in direct energy deposition. *Mater Des* 2020;194:108919. DOI
95. Chlebus E, Gruber K, Kuźnicka B, Kurzac J, Kurzynowski T. Effect of heat treatment on the microstructure and mechanical properties of Inconel 718 processed by selective laser melting. *Mater Sci Eng A* 2015;639:647-55. DOI
96. Ali H, Ghadbeigi H, Mumtaz K. Effect of scanning strategies on residual stress and mechanical properties of Selective Laser Melted Ti_6Al_4V. *Mater Sci Eng A* 2018;712:175-87. DOI
97. Chen C, Yin J, Zhu H, Xiao Z, Zhang L, Zeng X. Effect of overlap rate and pattern on residual stress in selective laser melting. *Int J Mach Tools Manuf* 2019;145:103433. DOI
98. Acharya R, Sharon JA, Staroselsky A. Prediction of microstructure in laser powder bed fusion process. *Acta Mater* 2017;124:360-71. DOI
99. Liu P, Wang Z, Xiao Y, Horstemeyer MF, Cui X, Chen L. Insight into the mechanisms of columnar to equiaxed grain transition during metallic additive manufacturing. *Addit Manuf* 2019;26:22-9. DOI
100. Wang T, Zhu Y, Zhang S, Tang H, Wang H. Grain morphology evolution behavior of titanium alloy components during laser melting deposition additive manufacturing. *J Alloys Compd* 2015;632:505-13. DOI
101. Ozcan H, Ma J, Wang S, et al. Effects of cyclic heat treatment and aging on superelasticity in oligocrystalline Fe-Mn-Al-Ni shape memory alloy wires. *Scripta Mater* 2017;134:66-70. DOI
102. Vollmer M, Krooß P, Kriegel M, et al. Cyclic degradation in bamboo-like Fe-Mn-Al-Ni shape memory alloys - the role of grain orientation. *Scripta Mater* 2016;114:156-60. DOI
103. Ueland SM, Chen Y, Schuh CA. Oligocrystalline shape memory alloys. *Adv Funct Mater* 2012;22:2094-9. DOI
104. Abbaschian R, Abbaschian L, Reed-Hill RE. Elements of grain boundaries. In physical metallurgy principles, Stamford, CT: Cengage learning; 2009, pp. 158-93.
105. Callister WD, Rethwisch DG. Dislocations and strengthening mechanisms. In materials science and engineering: an introduction. Hoboken, NJ: Wiley; 2014, pp. 216-50.
106. Xu Z, Hodgson MA, Cao P. A comparative study of powder metallurgical (PM) and wrought Fe-Mn-Si alloys. *Mater Sci Eng A* 2015;630:116-24. DOI
107. Fiocchi J, Lemke J, Zilio S, Biffi C, Coda A, Tuissi A. The effect of Si addition and thermomechanical processing in an Fe-Mn alloy for biodegradable implants: mechanical performance and degradation behavior. *Mater Today Commun* 2021;27:102447. DOI
108. Bergeon N, Guenin G, Esnouf C. Microstructural analysis of the stress-induced ε martensite in a Fe-Mn-Si-Cr-Ni shape memory alloy: Part I—calculated description of the microstructure. *Mater Sci Eng A* 1998;242:77-86. DOI
109. Gu Q, Van Humbeeck J, Delaey L. A review on the martensitic transformation and shape memory effect in Fe-Mn-Si alloys. *J Phys*

1994;04:C3-135. DOI
110. Putaux JL, Chevalier JP. HREM study of self-accommodated thermal ε-martensite in an F-Mn-Si-Cr-Ni shape memory alloy. *Acta Mater* 1996;44:1701-16. DOI
111. Jang W, Kang J, Jeeb K, Shinb M, Hong J. The effects of grain size and transformation texture on the shape memory effect in Fe-15Mn-5Cr-5Co-3Si alloy. In Ecomaterials, Yamamoto R, editor. Elsevier. 1994; pp. 993-6. DOI
112. Käfer KA, Bernardi HH, Santos ODS, Otubo L, Lima NBD, Otubo J. The influence of microstructure and mechanical resistance on the shape memory of ecae processed stainless Fe-Mn-Si-Cr-Ni-Co steel. *Mat Res* 2018:21. DOI
113. Onuki Y, Fujieda S, Shinoda K, Ohtani H, Maruyama T, Suzuki S. Depletion of manganese in the surface layers of Fe-Mn-Si shape memory alloys by annealing. *Defect Diffus Forum* 2015;363:196-201. DOI
114. Callister WD, Rethwisch DG. Imperfections in solids. In materials science and engineering: an introduction. Hoboken, NJ: Wiley; 2018, pp. 92-120.
115. Feng YP, Blanquer A, Fornell J, et al. Novel Fe-Mn-Si-Pd alloys: insights into mechanical, magnetic, corrosion resistance and biocompatibility performances. *J Mater Chem B* 2016;4:6402-12. DOI PubMed
116. Spandana D, Desai H, Chakravarty D, Vijay R, Hembram K. Fabrication of a biodegradable Fe-Mn-Si alloy by field assisted sintering. *Adv Powder Technol* 2020;31:4577-84. DOI
117. Eskil M, Kanca E. A new formulation for martensite start temperature of Fe-Mn-Si shape memory alloys using genetic programming. *Comput Mater Sci* 2008;43:774-84. DOI
118. Hsu T, Zuyao X. Martensitic transformation in Fe-Mn-Si based alloys. *Mater Sci Eng A* 1999;273-275:494-7. DOI
119. Balo ŞN. A comparative study on crystal structure and magnetic properties of Fe-Mn-Si and Fe-Mn-Si-Cr Alloys. *J Supercond Nov Magn* 2013;26:1085-8. DOI
120. Tomota Y, Strum M, Morris JW. Microstructural dependence of Fe-high Mn tensile behavior. *Metall Trans A* 1986;17:537-47. DOI
121. Zaefferer S, Elhami N, Konijnenberg P. Electron backscatter diffraction (EBSD) techniques for studying phase transformations in steels. In phase transformations in steels, Pereloma E, Edmonds DV, editor. Woodhead Publishing; 2012, pp. 557-87. DOI
122. Roberts G, Ward RM, Strangwood M, Davis CL. Use of misorientation values to further understand deformation in rail steels. *Ironmak Steelmak* 2013;40:92-7. DOI
123. Wright SI, Nowell MM, Field DP. A review of strain analysis using electron backscatter diffraction. *Microsc Microanal* 2011;17:316-29. DOI PubMed
124. Brewer LN, Field DP, Merriman CC. Mapping and assessing plastic deformation using EBSD. In electron backscatter diffraction in materials science, Schwartz AJ, editor. Boston, MA: Springer; 2009, pp. 251-62. DOI
125. Hou J, Peng Q, Shoji T, Wang J, Han E, Ke W. Effects of cold working path on strain concentration, grain boundary microstructure and stress corrosion cracking in Alloy 600. *Corros Sci* 2011;53:2956-62. DOI
126. Hu X, Chai L, Zhu Y, et al. Quantitative study of microstructural, textural and hardness evolution of high-purity Ti sheet during rolling from low to medium strains. *Mater Today Commun* 2021;29:102989. DOI
127. Qiao D, Zhang W, Pan T, Crooker P, David S, Feng Z. Evaluation of residual plastic strain distribution in dissimilar metal weld by hardness mapping. *Sci Technol Weld Join* 2013;18:624-30. DOI
128. Fukui D, Nakada N, Onaka S. Internal residual stress originated from Bain strain and its effect on hardness in Fe-Ni martensite. *Acta Mater* 2020;196:660-8. DOI
129. Mercelis P, Kruth J. Residual stresses in selective laser sintering and selective laser melting. *Rap Prototyp J* 2006;12:254-65. DOI
130. Vrancken B, Cain V, Knutsen R, Van Humbeeck J. Residual stress via the contour method in compact tension specimens produced via selective laser melting. *Scripta Mater* 2014;87:29-32. DOI
131. Lu L, Wu C, Wang J, Liu Y, Tu H, Su X. Experimental investigation and thermodynamic calculation of the Zn-Fe-Ce system. *J Alloys Compd* 2015;648:881-9. DOI
132. Liu Y, Yang Y, Wang D. A study on the residual stress during selective laser melting (SLM) of metallic powder. *Int J Adv Manuf Technol* 2016;87:647-56. DOI
133. Mishurova T, Cabeza S, Artzt K, et al. An assessment of subsurface residual stress analysis in SLM Ti-6Al-4V. *Materials* 2017;10:348. DOI PubMed PMC

Yang *et al. Microstructures* 2023;3:2023013
DOI: 10.20517/microstructures.2022.30

Microstructures

Review

Open Access

Check for updates

Recent progress on alloy-based anode materials for potassium-ion batteries

Qiuran Yang, Qining Fan, Jian Peng, Shulei Chou, Huakun Liu, Jiazhao Wang

Institute for Superconducting and Electronic Materials, Australian Institute for Innovative Materials, University of Wollongong, North Wollongong, New South Wales 2522, Australia.

Correspondence to: Prof. Jiazhao Wang, Institute for Superconducting and Electronic Materials, Australian Institute for Innovative Materials, University of Wollongong, North Wollongong, New South Wales 2522, Australia. E-mail: jiazhao@uow.edu.au

How to cite this article: Yang Q, Fan Q, Peng J, Chou S, Liu H, Wang J. Recent progress on alloy-based anode materials for potassium-ion batteries. *Microstructures* 2023;3:2023013. https://dx.doi.org/10.20517/microstructures.2022.30

Received: 26 Sep 2022 **First Decision:** 31 Oct 2022 **Revised:** 12 Dec 2022 **Accepted:** 5 Jan 2023 **Published:** 22 Feb 2023

Academic Editor: Xiaozhou Liao **Copy Editor:** Fangling Lan **Production Editor:** Fangling Lan

Abstract

Potassium-ion batteries (PIBs) are considered as promising alternatives to lithium-ion batteries due to the abundant potassium resources in the Earth's crust. Establishing high-performance anode materials for PIBs is essential to the development of PIBs. Recently, significant research effort has been devoted to developing novel anode materials for PIBs. Alloy-based anode materials that undergo alloying reactions and feature combined conversion and alloying reactions are attractive candidates due to their high theoretical capacities. In this review, the current understanding of the mechanisms of alloy-based anode materials for PIBs is presented. The modification strategies and recent research progress of alloy-based anodes and their composites for potassium storage are summarized and discussed. The corresponding challenges and future perspectives of these materials are also proposed.

Keywords: Potassium-ion batteries, mechanism, alloy-based anode materials

INTRODUCTION

With the rapidly growing demand for energy globally, unrenewable traditional fossil fuels, such as coal, oil and gas, are facing depletion[1-9]. Clean and renewable energy resources, such as solar, wind and tidal energy, are among the most abundant and promising available resources to take the place of fossil fuels in the

© The Author(s) 2023. **Open Access** This article is licensed under a Creative Commons Attribution 4.0 International License (https://creativecommons.org/licenses/by/4.0/), which permits unrestricted use, sharing, adaptation, distribution and reproduction in any medium or format, for any purpose, even commercially, as long as you give appropriate credit to the original author(s) and the source, provide a link to the Creative Commons license, and indicate if changes were made.

future. It is necessary to combine electrical energy storage devices with these renewable energies. Rechargeable lithium-ion batteries (LIBs) are high-energy electrical energy storage devices that have been commercialized for around three decades. LIBs cannot only be used with natural clean renewable energies but are also ubiquitous in our daily lives for powering electronics, including cell phones, electric cars and laptops. However, their high-cost resources and the uneven distribution of lithium in the Earth's crust make it imperative to develop alternatives to LIBs with comparable performance[10-12].

Potassium-ion batteries (PIBs) are possible alternatives to LIBs. Compared to lithium resources in the Earth's crust, potassium resources are significantly more abundant in the Earth's crust at ~1.5 wt.%. The price of potassium salts, such as K_2CO_3, is far less compared to Li_2CO_3. In addition to the lower cost of potassium resources, inexpensive aluminum current collectors can be used together with PIBs to offer a low-cost method based on economical salts[13-15]. In addition, potassium ions exhibit much weaker Lewis acidity, which results in smaller solvated ions compared to lithium and sodium ions. Therefore, the ionic conductivity of solvated K^+ is higher than that of lithium and sodium ions[16,17]. In addition, the lower energy required to dissolve potassium ions also results in their fast diffusion kinetics.

Similar to LIBs and sodium-ion batteries (SIBs), the study of cathode materials for PIBs mainly includes layered transition metal oxides, Prussian blue analogs (PBAs) and polyanionic compounds. Layered transition metal oxides based on K_xMO_2 ($x \leq 1$, M = Co, Cr, Mn, Fe or Ni) deliver high capacity but face the critical problems of multiple plateaus and large structural changes during potassium-ion intercalation/deintercalation[18,19]. The chemical formula of PBAs is represented as $K_xM1[M2(CN)_6]_n\ H_2O$ ($0 \leq x \leq 2$), where M1 and M2 represent various metals, such as Fe, Cr, Co and Ni[20-23]. One advantage of PBAs is their three-dimensional (3D) open frameworks that are available for large K^+ to diffuse. Another advantage of PBAs in PIBs is their high average working potential of 3.5 V. Currently, the disadvantages of PBAs are their low conductivity and bulk density[24,25]. Polyanionic compounds also have 3D open channels that are available for the fast diffusion of large K ions[26,27]. The study of PIB cathode materials makes the development of full-cell PIBs possible and promising.

The search for anode materials is also an important part of PIB research and development. Commercialized graphite has been widely applied in LIBs; however, it is not an ideal anode candidate. Even though graphite has a theoretical capacity of ~280 mAh g^{-1} from the formation of KC_8[28,29], the large radius of the potassium ions results in sluggish diffusion kinetics and the formation of an unstable SEI. Therefore, graphite anodes deliver limited experimental capacity and cycling life in PIBs. As a result, it is crucial to develop high-performance anode materials with high specific capacity and long cycling life for practical application. In the past five years, there has been a large volume of research regarding electrode materials for PIBs, including metal-organic structure design[30,31] for electrodes and the modification of electrode surfaces[32,33]. However, there have been few review papers that focus on anode materials for PIBs, especially on high-performance alloy-based anode materials, including their modification and mechanisms in PIBs[34]. In this review, we comprehensively summarize the current understanding of alloy-based anode materials and their composites for PIBs, as shown in Figure 1, including their mechanisms, modification strategies and recent research progress for potassium storage. The challenges and future perspectives corresponding to these materials are also presented.

Alloy-based elements can deliver high-capacity anode materials via the formation of potassium-rich materials. For example, Bi has a high theoretical capacity of 385 mAh g^{-1} PIBs. Sb has a high theoretical capacity of 687 mAh g^{-1}. P has the highest theoretical capacity among alloy-based anodes in PIBs of 865 mAh g^{-1}. Ge has a high theoretical capacity of 369 mAh g^{-1} and Sn has a theoretical capacity of

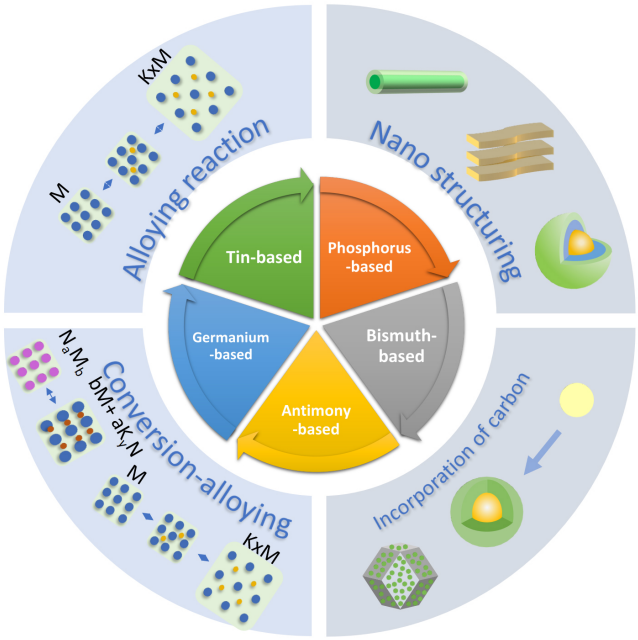

Figure 1. Alloy-based anode materials for PIBs.

226 mAh g^{-1} in PIBs. We calculated the theoretical volumetric and gravimetric capacities of P, Bi, Sb, Ge and Sn, as shown in Figure 2. The volumetric capacities are calculated based on the density of the materials and their theoretical weight capacities. Based on the calculation, the volumetric capacities of P, Bi, Sb, Ge and Sn are 1574, 2753, 4597, 1964 and 1652 mAh cm^{-3}. While the study of alloy-based anode materials in LIBs and SIBs has been extensive in recent years, the study of PIBs remains at the early stage. Therefore, high-capacity alloy-based anodes are worthy of further study.

Potassium storage mechanism of alloy-based anode materials for PIBs

Potassium storage in anode materials for PIBs can be classified into three categories: intercalation, alloying and conversion. The intercalation reaction results in a smaller volume change and higher reversible capacity than the other potassium storage mechanisms. During the interaction reaction, potassium ions are inserted into the anode material and form a new phase. This reaction usually takes place in materials with a layered structure, such as graphite[35,36] and $K_2Ti_4O_9$. The alloy-based anode material SnS_2 undergoes an intercalation reaction in the first step and conversion and alloying reactions in the following steps. The intercalation reaction can be expressed as $M_xN_y + aK^+ + ae^- \leftrightarrow K_aM_xN_y$. Typical intercalation reactions deliver high reversible capacity because of the low volume change of the crystal during the electrochemical reaction. Due to the large radius of the potassium ion, however, anode materials with an intercalation-type potassiation process experience a larger volume change and have less reversible capacity in their performance in LIBs and SIBs.

Compared to the intercalation reaction, alloying-reaction materials undergo a larger volume change and have higher theoretical capacities. Alloying-type materials react with K to form the binary compound K_xM. The reaction process can be expressed as $aM + bK^+ + be^- \leftrightarrow K_bM_a$. In this reaction, M represents Sn, Bi, Sb, P or Ge. These alloying-type materials can form binary metallic materials that undergo conversion-alloying reactions, in which the compound decomposes and further alloys with potassium. For example, Sn_4P_3 undergoes the following reaction: $Sn_4P_3 + 11K \leftrightarrow 4KSn + 3K_3P$[26]. Similarly, Sb_2Se_3 goes through the following conversion-alloying reaction: $Sb_2Se_3 + 12K^+ + 12e^- \leftrightarrow 3K_3Sb + 2K_2Se_3$[27].

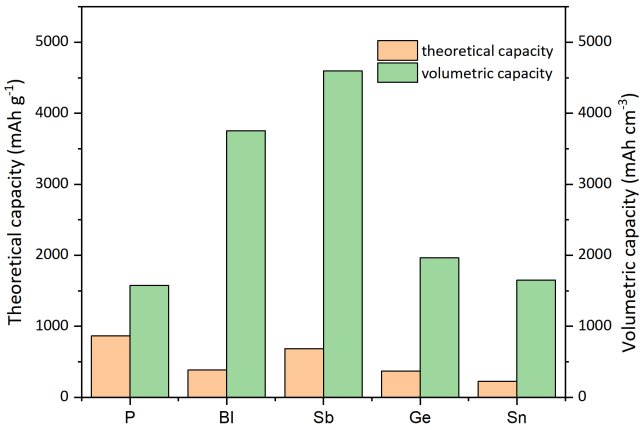

Figure 2. Theoretical and volumetric capacities of P, Bi, Sb, Ge and Sn.

These conversion-alloying type reactions can be expressed as $M_xN_y + (xn + ym)K^+ + (xn + ym)e^- \leftrightarrow xK_nM + yK_mN$. Similarly, the metallic compounds that go through conversion-alloying type reactions also deliver high theoretical capacities. For example, Sn_4P_3 delivers a high capacity of 585 mAh g^{-1} while the experimental capacity is ~384 mAh g^{-1}.

Challenges

Although alloying-type anode materials deliver high theoretical capacities, their practical reversible capacities are far below their theoretical capacities. The severe volume change causes capacity decay, poor cycle life, inferior rate performance, sluggish kinetics and limited cycling lifespans.

The initial capacity is a key factor, especially for the anode material, which contributes to the energy density of the full cell. The significant volume changes during the discharge-charge processes cause pulverization of the active materials, which results in discontinuous particles. Due to the large resistance within the particles, the potassium ions cannot be fully extracted, which results in irreversible capacity and low Coulombic efficiency. In addition, the stress generated in the electrode during the discharge process damages the SEI, resulting in its breakdown and the reformation of a new SEI film. In addition, the pulverized particles inevitably go through crystallization and aggregation, which increase the diffusion length of the potassium ions and also lead to irreversible capacity loss. The decreasing reversible capacity results in a rapid capacity drop and short cycling life.

ALLOY-BASED ANODES FOR PIBS

Phosphorus-based anode materials

Among alloying-typed anode materials, phosphorus is very attractive because it has a high theoretical capacity of 2596 mAh g^{-1} in LIBs and SIBs and a low work potential (~0.3 V vs Na/Na^+). In PIBs, it has a high theoretical capacity of 2590 mAh g^{-1} based on the three-electron alloying mechanism.

Mechanism of phosphorus and metal phosphides in PIBs

There are three main types of phosphorus in nature, namely, white phosphorus (WP), red phosphorus (RP) and black phosphorus (BP). WP is toxic and has a low ignition point, so it is unsuitable as an electrode. RP exists in a non-crystalline form and has a low conductivity of 10^{-12} S m^{-1}. BP is a layered structure semiconductor material, which has a wide interlayer spacing of 5.2 Å and a higher conductivity at 300 S m^{-1}. BP has a high theoretical capacity of 2600 mAh g^{-1} for LIBs and NIBs and also has a low diffusion barrier of 0.035 eV for Li^+ and 0.064 eV for Na^+, which makes it a promising anode material to explore for PIBs. There

are two interlayer migration paths: zigzag- and armchair-type migration paths. The zigzag path has a much lower energy barrier. Based on calculations, K has the lowest energy barriers for both paths compared to Li and Na, which endow PIBs with fast discharging and charging. The corresponding voltage can be calculated based on the following equation:

$$V = -\frac{\mu}{q} = -\frac{\Delta G}{e\Delta N} \quad (1)$$

where V, μ, q, G, e and N are the voltage, chemical potential, charge, absolute electron charge, Gibbs free energy and the number of K ions, respectively.

Thus, the calculated potassium-ion insertion process is BP → K_2P_3 → KP. A previous study of the potassiation mechanism indicated that the final product was KP[36-39], which was first revealed by the group of Glushenkov. Compared to this result, a further study by Jin *et al.* used X-ray absorption near-edge structure and *ex-situ* X-ray diffraction (XRD) methods to analyze the mechanism[38]. The results demonstrated that the potassiation process of BP was $K^+ + P + e^- \rightarrow KP$. An RP-based nanocomposite was studied by the group of Xu[39]. The composite was synthesized by anchoring RP nanoparticles on a 3D nanosheet framework. The reaction mechanism of the composite was explored by transmission electron microscopy (TEM) and selected area electron diffraction (SAED). Based on the first cycle reaction results, KP was proposed to be the final product, corresponding to a capacity of 865 mAh g^{-1}, which is lower than the theoretical capacity. Yu *et al.* synthesized an RP/carbon nanocomposite by embedding RP into free-standing nitrogen-doped porous hollow carbon[40]. Using *in-situ* Raman spectroscopy and *ex-situ* XRD, the final product in the discharge process was directly proved to be K_4P_3.

One challenge for BP and RP in the potassiation process compared to lithiation is the lower capacity. A BP-graphite composite had only 42% of the capacity for lithiation. The other issue is their large volume expansion. BP-graphite showed a 200% volume expansion when discharged to 0.01 V[41].

The large volume expansion during the potassiation process and low conductivity of RP severely limit the application of phosphorus-based anode materials in PIBs. To overcome this, active (Sn, Ge and Se) and inactive metals (Co, Fe and Cu) have been hybridized with P to form phosphides. During the discharge process, the decomposed nanocrystals form a conductive and elastic matrix to enable faster charge transfer and hinder volume expansion. In addition, the active metals become alloyed with potassium ions and also make contributions to the capacity. Metal phosphides can be classified into two categories based on active and inactive metals. For the inactive metals, the storage mechanism reaction can be summarized as follows:

$$M_xP_y + zK^+ + ze^- = xM + K_zP_y \quad (2)$$

For the active metal phosphides, the reaction can be summarized as follows:

$$M_xP_y + (xn + ym)K^+ + (xn + ym)e^- = xK_nM + yK_mP \quad (3)$$

The original phosphide M_xP_y decomposes and the phosphorus is converted into $K_{3-x}P$, while inactive metal M is dispersed as a matrix and active metal M is also alloyed with K to produce K_nM.

Unlike phosphides in LIBs and SIBs, to date, the reported phosphide potassiation mechanisms are conversion-type mechanisms. For example, the electrochemical reaction of Sn_4P_3 in PIBs is a typical conversion reaction, as first studied by the group of Guo based on an *in-operando* synchrotron XRD investigation. In the initial discharge stage, Sn_4P_3 breaks into Sn particles and the P component precipitates in an amorphous form to react with potassium. Sn is alloyed with K and the KSn phase is formed. K_3P_{11} further reacts with K, starting from ~0.17 V. The reaction process could be divided into three steps, namely, $Sn_4P_3 + (9\text{-}3x)K \leftrightarrow 4Sn + 3K_{3-x}P$, $23Sn + 4K \leftrightarrow K_4Sn_{23}$ and $K_4Sn_{23} + 19K \leftrightarrow 23KSn$, as shown in Figure 3A[42]. The Sn_4P_3@carbon fiber electrode delivered cycling stability and a high-rate capability of 160.7 mAh g^{-1} after 1000 cycles at a current density of 500 mA g^{-1}. Like Sn_4P_3, GeP_5 also has a similar conversion reaction. Based on *in-operando* synchrotron XRD measurements, a two-step reaction was observed as follows: $GeP_5 + 20/3K \leftrightarrow 5/3K_4P_3 + Ge$, $Ge + K \leftrightarrow KGe$. These two steps can be summarized into one equation as follows: $3GeP_5 + 23K \leftrightarrow 5K_4P_3 + 3KGe$[43]. This potassiation process is shown in Figure 3B. Similarly, in the first stage of the reaction, GeP_5 decomposes into Ge and P particles and the P component reacts with K to form K_4P_3. In the following stage of the reaction, Ge alloys with K to form KGe. Se is also an active element that can form K_2Se through a two-electron transfer reaction. Se_3P_4 exhibited a high reversible capacity of 1036 mAh g^{-1} in PIBs[44]. Based on *ex-situ* XRD and X-ray photoelectron spectroscopy (XPS) results, Se_3P_4 delivered a reversible conversion-type reaction as follows: $Se_3P_4 + (18\text{-}4x)K^+ + 18e^- \leftrightarrow 4K_{3-x}P + 3K_2Se$[44], as shown in Figure 3C and D. The inactive material, such as Cu_3P, undergoes the reaction of $2Cu_3P + (3\text{-}x)K^+ + (3\text{-}x)e^- \leftrightarrow K_{3-x}P + 6Cu + P(amorphous)$ and the final discharge product is also K_3P[45].

In summary, until now, the reported phosphide potassiation mechanisms have been conversion-type mechanisms, which are different from phosphides in SIBs and LIBs. In the first discharge step, the phosphide decomposes into metal and phosphorus. After the anode has been fully discharged, the active metal reacts with K and forms K_nM compounds, with the phosphorus alloyed with K to form K_mP.

Modification strategies for P and phosphides

Carbon materials, including nanosheets[39], nanofibers[40] and graphite[45], have been applied in phosphorus and phosphides. The hybridization of phosphorus and phosphides with carbon materials has been proven to be an efficient method to improve the electrochemical performance. The introduction of carbon can enhance the electron conductivity, accommodate the volume change and also shorten the potassium-ion diffusion length. Furthermore, the induced carbon can form covalent P-C interfaces to prevent edge reconstruction and ensure ion insertion and diffusion[35]. In addition, the formation of P-C bonds[46-49] by hybridizing BP with carbon materials can afford high capacity and cycling stability in PIBs by connecting particles. This can also be seen from the work of Verma *et al.*, where the electrochemical performance of SnP_3 was efficiently improved by hybridizing with carbon[50]. The electrode maintained a reversible capacity of 225 mAh g^{-1} after 80 cycles, which was an improvement compared to the previous rapid capacity drop of the SnP_3 electrode in cycling performance. Similarly, the group of Zhu[51] designed a flexible and hierarchically porous 3D graphene/FeP composite via a one-step thermal transformation strategy. The interconnected porous conducting network sufficiently buffered stress due to the nano-hollow spaces and greatly promoted the charge transfer. Thus, the composite delivered a high-capacity retention of 97.2% over 2000 cycles at a high rate of 2 A g^{-1} in PIBs.

Synthesizing nanostructured phosphorus and phosphide materials, such as yolk-shell structures[52], hollow structures and nanowires, is another efficient method to improve the electrochemical performance of phosphide and phosphorus anodes. For example, Yu *et al.* designed a one-dimensional electrode by embedding RP into free-standing nitrogen-doped porous carbon nanofibers[40]. This design was favorable for reducing the absolute strain and preventing pulverization and agglomeration. As can be seen from their

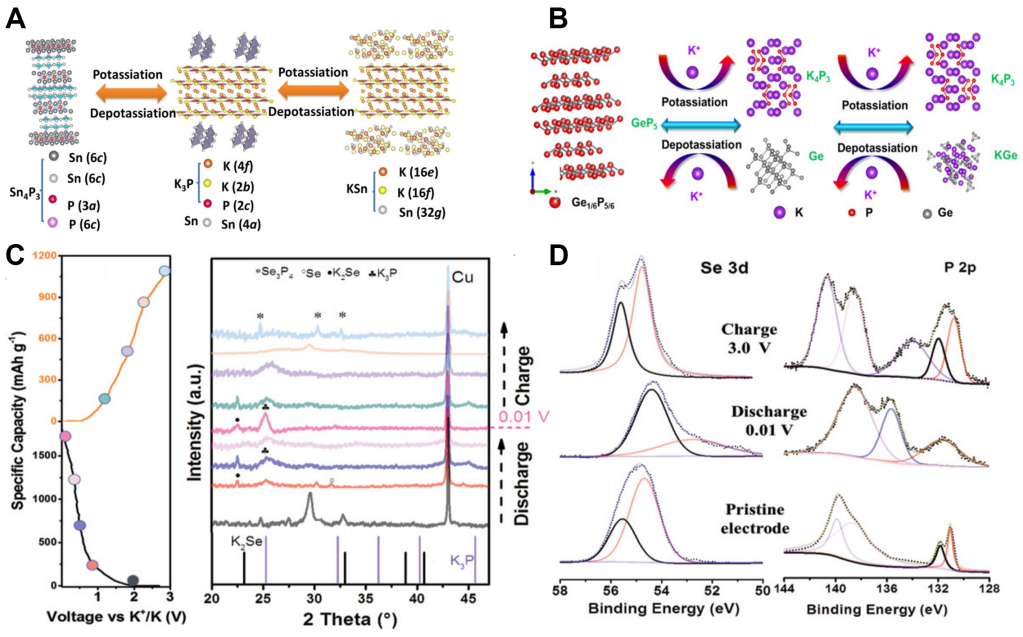

Figure 3. (A) Potassiation/depotassiation process in Sn_4P_3/C[42].Copyright 2017, American Chemical Society. (B) Potassiation/depotassiation process in GeP_5 electrodes[43].Copyright 2018, Elsevier. (C) Discharge/charge curves of Se_3P_4@C and XRD patterns of Se_3P_4@C anode in the first cycle at different cut-off voltages. (D) XPS spectra of Se_3P_4@C electrode at different cut-off voltage states[44].Copyright 2020, Wiley VCH.

images, during potassiation, the thickness changed from 74 to 93 nm with a volume expansion of only 26%. Because of its nanowire structure, the composite exhibited a high reversible capacity of 465 mAh g^{-1} after 800 cycles at a high current density of 2 A g^{-1}. The yolk-shell and hollow structures have void space that can accommodate the significant volume change, so that particles can expand without deforming the carbon shell during potassiation[52]. The potassium-ion transport in BP is mostly in the armchair direction, as shown in Figure 4A and B. The potassiation process includes several steps with the formation of binary phosphide, as displayed in Figure 4C. Figure 4D shows that the composite delivered stable cycling performance with a reversible capacity of 205 mAh g^{-1} after 300 cycles. A comparison of the electrochemical performance of phosphides and their composites is shown in Table 1.

The theoretical capacity of phosphorus in PIBs is 2596 mAh g^{-1} based on the three-electron alloying mechanism; however, the experimental capacity varies with different final products. There are currently three known types of final potassiation products of phosphides, namely, KP, K_4P_3 and K_3P. In addition, the final and intermediate products of phosphides in PIBs are different even though the reactions are typically conversion-alloying mechanisms. Due to the significant volume change during the potassiation processes of phosphorus and phosphides and the low conductivity of phosphorus, various modification methods have been applied. Synthesizing nanostructures, such as yolk-shell, nanowire and hollow structures, and hybridization with graphite, graphene, nanotubes and porous carbon have significantly improved the electrochemical performance.

Bi-based electrodes for PIBs

Bi is an attractive low-cost and non-toxic anode material. Due to its large interlayer spacing (d) along the c-axis, d (003) = 3.95 Å, Bi is a promising anode material for PIBs. The theoretical weight capacity of Bi is 385 mAh g^{-1}. Furthermore, Bi has a high theoretical volumetric capacity of 3800 mAh cm^{-3}, which also makes it a novel potential anode.

Table 1. Summary of electrochemical performance of P-based anodes for PIBs

	Anode materials	Synthesis method	Modification methods	Redox potential (*vs.* K/K^+)	Current density ($mA\ g^{-1}$)	Initial capacity (potassiation) ($mAh\ g^{-1}$)	Initial depotassiation	1st CE	Reversible capacity	Best rate capability	Electrolyte	Ref.
BP	BP/graphite	Vaporization-condensation	Hybridized with graphite	~0.5 V	250	1430	600	42%	340 $mAh\ g^{-1}$ after 100 cycles at current density of 0.75 $A\ g^{-1}$	340 $mAh\ g^{-1}$ at 750 $mA\ g^{-1}$	1 M KPF_6 in EC:DEC	[38]
RP	RP/carbon nanosheet	Heat treatment	Hybridized with carbon nanosheets/design of 2D nanostructure	0.16-1.0 V	100	1212	715	59%	427.4 $mAh\ g^{-1}$ after 40 cycles at current density of 100 $mA\ g^{-1}$	323.7 $mAh\ g^{-1}$ at 2000 $mA\ g^{-1}$	0.8 M KPF_6 in EC:DEC	[39]
	Yolk-shell FeP/C		Hybridized with carbon/design of 3D nanostructure	0.05-1.2 V	100	561	264	47%	205 $mAh\ g^{-1}$ after 300 cycles	37 $mAh\ g^{-1}$ at 2000 $mA\ g^{-1}$	0.8 M KPF_6 in EC:DEC	[52]
Phosphide (inactive metal)	CuP_2/Carbon nanosphere	Wet chemical and heat treatment	Hybridized with carbon/design of 2D nanostructure		100	~700	~490	~70%	400 $mAh\ g^{-1}$ over 300 cycles	170 $mAh\ g^{-1}$ at 2 $A\ g^{-1}$	4 M KFSI in DME	[53]
	CoP/C	Heat treatment	Hybridized with carbon	0.01-1.26 V	50	706	301	42.7%	40 $mAh\ g^{-1}$ at 1000 $mA\ g^{-1}$ after 400 cycles	106 $mAh\ g^{-1}$ at 1000 $mA\ g^{-1}$	1 M KPF_6 EC:PC	[54]
Phosphide (active metal)	SnP_3/C	Mechanical milling	Hybridized with carbon	0.01-0.8 V	50	697	410	58.8%	408 $mAh\ g^{-1}$ after 50 cycles	225 $mAh\ g^{-1}$ at 500 $mA\ g^{-1}$	0.75 M KPF_6 EC:DEC	[50]
	Se_3P_4/C	Mechanical milling and heat treatment	Hybridized with carbon	1.3-1.9 V 0.37 V	50	1505	1036	68.9%	783.4 $mAh\ g^{-1}$ after 100 cycles at 100 $mA\ g^{-1}$	388 $mAh\ g^{-1}$ at 1000 $mA\ g^{-1}$	0.8 M KPF_6 EC:DEC:FEC	[44]
	Sn_4P_3/C	Mechanical milling	Hybridized with carbon	0.01-1.15 V	50	588.7	384.8	65%	307.2 $mAh\ g^{-1}$ at 50 $mA\ g^{-1}$ after 50 cycles	221.9 $mAh\ g^{-1}$ at 1000 $mA\ g^{-1}$	1 M KPF_6 EC:DEC	[51]
	Sn_4P_3/carbon fiber	Mechanical milling and electrospinning	Hybridized with carbon/design of nanostructure	0.01-0.5 V	50	803	514	64%	403 $mA\ g^{-1}$ at 50 $mA\ g^{-1}$ after 200 cycles	160.7 $mA\ g^{-1}$ after 1000 cycles at 500 $mA\ g^{-1}$	1 M KFSI EC:DEC	[55]
	Sn_4P_3/C	Wet chemical and heat treatment	Hybridized with porous carbon/design of nanostructure	0.01-0.4 V 1.1-1.6 V	100	845	431	51%	315 $mA\ g^{-1}$ at 1000 $mA\ g^{-1}$ after 100 cycles	186 $mAh\ g^{-1}$ at 2000 $mA\ g^{-1}$	0.8 M KPF_6 EC:DEC	[56]
	GeP_5	Mechanical milling	Nanostructural design	0.10-0.45 V	50	2038	934	45.81%	495.1 $mA\ g^{-1}$ at 50 $mA\ g^{-1}$ after 50 cycles	213 $mA\ g^{-1}$ at 500 $mA\ g^{-1}$ after 2000 cycles	1 M KFSI EC:DEC	[43]

CE: Coulombic efficiency.

K-ion storage mechanism of Bi-based anodes

Based on the K-Bi equilibrium diagram with the KBi_2, K_3Bi_2, $K_3Bi(\alpha)$, $K_3Bi(\beta)$ and K_5Bi_4 phases, Huang *et al.* first studied the potassium-ion storage mechanism in Bi microparticles[57]. They revealed stepwise Bi → KBi_2 → K_3Bi_2 → K_3Bi dealloying-alloying electrochemical processes after the initial surface potassiation. Similarly, a bulk Bi anode delivered a reversible three-step reaction during cycling, with K_3Bi as the fully discharged product[58]. Bi microparticles have the same mechanism as shown in Figure 5A and B, with K_3Bi as the final discharged product. As shown in Figure 5C, the observation of K_5Bi_4 during the potassiation process was first reported by the group of Guo[59]. They found a different transition process, in which the potassiation of Bi nanoparticles proceeds through a solid-solution reaction, followed by a two-step reaction, corresponding to Bi → Bi(K) and Bi(K) → K_5Bi_4 → K_3Bi. Xie *et al.* constructed dual-shell-structured Bi box particles and microsized Bi, which had different appearances during the transformation from K_3Bi_2 to K_3Bi under a low current density[60]. In the case of nanostructured Bi, the K_3Bi_2 phase went through a transformation to K_3Bi, as shown in Figure 5D. In comparison, the microstructure of Bi retained the K_3Bi_2 phase and no significant K_3Bi phase was formed. Interestingly, when the current was increased, no significant K_3Bi_2 or K_3Bi phase was observed, indicating that the main mechanism was a surface-driven adsorption reaction under a high current.

The study of the potassiation mechanism in Bi-based alloys has also attracted significant attention. The reaction process includes two stages. The first step was an intercalation reaction: $Bi_2S_3 + xK^+ + xe^- \rightarrow K_xBi_2S_3$. The second step was a conversing-alloying reaction: $K_xBi_2S_3 + (6\text{-}x)K^+ + (6\text{-}x)xe^- \rightarrow 3K_2S + 2Bi$ and $Bi + 3K^+ + 3e^- \rightarrow K_3Bi$[61]. Chen *et al.* also studied the reaction mechanism of Bi_2Se_3 using *in-situ* operando XRD[62]. The results indicated that the potassiation process also undergoes an intercalation reaction in the first steps, with a conversion-alloying reaction in the following step. The electrochemical process was summarized as follows: $2Bi_2Se_3 + 4xK^+ + 4xe^- \rightarrow 4K_xBiSe_3$, $K_xBiSe_3 + (6\text{-}x)K^+ + (6\text{-}x)e^- \rightarrow 3K_2Se + Bi$ and $i + 3K^+ + 3e^- \rightarrow K_3Bi$[62].

The above results illustrate the diverse potassiation mechanisms. The differences in the potassiation and depotassiation processes were mainly because of the following reasons: (1) the mechanisms are strongly dependent on the sizes of the materials; (2) the unique structure of the Bi-based anodes; and (3) the current density of the electrochemical reaction. The small particle sizes, well-constructed nanostructure and low current density resulted in full potassiation and transformation that involved several transition phases.

Modification strategies for Bi-based anodes

The main challenge for Bi-based anode materials is the pulverization and fracturing of the electrode during the cycling process that are driven by the significant volume changes, resulting in capacity fading.

To improve the electrochemical performance of Bi, various methods have been applied. One method is to combine Bi with carbon materials. Various porous carbon materials have been applied, such as porous graphene[63] and carbon nanosheets[64]. Both of these porous carbons were synthesized using freeze drying assisted by a pyrolysis method. The Bi/macroporous graphene composite delivered an excellent rate performance of 185 mAh g^{-1} at a high current density of 10 A g^{-1}. This was because the 3D interconnected macroporous graphene framework could provide robustness to maintain the structural stability.

N-doped carbons were demonstrated to simultaneously improve the conductivity and electrochemical activity of carbon materials and were applied in combination with Bi[63,64], as shown in Figure 6A-F. Similarly, Shi *et al.* designed a multicore-shell Bi-N nanocomposite using a facile self-template method. The anode delivered a stable performance of 266 mAh g^{-1} after 1000 cycles at 20 A g^{-1}, as shown in Figure 6G-I[65]. Li *et al.* used hollow N-doped carbon to coat bismuth nanorods, which showed the best long-cycling

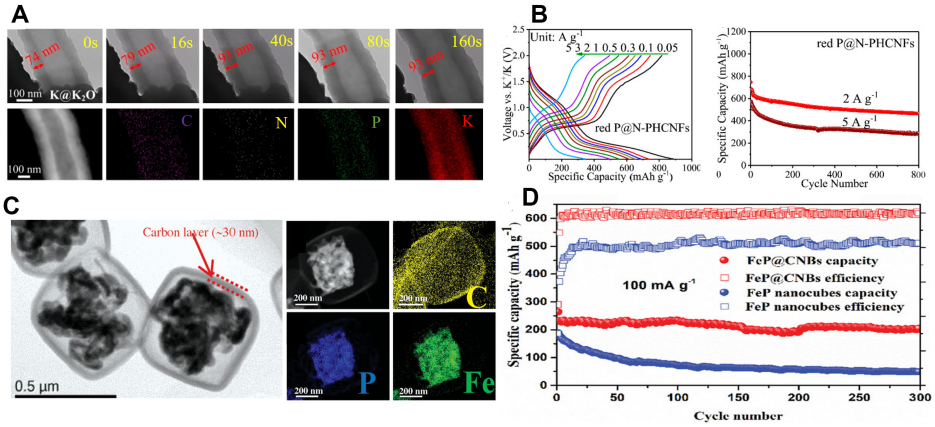

Figure 4. (A) Time-lapse TEM images for single RP@N-PHCNFs, where PHCNFs are porous hollow nanofibers, during potassiation process. (B) Charge/discharge profiles of RP@N-PHCNF electrode at various current densities and cycling performance of RP@N-PHCNF anodes[40]. Copyright 2019, American Chemical Society. (C) Bright-field TEM images and elemental mapping analysis of FeP@CNBs, where CNBs are carbon nanoboxes. (D) Cycling performance of FeP@CNBs and FeP nanocubes at 0.1 A g^{-1} [52]. Copyright 2019, Wiley VCH.

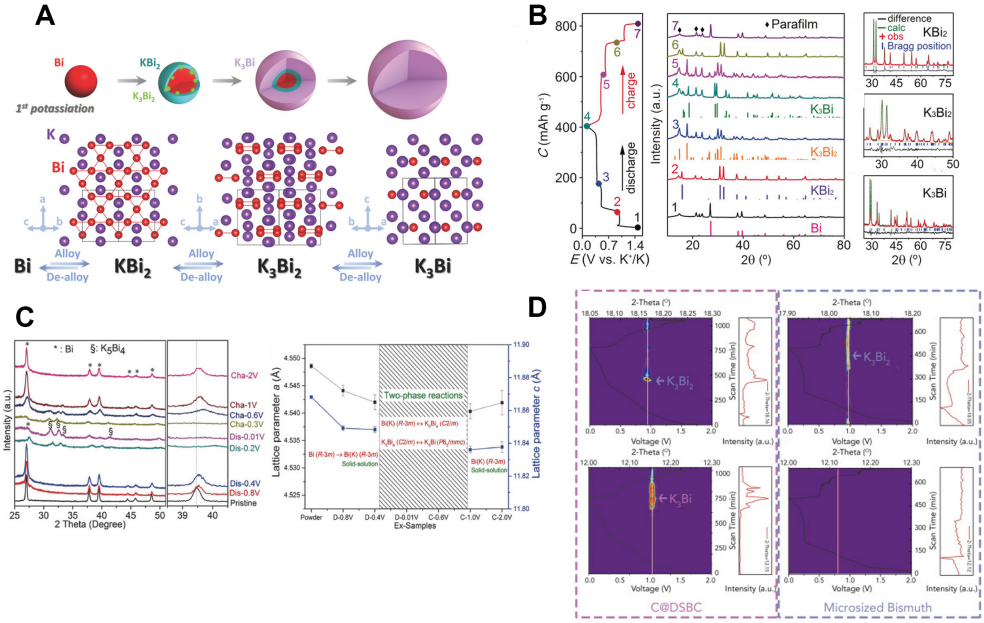

Figure 5. Different potassiation and depotassiation mechanisms of Bi. (A) Alloying and dealloying processes in microparticle Bi electrode[57]. Copyright 2018, Wiley-VCH. (B) Discharge/charge curves for XRD patterns and XRD patterns with Rietveld refinement of intermediates of porous Bi electrode[58]. Copyright 2018, Wiley-VCH. (C) *Ex-situ* XRD patterns collected at different charge/discharge states with refined lattice parameters and proposed potassiation/depotassiation mechanism of Bi@reduced graphene oxide (rGO) electrode[59]. Copyright 2018, Wiley-VCH. (D) *Operando* XRD pattern with superimposed voltage profiles of C@DSBC and microsized Bi[60]. Copyright 2019, Elsevier.

performance among the Bi/C composite anodes and had a high capacity of 297 mAh g^{-1} over 1000 cycles at 20 C[66].

Another important method to improve the electrochemical performance of Bi is nanoengineering. In addition to the multicore-shell structures mentioned above, which are typical designs for Bi-based anodes, Xie *et al.* designed a dual-shell bismuth box (DSBC) anode[60], which delivered a high-rate capacity of

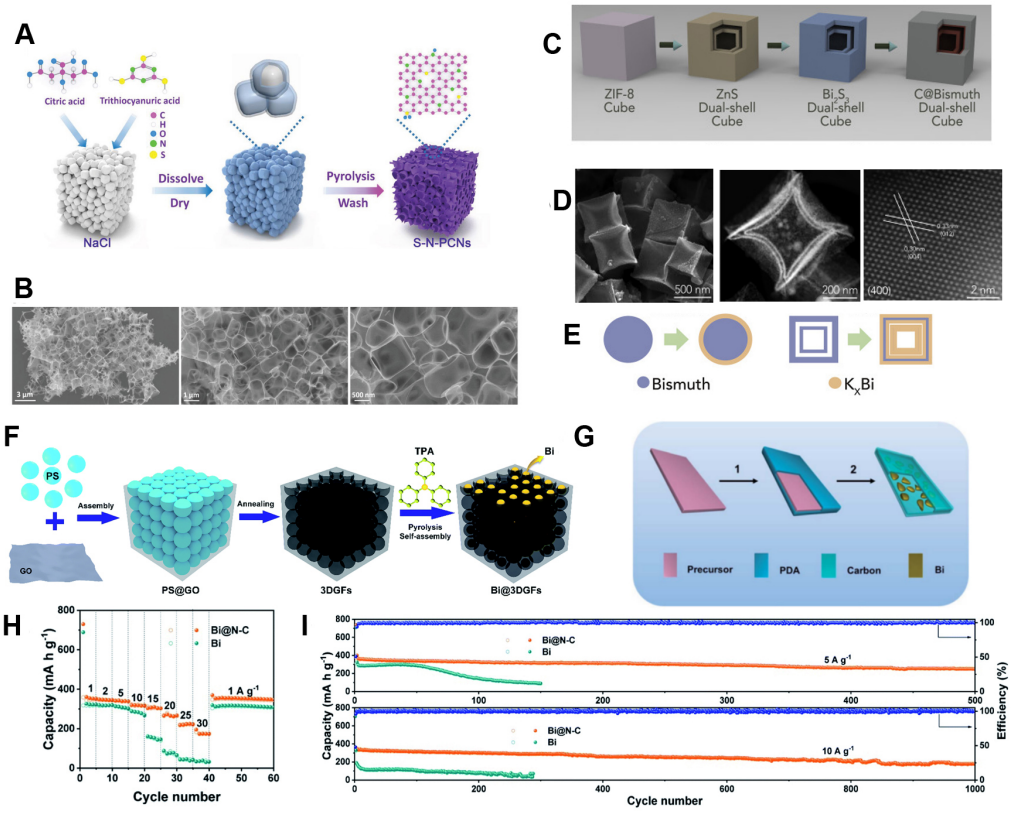

Figure 6. (A) Schematic illustration and (B) TEM images of Bi@porous carbon composite[64]. Copyright 2019, Wiley-VCH. (C) Schematic illustration of synthetic procedure and (D) TEM images of C@DSBC. (E) Schematic illustration of superior electrochemical performance of C@DSBC under high current density[60]. Copyright 2019, Elsevier. (F) Schematic illustration of synthesis procedure for Bi@3D graphene foams (GFs)[63]. Copyright 2019, Royal Society of Chemistry. (G) Schematic illustration of synthesis of Bi@N-C composite. (H) Rate performance of Bi@N-C and Bi anodes from 1 to 30 A g^{-1} and (I) long-term cycling stability of Bi@N-C and Bi anodes at high rates of 5 and 10 A g^{-1}[65]. Copyright 2020, Royal Society of Chemistry.

222 mAh g^{-1} at a current density of 0.8 A g^{-1}. The as-prepared anode had a potassium storage potential of ~0.7 V. The anode material had a large surface area, which could offer more sites for electrochemical reactions, resulting in a lower average oxidation stage and indicating a higher energy density. Designing two-dimensional (2D)-layered structures is another efficient nanoengineering method. The layered structure and weak van der Waals forces of Bi offer the possibility of exfoliating Bi into 2D-layered structures. Recently, bismuthene was prepared using an ultrasonication-assisted electrochemical exfoliation method[67-69]. The as-prepared anode delivered highly stable capacities of 423, 356, 275 and 227 mAh g^{-1} at current densities of 2.5, 5, 10 and 15 A g^{-1}, respectively. It delivered a stable cycling performance with a capacity of over 200 mA h g^{-1} at 20 A g^{-1} after 2500 cycles.

As reported, K^+ ions have lower Lewis acidity than Li^+ and Na^+ ions, indicating a lower ability to accept electrons from anions and solvents. Thus, potassium salts have a lower degree of dissociation. The salt solubility is based on the Born-Haber cycle:

$$\Delta G^0_{dissolution} = \Delta G^0_{solvation} - \Delta G^0_{lattice} \quad (4)$$

where $\Delta G^0_{dissolution}$ represents the Gibbs free energy of dissolution and $\Delta G^0_{lattice}$ and $\Delta G^0_{solvation}$ represent the Gibbs energies of the salt lattice and the solvation of salts, respectively[70].

To date, the reported potassium salts used in Bi-based anodes are KPF_6 and potassium bis(fluorosulfonyl)imide (KFSI). KPF_6 has a high calculated Kapustinskii lattice energy of 564.9 kJ mol^{-1}, while KFSI has a lower lattice energy[70], indicating that KFSI has higher solubility compared to KFP_6. KFSI also has higher ionic conductivity than KPF_6 and KFSI-based electrolytes can form more stable SEI layers. This is because the FSI^- anion has weak S-F bonds that make it easier to form KF, which is a main component in the SEI layer[71].

Zhang *et al.* first used KFSI as the electrolyte salt in Bi-based anode materials with ethylene carbonate (EC) and diethyl carbonate (DEC) as solvents[59]. The results indicated that the KFSI-based electrolyte had better cycling performance compared to the KPF_6-based electrolyte. The morphological and mechanical properties of the KFSI and KPF_6 electrolytes were investigated using atomic force microscopy, Kelvin probe microscopy and TEM. The results demonstrated that the KPF_6-based electrolyte formed a thicker and more heterogeneous SEI layer, while the SEI layer in the KFSI-based electrolyte was more uniform.

Ether solvents are the most used solvents for Bi-based anode materials. As discussed above, the highest occupied molecular orbital (HOMO) and lowest unoccupied molecular orbital (LUMO) energy levels of solvents or anions are lower when solvents or anions modify a cation through coordination. This is because an electron pair is donated to the cation. Thus, an anode with chemical potential $\mu > E_{lumo}$ can spontaneously transfer electrons to the LUMO of the electrolyte and trigger reduction. In ether solvents, the HOMO values of the ion-solvent complexes are of the order of $Li^+ > Na^+ > K^+$, while the LUMO values follow the order of $Na^+ > K^+ > Li^+$[13]. Therefore, the reduction and oxidation products in ether-based PIBs are complicated. Huang *et al.* first used dimethoxyethane (DME) as their ether-based solvent in Bi-based PIBs[57]. Using XPS and *in-situ* Raman spectroscopy to probe the SEI components, it was revealed that C-C(H), C-O, C=O and K-O bonds were formed and the SEI consisted of organic and inorganic compounds, such as $(CH_2CH_2\text{-}O\text{-})_nK$, $(CH_2CH_2\text{-}OCH_2\text{-}O\text{-})_nK$, (RCO_2K) and K_2O_x. In addition, the oligomers were from the reduction of DME. This ether-derived SEI possessed better mechanical flexibility because of the strong binding in alkoxy (O-K) edge groups and the elastic properties of the as-formed SEI. This SEI could effectively restrain the volume change of the particles. Density functional theory (DFT) calculations were performed to analyze the interaction between Bi and DME. Three adsorption models of a DME molecule on the (012) crystal plane of Bi were applied. Based on the models, the adsorption energies were 1.76, 0.65 and 0.60 eV. These adsorption energies were higher than for ester-based propylene carbonate (PC) molecules on Bi, which favored the formation of a 3D porous structure in potassiation and depotassiation[58].

Generally, electrolytes for Bi-based PIBs contain 1 M K salts. Based on recent reports, ~70% of the electrolytes applied in Bi-based PIBs are 1 M K dissolved in DME. Increasing the salt content results in enhanced interactions between cations and anions. Increasing the salt concentration also decreases the content of free-state solvent molecules. When the concentration is increased (>3 M), however, the free molecules decrease, leading to a change in the solution structure, which usually gives rise to extraordinary electrochemical properties and shifts the location of the LUMO from the solvent molecules to the salt. Thus, the reductive decomposition of salts takes place before the decomposition of the solvent, which results in the formation of a stable SEI[69,72]. Zhang *et al.* first used a concentrated electrolyte in Bi-based PIBs[73]. The Bi@C anode delivered the highest capacity of 202 mAh g^{-1} in a 5 M KFSI-diethylene glycol dimethyl ether electrolyte, which was higher than those in 1 M (163 mAh g^{-1}), 3 M (153 mAh g^{-1}) and 7 M (93 mAh g^{-1}) electrolytes. Based on this study, the differences in the electrochemical performance were due to the

different reduction resistances. The decreased reduction resistance in the 5 M electrolyte depressed the irreversible electrochemical reaction and formed less SEI compared to the less concentrated electrolytes[73]. A comparison of the electrochemical performance of Bi-based anode materials in PIBs is shown in Table 2.

Based on the current study of Bi-based PIBs, KFSI-based electrolytes have better electrochemical performance compared to KPF_6-based electrolytes because of the higher ionic conductivity and the formation of a more stable and uniform SEI. Some ether-based electrolytes have extraordinary performance in half cells because their ether-derived SEI possesses better mechanical flexibility. The concentrated electrolyte can improve the electrochemical performance to a certain extent due to the lower resistance of the electrolyte.

Sb-based electrodes for PIBs

Antimony is a layered structure hexagonal element with a high electrical conductivity of 2.5×10^6 S·m^{-1}. Studies of Sb as anode applied in batteries can be traced back to the 1970s[77] when Weppner first studied its kinetic parameters and thermodynamic properties in mixing conducting electrodes to be applied in a Li_3Sb system. Theoretically, one mole of Sb can alloy with three moles of lithium, sodium or potassium. The first study of Sb in PIBs was in 2015[78]. Sb is a promising anode material with a high theoretical capacity of 687 mAh g^{-1} in PIBs, which makes it a novel potential anode material.

K-ion storage mechanism of Sb

Based on the Sb-K phase diagram, there are four K-Sb binary phases going through K_3Sb, K_5Sb_4, KSb and KSb_2 with decreasing K content[79]. The corresponding equilibrium potentials of KSb_2, KSb, K_5Sb_4 and K_3Sb are 0.890, 0.849, 0.439 and 0.398 V, respectively, based on DFT computations[74], which are shown in Figure 7A-C. *In-situ* XRD experiments and cyclic voltammetry (CV) were carried out to analyze the phase changes[80]. In the discharge process, the first step was the transformation of hexagonal Sb to amorphous Sb. As reported, the peak at 28.6° corresponding to the (012) phase of Sb gradually became weaker[81], as shown in Figure 7D. In the amorphous region, KSb_2 and KSb phases can form at the potential of 0.78 V and at the potential of 0.23 V, K_5Sb_4 phase can form based on the CV results. When fully discharged to ~0.2 V, the cubic K_3Sb phase with *Fm3m* symmetry forms as the final potassiation product. Upon charging, the K_3Sb phase gradually decreases by the formation of the intermediate phase K_xSb. When further charging, the Sb phase forms with the decomposition of intermediate K_xSb. In addition, the cubic K_3Sb phase can be observed in the second cycle, while no crystalline Sb can be observed[82].

One interesting observation is the formation of the cubic K_3Sb phase as the fully discharged product. There are two polymorphs of K_3Sb, hexagonal K_3Sb (h-K_3Sb) and cubic K_3Sb (c-K_3Sb). Based on the DFT calculations, h-K_3Sb is more stable than c-K_3Sb, as shown in Figure 7E[83]. If we consider the crystalline energy and the reaction activation energy, however, the results are different. The following equation represents the activation barrier $\Delta E^*(x)$:

$$\Delta E^*(x) = 16\pi\gamma^3/3(\Delta E_g(x)/p(x)V_0)^2. \quad (5)$$

where γ represents the surface energy, ΔE_g represents the energy gain on passing from the crystalline to amorphous phase and V_o is the molar volume of the crystalline phase, as shown in Figure 7E and F. Even the molar energy gain of h-K_3Sb is higher than that of c-K_3Sb by ~0.12 eV and h-K_3Sb also has a higher surface energy and lower density. As a result, h-K_3Sb has a higher activation barrier, which results in the final formation of c-K_3Sb instead of h-K_3Sb[83]. Thus, based on current reports, the reaction can be concluded as $Sb_{crystal} \rightarrow Sb_{amorphous}$, $Sb_{amorphous} + xK^+ + xe^- \leftrightarrow K_xSb_{amorphous}$ and $K_xSb_{amorphous} + (3\text{-}x)K^+ + (3\text{-}x)e^- \leftrightarrow c\text{-}K_3Sb_{crystalline}$.

Table 2. Summary of electrochemical performance of Bi-based anodes for PIBs

	Anode materials	Modification methods	Synthesis method	Redox potential (*vs.*K/K$^+$)	Current Density (mA g^{-1})	Initial capacity (potassiation) (mAh g^{-1})	Initial depotassiation (mAh g^{-1})	1st CE	Cycling performance	Best rate capability	Electrolyte	Ref.
Bi/rGO	Bi/rGO	Hybridized with graphene	Simple room-temperature solution synthesis method	1.29 V 0.72-0.23 V	50	700	441	63%	Reversible capacity of 290 mAh g^{-1} after 50 cycles at current density of 50 mA g^{-1}	290 mAh g^{-1} after 50 cycles at current density of 50 mA g^{-1}	1 M KFSI in EC/DEC (1:1, v/v)	[59]
	Porous Bi	Nanostructural design	Commercial	0.93-0.30 V	2C	371.4	322	87.2%	After 300 cycles, the capacity remained at 282 mAh g^{-1}	At 3C, the capacity is still high at up to 321.9 mAh g^{-1}	1 M KPF_6 in DME.	[58]
	Bi@3DGFs	Hybridized with 3D porous graphene/design of 2D nanostructure	Solid-state reaction	0.4-0.5 V 0.6-0.7 V	100	671	241	36%	185.2 mAh g^{-1} at 10 A g^{-1} after 2000 cycles	Rate capability of 180 mAh g^{-1} at 50 A g^{-1}	1 M KPF_6 in DME	[63]
	Bi-doped porous carbon	Hybridized with porous carbon/design of nanostructure	Wet chemistry/thermal treatment	/	200	656	382	58.2%		High capacity of 107 mAh g^{-1} at 20 A g^{-1}	0.8 M KPF_6 in EC/DEC	[64]
	Bi nanorod/ carbon	Hybridized with carbon	Wet chemistry/thermal treatment	0.2-0.5 V	1000	723	470	65%	91% capacity retention at 5 A g^{-1} after 1000 cycles	289 mA h g^{-1} at current density of 6 A g^{-1}	1 M KPF_6 in DME	[74]
	Bi nanorod/ N-doped carbon	Hybridized with carbon/design of nanostructure	Thermal method	0.3-0.5 V	385	450	316	70%	266 mA h g^{-1} over 1000 cycles at 10C	297 mA h g^{-1} at 20C	1 M KPF_6 in DME	[66]
	Bi@N-doped carbon nanosheets	Hybridized with N-doped carbon/design of nanostructure	Wet chemistry/thermal treatment	0.3-0.5 V	1000	721	346	48%	180 mAh g^{-1} at 30 A g^{-1} after 1000 cycles	175 mAh g^{-1} at 30 A g^{-1}	1 M KPF_6 in DME	[65]
	Bi@N-doped carbon	Hybridized with N-doped carbon/design of nanostructure	Evaporation method	0.25-0.81 V	50	624	373	59.7%	179.1 mAh g^{-1} at 50 mA g^{-1} after 300 cycles	162 mA h g^{-1} at 1.5 A g^{-1}	1 M KFSI in DME	[75]
	Multicore-shell Bi@N-C	Hybridized with Carbon/design of nanostructure	Solvothermal method/ Thermal treatment	0.77-0.32 V	1000	972	355	36.5%	235 mAh g^{-1} after 2000 cycles at 10 A g^{-1}	152 mAh g^{-1} at 100 A g^{-1}	1 M KPF_6 in DME	[76]

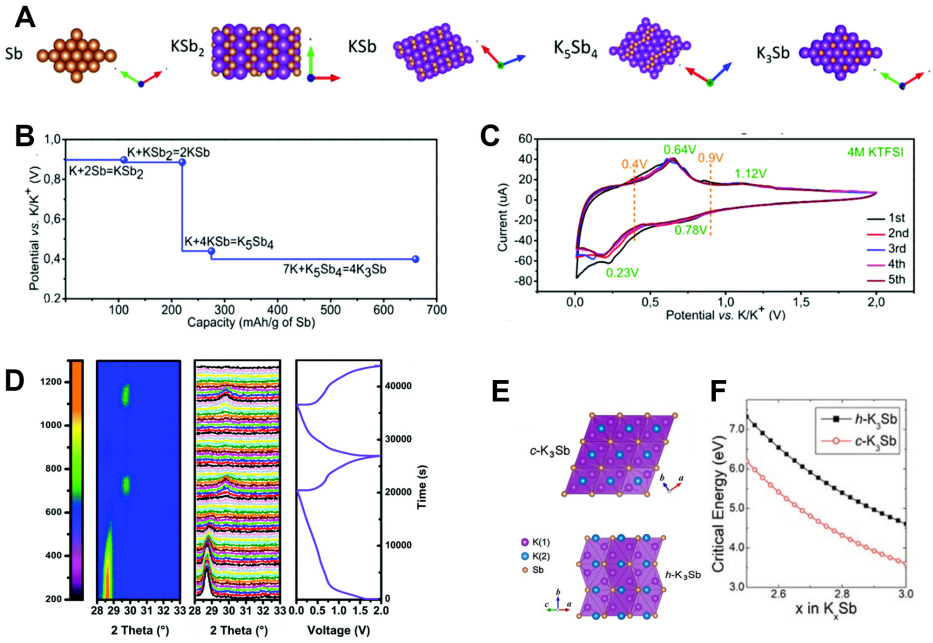

Figure 7. (A) Crystal structures of Sb and K-Sb binary phases. (B) DFT-calculated equilibrium voltages (*vs.* K/K^+) for potassiation process. (C) CV curves of Sb-based electrode at a scan rate of 0.05 mV s^{-1} [80]. Copyright 2019, Royal Society of Chemistry. (D) *In-situ* XRD patterns of 3D Sb nanoparticle (NP)@C electrode during a potassiation/depotassiation/potassiation process at 100 mA g^{-1} and the corresponding discharge/charge curves[81]. Copyright 2018, Royal Society of Chemistry. (E) Crystal structures of c-K_3Sb and h-K_3Sb. (F) Critical energies for nucleation of K_3Sb phase[83]. Copyright 2019, American Chemistry Society.

The study of the potassiation mechanisms of Sb-based alloy compounds has also attracted significant attention. Liu *et al.* were the first to report the potassiation/depotassiation process of Sb_2S_3 [84]. The process includes three steps. The first step is an intercalation reaction: $Sb_3S_3 + xK^+ + xe^- \rightarrow K_xSb_2S_3$. The following two steps are the conversion-alloying reaction of $Sb_2S_3 + xK^+ + xe^- \leftrightarrow yK_3Sb + zK_2S_3$. Their results showed no interaction process but only an alloying-conversion process with extra electron transfer. Sb_2Se_3-based microtubes were prepared and analyzed by Yi *et al.*[85]. Based on their study, the potassium insertion reaction in the composite delivered a conversion-alloying reaction. The reaction process can be concluded to be $Sb_2Se_3 + 12K^+ + 12e^- \leftrightarrow 3K_3Sb + 2K_2Se_3$. The Sb_2Se_3 compound first reacted with potassium to form the K_2Se and Sb phases, which were further alloyed with potassium. In the reduction process, K_2Se can be observed as an intermediate phase, which is reconverted to form Sb_2Se_3. The whole process is reversible.

As discussed above, Sb will alloy with K to form the K_3Sb phase as the final alloying product, while Sb-based compounds will first undergo a conversion reaction with a subsequent alloying reaction.

Modification strategies for Sb-based anode materials

As discussed above, Sb will form K_3Sb as the final product. Sb has a high theoretical capacity of 660 mAh g^{-1}. It also has a safe operation voltage and high conductivity, which makes it a promising anode material for PIBs. Sb suffers, however, from large volume changes during the K^+ insertion and extraction processes. To relieve the large volume changes of Sb and improve its electrochemical performance, various methods have been applied, such as the utilization of nanostructures and combination with carbon materials[86-90].

Nanostructural engineering combined with carbon materials has been a widely practiced method to improve the electrochemical performance of Sb. Huang *et al.* designed a hybrid structure with Sb nanoparticles as yolk confined in a carbon box shell, which was prepared using metal-organic frameworks

as precursors[86]. As observed by *in-situ* TEM, this hybrid material, which consists of carbon fibers with yolk-shell Sb@C, has structural advantages in the potassiation and depotassiation processes, as shown in Figure 8A-D. The inner Sb nanoparticles suffer from significant volume expansion during the potassiation process, while the void space effectively relieves the volume changes and the carbon fiber shell maintains the integrity of the structure and improves the conductivity. As a result, it delivered a capacity of 227 mAh g^{-1} after 1000 cycles and had a high Coulombic efficiency of ~100%. Liu *et al.* designed and constructed Sb nanoparticles confined by carbon, which exhibited long cycling stability over 800 cycles with a capacity retention as high as 72.3%[87], as shown in Figure 8E.

A variety of porous structures have been applied to hinder the volume change during cycling[88-91]. A microsized nanoporous antimony potassium anode was designed with tunable porosity[88]. The nanoporous structure can accommodate volume expansion and accelerate ion transport. Similarly, Zhao also encapsulated Sb nanoparticles within a porous architecture[89]. The composite delivered a high capacity of 392.2 mAh g^{-1} at 0.1 A g^{-1} after 450 cycles. Carbon nanofibers have also been applied as nanochannels to solve the issues of poor potassium-ion diffusion and significant volume variation. The Sb@CNFs delivered a reversible capacity of 225 mAh g^{-1} after 2000 cycles[90]. Cheng *et al.* utilized a single-crystal nanowire structure to improve the electrochemical performance of a Sb_2S_3 anode material[91]. After full potassiation, no obviously pulverization was observed, although the diameter of the as-prepared Sb_2S_3@C nanowires increased from 83 to 120 nm with a 45% expansion. The overall expansion of Sb_2S_3@C is ~111%, which is lower than the Sn-K alloying reaction (≈ 197%), indicating that the nanowire structure can effectively hinder the volume change during the potassiation/depotassiation process. Similarly, Jiao and Yu[92,93] also utilized a one-dimensional structure. A 2D structure was also applied to improve the electrochemical performance of Sb-based anode materials. Wang *et al.* designed a Sb_2S_3 nanoflower/MXene composite that exhibited a high reversible capacity of 461 mAh g^{-1} at a current density of 100 mA g^{-1}[94]. Its structural stability was enhanced by the strong interfacial connection between Sb_2S_3 and the matrix. A 3D structure was also applied in Sb-based anode materials. A core-shell Sb@Sb_2O_3 heterostructure was fabricated, which delivered an excellent capacity of 239 mAh g^{-1} at 5 A g^{-1} in PIBs[95]. These methods efficiently improved the electrochemical performance of Sb-based anode materials.

Another important method is improving the binder for the electrodes. He *et al.* used a polyvinylidene fluoride (PVDF) binder, which has a high capacity of 226 mAh g^{-1} over 400 cycles[96]. Compared to PVDF, sodium carboxymethyl cellulose (CMC) can improve the initial columbic efficiency due to the pre-formed SEI. In addition to these traditional binders applied in PIBs, the group of Guo developed a CMC-polyacrylic acid (PAA) binder for a Sb-based composite[97]. The cycling performance of the CMC-PAA binder was improved due to the condensation reaction between the hydroxyl groups of CMC and the carboxylic acid moieties of PAA, which effectively increased the viscoelastic properties of the binder and increased the mechanism properties of the electrodes.

In summary, the modification methods for Sb-based anode materials are mainly nanostructural engineering by designing nanofibers, nanoflowers, box shell structures and nanoporous structures in combination with carbon fibers, MXenes, carbon shells, and so on. Multistructural design efficiently hinders the significant volume change and efficiently alleviates the structural degradation.

Ge-based anode materials

Ge has a diamond cubic crystal structure, which is the same as silicon, and it is in the IVA group. Germanium is an attractive non-toxic alloy-based anode material. The original study of Ge-based anode materials can be dated back to the 1980s when the formation of the Ge-Li binary was first discovered.

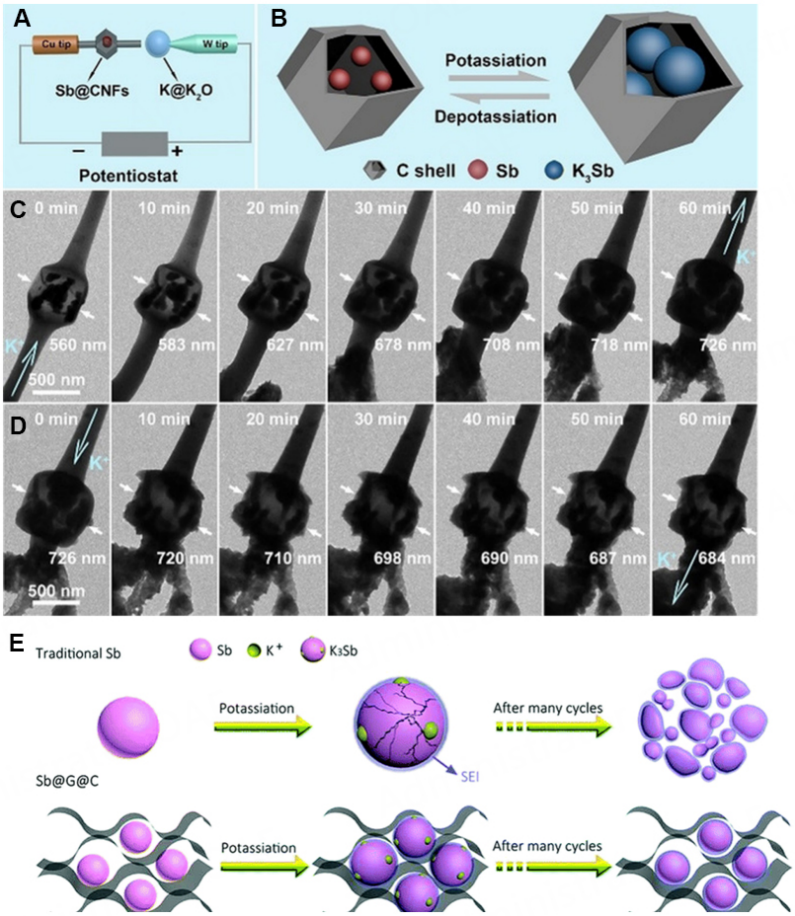

Figure 8. (A) Illustration of TEM device and (B) potassiation/depotassiation processes of Sb@carbon nanofibers (CNFs) with Sb nanoparticles confined in carbon shell. (C and D) Potassiation and depotassiation processes of Sb@CNFs[86]. Copyright 2020, Wiley-VCH. (E) Schematic illustration of traditional Sb and Sb@graphene (G)@C electrodes during potassiation/depotassiation processes[87]. Copyright 2018, Royal Society of Chemistry.

Mechanism of Ge-based anodes in PIBs

Ge has a high capacity of 1623 or 1384 mAh g^{-1} by the formation of the lithium-rich compounds $Li_{55}Ge_5$ and $Li_{15}Ge_4$, respectively[98-102], which makes it a promising anode material in LIBs. In SIBs, germanium delivers a high capacity of 389 mAh g^{-1} by forming the binary compound NaGe[103-106] at a voltage plateau of 0.15-0.60 V *vs.* Na/Na^+. Based on the formation of KGe as the final product, germanium has a theoretical capacity of 369 mAh g^{-1} in PIBs. To date, the study of the potassium-ion storage mechanism for Ge in PIBs has been limited. Based on the previous studies of the performance of Ge in SIBs and LIBs, the mechanism of potassium-ion insertion obeys the following equation: $Ge + K^+ + e^- \leftrightarrow KGe$. This mechanism was proved using SAED[107]. For Ge-based compounds, the mechanism can be simplified to $Ge_xM_y + (x + zy)K^+ + (x + zy)e^- = xKGe + yK_zM$[42]. In this process, the compound first decomposes, the Ge reacts with K to form KGe and the active material reacts with K to form a compound. When the Ge-based compounds are 2D materials, such as GeSe, the reaction can be considered as $GeSe + xK^+ + xe^- \leftrightarrow K_xGeSe$ based on calculations[108,109].

Modification strategies for Ge-based anode materials

Compared to other alloy-based anode materials, germanium has a relatively lower theoretical capacity. It experiences a limited volume change during ion insertion and extraction processes; however, compared to

other alloy-based anodes, which amount to ~272% in LIBs and 120% in SIBs. Similarly, Ge undergoes a significant volume change in the discharge/charge process in PIBs. Although the volume changes of germanium are less compared to other alloy-based materials, they can cause pulverization and result in a capacity decrease in the same manner.

In order to improve the electrochemical performance of germanium-based anode materials, the ordinary methods include constructing nanostructures combining Ge with carbon materials[110-114] in LIBs and SIBs. Li *et al.* designed hollow carbon spheres with germanium encapsulated inside by introducing a germanium precursor into the hollow carbon particles and then followed this with a thermal reduction[114]. The hollow carbon spheres served as a physical matrix that could effectively protect the germanium core from coalescing or pulverization. Similarly, Mo *et al.* designed a 3D-interconnected porous graphene foam with germanium quantum dots doped into it by a facile approach[112]. This structure provided close contact between the electrode materials and the current collector, and the yolk-shell structure effectively alleviated the significant volume changes and provided a stable SEI. Designing nanostructures in combination with carbon materials are also an efficient method to improve the electrochemical performance of Ge-based materials in PIBs. Liu *et al.* synthesized a dual carbon structure with germanium encapsulated inside[106]. The as-prepared dual carbon matrix was composed of mesoporous carbon and an amorphous carbon layer, as shown in Figure 9. Using this structure, the dual carbon effectively alleviated the expansion of germanium. Yang *et al.* designed a nanoporous structure Ge with small ligaments and interconnected porous prepared by a chemical-dealloying method[107]. The nanoporous germanium delivered a high initial capacity of 290 mAh g^{-1} and a stable capacity of 120 mAh g^{-1} over 400 cycles[107].

Using active or inactive elements to form Ge-based binaries or composites is another effective method to improve the electrochemical performance. The inactive metals alloyed with Ge include Co[115] and Cu[116], which can improve the conductivity. The active materials have been applied in the formation of Ge-based compounds are Si[117], Sn[118], Sb[119], Te[120] and Se[121], which have high theoretical capacities. As discussed above, phosphorus has the highest theoretical capacity in PIBs and can increase the capacity of the total capacity by the formation of GeP_x. Zhang *et al.* prepared GeP_5, which delivered a stable capacity of 213.7 mAh g^{-1} in PIBs for 2000 cycles at a current density of 500 mA g^{-1}[51]. The active Se metal can form layered metal selenides with Ge, which has a large interlayer distance of 5.41 Å. The GeSe/CNT composite synthesized by a simple ball-milling method delivered a stable cycling performance with 311 mAh g^{-1} retention after 400 cycles. Furthermore, the electrode delivered a capacity of ~200 mAh g^{-1} at a high current density of 5 A g^{-1}[122]. Ge-based anode materials exhibit larger volume changes in PIBs compared to the volume changes in LIBs and SIBs because of the larger size of potassium ions. The construction of 3D porous and yolk-shell structures in combination with carbon materials, such as carbon spheres, graphene or amorphous carbon, can efficiently ameliorate the volume changes and improve the electrochemical performance.

Sn-based anode materials for PIBs

Sn has been an attractive anode material for LIBs and SIBs for a long time and has high theoretical capacities of 991 and 845 mAh g^{-1} via the formation of $Li_{4.4}Sn$ and $Na_{15}Sn_4$, respectively. The study of Sn in PIBs started in 2016[123], with the formation of KSn. Sn has a theoretical capacity of 226 mAh g^{-1} in PIBs.

Mechanism of Sn-based anode materials

Based on the K-Sn phase diagram, K_2Sn, KSn, K_2Sn_3, KSn_2 and K_4Sn_{23} can form at different temperatures. Wang *et al.* were the first to study the reaction mechanism of Sn in PIBs using *in-situ* TEM and XRD methods[124]. They revealed a two-step process corresponding to Sn → amorphous K_4Sn_9 → KSn. A similar

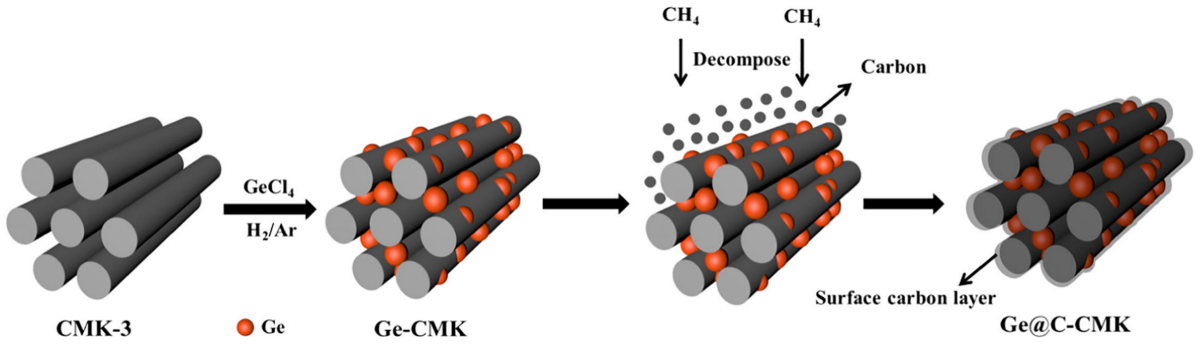

Figure 9. Schematic illustration of preparation of Ge-CMK and Ge@C-CMK composites[106]. Copyright 2021, Elsevier.

potassiation process was evaluate, as shown in Figure 10A-C. The results revealed that the tetragonal K_4Sn_4 phase was formed at a voltage of ~0.01 V. Their study indicated that K_4Sn_4 and KSn are overall identical phases in terms of their crystal structure. In the de-alloying process, K_4Sn_4 decomposed at 0.98 V[125].

The study of the mechanism of Sn-based alloys has also attracted significant attention. The teams of Ma and Ci have both studied the potassium-ion storage mechanism in SnS_2[126,127] and their results are similar. In the discharge process, $SnS_2 \rightarrow SnS + K_2S_5 \rightarrow Sn + K_2S_5 + K_4Sn_{23} \rightarrow K_2S_5 + KSn$, as shown in Figure 10D. Like the alloying process of crystalline Sn in PIBs, the final product, KSn phase, is formed within the voltage range of 0.20-0.01 V. For SnSe, based on the study of Verma *et al.*, the potassiation process is $SnSe \rightarrow Sn + K_2Se_5 \rightarrow K_4Sn_{23} + K_2Se_5$, which is reversible[128]. The KSn phase was not detected, as shown in Figure 10E.

Modification strategies for Sn-based anode materials

Sn-based alloys suffer from significant volume expansion in PIBs, which results in pulverization and capacity drop. Various methods have been applied to ameliorate the volume change and improve the electrochemical performance. To solve these drawbacks, hierarchical nanostructural design is an effective strategy. 2D nanosheet structures have been applied to improve the electrochemical performance of Sn-based anode materials. Lakshimi *et al.* studied an SnS_2/graphene composite in PIBs, which delivered a high capacity of 350 mAh g^{-1}[129]. Qin *et al.* designed hierarchical polyaspartic acid-modified SnS_2 nanosheets embedded into carbon[126]. The as-prepared electrode enlarged the interlamellar space of 6.8 Å and delivered a high-rate performance of 273 mAh g^{-1} at a current density of 2 A g^{-1}[126]. Cao *et al.* also designed a 2D SnS nanosheet composite that exhibited an ultralong lifespan[130]. Sun *et al.* used a nanosheet structure with strong interactions between the layers, which can efficiently accelerate electron and ion transfer and hinder the volume change[131]. The as-prepared composite delivered a stable long-term cycling performance of 165 mAh g^{-1} at a current density of 10 A g^{-1} after 5000 cycles[131].

The group of Yang also designed a nanosheet structure, which delivered a high capacity of 206.1 mAh g^{-1} after 800 cycles[132]. Zhou *et al.* designed a sheet-like tin sulfide composite, as shown in Figure 11A, which delivered a rapid rate capacity of 460 mAh g^{-1} at a current density of 2A g^{1} and an excellent cycling stability of over 500 cycles at a current density of 1 A g^{-1}[133]. The utilization of the 2D structure efficiently hinders the volume change and improves the electronic and ionic conductivity. Combining Sb-based alloys with 3D structures has been an effective method to improve the electrochemical performance of PIBs. Yolk-shell 3D carbon boxes were designed as a matrix to accommodate SnS_2, as shown in Figure 11B. Introducing interior void space has been an effective strategy to accommodate the volume changes. The composite delivered a stable cycling performance of 352 mAh g^{-1} at 1 A g^{-1}, as shown in Figure 11C[134].

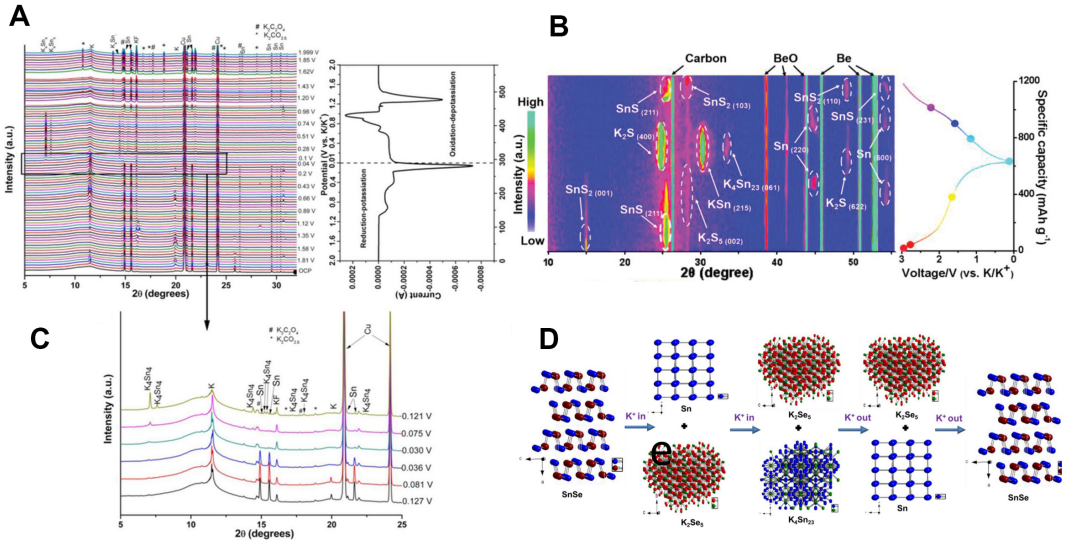

Figure 10. (A) Synchrotron XRD data obtained *in situ* during (B) CV scans of 1 μm-thick Sn film electrode in K half-cell and (C) zoomed-in *in-situ* XRD patterns corresponding to region associated with phase transformation of primary interest during electrochemical potassiation of Sn[125]. Copyright 2017, Electrochemical Society. (D) *In-situ* XRD results for hierarchical polyaspartic acid-*modified* SnS_2 nanosheets embedded into hollow N-doped carbon fibers (PASP@SnS_2@CN) electrode at different charge/discharge states[126]. Copyright 2020, Wiley-VCH. (E) Schematic illustration of potassiation/depotassiation process in SnSe@C nanocomposite[128]. Copyright 2021, Elsevier Ltd.

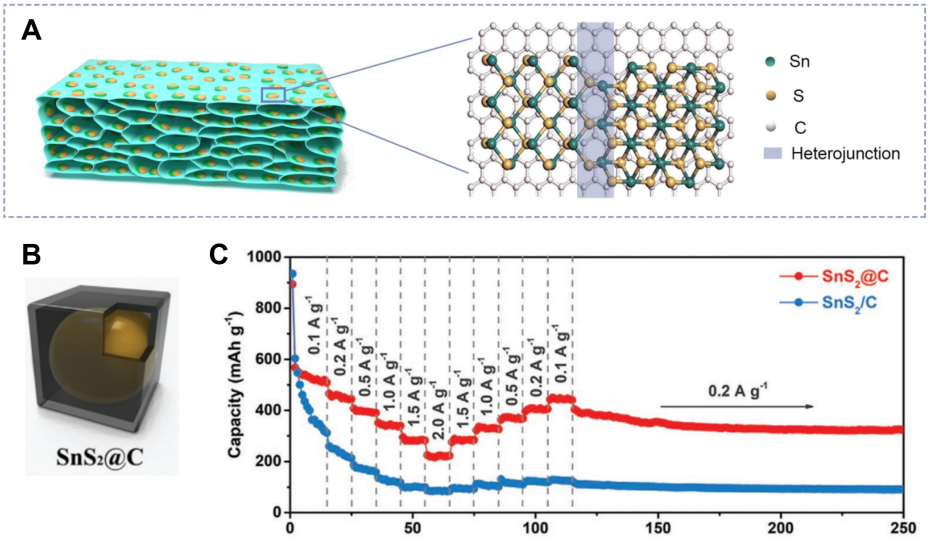

Figure 11. (A) Morphological and structural characterization of SnS/SnS_2/rGO materials[133]. Copyright 2021, Elsevier Ltd. (B) Schematic illustration of SnS_2@C and (C) long-term cycling stability evaluation of SnS_2@C and SnS_2/C electrodes in PIBs[134]. Copyright 2020, Wiley-VCH.

Another alternative method to enhance electrochemical performance is using the proper salt to form a robust SEI. Compared KFSI and KPF_6 with the same solvent. The results indicated that the Sn-based composite in the KFSI-based electrolyte exhibited a highly stable cycling performance of 450 mAh g^{-1} over 400 cycles. The KFSI salt in an ethylene carbonate/diethyl carbonate solvent more easily forms a K-F-rich inorganic SEI due to the critical role of FSI^{-1} anions, which can inhibit the decomposition of the electrolyte[135], as shown in Figure 12A. Similarly, the group of Chen also studied the different salts in

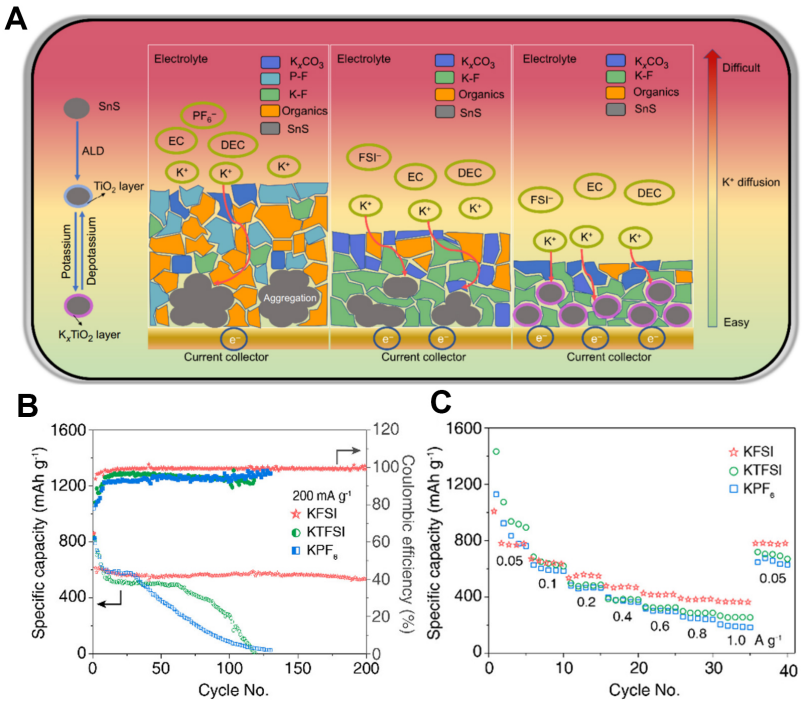

Figure 12. (A) Schematic illustration of chemical composition and ionic transport of electrode/electrolyte interface[135]. Copyright 2021, Springer Nature. (B) Capacity retention of SnS_2/N-rGO composite electrodes in EC/DEC electrolytes with various K^+ salts at a current density of 200 mA g^{-1}. (C) Rate capability of cells with various K^+ salts at current densities from 0.05 to 1 A g^{-1}[136]. Copyright 2021, American Chemical Society.

electrolytes resulting in the differences in SEI formations. Their results indicated that batteries with KFSI featured better performance than those with KTFSI and KPF_6. The composition of the SEI formed in the KFSI-based electrolyte is mainly K-F, which can effectively enhance the mechanical properties of the SEI. The SEI from the KFSI-based electrolyte also stops growing after 20 cycles, while the SEIs of the KTFSI and KPF_6-based electrolytes continue to grow thicker, thereby hindering the potassium-ion transportation, as shown in Figure 12B and C[136]. Sn has a high theoretical capacity of 226 mAh g^{-1} in PIBs, with the formation of KSn as the final product. The challenge facing Sn-based alloy anode materials in PIBs is their significant volume change and pulverization. In order to hinder the volume change of Sn-based alloys, modification methods have been applied. The design of 2D nanosheets, 3D nanoboxes and SEIs has been applied in the modification and has efficiently improved the electrochemical performance.

SUMMARY AND OUTLOOK

Their low cost and the natural abundance of their raw materials make PIBs promising next-generation energy storage devices. The large radius of the potassium ion results, however, in slower ion transport and limited cycling life. Recently, significant research has been completed on PIBs, but one of the major challenges is to develop high-performing anodes.

This review summarizes the recent research progress on alloy-type anodes for PIBs, including P-, Bi-, Sb-, Ge- and Sn-based compounds and composites. Alloy-based anode materials undergo alloy conversion reactions in which the material finally reacts with K to form K_xM. Therefore, alloy-based materials have high theoretical capacities of 2596, 385, 687, 369 and 226 mAh g^{-1}, respectively, and volumetric capacities of 4750, 3752, 4596, 1964 and 1653 mAh cm^{-3} make them high potential anode materials for PIBs. The

mechanisms of the potassiation and depotassiation processes have been deeply discussed and analyzed. For an elementary substance, the mechanism is a simple alloying reaction. For compound materials, the reaction process is mainly a conversion-alloying reaction. The various formations of the intermediate product in the potassium ion for the same material are mainly due to the various nanostructures and grain sizes of the materials. Modifications of the materials have also been explored and investigated. The approaches can be classified as the hybridization of active materials with high conductivity and architectural engineering. Highly conductive materials, including graphene, carbon nanotubes, graphite, N-doped carbon and carbon nanosheets. The architectural engineering methods, including the design of one-dimensional nanotubes, 2D nanosheets and 3D structural materials, such as core-shell structures and their combinations. By using these modification methods, the significant volume change and sluggish reaction kinetics can be effectively solved.

The electrochemical performance of alloy-based electrodes has now been greatly improved and the reaction processes have also been deeply analyzed. Further research can be carried out on the following aspects:

(1) Low initial Coulombic efficiency is the main problem that remains for anode materials, which might be ascribed to the irreversible insertion of potassium ions and the decomposition of the electrolyte. In the full cell, the maximum cell energy is obtained when the anode irreversible capacity exactly matches that of the cathode material. The low initial Coulombic efficiency (ICE) indicates the large consumption of K^+ provided from cathode, which results in lower energy density in the full cell and faster capacity drop. Improving electrolytes with higher ion conductivity will increase the ICE.

(2) Although fabricated nanostructures and hybrids with carbon will significantly hinder the volume changes, alloy-based anode materials still face the problem of volume expansion and pulverization during cycling. Furthermore, this problem may bring the severe side effect of the reaction between the electrolyte and the new surface of the electrode, leading to the formation of the SEI on the new surface, which results in a capacity decrease and instability of the cycling performance. This side effect may also result in the maldistribution of electrons, leading to dendrite growth and the polarization of electrodes. This will limit the application and manufacturing of PIBs. Electrolyte and electrode interface engineering or controlling the content and structure of the SEI layer or designing an artificial SEI layer can make up for the shortage.

(3) Safety problems are still an issue for future development. Alloy-based anode materials are currently limited in their application at high and low temperatures. Aqueous electrolyte and flame-retardant electrolyte systems could be promising designs for future applications. In addition, non-flammable carbonate electrolytes can also be used to address battery safety issues.

In light of the abundance of potassium resources and the significant progress that has been made in the research on alloy-based anodes for PIBs, these anodes will be promising for commercialization in the near future.

DECLARATIONS

Acknowledgments

The authors thank Dr. Tania Silver for her critical reading of the manuscript.

Authors' contributions

Characterizing, writing original draft: Yang Q

Review, and supervision: Chou S, Liu H, Wang J
Editing: Fan Q, Peng J

Availability of data and materials
Not applicable.

Financial support and sponsorship
This work is financially supported by Australian Research Council (ARC) Discovery Project (DP180101453).

Conflicts of interest
All authors declared that there are no conflicts of interest.

Ethical approval and consent to participate
Not applicable.

Consent for publication
Not applicable.

Copyright
© The Author(s) 2023.

REFERENCES
1. Scott V, Haszeldine RS, Tett SFB, Oschlies A. Fossil fuels in a trillion tonne world. *Nat Clim Chang* 2015;5:419-23. DOI
2. Mohr S, Wang J, Ellem G, Ward J, Giurco D. Projection of world fossil fuels by country. *Fuel* 2015;141:120-35. DOI
3. Abas N, Kalair A, Khan N. Review of fossil fuels and future energy technologies. *Futures* 2015;69:31-49. DOI
4. Höök M, Tang X. Depletion of fossil fuels and anthropogenic climate change - A review. *Energy Policy* 2013;52:797-809. DOI
5. Armaroli N, Balzani V. The legacy of fossil fuels. *Chem Asian J* 2011;6:768-84. DOI PubMed
6. Berner RA. The long-term carbon cycle, fossil fuels and atmospheric composition. *Nature* 2003;426:323-6. DOI PubMed
7. Gustavsson L, Börjesson P, Johansson B, Svenningsson P. Reducing CO_2 emissions by substituting biomass for fossil fuels. *Energy* 1995;20:1097-113. DOI
8. Withagen C. Pollution and exhaustibility of fossil fuels. *Resour Energy Econ* 1994;16:235-42. DOI
9. Barbir F, Veziroğlu T, Plass H. Environmental damage due to fossil fuels use. *Int J Hydrog Energy* 1990;15:739-49. DOI
10. Hameer S, van Niekerk JL. A review of large-scale electrical energy storage: this paper gives a broad overview of the plethora of energy storage. *Int J Energy Res* 2015;39:1179-95. DOI
11. Castillo A, Gayme DF. Grid-scale energy storage applications in renewable energy integration: a survey. *Energy Convers Manag* 2014;87:885-94. DOI
12. Etacheri V, Marom R, Elazari R, Salitra G, Aurbach D. Challenges in the development of advanced Li-ion batteries: a review. *Energy Environ Sci* 2011;4:3243. DOI
13. Hosaka T, Kubota K, Hameed AS, Komaba S. Research development on K-ion batteries. *Chem Rev* 2020;120:6358-466. DOI
14. Kim H, Kim JC, Bianchini M, Seo D, Rodriguez-garcia J, Ceder G. Recent progress and perspective in electrode materials for K-ion batteries. *Adv Energy Mater* 2018;8:1702384. DOI
15. Hwang J, Myung S, Sun Y. Recent progress in rechargeable potassium batteries. *Adv Funct Mater* 2018;28:1802938. DOI
16. Anoopkumar V, John B, Mercy T. Potassium-ion batteries: key to future large-scale energy storage? *ACS Appl Energy Mater* 2020;3:9478-92. DOI
17. Zhang W, Liu Y, Guo Z. Approaching high-performance potassium-ion batteries via advanced design strategies and engineering. *Sci Adv* 2019;5:eaav7412. DOI PubMed PMC
18. Li W, Bi Z, Zhang W, et al. Advanced cathodes for potassium-ion batteries with layered transition metal oxides: a review. *J Mater Chem A* 2021;9:8221-47. DOI
19. Zhang X, Wei Z, Dinh KN, et al. Layered oxide cathode for potassium-ion battery: recent progress and prospective. *Small* 2020;16:e2002700. DOI PubMed
20. Eftekhari A. Potassium secondary cell based on Prussian blue cathode. *J Power Sources* 2004;126:221-8. DOI
21. Li L, Hu Z, Liu Q, Wang J, Guo Z, Liu H. Cathode materials for high-performance potassium-ion batteries. *Cell Rep Phys Sci* 2021;2:100657. DOI

22. Li L, Hu Z, Lu Y, et al. A low-strain potassium-rich prussian blue analogue cathode for high power potassium-ion batteries. *Angew Chem Int Ed* 2021;60:13050-6. DOI PubMed
23. Qin M, Ren W, Meng J, et al. Realizing superior prussian blue positive electrode for potassium storage via ultrathin nanosheet assembly. *ACS Sustain Chem Eng* 2019;7:11564-70. DOI
24. Liu S, Kang L, Jun SC. Challenges and strategies toward cathode materials for rechargeable potassium-ion batteries. *Adv Mater* 2021;33:e2004689. DOI PubMed
25. Yang Y, Zhou J, Wang L, et al. Prussian blue and its analogues as cathode materials for Na-, K-, Mg-, Ca-, Zn- and Al-ion batteries. *Nano Energy* 2022;99:107424. DOI
26. Min X, Xiao J, Fang M, et al. Potassium-ion batteries: outlook on present and future technologies. *Energy Environ Sci* 2021;14:2186-243. DOI
27. Zhang K, Gu Z, Ang EH, et al. Advanced polyanionic electrode materials for potassium-ion batteries: Progresses, challenges and application prospects. *Mater Today* 2022;54:189-201. DOI
28. Jian Z, Luo W, Ji X. Carbon electrodes for K-ion batteries. *J Am Chem Soc* 2015;137:11566-9. DOI PubMed
29. Luo W, Wan J, Ozdemir B, et al. Potassium ion batteries with graphitic materials. *Nano Lett* 2015;15:7671-7. DOI PubMed
30. Zhan F, Wang H, He Q, et al. Metal-organic frameworks and their derivatives for metal-ion (Li, Na, K and Zn) hybrid capacitors. *Chem Sci* 2022;13:11981-2015. DOI PubMed PMC
31. Liu S, Kang L, Zhang J, Jung E, Lee S, Jun SC. Structural engineering and surface modification of MOF-derived cobalt-based hybrid nanosheets for flexible solid-state supercapacitors. *Energy Stor Mater* 2020;32:167-77. DOI
32. Tu J, Tong H, Zeng X, et al. Modification of porous N-doped carbon with sulfonic acid toward high-ICE/capacity anode material for potassium-ion batteries. *Adv Funct Mater* 2022;32:2204991. DOI
33. Tian S, Zhang Y, Yang C, Tie S, Nan J. Nitrogen-doped carbon nanosheet coated multilayer graphite as stabilized anode material of potassium-ion batteries with high performances. *Electrochim Acta* 2021;380:138254. DOI
34. Sultana I, Rahman MM, Chen Y, Glushenkov AM. Potassium-ion battery anode materials operating through the alloying-dealloying reaction mechanism. *Adv Funct Mater* 2018;28:1703857. DOI
35. Komaba S, Hasegawa T, Dahbi M, Kubota K. Potassium intercalation into graphite to realize high-voltage/high-power potassium-ion batteries and potassium-ion capacitors. *Electrochem Commun* 2015;60:172-5. DOI
36. Cao K, Liu H, Li W, et al. CuO nanoplates for high-performance potassium-ion batteries. *Small* 2019;15:e1901775. DOI PubMed
37. Sultana I, Rahman MM, Ramireddy T, Chen Y, Glushenkov AM. High capacity potassium-ion battery anodes based on black phosphorus. *J Mater Chem A* 2017;5:23506-12. DOI
38. Jin H, Wang H, Qi Z, et al. A black phosphorus-graphite composite anode for Li-/Na-/K-ion batteries. *Angew Chem Int Ed* 2020;59:2318-22. DOI PubMed
39. Xiong P, Bai P, Tu S, et al. Red phosphorus nanoparticle@3D interconnected carbon nanosheet framework composite for potassium-ion battery anodes. *Small* 2018;14:e1802140. DOI PubMed
40. Wu Y, Hu S, Xu R, et al. Boosting potassium-ion battery performance by encapsulating red phosphorus in free-standing nitrogen-doped porous hollow carbon nanofibers. *Nano Lett* 2019;19:1351-8. DOI PubMed
41. Liu D, Huang X, Qu D, et al. Confined phosphorus in carbon nanotube-backboned mesoporous carbon as superior anode material for sodium/potassium-ion batteries. *Nano Energy* 2018;52:1-10. DOI
42. Zhang W, Mao J, Li S, Chen Z, Guo Z. Phosphorus-based alloy materials for advanced potassium-ion battery anode. *J Am Chem Soc* 2017;139:3316-9. DOI
43. Zhang W, Wu Z, Zhang J, et al. Unraveling the effect of salt chemistry on long-durability high-phosphorus-concentration anode for potassium ion batteries. *Nano Energy* 2018;53:967-74. DOI
44. Li B, He Z, Zhao J, Liu W, Feng Y, Song J. Advanced Se_3P_4@C anode with exceptional cycling life for high performance potassium-ion batteries. *Small* 2020;16:e1906595. DOI
45. Yang Q, Tai Z, Xia Q, et al. Copper phosphide as a promising anode material for potassium-ion batteries. *J Mater Chem A* 2021;9:8378-85. DOI
46. Xu GL, Chen Z, Zhong GM, et al. Nanostructured black phosphorus/ketjenblack-multiwalled carbon nanotubes composite as high performance anode material for sodium-ion batteries. *Nano Lett* 2016;16:3955-65. DOI PubMed
47. Yang W, Lu Y, Zhao C, Liu H. First-principles study of black phosphorus as anode material for rechargeable potassium-ion batteries. *Electron Mater Lett* 2020;16:89-98. DOI
48. Yuan D, Cheng J, Qu G, et al. Amorphous red phosphorous embedded in carbon nanotubes scaffold as promising anode materials for lithium-ion batteries. *J Power Sources* 2016;301:131-7. DOI
49. Ramireddy T, Xing T, Rahman MM, et al. Phosphorus-carbon nanocomposite anodes for lithium-ion and sodium-ion batteries. *J Mater Chem A* 2015;3:5572-84. DOI
50. Verma R, Didwal PN, Ki HS, Cao G, Park CJ. SnP_3/Carbon nanocomposite as an anode material for potassium-ion batteries. *ACS Appl Mater Interfaces* 2019;11:26976-84. DOI PubMed
51. Zhang Z, Wu C, Chen Z, et al. Spatially confined synthesis of a flexible and hierarchically porous three-dimensional graphene/FeP hollow nanosphere composite anode for highly efficient and ultrastable potassium ion storage. *J Mater Chem A* 2020;8:3369-78. DOI
52. Yang F, Gao H, Hao J, et al. Yolk-shell structured FeP@C nanoboxes as advanced anode materials for rechargeable lithium-/potassium-ion batteries. *Adv Funct Mater* 2019;29:1808291. DOI

53. Yang F, Hao J, Long J, et al. Achieving high-performance metal phosphide anode for potassium ion batteries via concentrated electrolyte chemistry. *Adv Energy Mater* 2021;11:2003346. DOI
54. Liu Q, Hu Z, Liang Y, et al. Facile synthesis of hierarchical hollow CoP@C composites with superior performance for sodium and potassium storage. *Angew Chem* 2020;132:5197-202. DOI PubMed
55. Li D, Zhang Y, Sun Q, et al. Hierarchically porous carbon supported Sn_4P_3 as a superior anode material for potassium-ion batteries. *Energy Stor Mater* 2019;23:367-74. DOI
56. Zhang W, Pang WK, Sencadas V, Guo Z. Understanding high-energy-density Sn_4P_3 anodes for potassium-ion batteries. *Joule* 2018;2:1534-47. DOI
57. Huang J, Lin X, Tan H, Zhang B. Bismuth microparticles as advanced anodes for potassium-ion battery. *Adv Energy Mater* 2018;8:1703496. DOI
58. Lei K, Wang C, Liu L, et al. A porous network of bismuth used as the anode material for high-energy-density potassium-ion batteries. *Angew Chem* 2018;130:4777-81. DOI PubMed
59. Zhang Q, Mao J, Pang WK, et al. Boosting the potassium storage performance of alloy-based anode materials via electrolyte salt chemistry. *Adv Energy Mater* 2018;8:1703288. DOI
60. Xie F, Zhang L, Chen B, et al. Revealing the origin of improved reversible capacity of dual-shell bismuth boxes anode for potassium-ion batteries. *Matter* 2019;1:1681-93. DOI
61. Shen C, Song G, Zhu X, et al. An in-depth study of heteroatom boosted anode for potassium-ion batteries. *Nano Energy* 2020;78:105294. DOI
62. Chen K, Chong S, Yuan L, Yang Y, Tuan H. Conversion-alloying dual mechanism anode: Nitrogen-doped carbon-coated Bi_2Se_3 wrapped with graphene for superior potassium-ion storage. *Energy Stor Mater* 2021;39:239-49. DOI
63. Cheng X, Li D, Wu Y, Xu R, Yu Y. Bismuth nanospheres embedded in three-dimensional (3D) porous graphene frameworks as high performance anodes for sodium- and potassium-ion batteries. *J Mater Chem A* 2019;7:4913-21. DOI
64. Hu X, Liu Y, Chen J, Yi L, Zhan H, Wen Z. Fast redox kinetics in Bi-heteroatom doped 3D porous carbon nanosheets for high-performance hybrid potassium-ion battery capacitors. *Adv Energy Mater* 2019;9:1901533. DOI
65. Shi X, Zhang J, Yao Q, et al. A self-template approach to synthesize multicore-shell Bi@N-doped carbon nanosheets with interior void space for high-rate and ultrastable potassium storage. *J Mater Chem A* 2020;8:8002-9. DOI
66. Li H, Zhao C, Yin Y, et al. N-doped carbon coated bismuth nanorods with a hollow structure as an anode for superior-performance potassium-ion batteries. *Nanoscale* 2020;12:4309-13. DOI PubMed
67. Hussain N, Liang T, Zhang Q, et al. Ultrathin Bi nanosheets with superior photoluminescence. *Small* 2017;13:1701349. DOI PubMed
68. Zhou, J, Chen, J, Chen, M, et al. Few-layer bismuthene with anisotropic expansion for high-areal-capacity sodium-ion batteries. *Adv Mater* 2019;31:e1807874. DOI
69. Hagiwara R, Tamaki K, Kubota K, Goto T, Nohira T. Thermal properties of mixed alkali bis(trifluoromethylsulfonyl)amides. *J Chem Eng Data* 2008;53:355-8. DOI
70. Xu K. Electrolytes and interphases in Li-ion batteries and beyond. *Chem Rev* 2014;114:11503-618. DOI PubMed
71. Shen C, Cheng T, Liu C, et al. Bismuthene from sonoelectrochemistry as a superior anode for potassium-ion batteries. *J Mater Chem A* 2020;8:453-60. DOI
72. Hosaka T, Kubota K, Kojima H, Komaba S. Highly concentrated electrolyte solutions for 4 V class potassium-ion batteries. *Chem Commun* 2018;54:8387-90. DOI PubMed
73. Zhang R, Bao J, Wang Y, Sun CF. Concentrated electrolytes stabilize bismuth-potassium batteries. *Chem Sci* 2018;9:6193-8. DOI PubMed PMC
74. Jiao T, Wu S, Cheng J, et al. Bismuth nanorod networks confined in a robust carbon matrix as long-cycling and high-rate potassium-ion battery anodes. *J Mater Chem A* 2020;8:8440-6. DOI
75. Xiang X, Liu D, Zhu X, et al. Evaporation-induced formation of hollow bismuth@N-doped carbon nanorods for enhanced electrochemical potassium storage. *Appl Surf Sci* 2020;514:145947. DOI
76. Yang H, Xu R, Yao Y, Ye S, Zhou X, Yu Y. Multicore-shell Bi@N-doped carbon nanospheres for high power density and long cycle life sodium- and potassium-ion anodes. *Adv Funct Mater* 2019;29:1809195. DOI
77. Weppner W, Huggins RA. Determination of the kinetic parameters of mixed-conducting electrodes and application to the system Li_3Sb. *J Electrochem Soc* 1977;124:1569-77. DOI
78. McCulloch WD, Ren X, Yu M, Huang Z, Wu Y. Potassium-ion oxygen battery based on a high capacity antimony anode. *ACS Appl Mater Interfaces* 2015;7:26158-66. DOI PubMed
79. Liu Y, Xu J, Kang Z, Wang J. Thermodynamic descriptions and phase diagrams for Sb-Na and Sb-K binary systems. *Thermochim Acta* 2013;569:119-26. DOI
80. Zheng J, Yang Y, Fan X, et al. Extremely stable antimony-carbon composite anodes for potassium-ion batteries. *Energy Environ Sci* 2019;12:615-23. DOI
81. Han C, Han K, Wang X, et al. Three-dimensional carbon network confined antimony nanoparticle anodes for high-capacity K-ion batteries. *Nanoscale* 2018;10:6820-6. DOI PubMed
82. Yi Z, Lin N, Zhang W, Wang W, Zhu Y, Qian Y. Preparation of Sb nanoparticles in molten salt and their potassium storage performance and mechanism. *Nanoscale* 2018;10:13236-41. DOI PubMed

83. Ko YN, Choi SH, Kim H, Kim HJ. One-pot formation of Sb-carbon microspheres with graphene sheets: potassium-ion storage properties and discharge mechanisms. *ACS Appl Mater Interfaces* 2019;11:27973-81. DOI PubMed
84. Liu Y, Tai Z, Zhang J, et al. Boosting potassium-ion batteries by few-layered composite anodes prepared via solution-triggered one-step shear exfoliation. *Nat Commun* 2018;9:3645. DOI PubMed PMC
85. Yi Z, Qian Y, Tian J, Shen K, Lin N, Qian Y. Self-templating growth of Sb_2Se_3@C microtube: a convention-alloying-type anode material for enhanced K-ion batteries. *J Mater Chem A* 2019;7:12283-91. DOI
86. Huang H, Wang J, Yang X, et al. Unveiling the advances of nanostructure design for alloy-type potassium-ion battery anodes via in situ TEM. *Angew Chem Int Ed* 2020;59:14504-10. DOI PubMed
87. Liu Q, Fan L, Ma R, et al. Super long-life potassium-ion batteries based on an antimony@carbon composite anode. *Chem Commun* 2018;54:11773-6. DOI PubMed
88. An Y, Tian Y, Ci L, Xiong S, Feng J, Qian Y. Micron-sized nanoporous antimony with tunable porosity for high-performance potassium-ion batteries. *ACS Nano* 2018;12:12932-40. DOI PubMed
89. Wang Z, Dong K, Wang D, et al. A nanosized SnSb alloy confined in N-doped 3D porous carbon coupled with ether-based electrolytes toward high-performance potassium-ion batteries. *J Mater Chem A* 2019;7:14309-18. DOI
90. Ge X, Liu S, Qiao M, et al. Enabling superior electrochemical properties for highly efficient potassium storage by impregnating ultrafine Sb nanocrystals within nanochannel-containing carbon nanofibers. *Angew Chem Int Ed* 2019;58:14578-83. DOI PubMed
91. Cheng Y, Yao Z, Zhang Q, et al. In situ atomic-scale observation of reversible potassium storage in Sb_2S_3@Carbon nanowire anodes. *Adv Funct Mater* 2020;30:2005417. DOI
92. Liu H, He Y, Cao K, et al. Stimulating the reversibility of Sb_2S_3 Anode for high-performance potassium-ion batteries. *Small* 2021;17:e2008133. DOI
93. Sheng B, Wang L, Huang H, et al. Boosting potassium storage by integration advantageous of defect engineering and spatial confinement: a case study of Sb_2S_3. *Small* 2020;16:e2005272. DOI
94. Wang T, Shen D, Liu H, Chen H, Liu Q, Lu B. A Sb_2S_3 nanoflower/MXene composite as an anode for potassium-ion batteries. *ACS Appl Mater Interfaces* 2020;12:57907-15. DOI
95. Chen B, Yang L, Bai X, et al. Heterostructure Engineering of Core-Shelled Sb@ Sb_2S_3 encapsulated in 3D N-doped carbon hollow-spheres for superior sodium/potassium storage. *Small* 2021;17:e2006824. DOI
96. He X, Liao J, Wang S, et al. From nanomelting to nanobeads: nanostructured Sb_xBi_{1-x} alloys anchored in three-dimensional carbon frameworks as a high-performance anode for potassium-ion batteries. *J Mater Chem A* 2019;7:27041-7. DOI
97. Wu J, Zhang Q, Liu S, et al. Synergy of binders and electrolytes in enabling microsized alloy anodes for high performance potassium-ion batteries. *Nano Energy* 2020;77:105118. DOI
98. Liang S, Cheng Y, Zhu J, Xia Y, Müller-buschbaum P. A chronicle review of nonsilicon (Sn, Sb, Ge)-based lithium/sodium-ion battery alloying anodes. *Small Methods* 2020;4:2000218. DOI
99. Tian H, Xin F, Wang X, He W, Han W. High capacity group-IV elements (Si, Ge, Sn) based anodes for lithium-ion batteries. *J Materiomics* 2015;1:153-69. DOI
100. Yin L, Song J, Yang J, et al. Construction of Ge/C nanospheres composite as highly efficient anode for lithium-ion batteries. *J Mater Sci Mater Electron* 2021;32:6398-407. DOI
101. Hu Z, Zhang S, Zhang C, Cui G. High performance germanium-based anode materials. *Coord Chem Rev* 2016;326:34-85. DOI
102. Jung H, Allan PK, Hu Y, et al. Elucidation of the local and long-range structural changes that occur in germanium anodes in lithium-ion batteries. *Chem Mater* 2015;27:1031-41. DOI
103. Loaiza LC, Monconduit L, Seznec V. Si and Ge-Based Anode Materials for Li-, Na-, and K-Ion Batteries: A Perspective from Structure to Electrochemical Mechanism. *Small* 2020;16:e1905260. DOI PubMed
104. Wen N, Chen S, Feng J, et al. In situ hydrothermal synthesis of double-carbon enhanced novel cobalt germanium hydroxide composites as promising anode material for sodium ion batteries. *Dalton Trans* 2021;50:4288-99. DOI PubMed
105. Zeng T, He H, Guan H, Yuan R, Liu X, Zhang C. Tunable hollow nanoreactors for in situ synthesis of GeP electrodes towards high-performance sodium ion batteries. *Angew Chem Int Ed* 2021;60:12103-8. DOI PubMed
106. Liu R, Luo F, Zeng L, et al. Dual carbon decorated germanium-carbon composite as a stable anode for sodium/potassium-ion batteries. *J Colloid Interface Sci* 2021;584:372-81. DOI PubMed
107. Yang Q, Wang Z, Xi W, He G. Tailoring nanoporous structures of Ge anodes for stable potassium-ion batteries. *Electrochem Commun* 2019;101:68-72. DOI
108. He C, Zhang JH, Zhang WX, Li TT. GeSe/BP van der waals heterostructures as promising anode materials for potassium-ion batteries. *J Phys Chem C* 2019;123:5157-63. DOI
109. Zhou Y, Zhao M, Chen ZW, Shi XM, Jiang Q. Potential application of 2D monolayer β-GeSe as an anode material in Na/K ion batteries. *Phys Chem Chem Phys* 2018;20:30290-6. DOI PubMed
110. Hao J, Wang Y, Guo Q, Zhao J, Li Y. Structural strategies for germanium-based anode materials to enhance lithium storage. *Part Part Syst Charact* 2019;36:1900248. DOI
111. Balogun M, Yang H, Luo Y, et al. Achieving high gravimetric energy density for flexible lithium-ion batteries facilitated by core-double-shell electrodes. *Energy Environ Sci* 2018;11:1859-69. DOI
112. Mo R, Rooney D, Sun K, Yang HY. 3D nitrogen-doped graphene foam with encapsulated germanium/nitrogen-doped graphene yolk-shell nanoarchitecture for high-performance flexible Li-ion battery. *Nat Commun* 2017;8:13949. DOI PubMed PMC

113. Seo M, Park M, Lee KT, Kim K, Kim J, Cho J. High performance Ge nanowire anode sheathed with carbon for lithium rechargeable batteries. *Energy Environ Sci* 2011;4:425-8. DOI
114. Li D, Feng C, Liu HK, Guo Z. Hollow carbon spheres with encapsulated germanium as an anode material for lithium ion batteries. *J Mater Chem A* 2015;3:978-81. DOI
115. Kim D, Park C. Co-Ge compounds and their electrochemical performance as high-performance Li-ion battery anodes. *Mater Today Energy* 2020;18:100530. DOI
116. Zhao Z, Ma W, Wang Y, Lv Y, Ma C, Liu X. Boosting the electrochemical performance of nanoporous CuGe anode by regulating the porous structure and solid electrolyte interface layer through Ni-doping. *Appl Surf Sci* 2021;558:149868. DOI
117. Bensalah N, Matalkeh M, Mustafa NK, Merabet H. Binary Si-Ge Alloys as high-capacity anodes for Li-ion batteries. *Phys Status Solidi A* 2020;217:1900414. DOI
118. Doherty J, McNulty D, Biswas S, et al. Germanium tin alloy nanowires as anode materials for high performance Li-ion batteries. *Nanotechnology* 2020;31:165402. DOI PubMed
119. Rodriguez JR, Qi Z, Wang H, et al. $Ge_2Sb_2Se_5$ glass as high-capacity promising lithium-ion battery anode. *Nano Energy* 2020;68:104326. DOI
120. Kim WS, Vo TN, Kim IT. GeTe-TiC-C composite anodes for Li-ion storage. *Materials* 2020;13:4222. DOI PubMed PMC
121. Zhou X, Li T, Cui Y, et al. In situ and operando morphology study of germanium-selenium alloy anode for lithium-ion batteries. *ACS Appl Energy Mater* 2020;3:6115-20. DOI
122. Lee G, Jun Choi Y, Hwan Kim Y, et al. Amorphization of germanium selenide driven by chemical interaction with carbon and realization of reversible conversion-alloying reaction for superior K-ion storage. *Chem Eng J* 2022;430:132995. DOI
123. Sultana I, Ramireddy T, Rahman MM, Chen Y, Glushenkov AM. Tin-based composite anodes for potassium-ion batteries. *Chem Commun* 2016;52:9279-82. DOI PubMed
124. Wang Q, Zhao X, Ni C, et al. Reaction and capacity-fading mechanisms of tin nanoparticles in potassium-ion batteries. *J Phys Chem C* 2017;121:12652-7. DOI
125. Ramireddy T, Kali R, Jangid MK, Srihari V, Poswal HK, Mukhopadhyay A. Insights into electrochemical behavior, phase evolution and stability of Sn upon K-alloying/de-alloying via in situ studies. *J Electrochem Soc* 2017;164:A2360-7. DOI
126. Qin G, Liu Y, Han P, Wang L, Liu F, Ma J. Self-regulating organic polymer coupled with enlarged inorganic SnS_2 interlamellar composite for potassium ion batteries. *Adv Funct Mater* 2020;30:2005080. DOI
127. Hu R, Fang Y, Liu X, et al. Synthesis of SnS_2 ultrathin nanosheets as anode materials for potassium ion batteries. *Chem Res Chin Univ* 2021;37:311-7. DOI
128. Verma R, Didwal PN, Nguyen A, Park C. SnSe nanocomposite chemically-bonded with carbon-coating as an anode material for K-ion batteries with outstanding capacity and cyclability. *Chem Eng J* 2021;421:129988. DOI
129. Lakshmi V, Chen Y, Mikhaylov AA, et al. Nanocrystalline SnS_2 coated onto reduced graphene oxide: demonstrating the feasibility of a non-graphitic anode with sulfide chemistry for potassium-ion batteries. *Chem Commun* 2017;53:8272-5. DOI PubMed
130. Cao L, Luo B, Xu B, et al. Stabilizing intermediate phases via efficient entrapment effects of layered VS_4/SnS@C heterostructure for ultralong lifespan potassium-ion batteries. *Adv Funct Mater* 2021;31:2103802. DOI
131. Sun H, Zhang Y, Xu X, et al. Strongly coupled Te-SnS_2/MXene superstructure with self-autoadjustable function for fast and stable potassium ion storage. *J Energy Chem* 2021;61:416-24. DOI
132. Cao Y, Chen H, Shen Y, et al. SnS_2 Nanosheets anchored on nitrogen and sulfur Co-doped MXene sheets for high-performance potassium-ion batteries. *ACS Appl Mater Interfaces* 2021;13:17668-76. DOI PubMed
133. Zhou S, Lan J, Song K, Zhang Z, Shi J, Chen W. SnS/SnS_2/rGO heterostructure with fast kinetics enables compact sodium ion storage. *FlatChem* 2021;28:100259. DOI
134. Sun Q, Li D, Dai L, Liang Z, Ci L. Structural engineering of SnS_2 encapsulated in carbon nanoboxes for high-performance sodium/potassium-ion batteries anodes. *Small* 2020;16:e2005023. DOI PubMed
135. Wen S, Gu X, Ding X, et al. Constructing ultrastable electrode/electrolyte interface for rapid potassium ion storage capability via salt chemistry and interfacial engineering. *Nano Res* 2022;15:2083-91. DOI
136. Sheng C, Yu F, Li C, et al. Diagnosing the SEI layer in a potassium ion battery using distribution of relaxation time. *J Phys Chem Lett* 2021;12:2064-71. DOI PubMed

Wan *et al. Microstructures* 2023;3:2023014
DOI: 10.20517/microstructures.2022.36

Microstructures

Research Article

Open Access

The effect of chromium content on the corrosion behavior of ultrafine-grained $Cr_xMnFeCoNi$ high-entropy alloys in sulfuric acid solution

Tian Wan, Zhikun Huang, Zhuo Cheng, Mingyu Zhu, Weiwei Zhu, Zongyuan Li, Danni Fu, Fuzeng Ren

Department of Materials Science and Engineering, Southern University of Science and Technology, Shenzhen 518055, Guangdong, China.

Correspondence to: Prof. Fuzeng Ren, Department of Materials Science and Engineering, Southern University of Science and Technology, Shenzhen 518055, Guangdong, China. E-mail: renfz@sustech.edu.cn

How to cite this article: Wan T, Huang Z, Cheng Z, Zhu M, Zhu W, Li Z, Fu D, Ren F. The effect of chromium content on the corrosion behavior of ultrafine-grained $Cr_xMnFeCoNi$ high-entropy alloys in sulfuric acid solution. *Microstructures* 2023;3:2023014. https://dx.doi.org/10.20517/microstructures.2022.36

Received: 30 Oct 2022 **First Decision:** 1 Dec 2022 **Revised:** 6 Jan 2023 **Accepted:** 30 Jan 2023 **Published:** 22 Feb 2023

Academic Editors: Jun Chen, Shiqing Deng **Copy Editor:** Fangling Lan **Production Editor:** Fangling Lan

Abstract

Chromium (Cr) plays a critical role in the corrosion resistance of conventional alloys via the formation of a dense Cr oxide-based passive film. However, the exact role of Cr in the corrosion of high-entropy alloys (HEAs) remains unclear. The effect of Cr content on the corrosion behavior of the ultrafine-grained $Cr_xMnFeCoNi$ (x = 0, 0.6, 1, and 1.5) HEAs in the sulfuric acid solution (0.5 M H_2SO_4) was investigated. These HEAs were fabricated using a combination of mechanical alloying and spark plasma sintering. The electrochemical tests show that the passive film was more compact and thicker at higher Cr concentration, but the corrosion rate first increased and then decreased, due to the presence of the nanocrystalline-amorphous phase boundaries in the passive film. Long-time immersion tests show that the corrosion rate increased exponentially with the Cr content, due to the gradual accumulation of the galvanic corrosion.

Keywords: High-entropy alloy, polarization, galvanic corrosion, passive film

INTRODUCTION

High-entropy alloys (HEAs) have been reported with excellent mechanical properties at cryogenic temperatures[1-3] and high resistance to wear[4], irradiation[5] and corrosion[6,7], and are thus considered to be

© The Author(s) 2023. **Open Access** This article is licensed under a Creative Commons Attribution 4.0 International License (https://creativecommons.org/licenses/by/4.0/), which permits unrestricted use, sharing, adaptation, distribution and reproduction in any medium or format, for any purpose, even commercially, as long as you give appropriate credit to the original author(s) and the source, provide a link to the Creative Commons license, and indicate if changes were made.

promising candidates in extreme structural applications[8]. Among the HEAs, face-centered-cubic (fcc) CoCrFeMnNi HEA is of particular interest due to its excellent combination of high strength-ductility-toughness at cryogenic temperature[9-11]. For example, Gludovatz *et al.* reported that the CrMnFeCoNi HEA showed remarkable fracture toughness at cryogenic temperatures down to 77 K, comparable to the austenitic stainless steels and high Ni steels[10]. Such HEA and its sub-family generally have high Cr content, much above the required amount (12 at.%) to obtain "stainless" behavior on the surface for conventional corrosion-resistant alloys, such as stainless steel and nickel-based alloys[12], and thus, are expected to have superior corrosion resistance.

The mechanism of Cr to enhance the corrosion resistance of alloys is through the formation of a dense Cr oxide-based passive film[13,14], which serves as an effective barrier on an alloy across a wide range of pH[15]. There have been numerous reports on the corrosion behaviors of CoCrFeNi-based HEAs in recent few years[16-22]. Ye *et al.* found that the CrMnFeCoNi HEA coating showed nobler corrosion potential (E_{corr}) and lower corrosion current (I_{corr}) derived from the potentiodynamic polarization tests than 304 stainless steel (304SS) in a 0.5 M H_2SO_4 solution[21]. The AlCoCuFeNiCr HEA immersed in sulfuric acid solution showed better corrosion resistance than the Cr-free HEA, attributing to the formation of the compact Cr_2O_3 passive film on the surface[17]. However, the corrosion resistance of CrMnFeCoNi HEA was inferior when compared with 304 L stainless steel in a 0.1 M H_2SO_4 solution, because the passive film on the CrMnFeCoNi HEA was very unstable due to the low content of Cr and the extensive formation of metal hydroxide in the passive film[22]. Similar phenomena were also observed in several Cr-containing HEA systems, such as AlCoCrFeNi[18,19] and $FeCoNiCrCu_x$ HEAs[20]. For these HEAs, the distribution of Cr element in the matrix is relatively inhomogeneous and the Cr-depleted phase as anode would become a sensitive site to induce the formation of pitting. As a result, the general corrosion rate would be accelerated by the galvanic corrosion effect. Even with the same composition system of CoCrFeMnNi HEA, distinct corrosion behavior was observed[21-24]. Wang *et al.* found that the oxide film on HEA was duplex, comprising a Cr/Mn inner oxide layer and a Cr/Fe/Co outer oxide/hydroxide layer[25]. For now, the effect of Cr content on the corrosion mechanism in the HEAs has not been unraveled in detail. The matrix structure, composition, and the competing effect of the passive film and the pitting on the corrosion behavior can be revealed by exploring the Cr-containing HEAs with varying Cr concentrations.

In this work, the corrosion behavior of the Cr_xMnFeCoNi (x = 0, 0.6, 1, and 1.5, respectively) HEAs with varying Cr concentrations in a 0.5 M H_2SO_4 solution was investigated. The matrix microstructure was characterized using X-ray diffraction (XRD), scanning electron microscopy (SEM) and transmission electron microscopy (TEM) in detail. Moreover, the corrosion behavior of the Cr_xMnFeCoNi HEAs was examined using the potentiodynamic polarization tests and the electrochemical impendence spectroscope (EIS), along with the static immersion tests. Then, the corroded surface was analyzed using SEM, TEM, atomic force microscope (AFM) and X-ray photoelectron spectroscopy (XPS). Our main objective is to give an in-depth understanding of the effect of Cr on the corrosion behavior of the Cr_xMnFeCoNi HEAs in sulfuric solution.

EXPERIMENTAL PROCEDURE

Alloy fabrication

The Cr_xMnFeCoNi (x = 0, 0.6, 1, and 1.5) HEAs (hereafter denoted as Cr0, Cr0.6, Cr1, Cr1.5, respectively) were prepared using commercially pure (99.9 wt.%) elemental powder of Cr, Mn, Fe, Co and Ni as the starting material. The powder mixture was put into a stainless steel vial with a ball-to-powder mass ratio of 5:1 and subjected to high-energy ball milling for 9 h using a SPEX 8000D mill at ambient temperature in an argon glovebox. The ball-milled powders were consolidated by spark plasma sintering (SPS-211Lx,

Fujidempa Kogyo. Co., Ltd, Japan) at 950 °C for 5 min under a pressure of 45 MPa in vacuum condition (~ 6 Pa).

The sintered cylindrical HEAs were cut into discs using electrical discharge machining for subsequent characterization and tests. For electrochemical tests, the samples were cut into discs with a size of Φ = 10 mm × 3 mm, and sealed in epoxy with one surface exposed. The exposed surface was first mechanically ground using SiC paper down to 2400 grit, followed by vibratory polishing using a 0.06 μm alumina suspension. The polished samples were then cleaned with deionized water and alcohol and dried in air. For static immersion tests, both surfaces of the samples of the discs were ground and polished following the same procedure as those used for the electrochemical tests.

Microstructure characterization of the as-sintered HEAs

The phase of the as-sintered $Cr_xMnFeCoNi$ (x = 0, 0.6, 1, and 1.5) HEAs was identified using XRD patterns recorded on a Rigaku Smartlab-9KW diffractometer with Cu-Kα radiation (45 kV, 200 mA). The data were collected with 2θ in the range of 30° to 80° with a step size of 0.02° at a scanning speed of 10°/min. The surface morphology and composition were examined using SEM (TESCAN MIRA 3, Czech Republic) coupled with energy-dispersive X-ray spectroscopy (EDS). Electron backscatter diffraction (EBSD) was performed to characterize the grain structure of the HEAs. TEM (FEI Tecnai F30, USA) and high-angle annular dark-field scanning TEM (HAADF-STEM) were used to characterize the microstructure of the as-sintered HEAs. The TEM samples were prepared using site-specific focused ion beam (FIB; FEI Helios Nano Lab™ 600i) lift-out technique. Besides, platinum cap layers with a thickness of ~1 μm were deposited before milling the trench to protect the surface.

Electrochemical corrosion and immersion tests

Electrochemical measurements were performed in a 0.5 M H_2SO_4 solution at ambient temperature using a Princeton Applied Research Versa Studio (PARSTAT 4000A, Ametek Scientific Instruments, USA). A standard three-electrode cell system was performed during all the measurements using a platinum sheet as the counter electrode, a saturated calomel electron (SCE) as the reference electrode and the $Cr_xMnFeCoNi$ HEAs as the working electrode. Before EIS and potentiodynamic polarization tests, the specimens were subjected to the potentiostatic polarization at -0.6 V *vs.* SCE for 5 min to remove the surface oxidation, and then the open-circuit potential (OCP) was measured for 2 h in order to obtain a steady or quasi-steady potential value. EIS tests were performed at OCP with the sinusoidal potential amplitude of 10 mV in the frequency range from 100 kHz to 10 mHz. The data derived from EIS tests were fitted and analyzed using the Zsimpwin software. Then, the potentiodynamic polarization tests were conducted with the scanning range from -0.25 V *vs.* OCP to 1.3 V *vs.* SCE at a scan rate of 1 mV/s. Each electrochemical test was performed three times to confirm the reproducibility of the results.

The static immersion tests were performed in 0.5 M H_2SO_4 at ambient temperature for 15 days. Three parallel experiments were performed for each HEA. The average corrosion rate by mass loss C_w in mm/y was calculated using the following Eq. (1):

$$C_W = \frac{K\Delta W}{At\rho} \quad (1)$$

where k is the constant of 8.76×10^4, ΔW is the mass loss (g) after the immersion test, A is the surface area (cm^2), t is the immersion time (h), and ρ is the density (g/cm^3) of the sample, measured by Archimedes method.

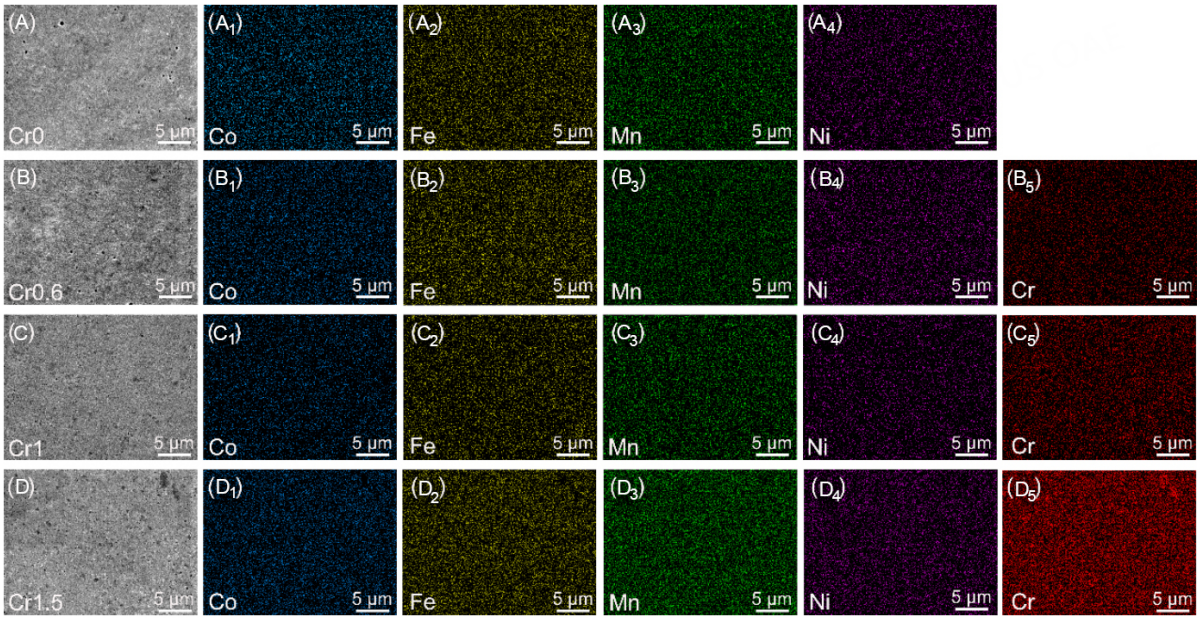

Figure 1. Surface morphology and EDS elemental maps of the as-sintered $Cr_xMnFeCoNi$ (x = 0, 0.6, 1, and 1.5) HEAs. (A-A_4) Cr0; (B-B_5) Cr0.6; (C-C_5) Cr1; and (D-D_5) Cr1.5. EDS: Energy-dispersive X-ray spectroscopy; HEAs: high-entropy alloys.

Corroded morphology and composition characterization

The corroded surface morphology was examined using SEM and AFM (Dimension edge, Bruker Corporation, Germany). The surface composition was analyzed using EDS and XPS (Thermo Scientific K-Alpha$^+$). The standard C 1s spectrum at a binding energy of 284.8 eV was employed to calibrate the original peaks, and the calibrated XPS data were analyzed and fitted by the software Avantage 5.9. TEM and HAADF-STEM coupled with EDS were used to analyze the typical corrosion micropores at the surface.

RESULTS

Phase, composition and microstructure of the as-sintered HEAs

The measured density of all the sintered $Cr_xMnFeCoNi$ HEAs exceeds ~ 98%. Very few pores were located on the surface [Figure 1A-D], confirming the high density of the HEAs. Some randomly distributed tiny dark spots were found on the surface. EDS line scanning profiles [Supplementary Figure 1] show that such dark spots are rich in Cr, Mn and O. EDS elemental maps [Figure 1] show the uniform distribution of Co, Fe, Mn and Ni, while Cr shows segregation and inhomogeneity. With a higher concentration of Cr, the Cr-rich region in the HEA is more obvious. Quantitative EDS analysis [Table 1] shows that the sintered HEAs have very close compositions to the nominal input ones.

XRD patterns of the $Cr_xMnFeCoNi$ HEAs [Figure 2] show that the spark-plasma-sintered HEAs have a dominant fcc matrix phase with a trace amount of (Cr, Mn)O_x oxides owing to the relatively low vacuum during the sintering process and the high chemical activity of Cr and Mn. The oxide phase content increases with the Cr concentration. The XRD patterns confirmed that the tiny dark particles found on the surface were oxides. EBSD inverse pole figure (IPF) maps [Figure 3] show that the $Cr_xMnFeCoNi$ HEAs have equi-axed grain structure and very similar average grain size, in the range of 312 to 360 nm. Furthermore, TEM-based techniques were used to characterize the microstructure in more detail. The HAADF-STEM image [Figure 4A] shows three contrasts. A considerable number of nano-sized precipitates in grey contrast are distributed at the grain boundaries and inside the grains of the matrix, where a few black precipitates are

Table 1. Quantitative EDS analysis (in atomic percentage) for the as-sintered Cr_xMnFeCoNi (x = 0, 0.6, 1, and 1.5) HEAs

Sample	Co	Fe	Mn	Ni	Cr
Cr0	25.0	25.4	25.0	24.6	-
Cr0.6	21.7	21.7	22.3	21.1	13.2
Cr1	19.4	20.3	20.2	19.7	20.4
Cr1.5	18.1	18.2	18.4	18.1	27.2

EDS: Energy-dispersive X-ray spectroscopy; HEAs: high-entropy alloys.

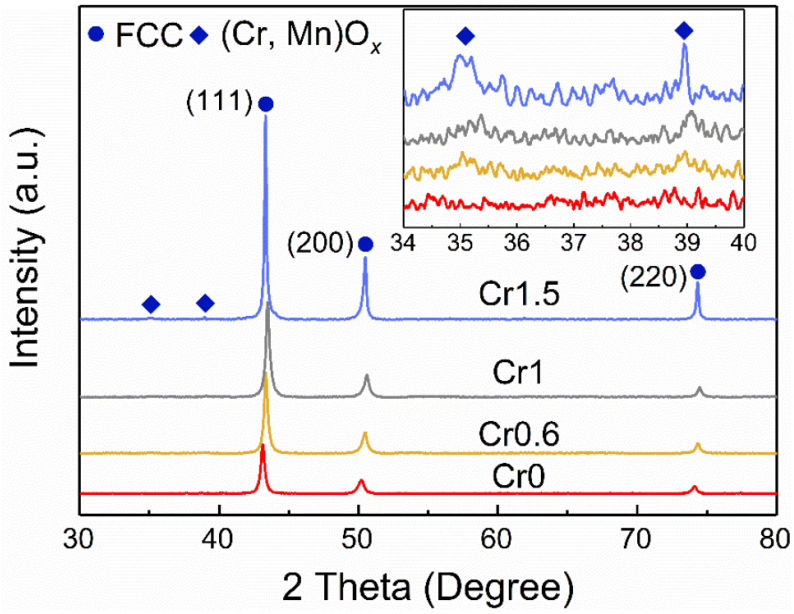

Figure 2. XRD patterns of the Cr_xMnFeCoNi (x = 0, 0.6, 1, and 1.5) HEAs. XRD: X-ray diffraction; HEAs: high-entropy alloys.

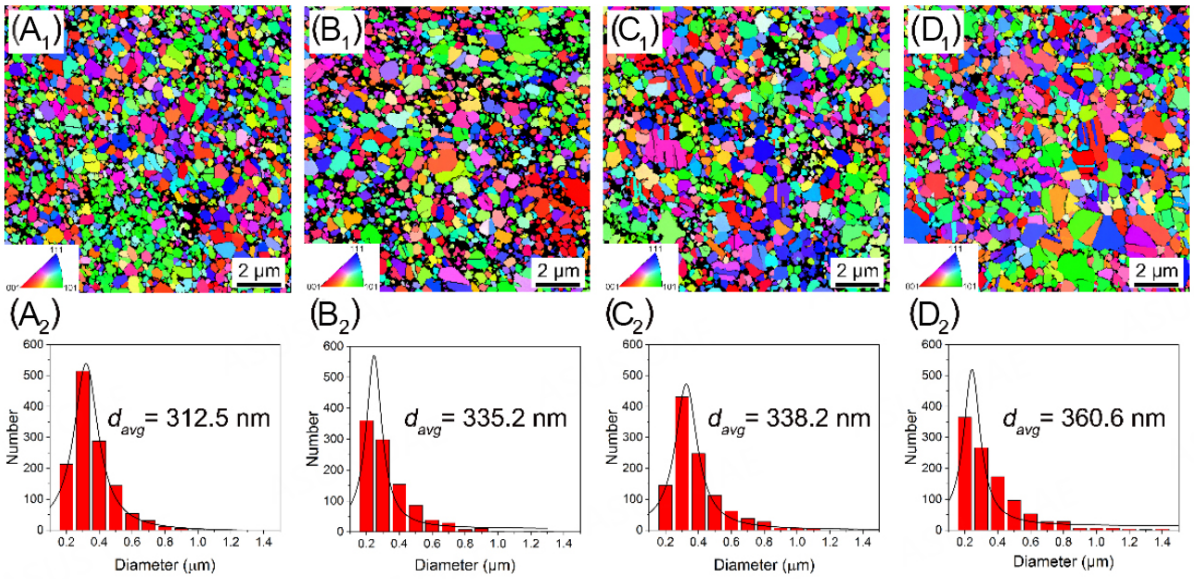

Figure 3. EBSD IPF maps and the average grain size distribution of the as-sintered Cr_xMnFeCoNi (x = 0, 0.6, 1, and 1.5) HEAs. (A) Cr0, (B) Cr0.6, (C) Cr1 and (D) Cr1.5. EBSD: Electron backscatter diffraction; IPF: inverse pole figure; HEAs: high-entropy alloys.

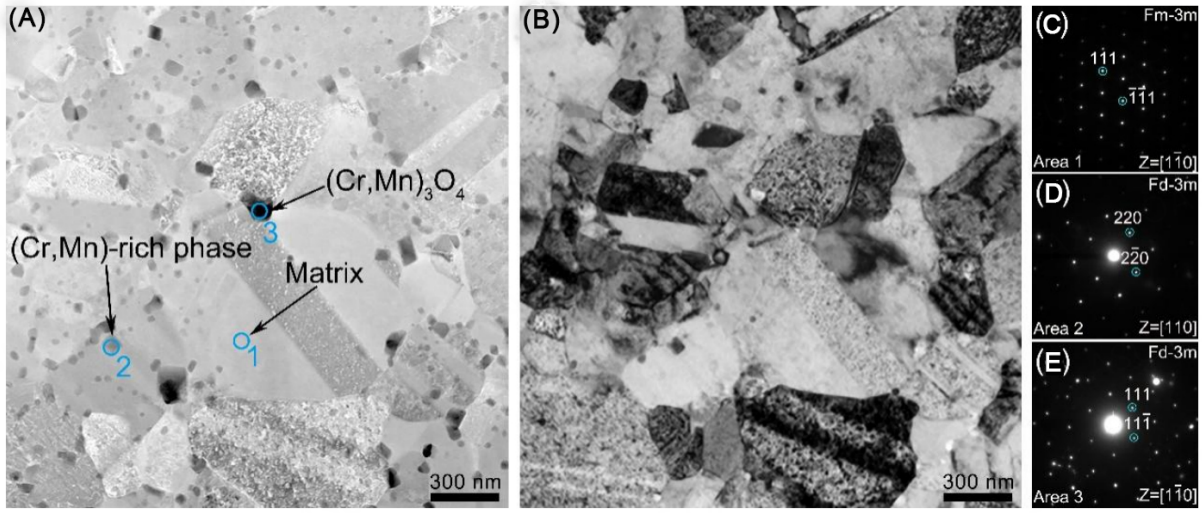

Figure 4. TEM characterization of the as-sintered CrMnFeCoNi (Cr1, x = 1) HEA. (A and B) are HAADF-STEM and corresponding bright-field TEM images; (C-E) are SAED patterns of the matrix, the grey precipitate and the black precipitate in (A), respectively. TEM: Transmission electron microscopy; HEA: high-entropy alloy; HAADF-STEM: high-angle annular dark-field scanning TEM; SAED: selected area electron diffraction.

located only at the grain boundaries. EDS quantitative analysis [Table 2] reveals that the matrix is depleted in Cr, while the grey precipitates are rich in Cr and Mn, and the black precipitates were identified to be (Cr, Mn)O_x, as detected in the XRD pattern in Figure 2. Bright-field TEM image [Figure 4B] clearly shows the microstructure of the Cr1 HEA. Selected area electron diffraction (SAED) patterns [Figure 4C-E] show that the matrix belongs to the Fm-3m space group, while both precipitates are in Fd-3m space group, consistent with the recent study[26] that also reported that the (Cr, Mn)O_x phase belonged to the Fd-3m space group in the Cr1 HEA fabricated using medium frequency induction melting. Combined with the EDS quantitative analysis, the black precipitates were identified to be (Cr, Mn)$_3O_4$.

Potentiodynamic polarization

Figure 5 shows the potentiodynamic polarization curves of Cr_xMnFeCoNi HEAs in a 0.5 M H_2SO_4 at room temperature. The values of E_{corr} and I_{corr} derived from the polarization curves were included in Table 3. With the increase of the Cr concentration, the E_{corr} shows more negative value from -0.40 V to -0.45 V, which suggests a more severe corrosion tendency, but not the actual corrosion rate at the moment in terms of kinetics[27,28]. The increment in the corrosion sensitivity may be due to the presence of more Cr-rich phases and the oxides precipitated in the matrix. In comparison with the CoFeMnNi HEA (Cr0) in the absence of the Cr, the I_{corr} of Cr0.6 HEA first increases and then gradually decreases with the increasing Cr concentration. The Cr0.6 HEA shows the highest I_{corr} of 5.36 μA/cm^2 and the Cr1.5 HEA shows the lowest I_{corr} of 2.75 μA/cm^2. Since the corrosion rate is positively correlated to I_{corr}, Cr0.6 has the lowest corrosion resistance, which may be attributed to the galvanic corrosion between the Cr-rich phase and the matrix as well as the lack of protection from the passive film. On the contrary, the Cr1.5 HEA has the highest corrosion resistance. However, when the applied potential reaches ~ 0.8 V, the current density of Cr1.5 increases faster than Cr0, suggesting that the Cr1.5 HEA has inferior pitting resistance.

Surface morphology and composition after polarization tests

After potentiodynamic polarization tests in the 0.5 M H_2SO_4 solution at room temperature, the Cr_xMnFeCoNi HEAs surfaces were covered with uniformly distributed micro-and nano-pores [Figure 6]. The average size of the pores increased, but the number reduced on the corroded surfaces of the HEAs with

Table 2. Quantitative EDS analysis (in atomic percentage) of Cr1 HEA in Figure 4A

Point	O	Cr	Mn	Fe	Co	Ni
1	-	16.3	21.3	21.6	19.8	21.0
2	10.4	26.4	22.1	13.4	13.3	14.4
3	47.3	31.1	21.6	-	-	-

EDS: Energy-dispersive X-ray spectroscopy; HEA: high-entropy alloy.

Table 3. Polarization parameters and equivalent circuit parameters for EIS of $Cr_xMnFeCoNi$ (x = 0, 0.6, 1 and 1.5) HEAs in a 0.5 M H_2SO_4 solution

Sample	E_{corr}/V	I_{corr}/μA/cm^2	Y_p/S·cm^{-2}·s^n	n_p	R_p/Ω·cm^2	*chsq*
Cr0	-0.40 ± 0.01	4.20 ± 0.08	2.60E-08	0.74	6113	2.28E-04
Cr0.6	-0.41 ± 0.03	5.36 ± 1.05	1.25E-08	0.79	3510	1.47E-04
Cr1	-0.44 ± 0.01	3.33 ± 1.61	9.35E-09	0.84	5506	1.85E-04
Cr1.5	-0.45 ± 0.01	2.75 ± 1.41	1.11E-08	0.82	7715	5.73E-04

EIS: Electrochemical impendence spectroscope; HEAs: high-entropy alloys.

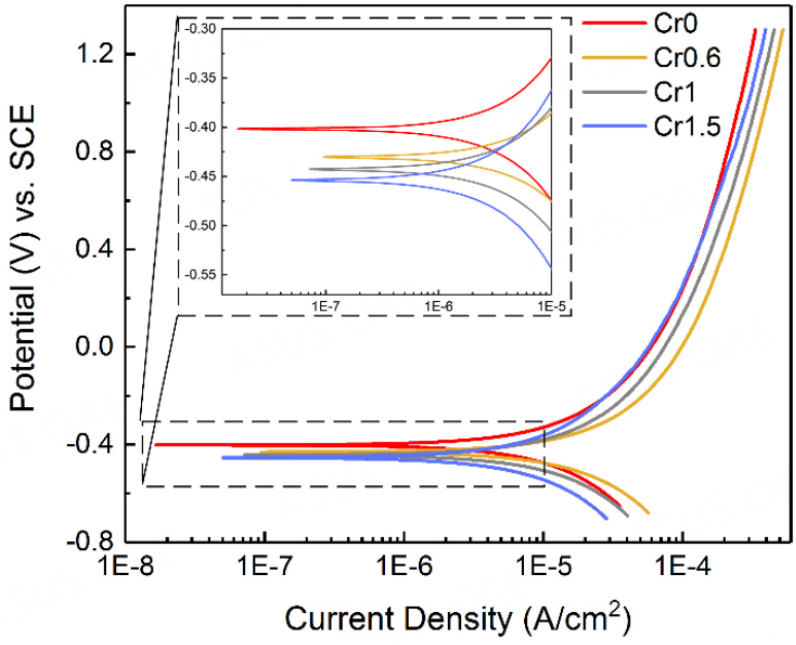

Figure 5. Potentiodynamic polarization curves of the as-sintered $Cr_xMnFeCoNi$ (x = 0, 0.6, 1, and 1.5) HEAs in a 0.5 M H_2SO_4 solution at room temperature.

a higher concentration of Cr, suggesting stronger tendency towards localized corrosion. AFM height images [Figure 6A3-D3] show that the depth of pores is in the range of 170 - 360 nm for Cr0, Cr0.6, and Cr1 HEAs. The Cr1 HEA shows the smallest depth of pores of ~ 180 nm, which might be attributed to the enhanced protective effect of the passive film to inhibit further corrosion from the etching solution. However, the surface micropores of the Cr1.5 HEA show much larger depth and reach ~1 μm, which could be liable to cause galvanic corrosion in the deep regions.

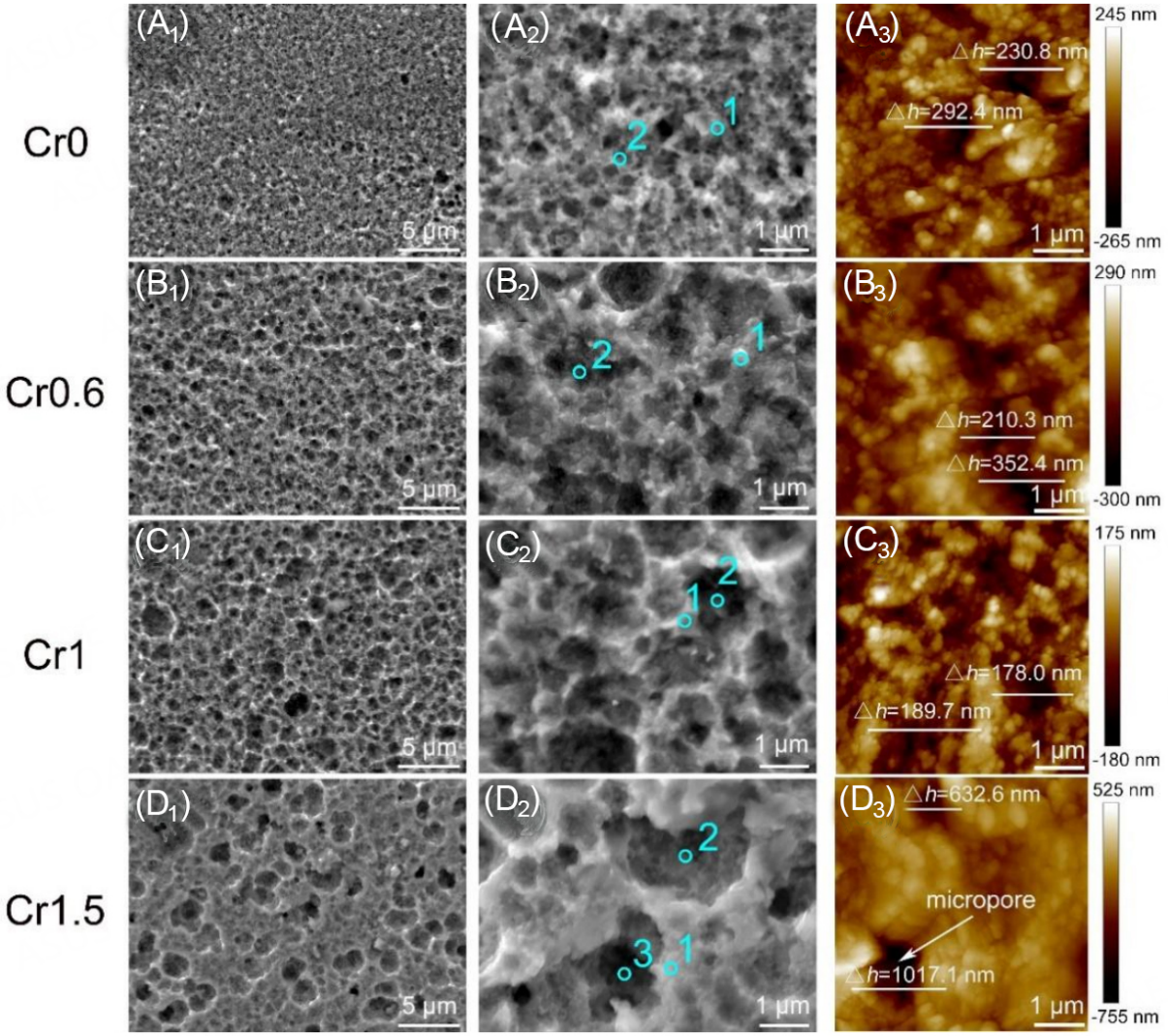

Figure 6. Surface morphology (A_1-D_1, A_2-D_2) and AFM height images (A_3-D_3) of the $Cr_xMnFeCoNi$ (x = 0, 0.6, 1, and 1.5) HEAs after polarization tests in a 0.5 M H_2SO_4 solution at room temperature.

Quantitative EDS analysis on the honeycomb-like surface of $Cr_xMnFeCoNi$ HEAs [Figure 6A2-D2] is included in Table 4. Inside the pores, all the four groups of HEAs have reduced content of Fe, Co and Ni but increased O, suggesting the selective dissolution of the elements Fe, Co and Ni and the formation of oxide films occurred simultaneously during the corrosion process. It is noted that the peak positions (point 1, Figure 6D2) of the Cr1.5 HEA surface contain a much higher content of O, indicating a better passivation effect on the region outside the micropores. However, the content of O in the deep valley of the pores (point 3, Figure 6D2) is lower than the shallow ones (point 2, Figure 6D2), and much lower than the peak positions (point 1, Figure 6D2), suggesting that the formation of oxide films was inhibited in the deep micropores. Hence, the region inside the deep micropores (point 3, Figure 6D2) of the Cr1.5 HEA would have the worst pitting corrosion resistance, as also confirmed by the content of selective dissolution elements. Furthermore, the corrosion behavior would be deteriorated due to the weak sites in sufficiently deep micropores during further corrosion and could cause pitting-like corrosion[29,30].

Table 4. Quantitative EDS analysis (in atomic percentage) on the corroded surface of $Cr_xMnFeCoNi$ (x = 0, 0.6, 1, and 1.5) HEAs in Figure 6

Sample	Point	O	Cr	Mn	Fe	Co	Ni
Cr0	(a_2)-1	-	-	24.8	25.0	25.6	24.6
	(a_2)-2	8.3	-	24.0	23.4	23.3	21.0
Cr0.6	(b_2)-1	5.9	12.5	20.3	20.6	20.2	20.5
	(b_2)-2	14.2	14.9	20.0	17.3	16.5	17.1
Cr1	(c_2)-1	-	20.3	19.9	20.3	20.1	19.4
	(c_2)-2	13.5	18.0	17.7	17.2	17.0	16.6
Cr1.5	(d_2)-1	16.0	24.6	16.8	14.5	13.6	14.5
	(d_2)-2	7.1	27.6	18.0	16.0	15.6	15.7
	(d_2)-3	2.4	34.0	23.8	14.7	12.8	12.3

EDS: Energy-dispersive X-ray spectroscopy; HEAs: high-entropy alloys.

XPS was performed to identify the chemical state of the corrosion products on the corroded surface of $Cr_xMnFeCoNi$ HEAs after polarization tests. The high-resolution XPS spectra and the quantitative analysis results were presented in Figure 7 and Table 5, respectively. For all the four groups of HEAs, the Co $2p_{3/2}$ spectrum is split into four constituent peaks, including Co (778.3 eV), CoO (780.2 eV), Co_2O_3 (781.3 eV), and $Co(OH)_2$ (782.1 eV). In addition, a Fe LM2 peak at 783.7 eV was also detected. The Fe $2p_{3/2}$ spectrum can be divided into four peaks as Fe at 707 eV, FeO at 709.3 eV, Fe_2O_3 at 710.8 eV, $Fe(OH)_3$ at 711.3 eV along with the Co LM2 at 712.7 eV, but the Fe in Cr0 HEA shows much lower intensity [Figure 7A2] compared with the Cr-containing HEAs. The Mn $2p_{3/2}$ spectrum is separated into four peaks as Mn at 638.8 eV, MnO at 640.5 eV, Mn_2O_3 at 641.5 eV, and MnO_2 at 642.6 eV along with Ni LM2 at 640.7 eV. The relative content of Mn oxides is larger than that of Co, Fe and Ni, especially for Cr0 and Cr1.5 HEAs. The Ni $2p_{3/2}$ spectrum is separated into four peaks with Ni at 853 eV, NiO at 854.2 eV, $Ni(OH)_2$ at 855.5 eV and Ni_{sat} at 859.4 eV. Based on the relative intensity of each element, it is concluded that the corroded surfaces are mainly composed of the metallic Ni and Co and small amounts of oxides/hydroxides. The Cr0 and Cr1.5 HEAs contain more Fe oxides/hydroxides. Moreover, the Cr $2p_{3/2}$ spectrum for Cr-containing HEAs is separated into three peaks as Cr at 574.2 eV, Cr_2O_3 at 576.1 eV and $Cr(OH)_3$ at 577.1 eV. The relative contents of Cr oxide and hydroxide are obviously higher compared to those of Co, Fe and Ni for Cr1.5 HEA.

Compared with Cr0 HEA in the absence of Cr, the Cr0.6 HEA shows significantly reduced content of Fe and Mn oxides/hydroxides in the oxide film, which thus shows weaker corrosion resistance. Likewise, as the Cr concentration increases from Cr 0.6 to Cr1.5, the increased amount of oxide/hydroxide of Cr, Mn and Fe provides denser and more protective oxide film for Cr1.5 HEA than Cr0.6 and Cr1 HEAs. However, the enrichment of Mn in the oxide film could degrade the stability of the passive film[31], which could lead to the breakdown of the oxide film in the local region of the Cr1.5 HEA during severe corrosion. On the whole, the quantitative analysis results suggest that Co and Ni are preferentially dissolved, which are in agreement with the results of the EDS point analysis in Table 4. The content of Fe does not reduce obviously for Cr0, Cr0.6 and Cr1, except for Cr1.5, showing that the selective dissolution of Fe is more difficult than Co and Ni. It also demonstrates that Cr oxide (Cr_2O_3) and hydroxide ($Cr(OH)_3$) are indeed generated on the surfaces of Cr-containing HEAs in the nominal Cr concentration of ~13.0 at.% at least, which is close to the threshold in conventional stainless steels[12].

In order to clarify the honeycomb-like structure of the surface, the cross-sectional microstructure of a typical corrosion micropore located on the surface of Cr1 was characterized by TEM in detail, as shown in

Table 5. The quantitative analysis (in atomic percentage) of the XPS spectra of the corroded surface on Cr0, Cr0.6, Cr1 and Cr1.5 in Figure 7

Spectrum	Substance	Cr0	Cr0.6	Cr1	Cr1.5
Co $2p_{3/2}$	Co	13.4	17.6	15.6	9.0
	CoO	2.8	0.2	0.9	0.9
	Co_2O_3	2.1	0.2	1.1	0.2
	$Co(OH)_2$	3.7	1.9	3.0	1.1
Fe $2p_{3/2}$	Fe	10.1	19.3	16.2	10.2
	FeO	11.0	0.3	1.6	1.1
	Fe_2O_3	3.6	0.7	2.0	3.8
	$Fe(OH)_3$	2.3	1.3	1.2	-
Mn $2p_{3/2}$	Mn	3.8	11.0	12.4	3.6
	MnO	3.4	2.1	2.1	4.2
	Mn_2O_3	10.1	6.8	4.2	10.0
	MnO_2	8.7	1.9	2.4	2.9
Ni $2p_{3/2}$	Ni	15.1	13.4	12.7	8.4
	NiO	4.6	1.8	2.2	1.8
	$Ni(OH)_2$	5.3	3.2	2.7	4.3
Cr $2p_{3/2}$	Cr	-	12.1	15.7	13.7
	Cr_2O_3	-	1.8	2.6	18.4
	$Cr(OH)_3$	-	4.4	1.4	6.4

Figure 8. The depth of the micropore is ~200 nm, in line with the result of the AFM height image in Figure 6. Furthermore, the selected cross-section can clearly be divided into two regions. The top region above the interface (the dotted line in Figure 8A) is referred to as the oxide film inside the micropore, while the region below the interface is the un-corroded matrix. High-resolution TEM image [Figure 8A] along with fast Fourier transform (FFT) patterns [Figure 8B and C] reveals that the oxide film consists of both amorphous and nanocrystalline (Cr, Mn)O_x. The boundaries between the nanocrystalline and the amorphous phases are considered to provide tunnels for species diffusion and transport, where the corrosive ions permeate preferentially, similar to the mechanism that the Cl^- ion attacks on the oxide film of the metals[32]. It might be induced by the detrimental effect of Mn, which could be concentrated in the oxide film to greatly affect the occurrence of the nanocrystalline phase. The EDS elemental maps [Figure 8E] indicate that the oxide film is rich in Mn, Cr and O, but deficient in Fe, Co and Ni.

EIS

To understand the corrosion mechanism of Cr_xMnFeCoNi HEAs in the 0.5 M H_2SO_4 solution, the EIS measurements under OCP conditions were conducted and analyzed in Figure 9. In terms of the Nyquist plots [Figure 9A], all HEAs have similar features where a depressed capacitive semicircle covers high frequency region and some scattered points are distributed randomly near the real axis in the low frequency region. The diameter of the capacitive semicircle first decreases from Cr0 to Cr0.6 and then increases to Cr1.5, indicating the same trend for the corrosion resistance[22,33]. It is found that only one time constant is presented in the high frequency of each Bode plot [Figure 9B], indicating the corrosion behavior of the passive film. With the decrease of the frequency, the phase angle reduces. The capacitance for the passive film increases and the corrosion resistance decreases, suggesting that the etching solution gradually sinks into the passive film. Moreover, in the wide range of the low frequency region, the phase angles are all approximately 0° and the values of $|Z|$ are constant, which are characteristic of the pure resistance, indicating that the passive films on the HEAs are not very compact. Likewise, the value of $|Z|$ at a fixed frequency of 0.1 Hz is usually equal to the polarization resistance related to the corrosion resistance[34].

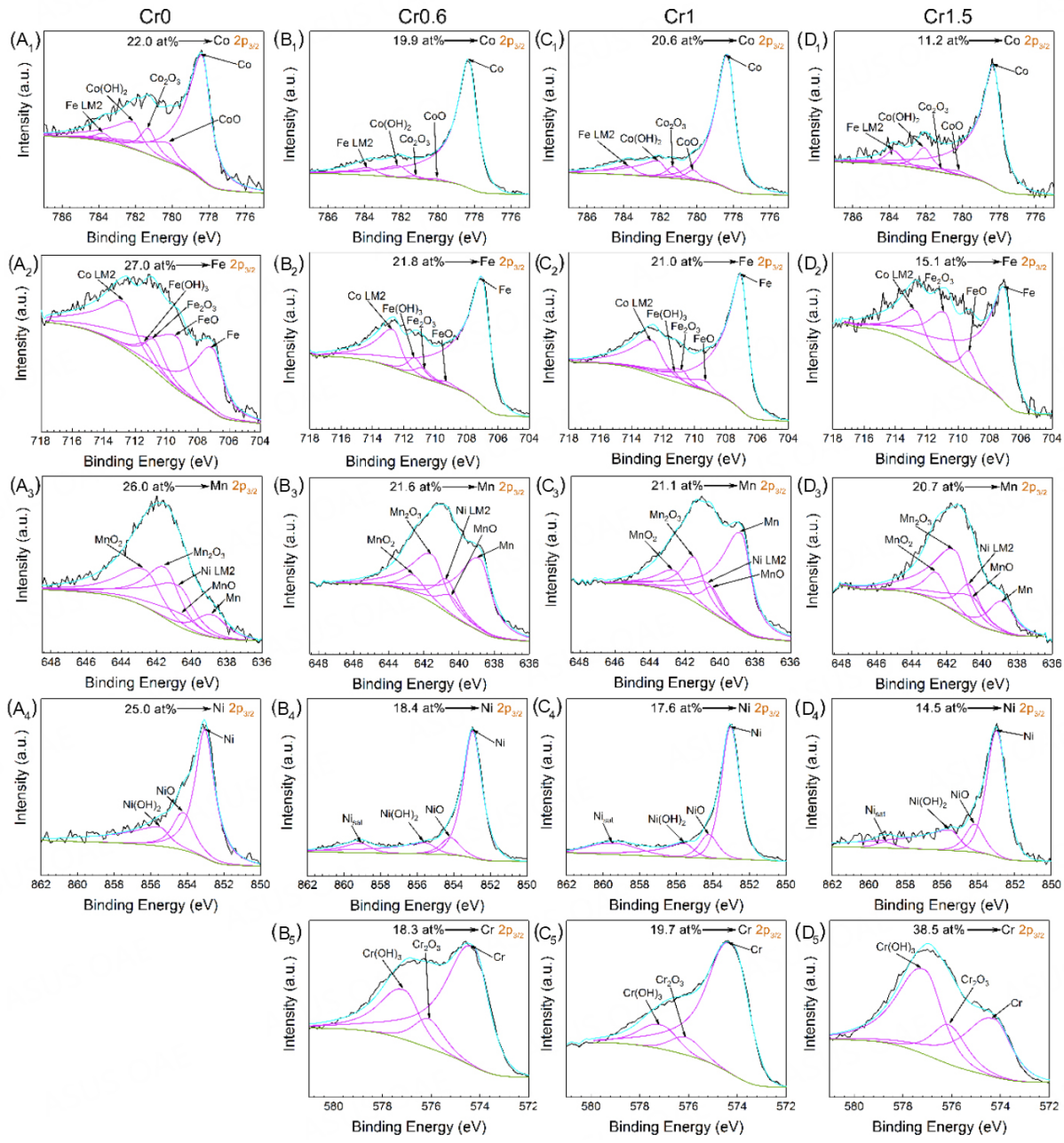

Figure 7. High-resolution XPS spectra of the corroded surface on Cr0 (A_1-A_4), Cr0.6 (B_1-B_5), Cr1 (C_1-C_5), and Cr1.5 (D_1-D_5) HEAs after polarization in a 0.5 M H_2SO_4 solution at room temperature. (A_1-D_1) Co $2p_{3/2}$; (A_2-D_2) Fe $2p_{3/2}$; (A_3-D_3) Mn $2p_{3/2}$; (A_4-D_4) Ni $2p_{3/2}$; and (B_5-D_5) Cr $2p_{3/2}$. XPS: X-ray photoelectron spectroscopy.

Therefore, the corrosion resistance follows the order of Cr1.5 > Cr0 > Cr1 > Cr0.6. On the other hand, there is no straight line representing the diffusion process or another capacitive semicircle corresponding pitting behavior present in the Nyquist plot, which is due to the simultaneous formation of the passive film at the corroded region when the etching solution reaches the matrix [Figure 6].

In order to fit the results of the EIS under the OCP condition, an electrical equivalent circuit (EEC) model (inset in Figure 9A) was used. In the EEC model, a parallel combination of a constant phase element Q_p and

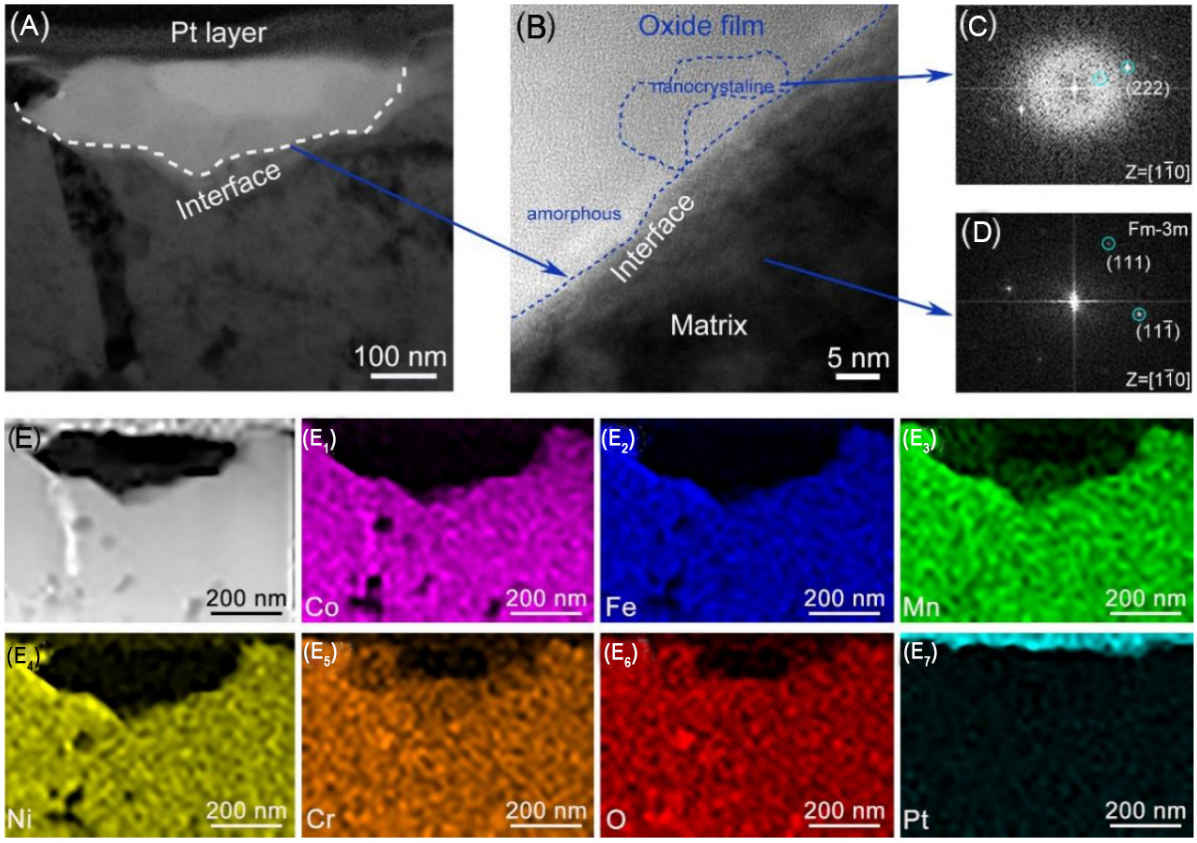

Figure 8. TEM characterization of a typical corrosion micropore on the surface of Cr1 HEA. (A) Bright-field TEM image; (B-D) are the high-resolution TEM image obtained from the interface region and the corresponding FFT patterns, respectively; and (E-E_7) HAADF-STEM image with the corresponding EDS elemental maps. TEM: Transmission electron microscopy; HEA: high-entropy alloy; FFT: fast fourier transform; HAADF-STEM: high-angle annular dark-field scanning TEM; EDS: energy-dispersive X-ray spectroscopy.

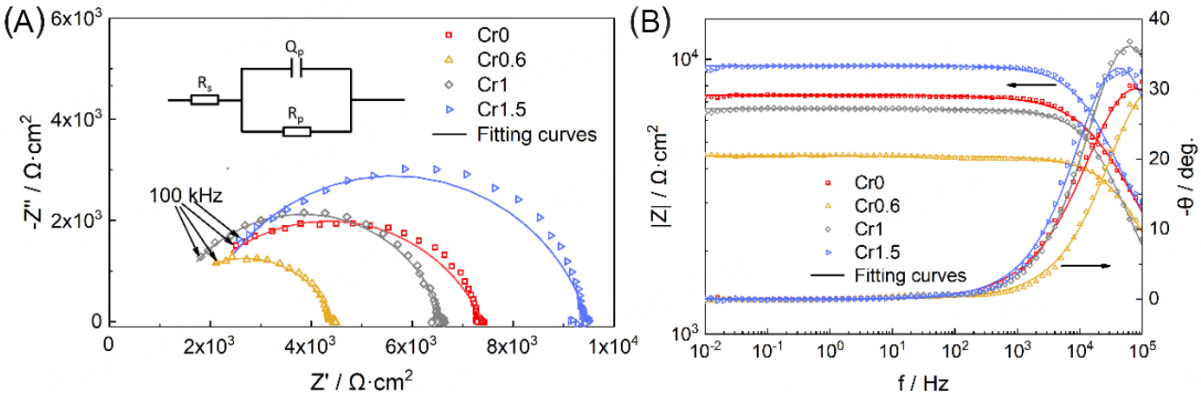

Figure 9. Nyquist (A) and Bode plots (B) of the $Cr_xMnFeCoNi$ (x = 0, 0.6, 1, and 1.5) HEAs in a 0.5 M H_2SO_4 solution under open circuit potential condition. The inset in (A) is the electrical equivalent circuit (EEC) for fitting the EIS results. HEAs: High-entropy alloys; EIS: electrochemical impendence spectroscope.

a passivation layer resistance R_p corresponding to one time constant is in series with a solution resistance R_s, which has good fitting reliability as the small chi-square values in the order of magnitudes of 10^{-4} listed in Table 3. Herein, the ideal capacitance C_p is replaced by the constant phase element Q_p to compensate for the

non-homogeneity and the capacity dispersion in the system[35], such as an uneven corroded surface. The Q_p impendence Z_Q is given as follows,

$$Z_Q = Y_p^{-1}(j\omega)^{n_p} \quad (2)$$

Where Y_p is the proportionality factor, j is the imaginary unit, ω is the phase frequency, and n is the phase shift, reflecting the degree of the dispersion for an ideal capacitance. For n_p = 1, Z_Q represents a pure capacitance with $C_p = Y_p$; for n_p = 0.5, it presents a Warburg resistance; and for n_p = 0, it presents a pure resistance with $R_p = Y_p^{-1}$. As a result, n_p increases from Cr0 to Cr1, implying that the passive film becomes more compact on the surface. While from Cr1 to Cr1.5, n_p decreases slightly, which is ascribed to the discontinuous passive film containing the weak site in the deep micropore, as shown in Figure 6. Moreover, as the value of n_p is in the range of 0.74-0.84, which is close to 1, the value of Y_p can be approximately regarded as capacitance C_p of the passive film. Considering the Helmholtz model[21,36], the value of Y_p is determined by the equation as follows,

$$Y_p \approx C_p = \frac{\varepsilon\varepsilon_0}{d}S \quad (3)$$

where d is the thickness of the passive film, S is the exposed surface area, ε_o is the permittivity of the vacuum, and ε is the dielectric constant of the surface which is mainly determined by the composition of the passive film. Therefore, the decrease of the value of Y_p from Cr0 to Cr1 and then the increase from Cr 1 to Cr1.5 can be affected by two factors for all samples: the change of the composition and the thickness of the passive film. Meanwhile, as Cr0.6 and Cr1 have a similar surface composition as analyzed by XPS [Figure 7], the larger Y_p of Cr1 is mainly induced by the thicker passive film than Cr0.6. Notably, the decreased Y_p for Cr1.5 should be mainly attributed to the change of the composition rather than the reduced thickness of the passive film. In terms of the resistance R_p, which reflects the corrosion resistance area of the passive film and the electron migration rate at the sample's surface/electrolyte interface, the smaller value of R_p indicates the lower corrosion resistance. Based on this, the corrosion resistance for the four groups of HEAs first decreases and then increases with the increasing concentration of Cr, in line with the results of the polarization tests.

Long-time immersion

Figure 10 shows the surface morphology and average corrosion rate of Cr_xMnFeCoNi HEAs after immersion in a 0.5 M H_2SO_4 solution for 15 days at room temperature. The distribution of the micropores on the surface has no difference from that after polarization tests, but the micropores are much larger and the surfaces become looser. The formation of a more honeycomb-like corrosion surface, especially for Cr1.5, suggests that the HEAs suffered from more severe corrosion during the immersion of the 15 days, due to the absence of the long-term stable passive film. Likewise, the average corrosion rate [Figure 10E] increases exponentially with the Cr concentration. The Cr1.5 HEA shows the highest corrosion rate, 6 times higher than that of Cr1, which seems in contradiction with the results of the electrochemical tests. The significant change in the corrosion behavior during the long-time immersion between the four groups of HEAs could be attributed to the transformed corrosion mechanism. The dominant galvanic corrosion behavior has a direct correlation with the Cr concentration, which would be discussed in detail later.

DISCUSSION

Honeycomb-like morphology after polarization tests

Interestingly, all samples show the honeycomb-like morphology after polarization tests, as shown in

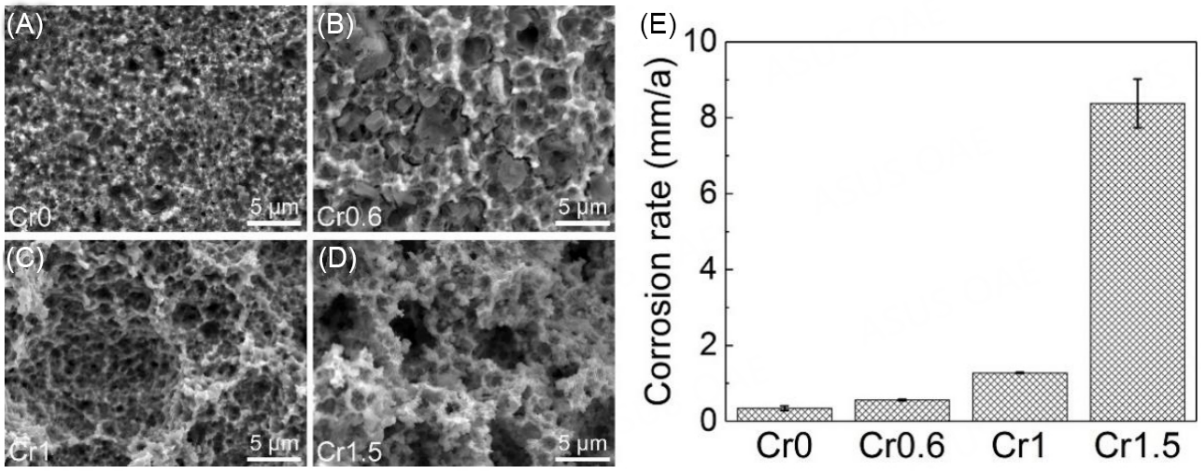

Figure 10. Surface morphology (A-D) and the average corrosion rate (E) by mass loss of the $Cr_xMnFeCoNi$ (x = 0, 0.6, 1, and 1.5) HEAs after immersion in a 0.5 M H_2SO_4 solution for 15 days at room temperature. HEAs: high-entropy alloys.

Figure 6, which means that the corroded micropores were uniformly distributed on the surfaces of $Cr_xMnFeCoNi$ HEAs. A similar phenomenon has also been observed in the Cr1 HEA corroded in H_2SO_4 solution[21,22]. Actually, such corrosion morphology for HEAs can be mainly affected by two factors: (i) the second phase; and (ii) the area of the grain boundaries. Considering that the four groups of HEAs show similar average grain sizes in the range of 312.5-360.6 nm (as shown in Figure 3), the difference in the area of the grain boundaries on the corrosion behavior should be negligible.

With the single fcc phase, the grain boundary has a dominant effect on the corrosion behavior for Cr0, which can act as a defect zone[37,38] and the galvanic corrosion between the grain boundary and the intragranular zone can occur during the corrosion process. Moreover, the grain size of Cr0 is ~ 300 nm, which is close to the diameters of micropores after the polarization tests in Figure 6A. Thus, it is confirmed that the intragranular zone as the anode for Cr0 was preferentially corroded and the grain boundary as the cathode acted as the corrosion barrier at the early stage in H_2SO_4 solution, so that many small micropores were generated on the surface. However, for Cr0.6, Cr1 and Cr1.5, the Cr-rich phase such as $(Cr, Mn)_3O_4$ dissolved out from the matrix, causing a greater impact than the grain boundary on the corrosion behavior. Meanwhile, the corrosion for the Cr-containing HEAs occurred mainly around the $(Cr, Mn)_3O_4$ phase zone and the galvanic corrosion mainly occurred between the second phases and the matrix. With more segregation of the Cr and the increase of the average size of the Cr-rich zone at higher Cr concentration [Figure 1], the galvanic corrosion effect would become stronger as the increasing area ratio of cathode to anode, resulting in the larger and more dispersed micropores in the honey-like morphology [Figure 6]. The depth of the micropores was mainly increased by the galvanic corrosion effect and restrained by the protective effect of the passive film. As more severe galvanic corrosion present in Cr1.5, also indicated by the value of E_{corr}, much deeper micropores were formed on the surface than the other HEAs. The smallest depth of the micropores of Cr1 should be mainly attributed to its dense passive film that has not been damaged by the insufficient galvanic effect at this stage. Moreover, the tiny height fluctuation in or out of the micropores was observed in Figure 6, which may be caused by the galvanic effect between the matrix and the heterogeneous nanoscale particles, such as the (Cr, Mn)-rich phase shown in Figure 4.

Corrosion process during the polarization tests

It is found that when the four groups of HEAs were corroded in the 0.5 M H_2SO_4 solution, the selective dissolution proceeded and the element Co, Ni and Fe were preferentially released from the matrix, which

may be attributed to the dissolution rate difference of the constituent elements in these HEAs in the corrosion environment[7,39]. The hydroxides of Cr, Mn and Fe were deposited on the surface of the HEAs by the hydrolysis reactions at the same time, then some hydroxides formed early in the inner layer may dehydrate to form the oxides[40,41], such as Cr_2O_3. Therefore, the complete passive films were formed. The major chemical reactions present in the above corrosion process are shown as follows:

Anodic reaction: $M \rightarrow M^{n+} + ne^-$ (M: constituent metal element of the HEAs)

Cathodic reaction: $2H^+ + 2e^- \rightarrow H_2$

$O_2 + 2H_2O + 4e^- \rightarrow 4OH^-$

Hydrolysis reaction: $M^{n+} + nH_2O \rightarrow M(OH)_n + nH^+$

Figure 11 shows the schematic diagrams of the corrosion process for these four groups of HEAs during polarization in the 0.5 M H_2SO_4 solution. As discussed above, the intragranular zone near the grain boundary of Cr0 starts to corrode preferentially as the galvanic corrosion effect. With the selective dissolution proceeding, the corroded zone gradually turns into the Mn-rich zone at noble potential, and then the corrosion spreads from the nearest zone to the grain boundary into the grain interior. As the gradually increased area ratio of cathode to anode, the central zone suffers from more severe corrosion than the zone adjacent to grain boundary and the micropores are formed on the surface. Additionally, as described in Figure 11A, more metal ions would be released into the solution than the uncorroded zone by the redox reaction. This would facilitate the hydrolysis reaction to form stable metal hydroxide/oxide, such as Fe and Mn hydroxide/oxide, on the corroded zone, which can retard the corrosion process effectively. Meanwhile, when a small amount of Cr was added in Cr0.6, as shown in Figure 11B, the second phase of $(Cr, Mn)_3O_4$ would precipitate from the matrix, and the corrosion process then occurred near the second phase zone. As the grain boundary can be regarded as the corrosion barrier[38], the corrosion process could end up in the grain boundary zone far away. Notably, such a corrosion process may have two routes: one is that the corrosion propagates along one direction, as the passive film in other directions is more compact; the other one is that the corrosion propagates around the second phase so that the second phase particles would locate in the micropores and peel off from the surface finally. Moreover, the passive film is not only formed in the corroded zone inside the micropores, but also out of the micropores as the slight corrosion by the effect of the nanoscale heterogeneous composition. In terms of Cr1 in Figure 11C, the alloy has the same corrosion mechanism as Cr0.6 except for the microstructure of the passive film. That is, Cr1 has a more compact and thicker passive film than Cr0.6 to provide effective protection to the matrix. However, the micropores for Cr1.5 are much larger and deeper than Cr1 and a few hydroxides/oxides are deposited in the micropores, as shown in Figure 11D. The larger micropores should be due to the larger second phase in the matrix, which would accelerate the corrosion in the local regions without enough protection from the passive film. It can be explained as follows: the dissolution rate of the anode in the micropores is so fast due to the strong galvanic effect that the concentrations of the metal ions are very high; when the diffusion rate of metal cations out of the micropore is much lower than the anodic dissolution rate in the activated region, the concentrations of the metal ions in the micropores could be maintained above a critical value, then the pH value decreases in the local regions by the excessive hydrolysis reactions, and thus causing a more aggressive environment[42,43], which not only restrains the formation of the stable passive film in the micropores, but also induces the formation of the additional (Mn, Cr)-rich layer on the inner surface. In contrast, compared with Cr1, in the larger region outside the micropores of Cr1.5, the more compact and flat passive film following the same passivation mechanism without dissolution process is generated based

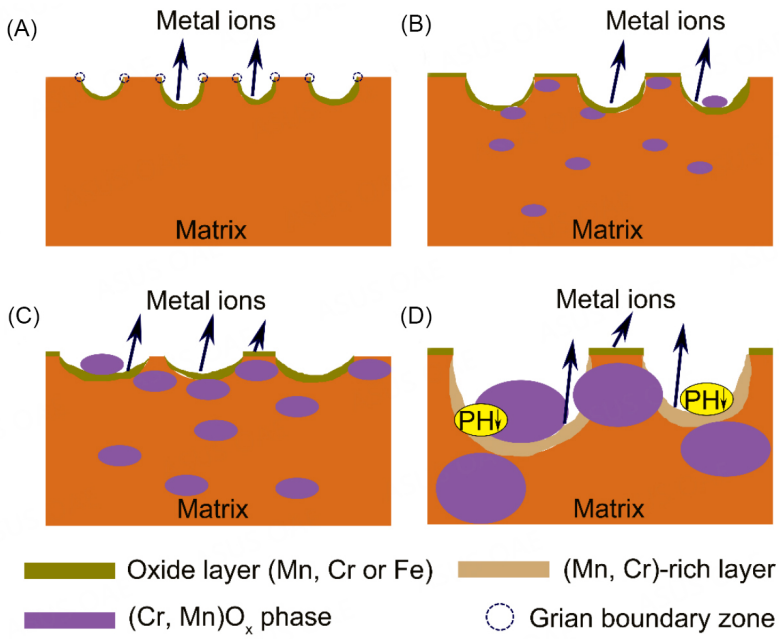

Figure 11. The schematic diagrams of the corrosion process during the polarization tests in 0.5 M H_2SO_4 for Cr0 (A), Cr0.6 (B), Cr1 (C) and Cr1.5 (D).

on the results shown in Figures 6 and 7, which has more effective protection against the matrix, resulting in the lower corrosion rate for Cr1.5 during the polarization tests.

Corrosion process during the long-time immersion tests

It is interesting to find that when the HEAs were immersed in the 0.5 M H_2SO_4 solution at room temperature for 15 days, the corrosion rates increased quickly with the Cr concentration, which seems in contradiction with the results of the polarization tests. This contradiction can mainly be attributed to the competition mechanism between the passivation effect and the galvanic corrosion effect on the honeycomb-like surface. At the early period of the immersion tests, the corrosion behavior can be regarded as the same with the polarization tests[44] and the EIS measurement after 2 h of immersion, as the EIS measurement is at a quasi-stable state and does not change the condition of the corroded surface, when the passivation effect plays an important role in the corrosion process for the samples. Therefore, with the addition of Cr, the stable Cr hydroxide/oxide would be deposited more on the surface, so that the passive film is more compact and thicker. As a result, Cr1.5 has the best corrosion resistance. With the extending time for Cr0, Cr0.6 and Cr1, the etching solution would gradually permeate the passive films in the micropores as the passive films are not very compact and stable. Meanwhile, the composition of the corroded area would convert to the Mn-rich or the (Cr, Mn)-rich region, which increases the area of the cathode. In the end, the enhanced galvanic corrosion effect is strong enough as that of Cr1.5 to increase the depth of micropores so that the passive films in the inner surfaces of the micropores would be dissolved. At this stage, the galvanic corrosion effect for all samples gradually accumulates and starts to transcend the impact of the passivation effect. Subsequently, the micropores continue to grow and the samples are corroded more severely. During this period, pitting-like corrosion is considered to proceed on the honeycomb-like surface, which is also promoted by the loose surface film. Therefore, the galvanic corrosion effect would play a dominant role during the following immersion. As mentioned, the galvanic corrosion would get more severe with the increase of the Cr concentration; hence, Cr1.5 gradually has the highest corrosion rate during the long-time immersion tests. Moreover, the porous structure is also found inside or outside of the micropores of the

samples in Figure 10, which evolved from the tiny height fluctuation during the initial period of the immersion, due to the intrinsic heterogeneous nanoscale particles.

In summary, the addition of Cr in Cr_xMnFeCoNi HEAs is indeed liable to form the Cr oxide in the passive film, which has good stability in the solution and improves the corrosion resistance of the HEAs[17,45]. On the other hand, the Cr can also precipitate from the matrix, which could accelerate corrosion by enhancing the galvanic corrosion effect. In addition, the formed honeycomb-like corroded surfaces on the HEAs would further deteriorate the corrosion resistance. Therefore, it is vital to optimize the matrix structure of the Cr-containing HEAs by changing the constituent elements as well as the processing methods to improve the corrosion resistance in future work. Generally, there are two methods to improve the corrosion resistance of the Cr-containing HEAs. One is to decrease or even eliminate the segregation of the Cr and homogenize the composition and the other is to optimize the structure and the composition of the passive film for high Cr-containing HEAs[46] and eliminate the nanocrystalline-amorphous phase boundaries.

CONCLUSION

The corrosion behavior of ultrafine-grained Cr_xMnFeCoNi HEAs with varying Cr contents in sulfuric acid solution (0.5 M H_2SO_4) was investigated. The Cr-containing HEAs consisted of an fcc matrix and a small amount of (Cr, Mn)$_3O_4$ at the grain boundaries and the (Cr, Mn)-rich phase due to the compositional segregation. During the polarization tests, the corrosion rate first increased and then decreased with the addition of Cr. The Cr1.5 HEA showed the lowest corrosion rate due to the effective passivation. The honeycomb-like surface was formed after electrochemical polarization tests. The passive film was mainly composed of (Mn, Fe) hydroxide/oxide for Cr0 and (Cr, Mn and Fe) hydroxide/oxide for the Cr-containing HEAs. The passive film was more compact and thicker with the increasing Cr concentration. However, the existence of the nanocrystalline-amorphous phase boundaries in the passive film could reduce its stability by providing the diffusion channel of the species. During the static long-time immersion tests, the HEAs showed distinct corrosion behavior from that of the polarization tests, where the corrosion rate increased exponentially from Cr0 to Cr1.5. This unexpected phenomenon should be due to the accumulation of the galvanic corrosion effect induced by the pitting-like corrosion accompanied by the failure of the passivation effect.

DECLARATIONS

Authors' contributions

Conceptualization, methodology, validation, formal analysis, investigation, data curation, visualization, writing - original draft: Wan T
Methodology, investigation: Huang Z
Investigation: Cheng Z, Zhu M, Li Z, Fu D
Methodology, investigation: Zhu W
Conceptualization, methodology, formal analysis, resources, data curation, visualization, writing - review & editing, supervision, project administration, funding acquisition: Ren F

Availability of data and materials

The raw/processed data required to reproduce these findings are available upon request to the corresponding author.

Financial support and sponsorship

This work was financially supported by the National Natural Science Foundation of China (No. 52122102), the Shenzhen Peacock Team Program (No. KQTD2016053019134356) and the Guangdong Innovative &

Entrepreneurial Research Team Program (No. 2016ZT06C279).

Conflicts of interest
All authors declared that there are no conflicts of interest.

Ethical approval and consent to participate
Not applicable.

Consent for publication
Not applicable.

Copyright
© The Author(s) 2023.

REFERENCES

1. George E, Curtin W, Tasan C. High entropy alloys: a focused review of mechanical properties and deformation mechanisms. *Acta Mater* 2020;188:435-74. DOI
2. Otto F, Dlouhý A, Somsen C, Bei H, Eggeler G, George E. The influences of temperature and microstructure on the tensile properties of a CoCrFeMnNi high-entropy alloy. *Acta Mater* 2013;61:5743-55. DOI
3. Zhang Z, Mao MM, Wang J, et al. Nanoscale origins of the damage tolerance of the high-entropy alloy CrMnFeCoNi. *Nat Commun* 2015;6:10143. DOI PubMed PMC
4. Chuang M, Tsai M, Wang W, Lin S, Yeh J. Microstructure and wear behavior of $Al_xCo_{1.5}CrFeNi_{1.5}Ti_y$ high-entropy alloys. *Acta Mater* 2011;59:6308-17. DOI
5. Granberg F, Nordlund K, Ullah MW, et al. Mechanism of radiation damage reduction in equiatomic multicomponent single phase alloys. *Phys Rev Lett* 2016;116:135504. DOI PubMed
6. Shi Y, Collins L, Feng R, et al. Homogenization of Al CoCrFeNi high-entropy alloys with improved corrosion resistance. *Corros Sci* 2018;133:120-31. DOI
7. Chen Y, Duval T, Hung U, Yeh J, Shih H. Microstructure and electrochemical properties of high entropy alloys-a comparison with type-304 stainless steel. *Corros Sci* 2005;47:2257-79. DOI
8. Miracle D, Miller J, Senkov O, Woodward C, Uchic M, Tiley J. Exploration and development of high entropy alloys for structural applications. *Entropy* 2014;16:494-525. DOI
9. Cantor B, Chang I, Knight P, Vincent A. Microstructural development in equiatomic multicomponent alloys. *Mater Sci Eng A* 2004;375-377:213-8. DOI
10. Gludovatz B, Hohenwarter A, Catoor D, Chang EH, George EP, Ritchie RO. A fracture-resistant high-entropy alloy for cryogenic applications. *Science* 2014;345:1153-8. DOI PubMed
11. Sun S, Tian Y, Lin H, et al. Temperature dependence of the Hall-Petch relationship in CoCrFeMnNi high-entropy alloy. *J Alloy Compd* 2019;806:992-8. DOI
12. Sieradzki K, Newman RC. A percolation model for passivation in stainless steels. *J Electrochem Soc* 1986;133:1979-80. DOI
13. Yuan S, Liang B, Zhao Y, Pehkonen S. Surface chemistry and corrosion behaviour of 304 stainless steel in simulated seawater containing inorganic sulphide and sulphate-reducing bacteria. *Corros Sci* 2013;74:353-66. DOI
14. Tan L, Ren X, Sridharan K, Allen T. Corrosion behavior of Ni-base alloys for advanced high temperature water-cooled nuclear plants. *Corros Sci* 2008;50:3056-62. DOI
15. Thomas S, Birbilis N, Venkatraman M, Cole I. Self-repairing oxides to protect zinc: review, discussion and prospects. *Corros Sci* 2013;69:11-22. DOI
16. Qiu Y, Thomas S, Gibson MA, Fraser HL, Birbilis N. Corrosion of high entropy alloys. *NPJ Mater Degrad* 2017;1:15. DOI
17. Xiao D, Zhou P, Wu W, et al. Microstructure, mechanical and corrosion behaviors of AlCoCuFeNi-(Cr,Ti) high entropy alloys. *Mater Des* 2017;116:438-47. DOI
18. Wang R, Zhang K, Davies C, Wu X. Evolution of microstructure, mechanical and corrosion properties of AlCoCrFeNi high-entropy alloy prepared by direct laser fabrication. *J Alloy Compd* 2017;694:971-81. DOI
19. Li QH, Yue TM, Guo ZN, Lin X. Microstructure and corrosion properties of AlCoCrFeNi high entropy alloy coatings deposited on AISI 1045 steel by the electrospark process. *Metall Mater Trans A* 2013;44:1767-78. DOI
20. Hsu Y, Chiang W, Wu J. Corrosion behavior of FeCoNiCrCux high-entropy alloys in 3.5% sodium chloride solution. *Mater Chem Phys* 2005;92:112-7. DOI
21. Ye Q, Feng K, Li Z, et al. Microstructure and corrosion properties of CrMnFeCoNi high entropy alloy coating. *Appl Surf Sci* 2017;396:1420-6. DOI
22. Luo H, Li Z, Mingers AM, Raabe D. Corrosion behavior of an equiatomic CoCrFeMnNi high-entropy alloy compared with 304

stainless steel in sulfuric acid solution. *Corros Sci* 2018;134:131-9. DOI

23. Wang C, Yu J, Yu Y, Zhao Y, Zhang Y, Han X. Comparison of the corrosion and passivity behavior between CrMnFeCoNi and CrFeCoNi coatings prepared by argon arc cladding. *J Mater Res Technol* 2020;9:8482-96. DOI
24. Wang C, Yu Y, Yu J, Zhang Y, Wang F, Li H. Effect of the macro-segregation on corrosion behavior of CrMnFeCoNi coating prepared by arc cladding. *J Alloy Compd* 2020;846:156263. DOI
25. Wang L, Mercier D, Zanna S, et al. Study of the surface oxides and corrosion behaviour of an equiatomic CoCrFeMnNi high entropy alloy by XPS and ToF-SIMS. *Corros Sci* 2020;167:108507. DOI
26. Pang J, Xiong T, Wei X, et al. Oxide $MnCr_2O_4$ induced pitting corrosion in high entropy alloy CrMnFeCoNi. *Materialia* 2019;6:100275. DOI
27. Li S, Dong H, Shi L, Li P, Ye F. Corrosion behavior and mechanical properties of Al-Zn-Mg aluminum alloy weld. *Corros Sci* 2017;123:243-55. DOI
28. Zhang X. Corrosion behavior of Al-3.0 wt.%Mg alloy by cold-drawing process. *Int J Electrochem Sci* 2020:1727-41. DOI
29. Soltis J. Passivity breakdown, pit initiation and propagation of pits in metallic materials - review. *Corros Sci* 2015;90:5-22. DOI
30. Yan Y, Cao H, Kang Y, et al. Effects of Zn concentration and heat treatment on the microstructure, mechanical properties and corrosion behavior of as-extruded Mg-Zn alloys produced by powder metallurgy. *J Alloy Compd* 2017;693:1277-89. DOI
31. Park K, Kwon H. Effects of Mn on the localized corrosion behavior of Fe-18Cr alloys. *Electrochim Acta* 2010;55:3421-7. DOI
32. Zhang B, Wang J, Wu B, et al. Unmasking chloride attack on the passive film of metals. *Nat Commun* 2018;9:2559. DOI PubMed PMC
33. Sun J, Zhang G, Liu W, Lu M. The formation mechanism of corrosion scale and electrochemical characteristic of low alloy steel in carbon dioxide-saturated solution. *Corros Sci* 2012;57:131-8. DOI
34. Rovere C, Alano J, Silva R, Nascente P, Otubo J, Kuri S. Characterization of passive films on shape memory stainless steels. *Corros Sci* 2012;57:154-61. DOI
35. Barsoukov E, Macdonald JR. Impedance spectroscopy: theory, experiment, and applications second edition. Evgenij Barsoukov and J. Ross Macdonald (eds). John Wiley & Sons, Inc., Hoboken, New Jersey, 2005. *J Raman Spectrosc* 2007;38:122. DOI
36. Kissi M, Bouklah M, Hammouti B, Benkaddour M. Establishment of equivalent circuits from electrochemical impedance spectroscopy study of corrosion inhibition of steel by pyrazine in sulphuric acidic solution. *Appl Surf Sci* 2006;252:4190-7. DOI
37. Tachibana S, Kuronuma Y, Yokota T, Yamada K, Moriya Y, Kami C. Effect of hot rolling and cooling conditions on intergranular corrosion behavior in Alloy625 clad steel. *Corros Sci* 2015;99:125-33. DOI
38. Aung NN, Zhou W. Effect of grain size and twins on corrosion behaviour of AZ31B magnesium alloy. *Corros Sci* 2010;52:589-94. DOI
39. Kao Y, Lee T, Chen S, Chang Y. Electrochemical passive properties of AlxCoCrFeNi (x = 0, 0.25, 0.50, 1.00) alloys in sulfuric acids. *Corros Sci* 2010;52:1026-34. DOI
40. Boudin S, Vignes J, Lorang G, et al. Analytical and electrochemical study of passive films formed on nickel-chromium alloys: influence of the chromium bulk concentration. *Surf Interface Anal* 1994;22:462-6. DOI
41. Huang J, Wu X, Han E. Electrochemical properties and growth mechanism of passive films on Alloy 690 in high-temperature alkaline environments. *Corros Sci* 2010;52:3444-52. DOI
42. Li T, Scully JR, Frankel GS. Localized corrosion: passive film breakdown vs. pit growth stability: part iii. a unifying set of principal parameters and criteria for pit stabilization and salt film formation. *J Electrochem Soc* 2018;165:C762-70. DOI
43. Li T, Swanson OJ, Frankel G, et al. Localized corrosion behavior of a single-phase non-equimolar high entropy alloy. *Electrochim Acta* 2019;306:71-84. DOI
44. Shi Z, Liu M, Atrens A. Measurement of the corrosion rate of magnesium alloys using Tafel extrapolation. *Corros Sci* 2010;52:579-88. DOI
45. Asami K, Hashimoto K, Shimodaira S. An XPS study of the passivity of a series of iron-chromium alloys in sulphuric acid. *Corros Sci* 1978;18:151-60. DOI
46. Quiambao KF, Mcdonnell SJ, Schreiber DK, et al. Passivation of a corrosion resistant high entropy alloy in non-oxidizing sulfate solutions. *Acta Mater* 2019;164:362-76. DOI

Viehland. *Microstructures* 2023;3:2023016
DOI: 10.20517/microstructures.2023.10

Microstructures

Commentary

Open Access

Check for updates

Commentary on "Heterogenous nature of enhanced piezoelectricity in relaxor-ferroelectric crystals"

D. Viehland

Materials Science and Engineering, Virginia Tech, Blacksburg, VA 24061, USA.

Correspondence to: Prof. D. Viehland, Materials Science and Engineering, Virginia Tech, Blacksburg, VA 24061, USA. E-mail: dviehlan@vt.edu

How to cite this article: Viehland D. Commentary on "Heterogenous nature of enhanced piezoelectricity in relaxor-ferroelectric crystals". *Microstructures* 2023;3:2023016. https://dx.doi.org/10.20517/microstructures.2023.10

Received: 16 Feb 2023 **Accepted:** 17 Feb 2023 **Published:** 9 Mar 2023

Academic Editor: Shujun Zhang **Copy Editor:** Fangling Lan **Production Editor:** Fangling Lan

Enhanced piezoelectricity in Pb-based perovskite ferroelectric single crystals has been of research interest for about 30 years since the early reports by Uchino[1] of high weak-field properties (d33~1500 pC/N) to subsequent ones by Park *et al.*[2] of large field-induced strains (ε = 1.5%, E = 120 kV/cm). The fundamental scientific question of what causes the enhanced piezoelectricity of the $Pb(Mg_{1/3}Nb_{2/3})O_3$-$PbTiO_3$ (PMN-PT) or $Pb(Zn_{1/3}Nb_{2/3})O_3$-$PbTiO_3$ (PZN-PT) type piezoelectric crystals naturally arose, as it has the potential to help guide ultrahigh piezoelectricity by design.

In the United States, under the support of the Office of Naval Research or ONR (Smith), much effort was expended to develop a theory of intermediate monoclinic (M) phases that structurally bridge rhombohedral (R) and tetragonal (T) ones across the morphotropic phase boundary (MPB)[3]. Ab-initio approaches predicted a monoclinic unit cell, indicating an intermediate M phase that is structurally homogeneous. The polarization vector within the unit cell rotated on application of electric field E, resulting in electromechanical transduction.

However, it must be remembered that the perovskite crystals which exhibit ultrahigh piezoelectricity are in solid solutions between end members having relaxor and normal ferroelectric behaviors. Relaxors are unique in that they are characterized by a structural heterogeneity of lower symmetry within an average cubic state[4]. Figure 1A shows data taken from the same (001) PMN-32at%PT crystal under different electrical histories. In the annealed condition (dotted lines)[5], typical relaxor ferroelectric behavior is

© The Author(s) 2023. **Open Access** This article is licensed under a Creative Commons Attribution 4.0 International License (https://creativecommons.org/licenses/by/4.0/), which permits unrestricted use, sharing, adaptation, distribution and reproduction in any medium or format, for any purpose, even commercially, as long as you give appropriate credit to the original author(s) and the source, provide a link to the Creative Commons license, and indicate if changes were made.

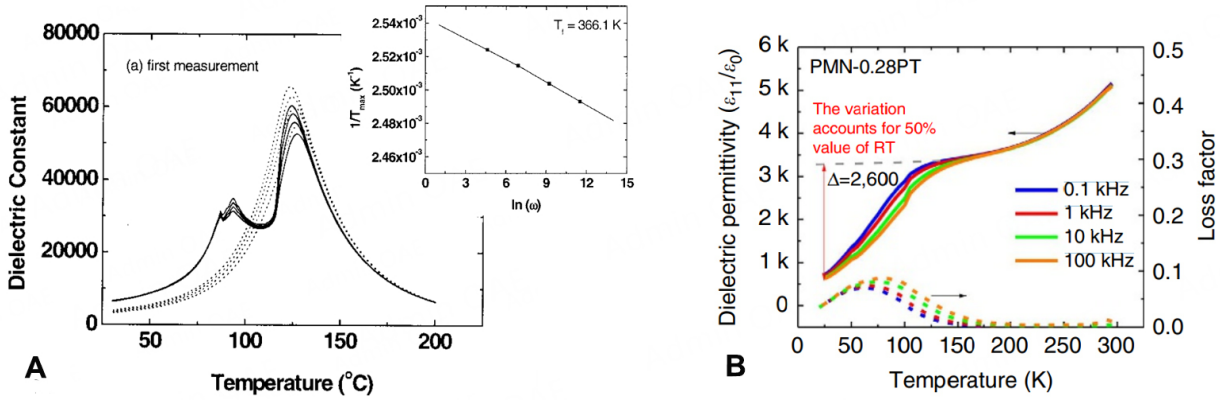

Figure 1. (A) Temperature-dependent dielectric response in the range above 300 K for a <001>- oriented PMN–PT crystal on heating from a poled condition under zero field, and subsequent re-cooling. The insert shows a Vogel-Fulcher fit to the frequency dependence of the dielectric constant in the zero-field cooled measurement. Reproduced with permission[5]. Copyright 2001 AIP Publishing LLC. (B) Temperature-dependent dielectric response in the range below 300 K for a <001> PMN-PT crystal on zero-field heating from a poled condition. Reproduced with permission[18]. Copyright 2016 Nature Publishing Group.

observed, where the temperature of the dielectric maximum (T_{max}) is frequency dependent. Analysis of the frequency dependence of T_{max} with the Vogel-Fulcher equation (see insert) yielded a freezing temperature of Tf = 366 K. Electric field cooling (FC) results in the emergence of a long-range ordered ferroelectric state that remains stable on the removal of E. On subsequent reheating under E = 0 from a previously FC state, a macrodomain to polar nanoregion transition occurs near Tf, somewhat similar to earlier reports by Yao *et al.*[6] for PLZT ceramics. Clearly, in these complex relaxor crystals, length scales are important to the structure-property relations and the average symmetry itself.

Other evidence exists supporting the proposition that the heterogeneous concept of relaxors can be extended to the poled piezoelectric state. Early electron microscopy studies by Randall *et al.* in 1987 demonstrated the existence of polar nanoregions in relaxors[7]. Subsequent studies in 1994 revealed that the nanoregions assembled into tweed-like structures on approaching the MPB[8], as shown in Figure 2A. In ferroelastic transformations, Khachaturyan has shown that tweed-like structures result in an apparent monoclinic MC structure[9], even though the local symmetry is tetragonal. Modelling by Bratkovsky, Salje and Heine in 1994[10] simulated the domain evolution pathway of elastic clusters to tweed microdomains. Kartha, Castan, Krumhansl and Sethna[11] in 1991 showed using a Landau-Ginsburg approach that a tweed mesophase could be trapped to low temperatures due to nonlinear non-local elasticity coupled to quenched compositional inhomogeneity. In 2006[12,13], piezo-force and polarized light microscopy studies of poled PMN-PT crystals revealed macrodomain plates having an internal fine (~200 nm) domain structure that was altered from a lamellar to zig-zag configuration under electric field application, as shown in Figure 2B. Finally, structural studies have shown that the thermodynamic phase space is quite flat[14]: for a fixed electric field and composition, simply changing the direction along which E is applied can result in changes between induced monoclinic, orthorhombic, and tetragonal/ rhombohedral phases.

Based on these experimental insights, a structurally heterogeneous model for the enhanced piezoelectricity of the PMN-PT type crystals was proposed[15-17]. The work was also supported by ONR (Lindberg). It is based on the concept of a mesoscale mechanism, where polar nanoregion activity within a poled ferroelectric condition is responsible for enhanced piezoelectricity. The model was an extension of an adaptive phase theory for ferroelastic and martensitic transformations[9] that was applied to ferroelectrics with large strain. Theoretically, it is based on the conformal miniaturization of domains with low domain

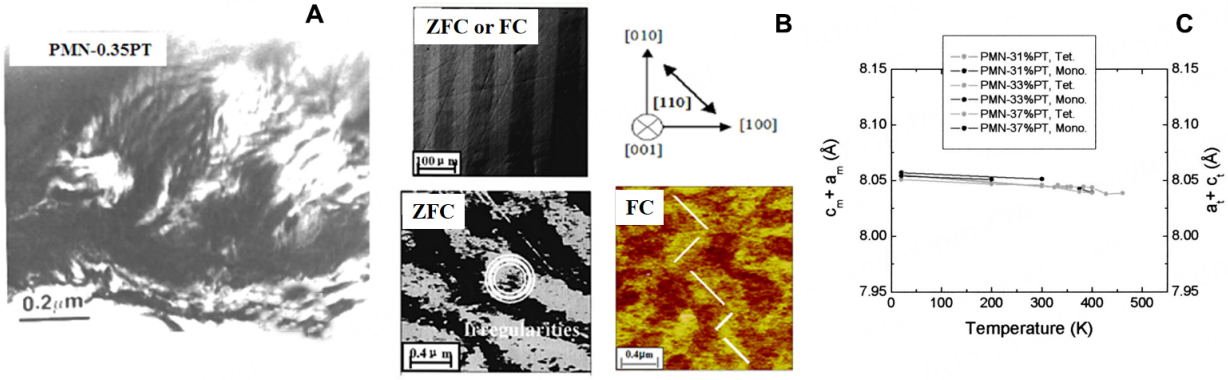

Figure 2. (A) Transmission electron microscopy image showing the presence of tweed-like structures in PMN-35PT. Reproduced with permission[8]. Copyright 1995 AIP Publishing LLC. (B) Polarized light PLM (top) and piezo-force PFM microscopy (bottom) images. Reproduced with permission[13]. Copyright 2005 AIP Publishing LLC. (C) Temperature dependence of the general invariance condition of equation (3.13). Reproduced with permission[16]. Copyright 2003 AIP Publishing LLC.

wall energies that are stress-accommodating (i.e., tweed). Experimentally, this requires the existence of structurally heterogeneous regions of nanometer size. The spatial and geometric distribution of the nanoregions is then controlled by special and general invariant conditions that minimize the excess elastic energy. In the case of PMN-PT type piezoelectric crystals, averaging over an ensemble of tetragonal polar nanoregions results in an apparent monoclinic MC-type structure by diffraction. Likewise, averaging over an ensemble of rhombohedral polar nanoregions results in an apparent monoclinic MA-type structure. In the monoclinic MA and MC phases, the changes in the lattice parameter with temperature and field are invariant to the geometric conditions of the adaptive phase theory, as shown in Figure 2C. Both the structurally homogeneous and heterogenous models require the anisotropy of the polarization direction to be small. In the homogenous case, the polarization vector rotates at the unit cell level; whereas in the heterogenous case, there is a change in the distribution of the polar nanoregions between equivalent orientations.

This brings me to the point that this commentary would like to make. It concerns a brief comparison of another approach to the heterogeneous concept by Li *et al.* that was put forward some years after the adaptive phase theory[18,19]. Let us be upfront and direct, the experimental observations that were cited in the preceding paragraph could equally provide support to either one of these heterogenous models, as the data reflects a critical role of the local structure on the average structure-property relations. The concept by Li *et al.* and the adaptive phase[15-17] are on the same general page[17,18]. It is only a question of details, many of which whose importance may not yet be realized, simply due to the predominance of investigations has focused on a conventional homogenous phase. Both approaches recognize the existence of polarization gradient terms in the Landau-Ginzburg (LG) phenomenology and the need to relax the elastic energy. Additionally, both approaches recognize the important role of the contribution of polar nanoregions within the average anisotropy set by the poling directions. A unique aspect of the adaptive phase theory that the LG theory cannot explain by itself is the observed special invariant conditions of the crystal lattice parameters.

Data reported by Li *et al.* shows that the dielectric constant in the poled piezoelectric state becomes strongly frequency dispersive at temperatures far below (ΔT = 250-350 K) the temperature of the dielectric maximum ($T_{max} \approx$ 400 K), as shown in Figure 1B[18,19]. This result clearly demonstrates that polar nanoregion contributions begin to freeze out on cooling below 100 K in the poled piezoelectric phase. It is only in the temperature range between 100 K [Figure 1B] and the macrodomain to polar nanoregion transition (see Figure 1A) that the dielectric constant appears to be nondispersive. It is believed this enhanced polarization

contribution in the poled condition is responsible for the high piezoelectricity of poled crystals[20]. One could also expect such low-temperature behavior in glassy tweed meso-states due to a coupling between non-local elasticity and compositional inhomogeneity[11].

The strength of the adaptive phase theory is in its simple elegance in making invariant the lattice parameter changes with temperature and field based on a crystallographic/geometric theory. The strength of the approach by Li *et al.* is in its ability to bring together numerous gradient contributions and elastic boundary conditions into a phase field theory that could be used for piezoelectricity by computational design[18-20]. The overall weakness has been that the majority of research efforts have been devoted to investigations within the framework of a homogenous single-phase monoclinic structure. To date, monoclinic phases in these complex Pb-based perovskites have only been reported in polydomain materials - there has yet to be the finding of a single-domain single-crystal monoclinic phase.

DECLARATIONS

Acknowledgments
Much thanks to prior authors of referenced papers in the figures, and to the American Institute of Physics and to the Nature Publishing Group for figure reproduction.

Authors' contributions
The author contributed solely to the article.

Availability of data and materials
Not applicable.

Financial support and sponsorship
None.

Conflicts of interest
The author declared that there are no conflicts of interest.

Ethical approval and consent to participate
Not applicable.

Consent for publication
Not applicable.

Copyright
© The Author(s) 2023.

REFERENCES

1. Kuwata J, Uchino K, Nomura S. Phase transitions in the $Pb(Zn_{1/3}Nb_{2/3})O_3$-$PbTiO_3$ system. *Ferroelectrics* 1981;37:579-82. DOI
2. Park S, Shrout TR. Ultrahigh strain and piezoelectric behavior in relaxor based ferroelectric single crystals. *J Appl Phys* 1997;82:1804-11. DOI
3. Fu H, Cohen RE. Polarization rotation mechanism for ultrahigh electromechanical response in single-crystal piezoelectrics. *Nature* 2000;403:281-3. DOI PubMed
4. Cross LE. Relaxor ferroelectrics. *Ferroelectrics* 1987;76:241-67. DOI
5. Viehland D, Powers J, Cross LE, Li JF. Importance of random fields on the properties and ferroelectric phase stability of <001> oriented $0.7Pb(Mg_{1/3}Nb_{2/3})O_3$-$0.3PbTiO_3$ crystals. *Appl Phys Lett* 2001;78:3508-10. DOI
6. Xi Y, Zhili C, Cross LE. Polarization and depolarization behavior of hot pressed lead lanthanum zirconate titanate ceramics. *Ferroelectrics* 1984;54:163-6. DOI

7. Randall CA, Barber DJ, Whatmore RW. In situ TEM experiments on perovskite-structured ferroelectric relaxor materials. *J Microsc* 1987;145:275-91.
8. Viehland D, Kim M, Xu Z, Li J. Long-time present tweedlike precursors and paraelectric clusters in ferroelectrics containing strong quenched randomness. *Appl Phys Lett* 1995;67:2471-3. DOI
9. Khachaturyan AG, Shapiro SM, Semenovskaya S. Adaptive phase formation in martensitic transformation. *Phys Rev B Condens Matter* 1991;43:10832-43. DOI PubMed
10. Bratkovsky AM, Salje EKH, Heine V. Overview of the origin of tweed texture. *Phase Transit* 1994;52:77-83. DOI
11. Kartha S, Castán T, Krumhansl JA, Sethna JP. Spin-glass nature of tweed precursors in martensitic transformations. *Phys Rev Lett* 1991;67:3630-3. DOI PubMed
12. Bai F, Li JF, Viehland D. Domain hierarchy in annealed (001)-oriented $Pb(Mg_{1/3}Nb_{2/3})O_3$-x%$PbTiO_3$ single crystals. *Appl Phys Lett* 2004;85:23135. DOI
13. Bai F, Li J, Viehland D. Domain engineered states over various length scales in (001)-oriented $Pb(Mg_{1/3}Nb_{2/3})O_3$-x%$PbTiO_3$ crystals: electrical history dependence of hierarchal domains. *J Appl Phys* 2005;97:054103. DOI
14. Cao H, Li J, Viehland D, Xu G. Fragile phase stability in (1-x)$Pb(Mg_{1/3}Nb_{2/3}O_3)$-x$PbTiO_3$ crystals: a comparison of [001] and [110] field-cooled phase diagrams. *Phys Rev B* 2006;73:184110. DOI
15. Jin YM, Wang YU, Khachaturyan AG, Li JF, Viehland D. Conformal miniaturization of domains with low domain-wall energy: monoclinic ferroelectric states near the morphotropic phase boundaries. *Phys Rev Lett* 2003;91:197601. DOI PubMed
16. Jin YM, Wang YU, Khachaturyan AG, Li JF, Viehland D. Adaptive ferroelectric states in systems with low domain wall energy: tetragonal microdomains. *J Appl Phys* 2003;94:3629-40. DOI
17. Viehland D, Salje EKH. Domain boundary-dominated systems: adaptive structures and functional twin boundaries. *Adv Phys* 2014;63:267-326. DOI
18. Li F, Zhang S, Yang T, et al. The origin of ultrahigh piezoelectricity in relaxor-ferroelectric solid solution crystals. *Nat Commun* 2016;7:13807. DOI PubMed PMC
19. Li F, Lin D, Chen Z, et al. Ultrahigh piezoelectricity in ferroelectric ceramics by design. *Nat Mater* 2018;17:349-54. DOI PubMed
20. Li F, Cabral M, Xu B, et al. Giant piezoelectricity of Sm-doped $Pb(Mg_{1/3}Nb_{2/3})O_3$-$PbTiO_3$ single crystals *Science* 2019;364:264-8. DOI

Lee *et al. Microstructures* 2023;3:2023021
DOI: 10.20517/microstructures.2023.08

Microstructures

Perspective

Open Access

Check for updates

Emerging microporous materials as novel templates for quantum dots

Jaeho Lee[1], Lianzhou Wang[1,2], Jingwei Hou[1]

[1]School of Chemical Engineering, The University of Queensland, Brisbane 4072, Australia.
[2]Australian Institute for Bioengineering and Nanotechnology, The University of Queensland, Brisbane 4072, Australia.

Correspondence to: Dr. Jingwei Hou, Chemical Engineering, The University of Queensland, Brisbane 4072, Australia. E-mail: jingwei.hou@uq.edu.au

How to cite this article: Lee J, Wang L, Hou J. Emerging microporous materials as novel templates for quantum dots. *Microstructures* 2023;3:2023021. https://dx.doi.org/10.20517/microstructures.2023.08

Received: 3 Feb 2023 **First Decision:** 27 Feb 2023 **Revised:** 11 Mar 2023 **Accepted:** 17 Apr 2023 **Published:** 26 Apr 2023

Academic Editors: Shujun Zhang, Zibin Chen **Copy Editor:** Fangling Lan **Production Editor:** Fangling Lan

Abstract

Microporous structures have attracted significant attention in recent years. In particular, metal-organic frameworks (MOFs) and covalent organic frameworks (COFs) have received considerable attention due to their tailorable structures that offer a wide range of choices in terms of molecular building blocks. Due to their high tunability, these materials are considered as ideal host matrices for templating and encapsulating guest materials, particularly quantum dots (QDs). QDs are investigated heavily for various applications such as light-emitting diodes (LED), biosensors, catalysts, and solar cells due to their unique properties from the quantum confinement effect. However, one of the drawbacks of QDs is their tendency to aggregate and exhibit low stability due to their small size and kinetic trapping in nanoparticle form. This perspective highlights promising approaches to enhance the performance and stability of QDs by using microporous materials as an encapsulation layer. Additionally, potential mitigating strategies are discussed to overcome current challenges and improve the practicality of QDs embedded in microporous nanocomposites.

Keywords: Metal-organic frameworks, covalent organic frameworks, zeolites, microstructures, QD encapsulation

INTRODUCTION

Quantum dots (QDs) are nanocrystals that behave similarly to an atom as a result of quantum physics. When the size of nanomaterials reaches a level comparable to or even smaller than the Bohr radius, the

© The Author(s) 2023. **Open Access** This article is licensed under a Creative Commons Attribution 4.0 International License (https://creativecommons.org/licenses/by/4.0/), which permits unrestricted use, sharing, adaptation, distribution and reproduction in any medium or format, for any purpose, even commercially, as long as you give appropriate credit to the original author(s) and the source, provide a link to the Creative Commons license, and indicate if changes were made.

materials will experience the quantum confinement effect. This phenomenon relates to the exciton and electronic energy level, which is continuous in bulk but becomes discrete in nanocrystals as the electron movement is confined to a specific energy level. An exciton is a bound state between an electron hole in valence band (VB) and an electron through Coulomb interaction. When a photon interacts with a semiconductor material and the energy of the photon exceeds or equals the bandgap (Eg), an electron in the VB is excited to the conduction band (CB), resulting in the formation of a positively charged hole referred to as an electron hole. As the excited electron and electron hole are confined within a limited space, more energy is required to excite them, which results in size-dependent band gaps and light emission. When a material is confined in one dimension, it forms a quantum well structure. Similarly, two-dimensional confinement results in a quantum wire, while three-dimensional confinement leads to a quantum dot, which is a material that is confined in all three dimensions[1-8]. This energy state results in unique characteristics, including long fluorescence lifetime, narrow and symmetrical photoluminescence emission, wide absorption, and high photoluminescence quantum yield (PLQY). Furthermore, the photoluminescence emission band gap can be tuned by varying the size of QDs. Traditionally, combinations of 0D core-shell structure materials and group 12-16 elements have been investigated as promising quantum dot materials, such as ZnSe, ZnO, InP, InAs, and CdSe[9-11]. Recently, organic-inorganic metal halide perovskites have been noticed as promising QD materials due to the recent successful development of photovoltaic (PV) cells, LEDs, and sensors based on perovskite QDs[12-17]. However, in light of increasing concerns about the potential toxicity of some materials, there is growing interest in developing alternatives that are more biocompatible and environmentally friendly. For instance, carbon quantum dots (CQDs) and graphene quantum dots (GQDs) are emerging as promising candidates[18-20]. Graphene Quantum Dots (GQDs) exhibit remarkable size-dependent luminescence properties that are attributed to their quantum confinement and edge effects. These properties make GQDs highly attractive for optoelectronic and photodetector applications, including LEDs and electroluminescent devices. However, GQDs often suffer from reduced fluorescence, which hampers their ability to function as optoelectronic devices due to phase separation and agglomeration in organic or inorganic solvents. Furthermore, the non-stoichiometric nature of GQDs makes it particularly challenging to achieve precise control over their chemical structure, size, shape, and structural defects, which are directly related to their optoelectronic properties. Therefore, there have been numerous attempts to incorporate GQDs into matrices such as polymer films or mesoporous solids in order to control the size of the nanoparticles and stabilise them. However, since many of the current fabrication methods are complicated and difficult to control, there is a need to investigate more reproducible and simpler methods to fully utilise the great fluorescence properties of GQDs[21-25].

Despite the promising potential of quantum dots (QDs) in various applications and the significant progress achieved in material sciences, several challenges continue to hinder their widespread implementation. These challenges include issues such as agglomeration, precise size control, and operational stability, which demand further research and development to mitigate effectively. Generally, QDs show a strong tendency to aggregate into larger particles due to their high surface energy, which leads to the loss of their unique characteristics. Several recent studies have tried to mitigate the limitations of QDs through solvent engineering, surface passivation using semiconducting film, encapsulation with polymers, or embedment of QDs within porous nanomaterials[26-29]. However, most of these strategies require complex fabrication processes, and it remains difficult to control the outcomes, which may reduce the efficacy of these methods.

Traditional nanomaterials with microporosity, such as mesoporous silica, zeolites, and porous carbon, have been investigated for various applications, including drug delivery, biosensing, separation, and catalysts[30,31]. Despite their great advantages, i.e., high surface area, tunable porosity, and biocompatibility, they tend to have limited chemical tunability. This limitation inspired scientists to develop microporous functional

materials that can be readily tailored. In recent years, covalent organic frameworks (COFs) and metal-organic frameworks (MOFs) have received tremendous attention from the materials science community as they can form tailored microstructures with metal-organic linker coordination bonds or covalent bonds[32-34]. In addition, the material itself can be chemically active and biocompatible, as some types of COFs are studied for cancer diagnosis and therapy[35-37]. Thanks to their high surface area, tunable structure, biocompatibility and diverse topology, these materials have been recognised as a promising functioning host matrix to mitigate some of the issues that quantum dots had. In view of this prosperous research area, we have outlined the quantum dots encapsulation in these emerging microporous materials and their potential applications. We believe that this Perspective will guide the potential future research directions in emerging QDs embedment in functional porous materials. The purpose of this Perspective is not to provide a comprehensive review and summary of these composite materials, but instead to give a brief history of the field, a summary of current progress, and, more importantly, highlight and discuss unsolved questions that are worth further investigation.

A HISTORICAL OVERVIEW OF QUANTUM DOTS WITHIN MICROPOROUS STRUCTURE

Quantum dots (QDs) are nanocrystals that exhibit quantum confinement effects due to their small size, leading to unique optical and electronic properties. These properties arise from the confinement of electrons and holes in a three-dimensional space, resulting in a behaviour similar to an atom because of quantum physics. It is generally agreed that the first QDs were discovered by Russian physicist Alexei Ekimov in the early 1980s. He synthesised copper chloride ($CuCl_2$) and cadmium selenide (CdSe) nanocrystals embedded in a glass matrix and observed a gradient of colours in the fluorescence emission spectra, which was dependent on the size of the nanocrystals[38]. Ever since their discovery, much of the research on QDs has focused on improving size control to reduce size variation, producing high-quality nanocrystals, and achieving tunable fluorescence colours. Recently, significant improvements have been made in the quality and tunability of QDs, as well as in their photovoltaic applications such as in solar cells. However, QDs have a tendency to aggregate into larger particles due to their high surface energy, which can lead to the loss of their unique characteristics and efficiency. To mitigate this drawback, there have been attempts to fabricate QDs within microporous matrices in order to not only control the size of the QDs but also provide a protective layer that prevents their aggregation and loss of unique characteristics.

Mesoporous silica, zeolites, and porous carbon have conventionally been studied as templates for the growth of QDs. Among these, zeolites have received extensive attention due to their unique tunable characteristics and excellent stability. Zeolites are crystalline aluminosilicate polymers with an inorganic framework consisting of SiO_4 and AlO_4 tetrahedra. They possess a three-dimensional nanometre-sized structure with uniform windows, channels, and cavities, and have been extensively studied. While this family of materials may not be considered as "emerging" compared to other types of microporous materials, they can still offer valuable insights into regulating the structure, interface, and chemistry between the microporous template and guest QDs. Therefore, this Perspective will first provide a brief summary of early studies on using zeolite templates for encapsulating QDs. The unique properties of zeolites that combine features of both ionic and covalent crystals arise from the covalent network structures formed by sharing oxygen atoms between SiO_4 and AlO_4 tetrahedra, which depends on the Si/Al ratio[39,40]. Materials exhibiting a ratio greater than 3 are categorised as high silica zeolites or zeolite Y. These high silica zeolites have good physical and chemical stability as well as hydrophobicity[41]. When the ratio is less than 3, it is called zeolite X or low-silica zeolites. These zeolites display high ion exchange capacity, which makes them good candidates as ion exchange agents[42]. Furthermore, pore size can also be tuned by changing the ratio and number of oxygen atoms connections to tetrahedra structure, or more directly through different synthetic conditions such as the use of surfactants. Their three-dimensional porous structure, along with their

tunability and uniformity, make these materials good candidates as host scaffolds for QDs.

An interesting topic in the field of synthesizing QDs in zeolites is the use of cadmium sulphide (CdS) QDs in zeolite Y. While this concept was established and researched in the 1980s, it continues to provide new insights for the next generation of researchers. CdS quantum dots are one of the most studied II-IV binary semiconductor materials due to their narrow band gap of 2.42 eV[43]. However, the performance of the material highly depends on its size and three-dimensional structure. Thus, much research effort has been dedicated to avoiding aggregation, size control and stabilisation of QD structure. Herron *et al.* introduced the idea of cadmium sulphide quantum dots (CdS QDs) in zeolite Y to improve their stability and optoelectronic properties[44]. In this work, CdS semiconductor clusters were synthesized using an aqueous solution process which involves cadmium ion exchange followed by hydrogen sulphide (H_2S) gas flowing to create CdS cluster within the zeolite pores. It was reported that during synthesis, QDs are formed in sodalite cages (5 Å) instead of supercage pores (13 Å) of zeolite Y structure through a percolative process [Figure 1A][45]. However, a recent study showed that CdS QDs exist in supercages rather than sodalite cages. The author found that the migrated Cd^{2+} ions in sodalite cage during drying process diffused back to supercage in later reaction process with H_2S to form QDs, showing the highly dynamic nature of the QD even in their condensed phase. The isolated CdS nanoclusters form interconnection through supercage window in $[CdS]_4$ unit, as shown in Figure 1B[46]. This example demonstrates the templated growth methodology to form QDs within the micropores, and it also clearly shows that the QDs in the template are still preserving their dynamic properties.

Another important guest material is lead sulphide (PbS) QD which has a narrow band gap and size-dependent optical properties due to its large exciton Bohr radius which makes it a good candidate for third-order nonlinear optical (3NLO) applications[47-49]. High 3NLO responses are enabled by smaller-size QDs and increased material density in the same matrix volume. However, the increased population of QDs in a small volume introduces aggregations and reduces the efficacy of the composite. Kim *et al.* demonstrated a significant increase in the third-order nonlinear optical (3NLO) activity of PbS quantum dots (QDs) by embedding them within the nanopores of zeolite Y[50]. This work also highlighted the interplay between the host and guest materials. By replacing of H^+ cation in the zeolite Y matrix with cations of different sizes, such as NH_4^+, Li^+, Na^+, K^+ and Rb^+, the stability and 3NLO activity of the composite were noticeably enhanced[50]. Considering it is difficult to tailor the chemical functionality or structure properties of zeolites based on guest materials, like other evolving porous materials, metal-organic frameworks (MOFs) or covalent organic frameworks (COFs), systematic replacement of zeolite's counter cations to guest material is one of the viable options to control pore volume, framework donor strength, cation acceptor strength, and electric field strength. This work shows a promising new approach to improve 3NLO activity within the zeolite matrix and the potential guest QDs.

In recent years, $CsPbX_3$ (X = Cl, Br, or I) perovskites QDs are receiving great attention as PVs or LEDs as they have a narrow emission band and high PLQY[51,52]. They can be easily processed in liquid form, making them particularly suitable for templated growth within zeolites[53]. Kim *et al.* used zeolite X as a host matrix for $Na_4Cs_6PbBr_4$ QDs, benefiting from its hydrophilic nature and relatively high aluminium content, which resulted in an increased number of extra framework cations (Na^+) that effectively enhanced the stability of the quantum dots when compared to zeolite Y[54]. This work was initially designed to create $CsPbBr_3$ QDs within zeolite X based on the previous research that encapsulates $CsPbX_3$ QDs within zeolite Y matrix. However, the author found out that the Cs^+ cations interact with counter cations (Na^+), forming new types of QDs, $Na_4Cs_6PbBr_4$. Those QDs are placed within the supercage of zeolite structure and interconnected through the window, as shown in Figure 2. The composite showed a much narrower light emission band

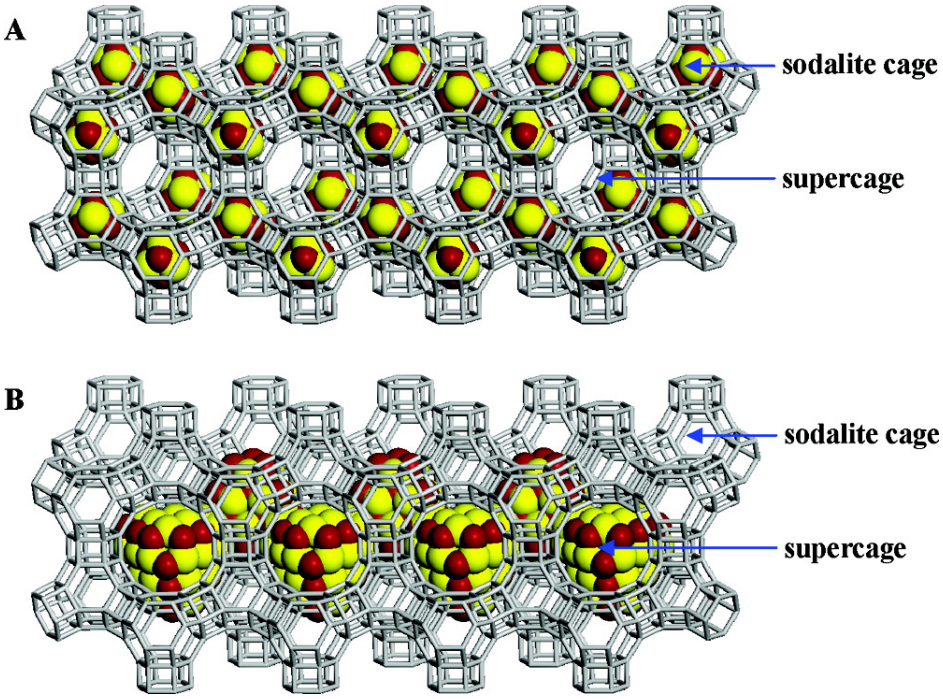

Figure 1. (A) Illustration of the zeolite-Y incorporating one $(CdS)_4$ unit in each sodalite cage and (B) the zeolite-Y incorporating a larger CdS QD in each supercage. Reprinted with permission[46]. Copyright © 2007 American Chemical Society.

and improved stability in water compared with unprotected $CsPbBr_3$ QDs, due to uniform distribution and interconnection of QDs within supercage of zeolite X structure[54]. This work suggests that counter cations of zeolite structures are important to improve stability and sensitivity while also forming more direct interaction with guest material to create new types of QDs. The discovery of this interaction opens a whole set of new research directions for the selection of QDs and cations of zeolite structure.

QUANTUM DOTS IN COVALENT ORGANIC FRAMEWORKS

Compared to zeolites, COFs are porous materials formed through chemical bonds between organic-organic moieties. These building blocks consist of organic molecules that are covalently linked to form a porous crystalline structure. The resulting chemical bonds between organic building blocks create a flexible and tunable framework structure that enables precise control over the size, shape, and chemical properties of the pores and channels within the material. This flexibility and tunability make COFs highly versatile and suitable for a wide range of applications, such as gas storage, separation, catalysis, and sensing. Additionally, zeolites are composed of rigid inorganic frameworks, which limits their flexibility and tunability, though they are still widely used in applications such as catalysis and adsorption.

Considering the dynamic interaction observed between zeolites and QDs, it is anticipated that COFs, in addition to their inherent structure, can provide further tunability to improve the performance of the resulting composites. The dynamic nature of COFs presents both opportunities and challenges for the generation of QDs within their pores. Obtaining a well-ordered three-dimensional crystalline COF structure and preserving its integrity during QD synthesis are among the most critical challenges that need to be overcome in the development of QD-COF composites. COFs can form two- or three-dimensional structures through covalent bonds between organic monomers composed of light elements such as C, H, N, B, and O[55,56]. In natural systems, covalent and noncovalent interactions play crucial roles in the formation

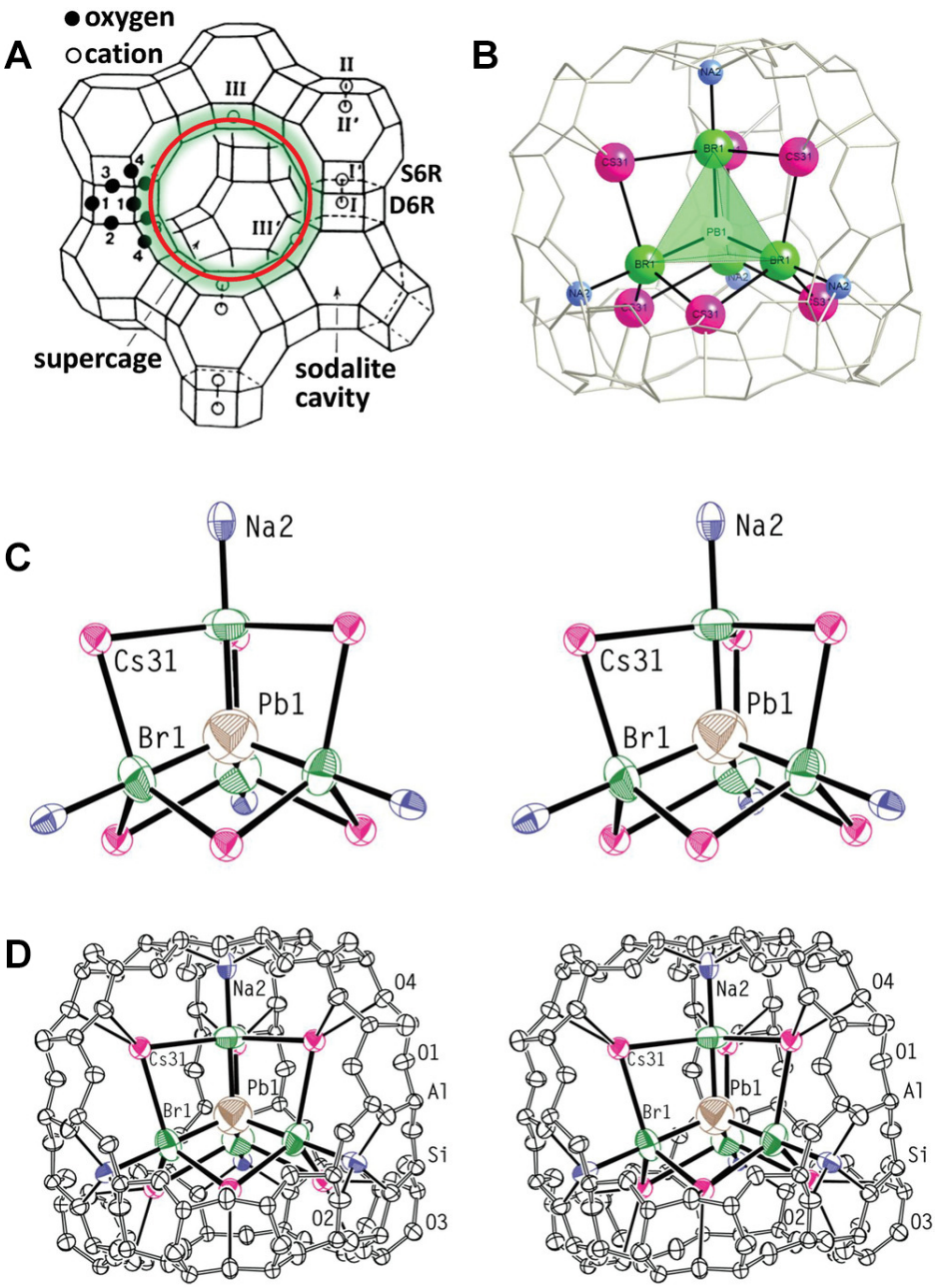

Figure 2. (A) Schematics of the framework structure of zeolite X. Near the center of each line segment is an oxygen atom. The nonequivalent oxygen atoms are indicated by the numbers 1-4. The common extraframework cation positions are labeled with Roman numerals. One of the four entrances to the supercage is highlighted in red. (B) The $[Na_4Cs_6PbBr_4]^{8+}$ quantum dot (QD) in a supercage of zeolite X. (C) Stereoview of the $[Na_4Cs_6PbBr_4]^{8+}$ QD. (D) Stereoview of the $[Na_4Cs_6PbBr_4]^{8+}$ QD in a Pb, Br, H, Cs, Na-X supercage. This structure may be viewed as a series of concentric spheres of alternating charge (48 O^{2-} ions of the zeolite framework, 10 Cs^+ and Na^+ ions, and 4 Br^- ions) with a Pb^{2+} ion at its center. The two water molecules (at O5 that bond to each Cs^+ ion at Cs31 are not shown. Reprinted with permission[54] © 2020 WILEY-VCH Verlag GmbH & Co. KGaA, Weinheim.

of pre-designed protein structures. For example, DNA and RNA utilise covalent bonds to regulate the sequence of their primary-order chain structure, while noncovalent interactions control their high-order morphology. Although biological polymer systems already use covalent interactions to form high-order structures, synthesising precise microporous organic coordination polymer structures was once considered

particularly challenging until Yaghi's team reported the first COFs in 2005[55]. To obtain well-ordered crystalline three-dimensional organic structures held together by strong covalent bonds between each block, it is crucial to carefully design the covalent and noncovalent interaction sites in the primary structure. In the absence of a proper guiding system, the organic chains may grow randomly on a two-dimensional plane, resulting in either an amorphous structure or a packed one-dimensional (linear) crystalline structure[57]. To address this issue, researchers have been studying different types of linkers, organic blocks, and fabrication conditions to tailor the COFs with diverse structures, as depicted in Figure 3[58]. These explorations opened new opportunities for COFs to be considered as porous host materials due to their high specific surface area, tailorable pores and structure, and low density.

Mn-ZnS QDs are considered as one of the promising materials for chemical contamination fluorescent detectors as ZnS has low toxicity and a wide band gap of 3.7 eV[59]. Furthermore, it has been broadly studied for metal ions, small molecules, and biopolymers detections. However, pure Mn-ZnS QDs have the limitation of low stability in a complex medium as the selectivity and sensitivity of the material reduce significantly over time[60]. To overcome these issues, molecularly imprinted polymers (MIPs) methods have been investigated. MIP is a procedure to generate specifically tailored cavities in polymers that works like antibody-antigen systems in our bodies to select precisely aimed molecules in the matrix[61]. This hybrid material showed great selectivity from shaped polymer and high sensitivity from QD material. However, achieving a uniform distribution and increasing the active material volume density remain challenging issues to address. Zhang *et al.* reported a new hybrid composite consisting of Mn-ZnS QDs embedded in TpPa-1 COFs with molecularly imprinted polymer (MIP) to improve the detection limit and stability of the composite in water[62]. This technique was further developed to fabricate fluorescent probes for ferulic acid with high selectivity and sensitivity, as demonstrated in Figure 4[63]. The fabricated composite demonstrated improved stability at room temperature, as well as a high photoluminescence quantum yield (PLQY) of 37%. In these applications, the COF serves not only as a passive protective framework but also as a platform for achieving even distribution and minimising aggregation of QDs.

Carbon quantum dots (CQDs) have been studied widely as a new type of fluorescent nanomaterials primarily due to their favourable characteristics such as environmental friendliness, functionalisability, excellent stability, biocompatibility, solubility, and low toxicity. These properties have rendered CQDs an ideal candidate for various applications such as sensing cellular copper, glucose, nucleic acids, and cancer detection and treatment. As a result, the investigation and exploration of CQDs continue to grow significantly[64,65]. Despite significant advantages, the limited size control, uniformity, and low quantum yield of carbon quantum dots present major challenges. To address these issues, researchers have attempted to improve synthesis methods using various techniques such as solvent engineering, electrochemical fabrication, and laser ablation, as well as fabricating hybrid composites that include encapsulating CQDs with polymers and embedding them within porous matrices. Recent progress in encapsulating carbon quantum dots (CQDs) involves surface functionalization by coating them with amphiphilic monomers or polymers. Amphiphilic molecules contain both hydrophilic and hydrophobic components, which allows them to interact with both water and the CQDs surface. This method can provide a protective layer around CQDs which can improve their stability, reduce aggregation, and provide other desirable properties such as solubility in different solvents[66-68]. Encapsulating CQDs within micro to mesoporous matrices such as mesoporous silica is a common approach to improve their stability and efficacy. Mesoporous silica, in particular, has attracted significant interest due to its large specific surface area, low toxicity, and good biocompatibility.

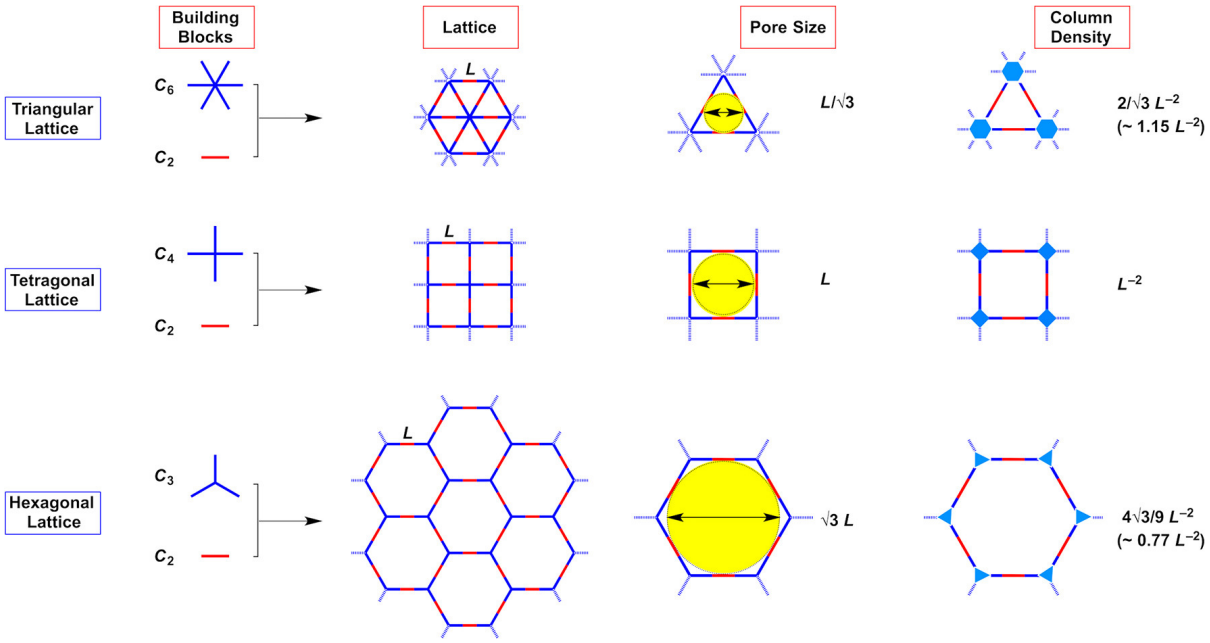

Figure 3. Dependency of pore size and column π-density of 2D COFs on topologies. Reprinted with permission[58]. Copyright © 2020 American Chemical Society.

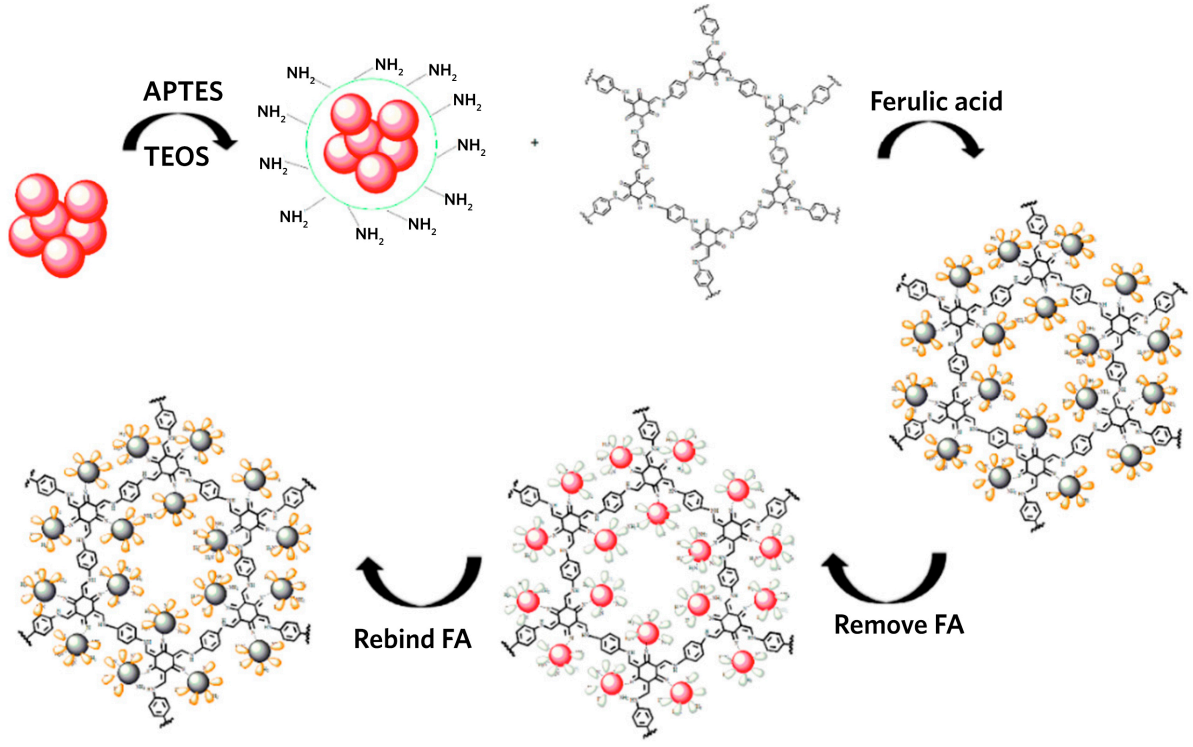

Figure 4. A schematic representation of the synthesis of molecularly imprinted polymers (MIPs) based on quantum dot-grafted covalent organic frameworks (QD-grafted COFs) for optosensing of ferulic acid (FA). Tetraethyl orthosilicate (TEOS) and (3-aminopropyl) triethoxysilane (APTES) are used as cross-linker and functional monomer, respectively, in MIP fabrication process. Reprinted with permission[63].

Recently, covalent organic frameworks have emerged as a promising alternative for encapsulating CQDs in microporous structures, offering advantages such as high stability, excellent control over pore size and shape, and the ability to tune the chemical and physical properties of the framework for specific applications. The presence of a large number of conjugated structures for both CQDs and COFs enables a unique opportunity to engineer their interfacial properties. Generally, CQDs have a size between 3 and 5 nm, which can be considered as a big molecular block within a typical COFs structure. Chen *et al*. formed, for the first time, two COFs consisting of carbon quantum dots which were generated through the Schiff base reactions with CQDs and phenylenediamine (pPDA) and BODIPY with two amino groups, as shown in Figure 5[69]. In this study, solvothermal methods were utilised to synthesise spherical CQDs with a size of ca. 5 nm. The synthesised CQDs were then dispersed in ethyl alcohol along with pPDA (p-phenylenediamine), and in a mixed solvent of ethyl alcohol and acetic acid with BODIPY, to form novel types of carbon dot-based covalent organic frameworks (CCOFs).

These newly synthesised CCOFs exhibit a bulk, spherical nanoparticle morphology, ranging in size from 200 to 500 nanometres. These structures are composed of carbon quantum dots, which are covalently bonded to organic ligands. Subsequently, the surfaces of these CCOFs are modified with polyethylene glycol (PEG) to further enhance their stability and dispersibility in aqueous environments. Following modification, the composite demonstrates no signs of aggregation for up to 24 h when exposed to a 10% fetal bovine serum (FBS) solution in water. By contrast, unmodified CCOFs exhibit aggregation under the same conditions. In addition, blood compatibility was evaluated by administering a dose of 10 mg/kg of modified CCOFs to mice, demonstrating no adverse effects on biosafety at that concentration. Furthermore, under green LED laser irradiation, the composite exhibited marked inhibition of tumour growth and size reduction. This carbon quantum dot-based covalent organic framework exhibits highly desirable characteristics, including excellent physiological stability, biocompatibility, and remarkable reactivity in oxygen generation, positioning them as a promising contender for cancer treatment[69].

QUANTUM DOTS IN METAL-ORGANIC FRAMEWORKS

Compared to zeolites and COFs, MOFs are a highly versatile family of microporous materials with a hybrid organic-inorganic continuous porous structure. They are formed by the coordination of metal ions with organic ligands, creating a three-dimensional network of pores and channels with high surface area and tunable properties. This material was introduced by Tomic in 1965 as a porous coordination framework. More than 80,000 types of MOFs have been reported so far, due to the wide selection of metal ions and organic ligands used to form a structure [Figure 6][70-73]. The presence of inorganic and organic coordination is a distinguishing factor of MOFs compared to covalent organic COFs, which are composed solely of light organic elements such as carbon, nitrogen, hydrogen, boron, and oxygen. High surface area, uniform structure, flexible choice of metal and organic ligands, structure tunability, and chemical functionality make this material unique and ideal for various applications such as separation, catalysis, sensing, and as a protective host matrix. One of the most extensively studied topics in the field of MOFs is hybrid nanocomposite materials. Due to the strong coordination between metal nodes and organic ligands, MOFs exhibit good chemical resistance to a wide range of solvents, including polar, nonpolar, and apolar solvents. Furthermore, porous structures can be tailored to a given requirement. These advantageous characteristics make this material a strong candidate as the protective host matrix for hybrid nanocomposites[74-77].

Organic-inorganic metal halide perovskites have been a trending subject in material science as a semiconducting light-harvesting material for various applications due to their outstanding properties, such as high light absorption coefficient, high defect tolerances and long charge carrier diffusion distances[78,79]. However, relatively low stability to moisture, heat and most common polar solvents limits the applicable

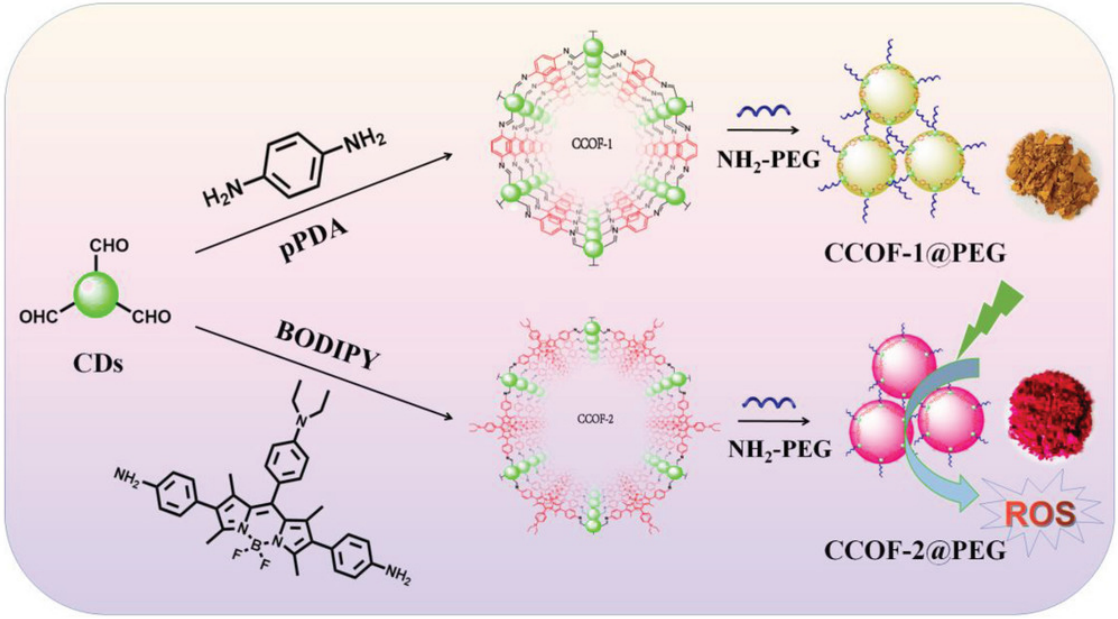

Figure 5. Schematic illustration of the synthesis of CCOF-1@PEG and CCOF-2@PEG and the application of CCOF-2@PEG for photodynamic therapy as reactive oxygen species (ROS) Carbon dots (CDs) and phenylenediamine (pPDA) and BODIPY are forming CCOF1 and CCOF2 respectively. Reprinted with permission[69] © 2020 Wiley-VCH GmbH

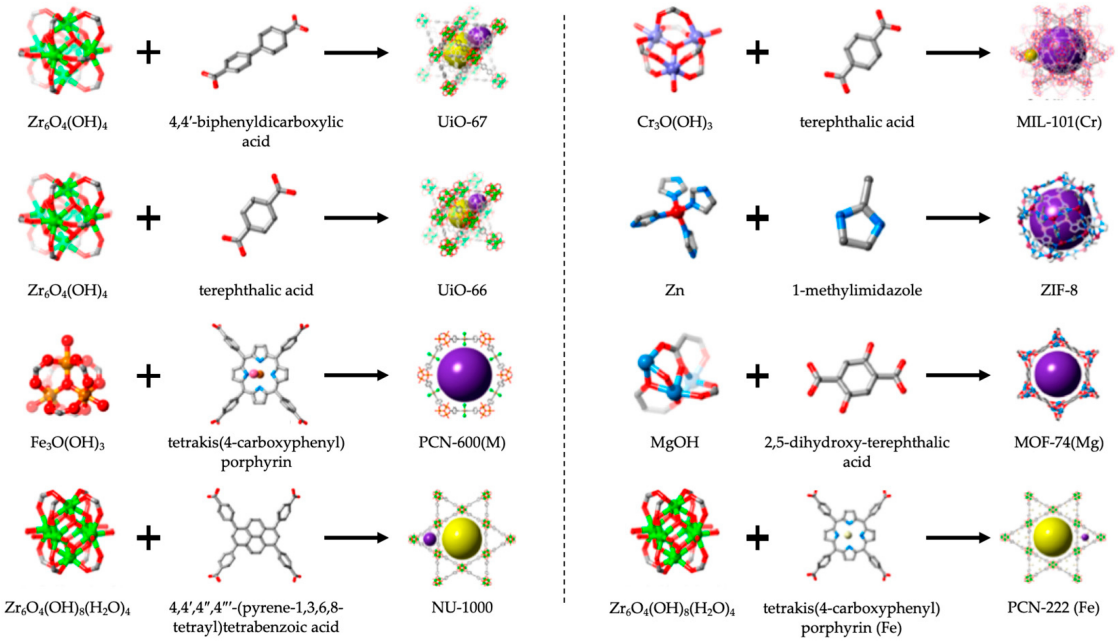

Figure 6. Representations of MOF structures and the corresponding node and linker constituents. Reprinted with permission[73,74]. Copyright © 2016 American Chemical Society.

devices and shortens the life expectancy of the application[80-82]. There have been various attempts to mitigate this major drawback of perovskite materials, such as compositional and interfacial engineering, surface passivation, and encapsulation[83]. Especially in the encapsulation process, the efficacy of the active material can often be reduced. Therefore, using a porous structure is crucial to minimise the unwanted sacrifices. In

this sense, MOFs are strong candidates as a protective layer since they can provide a hydrophobic surface and a uniformly tailored porous structure. A cesium lead bromide ($CsPbBr_3$), an inorganic halide perovskite, has garnered interest as a viable photocatalyst for CO_2 reduction. However, it shares similar limitations with other perovskites. Recently, researchers have made significant progress by employing zeolitic imidazolate frameworks (ZIFs), a subfamily of MOFs, as a host matrix for $CsPbBr_3$ quantum dots. Figure 7 illustrates the successful coating of $CsPbBr_3$ QDs with ZIFs through a "building a bottle around a ship" approach. The mild synthesis conditions of MOFs enable the fabrication of QD-MOF composites in this manner, providing reliable protection. The coated composite exhibits an improved CO_2 reduction efficiency due to its superior capturing ability and charge separation efficiency, as well as enhanced stability against moisture, compared to naked $CsPbBr_3$. However, this method may pose challenges in controlling QD particle size as the size is no longer restricted by the inherent pore structure of the template. Moreover, the synthesis solvent may cause partial dissolution/decomposition of QDs, which can adversely affect the overall efficiency. Thus, it is crucial to exercise caution in regulating the final solvent removal and nucleation process[84].

Typically, the pores in MOFs are considered too small to accommodate QDs, as most reported MOFs have microporous structures with pore diameters less than 2 nm. While this size range is suitable for the adsorption and separation of small molecules, such as gases, it is not ideal for QDs which are typically between 2 and 10 nm in size[85,86]. Synthesising QDs within the MOF cavity offers significant advantages in controlling QD crystal size through MOF pores and limiting aggregation during fabrication. However, the primary challenge lies in fabricating large-pore MOFs, as they can result in pore interpenetration and blockage. A meticulous design of the pore structure is also crucial, with an ideal cavity having a narrow entry to suppress the dissolution or dissociation of the encapsulated QDs[87]. To address this limitation, various efforts have been made to modify the pore sizes of MOFs to accommodate larger molecules such as QDs. One such approach involves introducing larger functional groups into the organic ligands or metal nodes, thereby expanding the pore size. Another approach is to employ post-synthesis modification techniques, including solvent or ligand exchange, to adjust the pore size of the MOF. These strategies have demonstrated promising outcomes in enlarging the pore size of MOFs, facilitating the integration of larger guest molecules like QDs[88-90].

In a recent advance, Qiao *et al.* reported the successful fabrication of $CsPbBr_3$ quantum dots within the PCN-33 MOF pores through a sequential deposition method[91]. PCN-333(Fe) possesses an extraordinary hierarchically porous structure with mesoporous cages ranging from ca. 4 to 5 nm and microporous cages with a diameter of around 1 nm, as well as excellent chemical stability. Its large mesoporous cages enable the accommodation of perovskite nanoparticles, while its microporous cages facilitate the diffusion of reactants for catalysis. In this study, $PbBr_2$ was positioned within the PCN-333(Fe) cavity, followed by the diffusion of CsBr into the pores to form $CsPbBr_3$ QDs within the mesoporous cage[91]. This composite showed green fluorescence under ultraviolet (UV) light, which confirms the formation of $CsPbBr_3$ QDs. Also, the resultant shows excellent stability, oxygen reduction, and evolving catalytic reaction in an aprotic medium. As these photoelectrochemical characteristics are desired for photocathodes in lithium-oxygen batteries, the material was tested as a cathode without any carbon support. The round-trip efficiency of the battery under illumination was 92.7%, which was comparably higher than that of pure $CsPbBr_3$ (82.8%) or PCN-333(Fe) (85.2%). Furthermore, it improved stability noticeably compared with pure $CsPbBr_3$ as the MOF provides the protective aspect. This work shows the potential compatibility of perovskite QDs and MOFs and also offers new promising directions and insights for photo-rechargeable batteries [Figure 8][91].

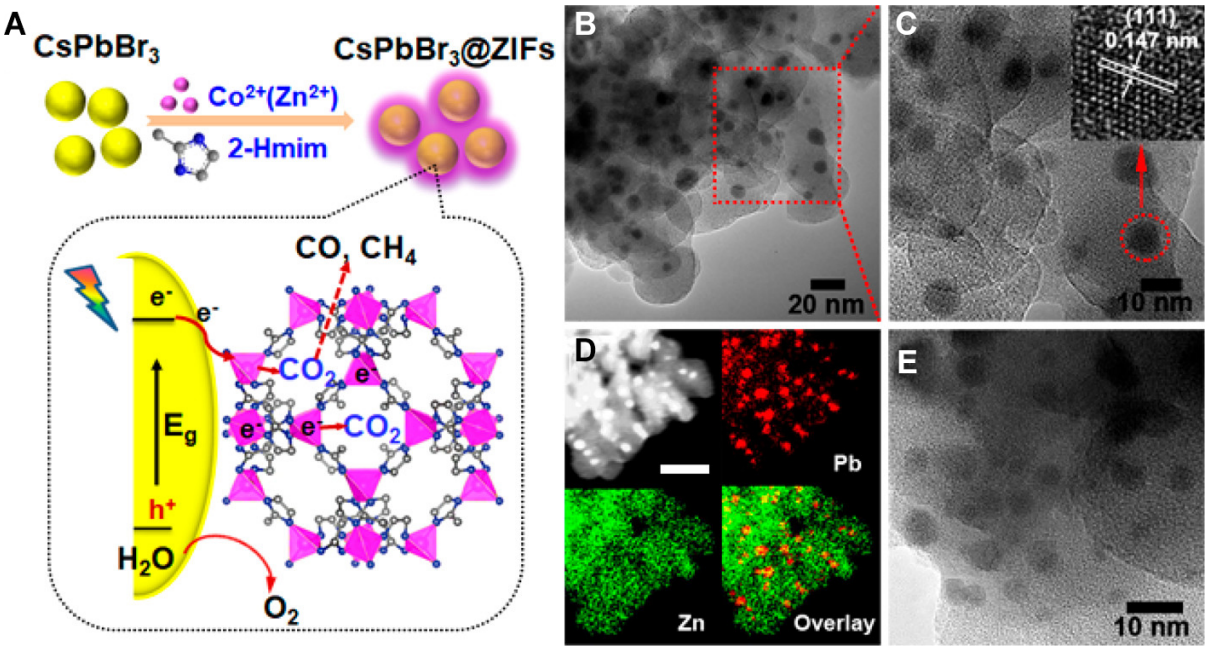

Figure 7. (A) Schematic illustration of the fabrication process and CO_2 photoreduction process of $CsPbBr_3$/ZIFs. (B and C) Low- and high-magnification TEM images of $CsPbBr_3$@ZIF-8. The inset of (C) is the high-resolution image of a single $CsPbBr_3$ QD marked with a red circle. (D) High-angle annular dark-field STEM image and elemental mapping of $CsPbBr_3$@ZIF-8. Scale bar: 50 nm. (E) TEM image of $CsPbBr_3$@ZIF-67. Reprinted with permission[84]. Copyright © 2018 American Chemical Society.

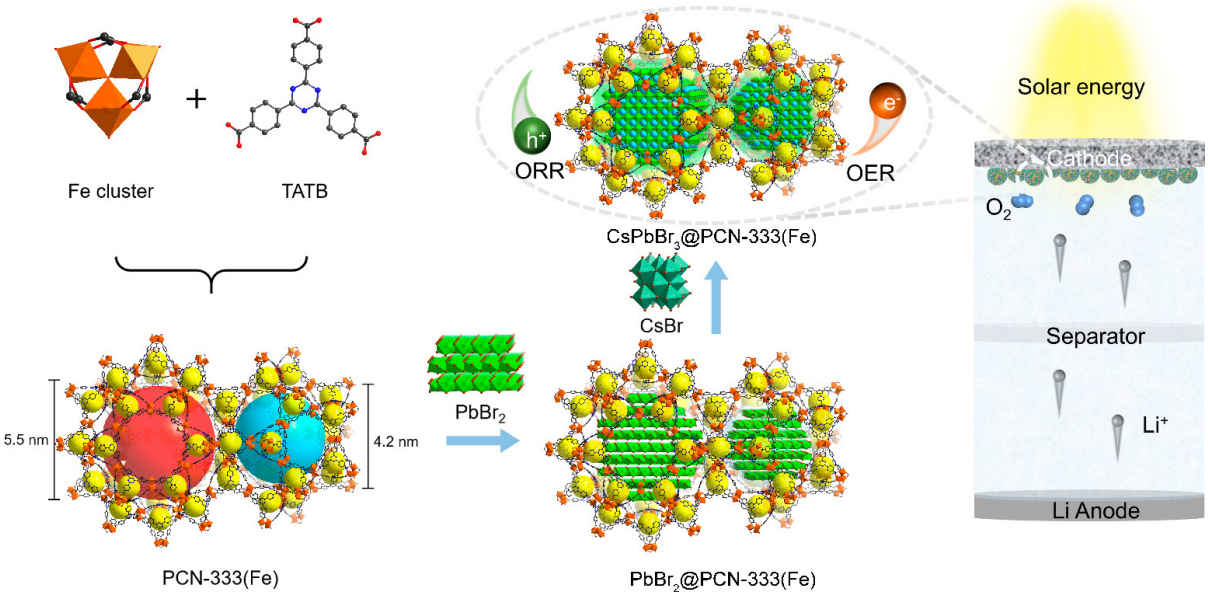

Figure 8. Schematic illustration of the Preparation of PCN-333(Fe) and $CsPbBr_3$@PCN-333(Fe) Composite $CsPbBr_3$@PCN-333(Fe) can be used as a photoelectric cathode material for light-assisted Li-O2 batteries. Reprinted with permission[91]. Copyright © 2021 American Chemical Society

So far, most research works on MOFs have focused on crystalline forms. However, limited processability and deprived interfacial bonding between host and guest materials have motivated the synthesis of non-crystalline structures. Recent studies showed that some of the MOFs, especially some of ZIFs, can form

amorphous structures via temperature-induced amorphisation through melting upon heating followed by a fast cooling (quenching) process at ambient pressure[92,93]. These ZIF glasses form a continuous random network similar to the amorphous structure of silica glass. Also, these emerging new types of glasses show structural diversity and unique properties compared to inorganic, organic and metallic glasses[94]. Recently, our group further developed this idea and successfully fabricated embedded perovskites within the ZIF glass matrix. This nanocomposite not only showed significantly improved photoluminescence under UV light in ambient conditions, but the stability also improved noticeably in most solvents. Figure 9 shows how $CsPbI_3$ perovskite is encapsulated within the ZIF-62 glass matrix after the sintering process and the phase distribution based on ADF and SED-STEM spectroscopy[95].

SUMMARY AND OUTLOOK

In conclusion, the embedment of various quantum dots into microporous materials has shown enormous potential for applications due to its ability to enhance long-term stability, reduce aggregation, improve efficiency, increase active material density, provide protective layers, and achieve uniform distribution. However, some of the methods are complicated and challenging to control during the fabrication process, which makes upscaling difficult. Although most of the studies are still in their early stages, especially QDs in COFs and MOFs, they have proved significant functionalities and potential. Based on above mentioned strategies, we hope this Perspective has highlighted the promising future research directions related to QDs in microporous structure.

(1) Biocompatible nanocomposite of QDs within microporous frameworks: The demand for biocompatible quantum dots and microporous templates is rapidly increasing for a wide range of applications, including disease detection, drug delivery, molecule detection, and cancer treatment. Currently, most of the research on biocompatible QDs is focused on surface engineering, including surface organic ligand exchange, polymer encapsulation and conjugation of biomolecules on the surface of QDs. However, those approaches still experience several issues such as size uniformity, aggregation, and stability in the biological environment. Furthermore, although there are numerous ongoing explorations for biocompatible and biodegradable MOFs and COFs for biomedicine applications, there have been limited investigations to combine biocompatible framework matrixes and QDs. Thus, by intermarriage of two biocompatible materials, QDs and specifically tailored flameworks matrix, can improve the selectivity of QDs and enable biological targeting of small molecules and antigens, as well as providing uniformity and stability to the composite.

(2) MOF glasses: one of the most recent and significant progress in porous materials is the development of MOF glasses. MOF glasses are new types of glasses that have unique characteristics compared with traditional glass materials. As these emerging materials have only been studied for less than 10 years, there are still many research gaps to investigate. We demonstrated a MOF glass with perovskite QD nanocomposites that greatly improved interfacial connectivity, which MOF crystals have not been able to achieve[95]. Furthermore, MOF glasses can be obtained through mechanical vitrification or direct synthesis as glass[96]. Thus, researching various types of MOFs and QDs hybrid materials as well as alternative fabrication routes of MOFs glass could open more new possibilities for QDs and MOF glasses nanocomposite.

(3) Fundamental study of QDs within microporous structure: Although great efforts have been made to fabricate QDs in microporous structures and improve their efficacy, there are remaining questions for a deeper understanding of the nanocomposite due to its set of rich physiochemical properties and dynamic interaction between two materials. In particular, x-ray-based techniques such as small-angle X-ray

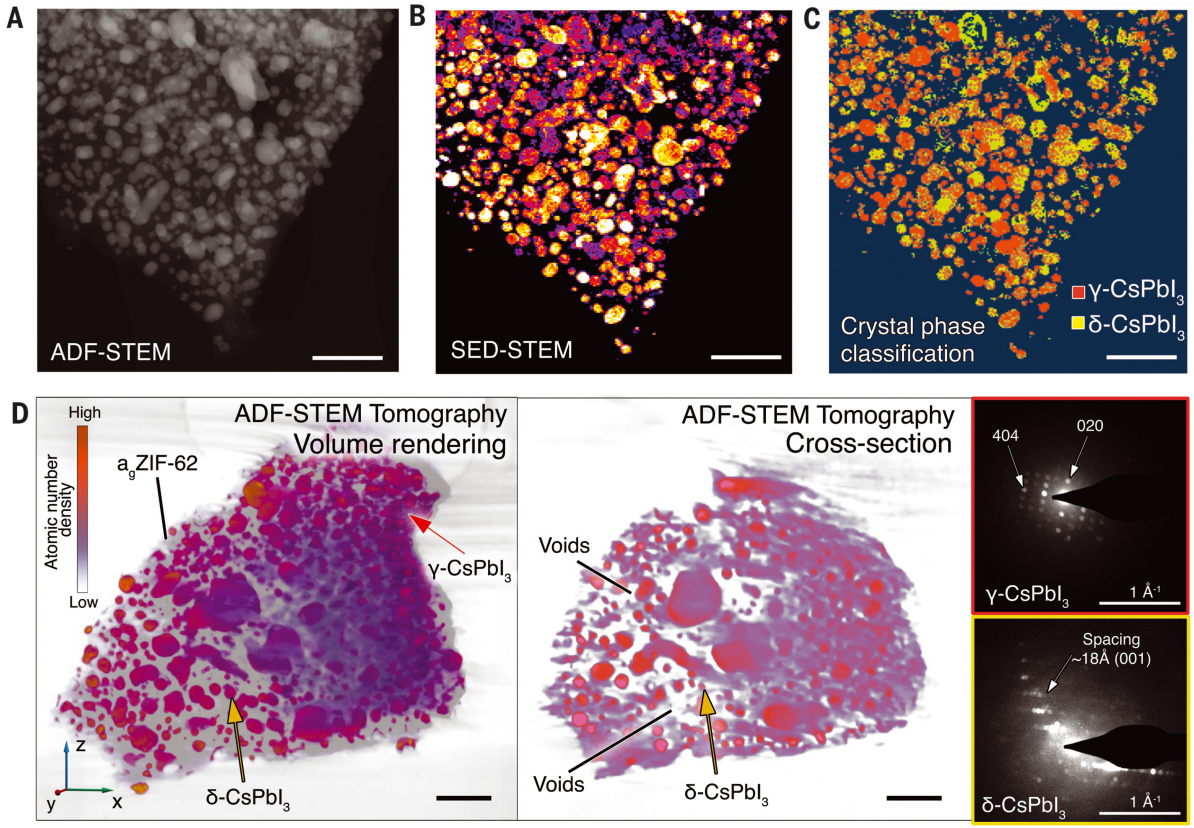

Figure 9. Phase distribution for the $(CsPbI_3)_{0.25}(a_gZIF\text{-}62)_{0.75}$ composite fabricated with 300 °C sintering. (A) ADF-STEM image, (B) SED-STEM mapping, and (C) $CsPbI_3$ crystal phase classification results for $(CsPbI_3)_{0.25}(a_gZIF\text{-}62)_{0.75}$ composite. (D) Volume rendering of tomographic reconstruction of $(CsPbI_3)_{0.25}(a_gZIF\text{-}62)_{0.75}$ and a single cross-sectional plane extracted from the volume. Color-coded arrows indicate the regions where electron diffraction data were collected. Scale bars, (A-D) 250 nm. Reprinted with permission[95]. Copyright © 2021 American Chemical Society

scattering (SAXS) and wide-angle X-ray scattering (WAXS) could show the micro to atomic scale structures and interactions of the composite materials. Recently, our group revealed the nanoparticle size, homogeneity, and internal structure behaviour during the liquid phase sintering process of pure MOF to MOF-glass and hybrid nanocomposite with perovskite, and MOF-glass using WAXS and SAXS analysis[92,94]. Furthermore, pair distribution functions (PDFs) from the X-ray diffusion pattern could explain the atomic structure formation, especially for composites with an amorphous matrix, as it can reveal information that X-ray diffraction is unable to obtain.

Terahertz/far-infrared (THz/far-IR) spectroscopy is another powerful technique that should be considered for investigating the dynamic properties of localised features within the composite. When paired with in-situ investigation capabilities, THz/far-IR spectroscopy can effectively identify the dynamic structural behaviour and emerging new chemical bonding between the guest and host materials. Hou *et al.* successfully integrated this technique to identify halogenation reactions during the melting process of MOF glass[95]. Combined with thermal behaviour analysis and X-ray-based techniques, this spectroscopy can reveal additional dynamic properties of QDs embedded in the microporous matrix and how they interface internally.

Overall, despite the significant and rapid progress in quantum dots (QDs) and tailorable microporous structures, they remain relatively immature technologies that have not yet been fully integrated into real-life applications, leaving significant space for exploration. A deeper and more fundamental understanding of complicated properties, such as interfacial bonding, conductivity, and structural and functional diversity, is expected to unlock new opportunities in the areas of light emission, biomedicine, catalysts, and energy storage.

DECLARATIONS

Authors' contributions

Conceptual design and manuscript draft: Lee J
Manuscript Revision and Project supervision: Wang L, Hou JW

Availability of data and materials

Not applicable.

Financial support and sponsorship

This research was partially financially supported by the Australian Research Council (ARC) through Future Fellowship, Laureate Fellowship programs (FT210100589 and FL190100139) and an Australian Government Research Training Program (RTP) Scholarship.

Ethical approval and consent to participate

Not applicable.

Consent for publication

Not applicable.

Conflicts of interest

All authors declared that there are no conflicts of interest.

Ethical approval and consent to participate

Not applicable.

Consent for publication

Not applicable.

Copyright

© The Author(s) 2023.

REFERENCES

1. Fujii M, Fujii R, Takada M, Sugimoto H. Silicon quantum dot supraparticles for fluorescence bioimaging. *ACS Appl Nano Mater* 2020;3:6099-107. DOI
2. Kwon J, Jun SW, Choi SI, et al. FeSe quantum dots for in vivo multiphoton biomedical imaging. *Sci Adv* 2019;5:eaay0044. DOI PubMed PMC
3. Shaik SA, Sengupta S, Varma RS, Gawande MB, Goswami A. Syntheses of N-doped carbon quantum dots (NCQDs) from bioderived precursors: a timely update. *ACS Sustain Chem Eng* 2021;9:3-49. DOI
4. Sun Y, Zheng S, Liu L, et al. The cost-effective preparation of green fluorescent carbon dots for bioimaging and enhanced intracellular drug delivery. *Nanoscale Res Lett* 2020;15:55. DOI PubMed PMC
5. Cho Y, Soufiani AM, Yun JS, et al. Mixed 3D-2D passivation treatment for mixed-cation lead mixed-halide perovskite solar cells for higher efficiency and better stability. *Adv Energy Mater* 2018;8:1703392. DOI
6. Cordero F, Craciun F, Trequattrini F, et al. Stability of cubic $FAPbI_3$ from X-ray diffraction, anelastic, and dielectric measurements. *J*

Phys Chem Lett 2019;10:2463-9. DOI

7. Rambabu D, Bhattacharyya S, Singh T, Maji TK. Stabilization of $MAPbBr_3$ perovskite quantum dots on perovskite MOFs by a one-step mechanochemical synthesis. *Inorg Chem* 2020;59:1436-43. DOI PubMed
8. Zhang Y, Zhou Z, Ji F, et al. Trash into treasure: δ-$FAPbI_3$ polymorph stabilized $MAPbI_3$ Perovskite with power conversion efficiency beyond 21. *Adv Mater* 2018;30:e1707143. DOI
9. Iravani S, Varma RS. Green synthesis, biomedical and biotechnological applications of carbon and graphene quantum dots: a review. *Environ Chem Lett* 2020;18:703-27. DOI PubMed PMC
10. Jouyandeh M, Mousavi Khadem SS, Habibzadeh S, et al. Quantum dots for photocatalysis: synthesis and environmental applications. *Green Chem* 2021;23:4931-54. DOI
11. Ye B, Jiang R, Yu Z, et al. Pt(111) quantum dot engineered Fe-MOF nanosheet arrays with porous core-shell as an electrocatalyst for efficient overall water splitting. *J Catal* 2019;380:307-17. DOI
12. Alsalloum AY, Turedi B, Zheng X, et al. Low-temperature crystallization enables 21.9% efficient single-crystal $MAPbI_3$ inverted perovskite solar cells. *ACS Energy Lett* 2020;5:657-62. DOI
13. Chen Z, Chen Z, Li H, Zhao X, Zhu M, Wang M. Investigation on charge carrier recombination of hybrid organic-inorganic perovskites doped with aggregation-induced emission luminogen under high photon flux excitation. *Adv Opt Mater* 2018;6:1800221. DOI
14. Masi S, Gualdrón-reyes AF, Mora-seró I. Stabilization of black perovskite phase in $FAPbI_3$ and $CsPbI_3$. *ACS Energy Lett* 2020;5:1974-85. DOI
15. Wang D, Wright M, Elumalai NK, Uddin A. Stability of perovskite solar cells. *Solar Energy Mater Solar Cells* 2016;147:255-75. DOI
16. Hou J, Wang Z, Chen P, Chen V, Cheetham AK, Wang L. Intermarriage of halide perovskites and metal-organic framework crystals. *Angew Chem Int Ed* 2020;59:19434-49. DOI
17. Hao M, Bai Y, Zeiske S, et al. Ligand-assisted cation-exchange engineering for high-efficiency colloidal Cs_1-xFAxPbI$_3$ quantum dot solar cells with reduced phase segregation. *Nat Energy* 2020;5:79-88. DOI
18. Nagaraj G, Mohammed MKA, Shekargoftar M, et al. High-performance perovskite solar cells using the graphene quantum dot-modified SnO_2/ZnO photoelectrode. *Mater Today Energy* 2021;22:100853. DOI
19. Zhao H, Yu X, Li C, et al. Carbon quantum dots modified TiO_2 composites for hydrogen production and selective glucose photoreforming. *J Energy Chem* 2022;64:201-8. DOI
20. Yoo D, Park Y, Cheon B, Park MH. Carbon dots as an effective fluorescent sensing platform for metal ion detection. *Nanoscale Res Lett* 2019;14:272. DOI PubMed PMC
21. Abbas A, Tabish TA, Bull SJ, Lim TM, Phan AN. High yield synthesis of graphene quantum dots from biomass waste as a highly selective probe for Fe^{3+} sensing. *Sci Rep* 2020;10:21262. DOI PubMed PMC
22. Ganganboina AB, Dega NK, Tran HL, Darmonto W, Doong RA. Application of sulfur-doped graphene quantum dots@gold-carbon nanosphere for electrical pulse-induced impedimetric detection of glioma cells. *Biosens Bioelectron* 2021;181:113151. DOI PubMed
23. Shi Y, Wang Z, Meng T, et al. Red phosphorescent carbon quantum dot organic framework-based electroluminescent light-emitting diodes exceeding 5% external quantum efficiency. *J Am Chem Soc* 2021;143:18941-51. DOI
24. Wang S, Kang G, Cui F, Zhang Y. Dual-color graphene quantum dots and carbon nanoparticles biosensing platform combined with Exonuclease III-assisted signal amplification for simultaneous detection of multiple DNA targets. *Anal Chim Acta* 2021;1154:338346. DOI
25. Biswal BP, Shinde DB, Pillai VK, Banerjee R. Stabilization of graphene quantum dots (GQDs) by encapsulation inside zeolitic imidazolate framework nanocrystals for photoluminescence tuning. *Nanoscale* 2013;5:10556-61. DOI PubMed
26. Swarnkar A, Marshall AR, Sanehira EM, et al. Quantum dot-induced phase stabilization of α-CsPbI3 perovskite for high-efficiency photovoltaics. *Science* 2016;354:92-5. DOI
27. Kar MR, Ray S, Patra BK, Bhaumik S. State of the art and prospects of metal halide perovskite core@shell nanocrystals and nanocomposites. *Mater Today Chem* 2021;20:100424. DOI
28. Yee PY, Brittman S, Mahadik NA, et al. Cu_{2-x} S/PbS core/shell nanocrystals with improved chemical stability. *Chem Mater* 2021;33:6685-91. DOI
29. Zhao Y, Xie C, Zhang X, Yang P. $CsPbX_3$ quantum dots embedded in zeolitic imidazolate framework-8 microparticles for bright white light-emitting devices. *ACS Appl Nano Mater* 2021;4:5478-85. DOI
30. Pham T, Lee B, Kim J, Lee C. Enhancement of CO_2 capture by using synthesized nano-zeolite. *J Taiwan Inst Chem Eng* 2016;64:220-6. DOI
31. Zahmakiran M. Preparation and characterization of LTA-type zeolite framework dispersed ruthenium nanoparticles and their catalytic application in the hydrolytic dehydrogenation of ammonia-borane for efficient hydrogen generation. *Mater Sci Eng B* 2012;177:606-13. DOI
32. Frentzel-beyme L, Kloß M, Pallach R, et al. Porous purple glass - a cobalt imidazolate glass with accessible porosity from a meltable cobalt imidazolate framework. *J Mater Chem A* 2019;7:985-90. DOI
33. Hou J, Ríos Gómez ML, Krajnc A, et al. Halogenated metal-organic framework glasses and liquids. *J Am Chem Soc* 2020;142:3880-90. DOI
34. Fang Q, Gu S, Zheng J, Zhuang Z, Qiu S, Yan Y. 3D microporous base-functionalized covalent organic frameworks for size-selective catalysis. *Angew Chem Int Ed* 2014;53:2878-82. DOI

35. Bhunia S, Deo KA, Gaharwar AK. 2D covalent organic frameworks for biomedical applications. *Adv Funct Mater* 2020;30:2002046. DOI
36. Chedid G, Yassin A. Recent trends in covalent and metal organic frameworks for biomedical applications. *Nanomaterials* 2018;8:916. DOI PubMed PMC
37. Feng L, Qian C, Zhao Y. Recent advances in covalent organic framework-based nanosystems for bioimaging and therapeutic applications. *ACS Mater Lett* 2020;2:1074-92. DOI
38. Ekimov A, Efros A, Onushchenko A. Quantum size effect in semiconductor microcrystals. *Solid State Commun* 1985;56:921-4. DOI
39. Davis ME. Ordered porous materials for emerging applications. *Nature* 2002;417:813-21. DOI PubMed
40. Kianfar E. Synthesis and characterization of $AlPO_4$/ZSM-5 catalyst for methanol conversion to dimethyl ether. *Russ J Appl Chem* 2018;91:1711-20. DOI
41. Yin T, Meng X, Jin L, Yang C, Liu N, Shi L. Prepared hydrophobic Y zeolite for adsorbing toluene in humid environment. *Microporous Mesoporous Mater* 2020;305:110327. DOI
42. Campanile A, Liguori B, Ferone C, Caputo D, Aprea P. Zeolite-based monoliths for water softening by ion exchange/precipitation process. *Sci Rep* 2022;12:3686. DOI PubMed PMC
43. Wang S, Yu J, Zhao P, Guo S, Han S. One-step synthesis of water-soluble CdS quantum dots for silver-ion detection. *ACS Omega* 2021;6:7139-46. DOI PubMed PMC
44. Herron N, Wang Y, Eddy MM, et al. Structure and optical properties of cadmium sulfide superclusters in zeolite hosts. *J Am Chem Soc* 1989;111:530-40. DOI
45. Moller K, Bein T, Herron N, Mahler W, Wang Y. Encapsulation of lead sulfide molecular clusters into solid matrixes. Structural analysis with X-ray absorption spectroscopy. *Inorg Chem* 1989;28:2914-9. DOI
46. Jeong NC, Kim HS, Yoon KB. New insights into CdS quantum dots in zeolite-Y. *J Phys Chem C* 2007;111:10298-312. DOI
47. Yin X, Zhang C, Guo Y, Yang Y, Xing Y, Que W. PbS QD-based photodetectors: future-oriented near-infrared detection technology. *J Mater Chem C* 2021;9:417-38. DOI
48. Zheng S, Chen J, Johansson EMJ, Zhang X. PbS colloidal quantum dot inks for infrared solar cells. *iScience* 2020;23:101753. DOI PubMed PMC
49. Kim HS, Lee MH, Jeong NC, Lee SM, Rhee BK, Yoon KB. Very high third-order nonlinear optical activities of intrazeolite PbS quantum dots. *J Am Chem Soc* 2006;128:15070-1. DOI PubMed
50. Kim HS, Yoon KB. Increase of third-order nonlinear optical activity of PbS quantum dots in zeolite Y by increasing cation size. *J Am Chem Soc* 2012;134:2539-42. DOI
51. Liu Y, Li Y, Hu X, et al. Ligands for $CsPbBr_3$ perovskite quantum dots: the stronger the better? *Chem Eng J* 2023;453:139904. DOI
52. Sun J, Rabouw FT, Yang X, et al. Facile two-step synthesis of all-inorganic perovskite $CsPbX_3$ (X = Cl, Br, and I) Zeolite-Y composite phosphors for potential backlight display application. *Adv Funct Mater* 2017;27:1704371. DOI
53. Wang HC, Lin SY, Tang AC, et al. Mesoporous silica particles integrated with all-inorganic $CsPbBr_3$ perovskite quantum-dot nanocomposites (MP-PQDs) with high stability and wide color gamut used for backlight display. *Angew Chem Int Ed* 2016;55:7924-9. DOI
54. Kim JY, Shim KI, Han JW, Joo J, Heo NH, Seff K. Quantum dots of $[Na_4Cs_6PbBr_4]^{8+}$, water stable in Zeolite X, luminesce sharply in the green. *Adv Mater* 2020;32:e2001868. DOI PubMed
55. Côté AP, Benin AI, Ockwig NW, O'Keeffe M, Matzger AJ, Yaghi OM. Porous, crystalline, covalent organic frameworks. *Science* 2005;310:1166-70. DOI PubMed
56. Ding SY, Wang W. Covalent organic frameworks (COFs): from design to applications. *Chem Soc Rev* 2013;42:548-68. DOI PubMed
57. Wang H, Yang Y, Yuan X, et al. Structure-performance correlation guided applications of covalent organic frameworks. *Mater Today* 2022;53:106-33. DOI
58. Geng K, He T, Liu R, et al. Covalent organic frameworks: design, synthesis, and functions. *Chem Rev* 2020;120:8814-933. DOI
59. Binu PJ, Ganesh RC, Muthukumaran S. Crystal structure, energy gap and photoluminescence investigation of Mn^{2+}/Cr^{3+}-doped ZnS nanostructures by precipitation method. *J Mater Sci Mater Electron* 2021;32:23174-88. DOI
60. Liu Z, Hou J, He Q, Luo X, Huo D, Hou C. New application of Mn-doped ZnS quantum dots: phosphorescent sensor for the rapid screening of chloramphenicol and tetracycline residues. *Anal Methods* 2020;12:3513-22. DOI
61. Li F, Gao J, Wu H, Li Y, He X, Chen L. A highly selective and sensitive fluorescent sensor based on molecularly imprinted polymer-functionalized Mn-doped ZnS quantum dots for detection of roxarsone in feeds. *Nanomaterials* 2022;12:2997. DOI PubMed PMC
62. Zhang Y, Yuan X, Jiang W, Liu H. Determination of nereistoxin-related insecticide via quantum-dots-doped covalent organic frameworks in a molecularly imprinted network. *Mikrochim Acta* 2020;187:464. DOI
63. Wang Y, Wang Y, Liu H. A novel fluorescence and SPE adsorption nanomaterials of molecularly imprinted polymers based on quantum dot-grafted covalent organic frameworks for the high selectivity and sensitivity detection of ferulic acid. *Nanomaterials* 2019;9:305. DOI PubMed PMC
64. Jana J, Lee HJ, Chung JS, Kim MH, Hur SH. Blue emitting nitrogen-doped carbon dots as a fluorescent probe for nitrite ion sensing and cell-imaging. *Anal Chim Acta* 2019;1079:212-9. DOI PubMed
65. Wang J, Sheng Li R, Zhi Zhang H, Wang N, Zhang Z, Huang CZ. Highly fluorescent carbon dots as selective and visual probes for sensing copper ions in living cells via an electron transfer process. *Biosens Bioelectron* 2017;97:157-63. DOI
66. Fowley C, McCaughan B, Devlin A, Yildiz I, Raymo FM, Callan JF. Highly luminescent biocompatible carbon quantum dots by

encapsulation with an amphiphilic polymer. *Chem Commun* 2012;48:9361-3. DOI PubMed

67. Sharma A, Das J. Small molecules derived carbon dots: synthesis and applications in sensing, catalysis, imaging, and biomedicine. *J Nanobiotechnol* 2019;17:92. DOI PubMed PMC
68. Wang F, Pang S, Wang L, Li Q, Kreiter M, Liu C. One-step synthesis of highly luminescent carbon dots in noncoordinating solvents. *Chem Mater* 2010;22:4528-30. DOI
69. Chen S, Sun T, Zheng M, Xie Z. Carbon dots based nanoscale covalent organic frameworks for photodynamic therapy. *Adv Funct Mater* 2020;30:2004680. DOI
70. Fonseca J, Gong T, Jiao L, Jiang H. Metal-organic frameworks (MOFs) beyond crystallinity: amorphous MOFs, MOF liquids and MOF glasses. *J Mater Chem A* 2021;9:10562-611. DOI
71. Hou J, Sutrisna PD, Wang T, et al. Unraveling the interfacial structure-performance correlation of flexible metal-organic framework membranes on polymeric substrates. *ACS Appl Mater Interfaces* 2019;11:5570-7. DOI
72. Baumann AE, Burns DA, Liu B, Thoi VS. Metal-organic framework functionalization and design strategies for advanced electrochemical energy storage devices. *Commun Chem* 2019:2. DOI
73. Howarth AJ, Peters AW, Vermeulen NA, Wang TC, Hupp JT, Farha OK. Best practices for the synthesis, activation, and characterization of metal-organic frameworks. *Chem Mater* 2017;29:26-39. DOI
74. Hong DH, Shim HS, Ha J, Moon HR. MOF-on-MOF architectures: applications in separation, catalysis, and sensing. *Bull Korean Chem Soc* 2021;42:956-69. DOI
75. Kalaj M, Bentz KC, Ayala S Jr, et al. MOF-polymer hybrid materials: from simple composites to tailored architectures. *Chem Rev* 2020;120:8267-302. DOI
76. Kwon O, Kim JY, Park S, et al. Computer-aided discovery of connected metal-organic frameworks. *Nat Commun* 2019;10:3620. DOI PubMed PMC
77. Tripathy SP, Subudhi S, Parida K. Inter-MOF hybrid (IMOFH): a concise analysis on emerging core-shell based hierarchical and multifunctional nanoporous materials. *Coord Chem Rev* 2021;434:213786. DOI
78. Chen P, Bai Y, Wang S, Lyu M, Yun J, Wang L. Perovskite solar cells: in situ growth of 2D perovskite capping layer for stable and efficient perovskite solar cells. *Adv Funct Mater* 2018;28:1870113. DOI
79. Peng J, Kremer F, Walter D, et al. Centimetre-scale perovskite solar cells with fill factors of more than 86 per cent. *Nature* 2022;601:573-8. DOI
80. Shi L, Wang J, Zhou L, Chen Y, Yan J, Dai C. Facile in-situ preparation of $MAPbBr_3$@UiO-66 composites for information encryption and decryption. *J Solid State Chem* 2020;282:121062. DOI
81. Zhang Y, Lyu M, Qiu T, et al. Halide perovskite single crystals: optoelectronic applications and strategical approaches. *Energies* 2020;13:4250. DOI
82. He R, Ren S, Chen C, et al. Wide-bandgap organic-inorganic hybrid and all-inorganic perovskite solar cells and their application in all-perovskite tandem solar cells. *Energy Environ Sci* 2021;14:5723-59. DOI
83. Lu H, Krishna A, Zakeeruddin SM, Grätzel M, Hagfeldt A. Compositional and interface engineering of organic-inorganic lead halide perovskite solar cells. *iScience* 2020;23:101359. DOI PubMed PMC
84. Kong Z, Liao J, Dong Y, et al. Core@Shell $CsPbBr_3$@Zeolitic imidazolate framework nanocomposite for efficient photocatalytic CO_2 reduction. *ACS Energy Lett* 2018;3:2656-62. DOI
85. Yuan S, Zou L, Qin JS, et al. Construction of hierarchically porous metal-organic frameworks through linker labilization. *Nat Commun* 2017;8:15356. DOI PubMed PMC
86. Aubert T, Golovatenko AA, Samoli M, et al. General expression for the size-dependent optical properties of quantum dots. *Nano Lett* 2022;22:1778-85. DOI
87. Wang T, Gao L, Hou J, et al. Rational approach to guest confinement inside MOF cavities for low-temperature catalysis. *Nat Commun* 2019;10:1340. DOI PubMed PMC
88. Jiang Z, Xue W, Huang H, Zhu H, Sun Y, Zhong C. Mechanochemistry-assisted linker exchange of metal-organic framework for efficient kinetic separation of propene and propane. *Chem Eng J* 2023;454:140093. DOI
89. Qi SC, Qian XY, He QX, et al. Generation of hierarchical porosity in metal-organic frameworks by the modulation of cation valence. *Angew Chem Int Ed* 2019;58:10104-9. DOI
90. Yang P, Mao F, Li Y, Zhuang Q, Gu J. Hierarchical porous Zr-based MOFs synthesized by a facile monocarboxylic acid etching strategy. *Chemistry* 2018;24:2962-70. DOI PubMed
91. Qiao GY, Guan D, Yuan S, et al. Perovskite quantum dots encapsulated in a mesoporous metal-organic framework as synergistic photocathode materials. *J Am Chem Soc* 2021;143:14253-60. DOI
92. Hou J, Sapnik AF, Bennett TD. Metal-organic framework gels and monoliths. *Chem Sci* 2020;11:310-23. DOI PubMed PMC
93. Tuffnell JM, Ashling CW, Hou J, et al. Novel metal-organic framework materials: blends, liquids, glasses and crystal-glass composites. *Chem Commun* 2019;55:8705-15. DOI
94. Hou J, Ashling CW, Collins SM, et al. Metal-organic framework crystal-glass composites. *Nat Commun* 2019;10:2580. DOI PubMed PMC
95. Hou J, Chen P, Shukla A, et al. Liquid-phase sintering of lead halide perovskites and metal-organic framework glasses. *Science* 2021;374:621-5. DOI
96. Keen DA, Bennett TD. Structural investigations of amorphous metal-organic frameworks formed via different routes. *Phys Chem*

Chem Phys 2018;20:7857-61. DOI PubMed

AUTHOR INSTRUCTIONS

1. Submission Overview

Before you decide to publish with *Microstructures*, please read the following items carefully and make sure that you are well aware of Editorial Policies and the following requirements.

1.1 Topic Suitability

The topic of the manuscript must fit the scope of the journal. Please refer to Aims and Scope for more information.

1.2 Open Access and Copyright

The journal adopts Gold Open Access publishing model and distributes content under the Creative Commons Attribution 4.0 International License. Copyright is retained by authors. Please make sure that you are well aware of these policies.

1.3 Publication Fees

Microstructures is an open access journal. When a paper is accepted for publication, authors are required to pay Article Processing Charges (APCs) to cover its editorial and production costs. The APC for each submission is $600. There are no additional charges based on color, length, figures, or other elements. For more details, please refer to OAE Publication Fees.

1.4 Language Editing

All submissions are required to be presented clearly and cohesively in good English. Authors whose first language is not English are advised to have their manuscripts checked or edited by a native English speaker before submission to ensure the high quality of expression. A well-organized manuscript in good English would make the peer review even the whole editorial handling more smoothly and efficiently.

If needed, authors are recommended to consider the language editing services provided by Charlesworth to ensure that the manuscript is written in correct scientific English before submission. Authors who publish with OAE journals enjoy a special discount for the services of Charlesworth via the following two ways.

Submit your manuscripts directly at http://www.charlesworthauthorservices.com/~OAE;

Open the link http://www.charlesworthauthorservices.com/, and enter Promotion Code “OAE” when you submit.

1.5 Work Funded by the National Institutes of Health

If an accepted manuscript was funded by National Institutes of Health (NIH), the author may inform editors of the NIH funding number. The editors are able to deposit the paper to the NIH Manuscript Submission System on behalf of the author.

2. Submission Preparation

2.1 Cover Letter

A cover letter is required to be submitted accompanying each manuscript. It should be concise and explain why the study is significant, why it fits the scope of the journal, and why it would be attractive to readers, etc.

Here is a guideline of a cover letter for authors’ consideration:

In the first paragraph: include the title and type (e.g., Research Article, Review Article, etc.) of the manuscript, a brief on the background of the study, the question the author sought out to answer and why;

In the second paragraph: concisely explain what was done, the main findings and why they are significant;

In the third paragraph: indicate why the manuscript fits the Aims and Scope of the journal, and why it would be attractive to readers;

In the fourth paragraph: confirm that the manuscript has not been published elsewhere and not under consideration of any other journal. All authors have approved the manuscript and agreed on its submission to the journal. Journal’s specific requirements have been met if any.

If the manuscript is contributed to a special issue, please also mention it in the cover letter.

If the manuscript was presented partly or entirely in a conference, the author should clearly state the background information of the event, including the conference name, time and place in the cover letter.

2.2 Types of Manuscripts

There is no restriction on the length of manuscripts, number of figures, tables and references, provided that the manuscript is concise and comprehensive. The journal publishes Research Article, Review Article, Editorial, Perspective etc. For more details about paper type, please refer to the following table.

Manuscript Type	Definition	Abstract	Keywords	Main Text Structure
Research Article	A Research Article describes detailed results from novel research. All findings are extensively discussed.	Structured abstract including Aim, Methods, Results and Conclusion. No more than 250 words.	3-8 keywords	The main content should include four sections: Introduction, Materials and Methods, Results and Discussion.
Review Article	A Review Article summarizes the literature on previous studies. It usually does not present any new information on a subject.	Unstructured abstract. No more than 250 words.	3-8 keywords	The main text may consist of several sections with unfixed section titles. We suggest that the author include an "Introduction" section at the beginning, several sections with unfixed titles in the middle part, and a "Conclusion" section in the end.
Meta-Analysis	A Meta-Analysis is a statistical analysis combining the results of multiple scientific studies. It is often an overview of clinical trials.	Structured abstract including Aim, Methods, Results and Conclusion. No more than 250 words.	3-8 keywords	The main content should include four sections: Introduction, Methods, Results and Discussion.
Technical Note	A Technical Note is a short article giving a brief description of a specific development, technique or procedure, or it may describe a modification of an existing technique, procedure or device applied in research.	Unstructured abstract. No more than 250 words.	3-8 keywords	/
Commentary	A Commentary is to provide comments on a newly published article or an alternative viewpoint on a certain topic.	Unstructured abstract. No more than 250 words.	3-8 keywords	/
Editorial	An Editorial is a short article describing news about the journal or opinions of senior editors or the publisher.	None required.	None required.	/
Letter to Editor	A Letter to Editor is usually an open post-publication review of a paper from its readers, often critical of some aspect of a published paper. Controversial papers often attract numerous Letters to Editor.	Unstructured abstract (optional). No more than 250 words.	3-8 keywords (optional)	/
Opinion	An Opinion usually presents personal thoughts, beliefs, or feelings on a topic.	Unstructured abstract (optional). No more than 250 words.	3-8 keywords	/
Perspective	A Perspective provides personal points of view on the state-of-the-art of a specific area of knowledge and its future prospects. Links to areas of intense current research focus can also be made. The emphasis should be on a personal assessment rather than a comprehensive, critical review. However, comments should be put into the context of existing literature. Perspectives are usually invited by the Editors.	Unstructured abstract. No more than 150 words.	3-8 keywords	/

2.3 Manuscript Structure

2.3.1 Front Matter

2.3.1.1 Title

The title of the manuscript should be concise, specific and relevant, with no more than 16 words if possible. When gene or protein names are included, the abbreviated name rather than full name should be used.

2.3.1.2 Authors and Affiliations

Authors' full names should be listed. The initials of middle names can be provided. Institutional addresses and email addresses for all authors should be listed. At least one author should be designated as corresponding author. In addition, corresponding authors are suggested to provide their Open Researcher and Contributor ID upon submission. Please note that any change to authorship is not allowed after manuscript acceptance.

2.3.1.3 Highlights

Highlights are mandatory because they can help increase the discoverability of your article through search engines. They consist of a short collection of bullet points that capture the novel results of your research as well as new methods that were used during the study (if any). They should be submitted in a separate editable file in the online submission system. Please use 'Highlights' in the file name and include 3 to 5 bullet points (maximum 85 characters per bullet point, including spaces).

2.3.1.4 Abstract

The abstract should be a single paragraph with word limitation and specific structure requirements (for more details please refer to Types of Manuscripts). It usually describes the main objective(s) of the study, explains how the study was done, including any model organisms used, without methodological detail, and summarizes the most important results and their significance. The abstract must be an objective representation of the study: it is not allowed to contain results which are not presented and substantiated in the manuscript, or exaggerate the main conclusions. Citations should not be included in the abstract.

2.3.1.5 Graphical Abstract

The graphical abstract is essential as this can catch first view of your publication by readers. We recommend you to submit an eye-catching figure. It should summarize the content of the article in a concise graphical form. It is recommended to use it because this can make online articles get more attention. The graphic abstract should be submitted as a separate document in the online submission system. Please provide an image with a minimum of 730 × 1,228 pixels (h × w) or proportionally more. The image should be readable at a size of 7 × 12 cm using a regular screen resolution of 96 dpi. Preferred file types: TIFF, PSD, AI, JPG, JPEG, EPS, PNG, ZIP and PDF files.

2.3.1.6 Keywords

Three to eight keywords should be provided, which are specific to the article, yet reasonably common within the subject discipline.

2.3.2 Main Text

Manuscripts of different types are structured with different sections of content. Please refer to Types of Manuscripts to make sure which sections should be included in the manuscripts.

2.3.2.1 Introduction

The introduction should contain background that puts the manuscript into context, allow readers to understand why the study is important, include a brief review of key literature, and conclude with a brief statement of the overall aim of the work and a comment about whether that aim was achieved. Relevant controversies or disagreements in the field should be introduced as well.

2.3.2.2 Materials and Methods

Materials and Methods should contain sufficient details to allow others to fully replicate the study. New methods and protocols should be described in detail while well-established methods can be briefly described or appropriately cited. Experimental participants selected, the drugs and chemicals used, the statistical methods taken, and the computer software used should be identified precisely. Statistical terms, abbreviations, and all symbols used should be defined clearly. Protocol documents for clinical trials, observational studies, and other non-laboratory investigations may be uploaded as supplementary materials.

2.3.2.3 Results and Discussion

This section should contain the findings of the study and discuss the implications of the findings in context of existing research and highlight limitations of the study. Future research directions may also be mentioned. Results of statistical analysis should also be included either as text or as tables or figures if appropriate. Authors should emphasize and summarize

only the most important observations. Data on all primary and secondary outcomes identified in the section Methods should also be provided. Extra or supplementary materials and technical details can be placed in supplementary documents.

2.3.2.4 Conclusions

It should state clearly the main conclusions and include the explanation of their relevance or importance to the field.

2.3.3 Back Matter

2.3.3.1 Acknowledgments

Anyone who contributed towards the article but does not meet the criteria for authorship, including those who provided professional writing services or materials, should be acknowledged. Authors should obtain permission to acknowledge from all those mentioned in the Acknowledgments section. This section is not added if the author does not have anyone to acknowledge.

2.3.3.2 Authors' Contributions

Each author is expected to have made substantial contributions to the conception or design of the work, or the acquisition, analysis, or interpretation of data, or the creation of new software used in the work, or have drafted the work or substantively revised it.

Please use Surname and Initial of Forename to refer to an author's contribution. For example: made substantial contributions to conception and design of the study and performed data analysis and interpretation: Salas H, Castaneda WV; performed data acquisition, as well as provided administrative, technical, and material support: Castillo N, Young V.

If an article is single-authored, please include "The author contributed solely to the article." in this section.

2.3.3.3 Availability of Data and Materials

In order to maintain the integrity, transparency and reproducibility of research records, authors should include this section in their manuscripts, detailing where the data supporting their findings can be found. Data can be deposited into data repositories or published as supplementary information in the journal. Authors who cannot share their data should state that the data will not be shared and explain it. If a manuscript does not involve such issue, please state "Not applicable." in this section.

2.3.3.4 Financial Support and Sponsorship

All sources of funding for the study reported should be declared. The role of the funding body in the experiment design, collection, analysis and interpretation of data, and writing of the manuscript should be declared. Any relevant grant numbers and the link of funder's website should be provided if any. If the study is not involved with this issue, state "None." in this section.

2.3.3.5 Conflicts of Interest

Authors must declare any potential conflicts of interest that may be perceived as inappropriately influencing the representation or interpretation of reported research results. If there are no conflicts of interest, please state "All authors declared that there are no conflicts of interest." in this section. Some authors may be bound by confidentiality agreements. In such cases, in place of itemized disclosures, we will require authors to state "All authors declare that they are bound by confidentiality agreements that prevent them from disclosing their conflicts of interest in this work.". If authors are unsure whether conflicts of interest exist, please refer to the "Conflicts of Interest" of *Microstructures* Editorial Policies for a full explanation.

2.3.3.6 Copyright

Authors retain copyright of their works through a Creative Commons Attribution 4.0 International License that clearly states how readers can copy, distribute, and use their attributed research, free of charge. A declaration "© The Author(s) 2023." will be added to each article. Authors are required to sign License to Publish before formal publication.

2.3.3.7 References

References should be numbered in order of appearance at the end of manuscripts. In the text, reference numbers should be placed in square brackets and the corresponding references are cited thereafter. If the number of authors is less than or equal to six, we require to list all authors' names. If the number of authors is more than six, only the first three authors' names are required to be listed in the references, other authors' names should be omitted and replaced with "et al.". Abbreviations of the journals should be provided on the basis of Index Medicus. Information from manuscripts accepted but not published should be cited in the text as "Unpublished material" with written permission from the source.

References should be described as follows, depending on the types of works:

Types	Examples
Journal articles by individual authors	Weaver DL, Ashikaga T, Krag DN, et al. Effect of occult metastases on survival in node-negative breast cancer. *N Engl J Med* 2011;364:412-21. [DOI: 10.1056/NEJMoa1008108]

Organization as author	Diabetes Prevention Program Research Group. Hypertension, insulin, and proinsulin in participants with impaired glucose tolerance. *Hypertension* 2002;40:679-86. [DOI: 10.1161/01.hyp.0000035706.28494.09]
Both personal authors and organization as author	Vallancien G, Emberton M, Harving N, van Moorselaar RJ; Alf-One Study Group. Sexual dysfunction in 1,274 European men suffering from lower urinary tract symptoms. *J Urol* 2003;169:2257-61. [DOI: 10.1097/01.ju.0000067940.76090.73]
Journal articles not in English	Zhang X, Xiong H, Ji TY, Zhang YH, Wang Y. Case report of anti-N-methyl-D-aspartate receptor encephalitis in child. *J Appl Clin Pediatr* 2012;27:1903-7. (in Chinese)
Journal articles ahead of print	Odibo AO. Falling stillbirth and neonatal mortality rates in twin gestation: not a reason for complacency. *BJOG* 2018; Epub ahead of print [DOI: 10.1111/1471-0528.15541]
Books	Sherlock S, Dooley J. Diseases of the liver and billiary system. 9th ed. Oxford: Blackwell Sci Pub; 1993. pp. 258-96.
Book chapters	Meltzer PS, Kallioniemi A, Trent JM. Chromosome alterations in human solid tumors. In: Vogelstein B, Kinzler KW, editors. The genetic basis of human cancer. New York: McGraw-Hill; 2002. pp. 93-113.
Online resource	FDA News Release. FDA approval brings first gene therapy to the United States. Available from: https://www.fda.gov/NewsEvents/Newsroom/PressAnnouncements/ucm574058.htm. [Last accessed on 30 Oct 2017]
Conference proceedings	Harnden P, Joffe JK, Jones WG, editors. Germ cell tumours V. Proceedings of the 5th Germ Cell Tumour Conference; 2001 Sep 13-15; Leeds, UK. New York: Springer; 2002..
Conference paper	Christensen S, Oppacher F. An analysis of Koza's computational effort statistic for genetic programming. In: Foster JA, Lutton E, Miller J, Ryan C, Tettamanzi AG, Editors. Genetic programming. EuroGP 2002: Proceedings of the 5th European Conference on Genetic Programming; 2002 Apr 3-5; Kinsdale, Ireland. Berlin: Springer; 2002. pp. 182-91.
Unpublished material	Tian D, Araki H, Stahl E, Bergelson J, Kreitman M. Signature of balancing selection in Arabidopsis. *Proc Natl Acad Sci U S A*. Forthcoming 2002.

For other types of references, please refer to U.S. National Library of Medicine.

The journal also recommends that authors prepare references with a bibliography software package, such as EndNote to avoid typing mistakes and duplicated references.

2.3.3.8 Supplementary Materials

Additional data and information can be uploaded as Supplementary Materials to accompany the manuscripts. The supplementary materials will also be available to the referees as part of the peer-review process. Any file format is acceptable, such as data sheet (word, excel, csv, cdx, fasta, pdf or zip files), presentation (powerpoint, pdf or zip files), image (cdx, eps, jpeg, pdf, png or tiff), table (word, excel, csv or pdf), audio (mp3, wav or wma) or video (avi, divx, flv, mov, mp4, mpeg, mpg or wmv). All information should be clearly presented. Supplementary materials should be cited in the main text in numeric order (e.g., Supplementary Figure 1, Supplementary Figure 2, Supplementary Table 1, Supplementary Table 2, etc.). The style of supplementary figures or tables complies with the same requirements on figures or tables in main text. Videos and audios should be prepared in English, and limited to a size of 500 MB.

2.4 Manuscript Format

2.4.1 File Format

Manuscript files can be in DOC and DOCX formats and should not be locked or protected.

2.4.2 Length

There are no restrictions on paper length, number of figures, or number of supporting documents. Authors are encouraged to present and discuss their findings concisely.

2.4.3 Language

Manuscripts must be written in English.

2.4.4 Multimedia Files

The journal supports manuscripts with multimedia files. The requirements are listed as follows:

Video or audio files are only acceptable in English. The presentation and introduction should be easy to understand. The frames should be clear, and the speech speed should be moderate.

A brief overview of the video or audio files should be given in the manuscript text.

The video or audio files should be limited to a size of up to 500 MB.

Please use professional software to produce high-quality video files, to facilitate acceptance and publication along with the submitted article. Upload the videos in mp4, wmv, or rm format (preferably mp4) and audio files in mp3 or wav format.

2.4.5 Figures

Figures should be cited in numeric order (e.g., Figure 1, Figure 2) and placed after the paragraph where it is first cited;
Figures can be submitted in format of TIFF, PSD, AI, EPS or JPEG, with resolution of 300-600 dpi;
Figure caption is placed under the Figure;
Diagrams with describing words (including, flow chart, coordinate diagram, bar chart, line chart, and scatter diagram, etc.) should be editable in word, excel or powerpoint format. Non-English information should be avoided;
Labels, numbers, letters, arrows, and symbols in figure should be clear, of uniform size, and contrast with the background;
Symbols, arrows, numbers, or letters used to identify parts of the illustrations must be identified and explained in the legend;
Internal scale (magnification) should be explained and the staining method in photomicrographs should be identified;
All non-standard abbreviations should be explained in the legend;
Permission for use of copyrighted materials from other sources, including re-published, adapted, modified, or partial figures and images from the internet, must be obtained. It is authors' responsibility to acquire the licenses, to follow any citation instruction requested by third-party rights holders, and cover any supplementary charges.

2.4.6 Tables

Tables should be cited in numeric order and placed after the paragraph where it is first cited;
The table caption should be placed above the table and labeled sequentially (e.g., Table 1, Table 2);
Tables should be provided in editable form like DOC or DOCX format (picture is not allowed);
Abbreviations and symbols used in table should be explained in footnote;
Explanatory matter should also be placed in footnotes;
Permission for use of copyrighted materials from other sources, including re-published, adapted, modified, or partial tables from the internet, must be obtained. It is authors' responsibility to acquire the licenses, to follow any citation instruction requested by third-party rights holders, and cover any supplementary charges.

2.4.7 Abbreviations

Abbreviations should be defined upon first appearance in the abstract, main text, and in figure or table captions and used consistently thereafter. Non-standard abbreviations are not allowed unless they appear at least three times in the text. Commonly-used abbreviations, such as DNA, RNA, ATP, etc., can be used directly without definition. Abbreviations in titles and keywords should be avoided, except for the ones which are widely used.

2.4.8 Italics

General italic words like vs., et al., etc., in vivo, in vitro; t test, F test, U test; related coefficient as r, sample number as n, and probability as P; names of genes; names of bacteria and biology species in Latin.

2.4.9 Units

SI Units should be used. Imperial, US customary and other units should be converted to SI units whenever possible. There is a space between the number and the unit (i.e., 23 mL). Hour, minute, second should be written as h, min, s.

2.4.10 Numbers

Numbers appearing at the beginning of sentences should be expressed in English. When there are two or more numbers in a paragraph, they should be expressed as Arabic numerals; when there is only one number in a paragraph, number < 10 should be expressed in English and number > 10 should be expressed as Arabic numerals. 12345678 should be written as 12,345,678.

2.4.11 Equations

Equations should be editable and not appear in a picture format. Authors are advised to use either the Microsoft Equation Editor or the MathType for display and inline equations.

2.5 Submission Link

Submit an article via https://oaemesas.com/login?JournalId=microstructures.

Microstructures

Los Angeles Office
245 E Main Street ste122, Alhambra,
CA 91801, USA
Tel: +1 323 9987086
E-mail: editorialoffice@microstructj.com
Website: https://www.oaepublish.com/microstructures